Chapter Five

Examination of the Small-Scale Spatial Variability of Keswick Clay

5.1 INTRODUCTION

As described in the previous chapter, an extensive field study, consisting of 223 CPTs drilled to a typical depth of 5 metres, was undertaken in order to provide accurate and closely-spaced data on which small-scale spatial variability analyses could be based. This chapter details these small-scale spatial variability analyses. The following sections are subdivided into the assessment of the vertical and the horizontal spatial variability of the Keswick Clay, using random field theory and geostatistics. However, before presenting these analyses, it is necessary, first, to discuss the development of 3 computer programs, *SemiAuto*, *Monte*, and *CPTSpace*, written by the author to facilitate these calculations.

5.2 DEVELOPMENT OF SOFTWARE

Details of the development, assessment, validation and an itemisation of the features of each of the three programs are given below.

5.2.1 *SemiAuto*

A number of relatively inexpensive and publicly available programs enable the user to perform time series and geostatistical analyses. For example, *PEST* (Brockwell and Davis, 1991), which is a time series modelling package; and *GEO-EAS* (Englund and Sparks, 1988) and *GSLIB* (Deutsch and Journel, 1991), which are geostatistical software, provide facilities for performing spatial variability analyses. However, while these packages are

very useful, as will be seen later, each of the programs suffer from a number of limitations. For example, *PEST*:

- makes no allowance for missing data which, as was shown in §3.4.3.2, is a fundamental aspect of the measured CPT data;

- restricts the calculation of the autocorrelation, and partial autocorrelation, coefficients to a maximum of 40 lags, which is equivalent to a distance of 200 mm when a sampling interval of 5 mm is used;

- allows only one column of data to be input, which implies that the CPT data files require extensive pre-processing.

On the other hand, *GEO-EAS* limits the input data to a maximum of 1,000 rows; that is, with a 5 mm sampling interval, a maximum CPT depth of 5 metres. Furthermore, *GEO-EAS* and *GSLIB* provide no data transformation facilities, such as trend removal and differencing. In addition, the process of model fitting is extremely inefficient due to the large amount of pre-processing required, as well as the fact that these programs are each based on the MS-DOS®[22] environment, which provides relatively cumbersome input and output facilities. As a consequence, a PC-based computer program, *SemiAuto*, was written: to provide an efficient and accurate tool to enable random field theory and geostatistical analyses to be carried out simultaneously; to account for missing data within these analyses; and to simplify the process of model fitting. *SemiAuto* was written using Visual Basic® Version 3.0 Professional Edition, and was chosen because of its straightforward ability to utilise many of the excellent graphical features which are characteristic of the Windows™ environment. The output of *SemiAuto* was extensively checked and compared with similar results generated by *PEST*, *GEO-EAS* and *GSLIB*, using data obtained from a number of sources (e.g. Bowerman and O'Connell, 1979; Clark, 1979; Brockwell and Davis, 1987). As an example, Clark (1979) presented percentage zinc data from a hypothetical lead/zinc deposit, which included missing data, as well as results of semivariogram calculations. These data were input into *SemiAuto*, and the results are shown in Figure 5.1. As is evident from this figure, the experimental semivariogram results given by *SemiAuto* are identical to those given by Clark (1979).

Among its features, *SemiAuto* reads a CPT, or other data file, and allows the user to:

- evaluate the basic statistics of the data, e.g. mean, standard deviation, variance, *CV*, etc.;
- perform data transformation (removal of the mean or trend function, in addition to performing first-, and second-order differencing);

[22] **M**icro**s**oft **D**isk **O**perating **S**ystem.

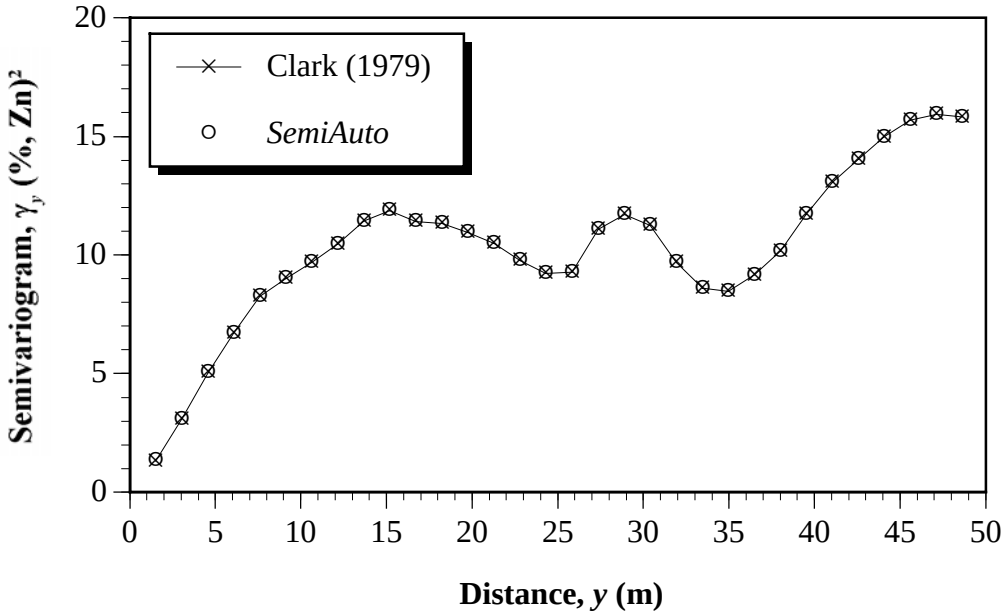

Figure 5.1 Comparison of semivariogram output by *SemiAuto* with that given by Clark (1979).

- calculate the undrained shear strength from the measured values of q_c;
- plot the data and trend function (linear, quadratic, or cubic) with depth;
- calculate and plot the semivariogram, and autocorrelation, partial autocorrelation and cross-correlation functions;
- assess the stationarity of the data by performing the runs test and Kendall's τ test;
- fit standard models to the semivariogram, e.g. spherical, linear, exponential, etc.;
- evaluate the global statistics, maxima and minima, and histograms of several CPT data files;
- save the transformed data, and the calculated semivariograms and time series functions, to a text file for subsequent analyses and presentation.

An example of a typical screen from *SemiAuto* is shown in Figure 5.2. The majority of the spatial variability analyses presented in this chapter utilise *SemiAuto*, in one form or another.

5.2.2 *Monte*

The computer program, *Monte*, was written to allow the user to generate random realisations of various ARIMA models. *Monte* uses the *Monte Carlo Method* to produce a given number of random realisations of time series models, using either classically

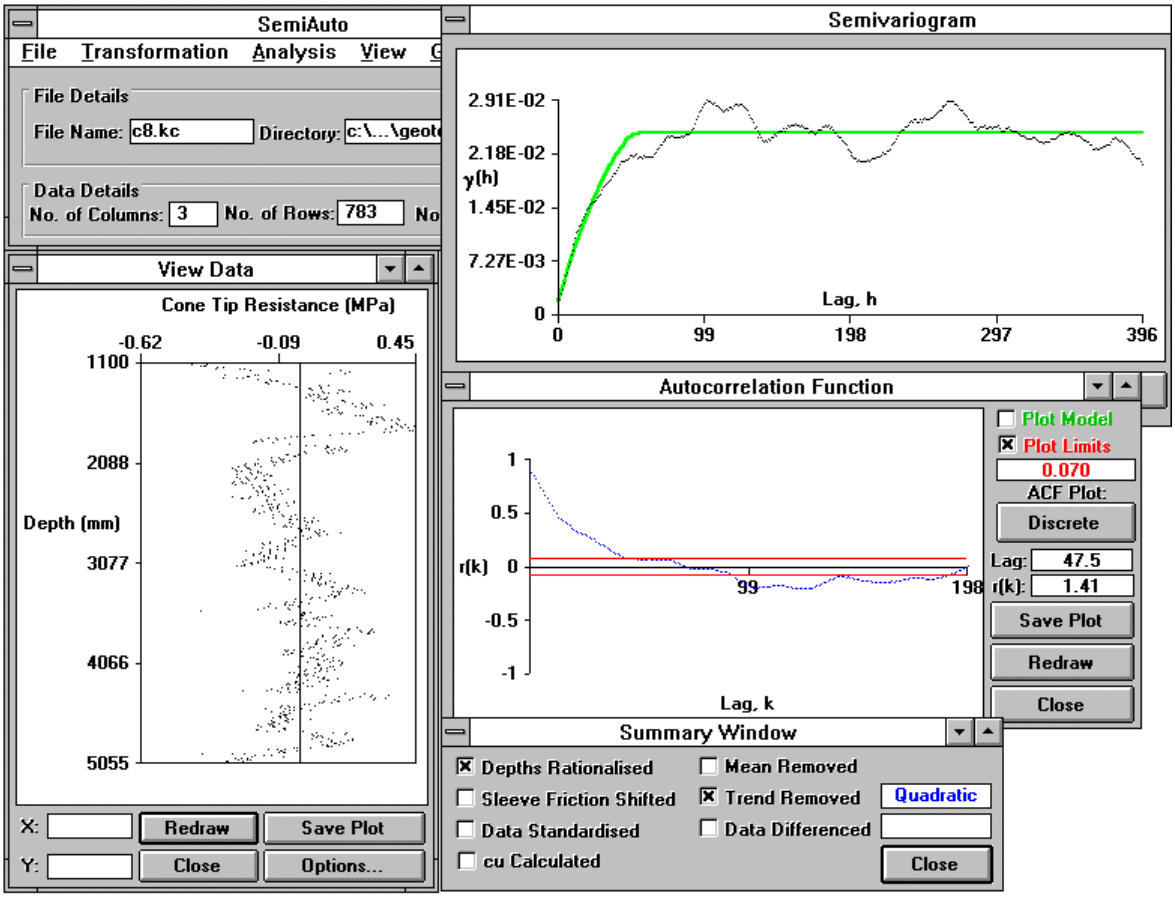

Figure 5.2 A typical screen from *SemiAuto*.

transformed data or differenced data. *Monte* was also written using the Visual Basic programming environment, and allows the user to specify: the number of realisations; the depth range over which data will be generated; the ARIMA parameters and the distribution of the random process, a_t. In addition, *Monte* enables the user to save to a file: the individual realisations; the minimum and maximum envelopes of the realisations; the histogram of the generated data; as well as the histogram of a_t. A typical screen from *Monte* is shown in Figure 5.3.

Monte is used in §5.4.2.3 to demonstrate the usefulness of ARIMA models as data simulators. The results given by *Monte* were thoroughly tested by comparing them with the original data, and by relating the autocorrelation and partial autocorrelation functions with those of the ARIMA model. Typical results are presented in §5.4.2.3.

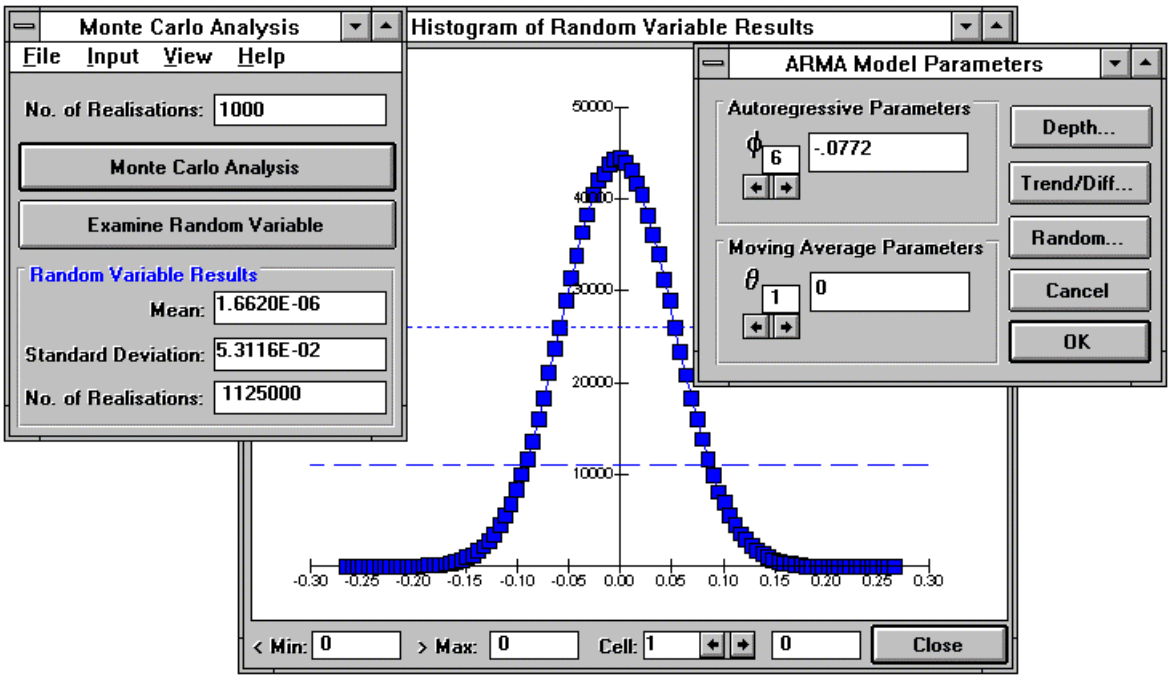

Figure 5.3 A typical screen from the program *Monte*.

5.2.3 *CPTSpace*

Lastly, the program *CPTSpace* was developed to allow the user to generate data sets with a specified data spacing and start depth. *CPTSpace* was written in Turbo Pascal Version 6.0, and is similar in operation and appearance to *CPTView* and *CPTPlot*. By specifying a data spacing of *n*, and a starting depth, *CPTSpace* first rationalises the data and then saves every *n*th row of measurements, commencing at the start depth, to a user specified data file. *CPTSpace* is used in §5.4.3.1 to enable forecasts to be made using geostatistics, and in §5.5 to investigate the sensitivity of spatial variability parameters with respect to sample spacing.

5.3 ANALYSIS OF SPATIAL VARIABILITY OF KESWICK CLAY

This section details both random field theory and geostatistical analyses, performed to quantify the small-scale spatial variability of the undrained shear strength of the Keswick Clay, and will be confined to the data obtained at the South Parklands and Keswick sites. (The large-scale spatial variability of the undrained shear strength of the Keswick Clay will be examined in Chapter 7). As detailed in the previous chapter, because of the uncertainty associated with the evaluation of N_k and, hence, the conversion of q_c to s_u, the spatial variability analyses are based on 'actual' measured values of q_c and f_s, and not 'derived'

values of s_u. Since q_c is related to s_u, it is assumed that the spatial variability models and results pertain to q_c, as well as to the undrained shear strength, s_u, of the Keswick Clay.

5.3.1 Vertical Spatial Variability

Firstly, in order to evaluate the global statistics, maxima and minima, and histograms of q_c for the entire CPT data set obtained from the South Parklands, the program *SemiAuto* was used[23]. Since the field study was carried out over two separate periods, it is necessary to distinguish between the two sets of results. The general statistics of the entire set of q_c data from the South Parklands site are summarised in Table 5.1. The measurements have been divided into two data sets because of the two distinct periods over which the CPTs were performed, as detailed in §4.3.2.

Table 5.1 Global statistics of measurements of q_c from all CPTs performed at the South Parklands site.

CPT Data	No. of Data	Mean (MPa)	Std. Dev.	*CV* (%)	Skew.	Kurt.
All CPTs except CD1 to CD50	182,088	2.953	1.737	58.82	2.422	10.93
CD1 to CD50	49,533	3.284	2.686	81.79	2.638	9.544

It is evident from Table 5.1 that the global statistics for both the data sets are similar, though the data from CD1 to CD50 exhibit a greater variation than the former measurements, as indicated by the higher value of *CV*. Figures 5.4 and 5.5 show the envelopes of maxima and minima for the two data sets. These figures clearly demonstrate a significant variation in the measurements of q_c across the study region. The figures also demonstrate that the depth over which large values of q_c occur are approximately 3.5 metres in Figure 5.4, and 1.8 metres in Figure 5.5. These values are associated with the largest depths at which the upper surface of the Keswick Clay was encountered.

Figure 5.6 shows a histogram of measurements of q_c for each of the two data sets. It is evident from this figure that both histograms are essentially the same and, hence, there are no significant differences in the shear strength of the soil between the two periods of field testing measurement. One likely reason that the histogram for measurements from CPTs CD1 to CD50 has a higher peak than the former data set is that the CD1 to CD50 data set

[23] The measurements of f_s are examined in §5.5.3.4.

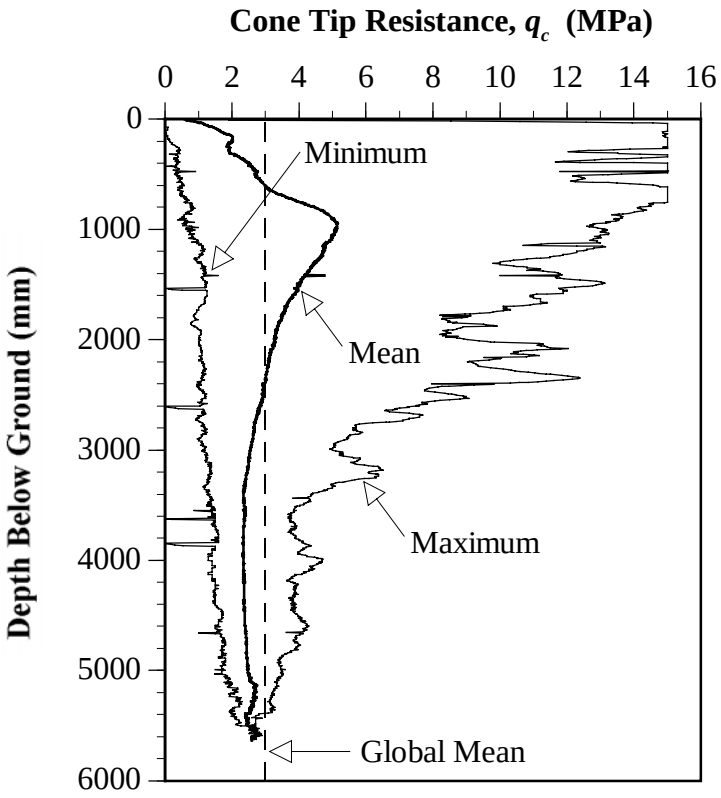

Figure 5.4 Envelope of maxima and minima of measurements of q_c from all CPTs performed at the South Parklands site, except for CD1 to CD50.

contains a larger population of Keswick Clay measurements, as shown previously in Figures 5.4 and 5.5. In addition, Figure 5.6, as well as the values of skewness and kurtosis given in Table 5.1, indicate that the histograms are skewed to the right-hand side and exhibit a sharply peaked distribution.

Of the 222 vertical CPTs performed at the South Parklands site, the results of 30 have been investigated in detail in order to examine the small-scale, vertical spatial variability of the Keswick Clay. For each CPT the following steps were carried out:

1. The CPT profile was first edited to remove measurements performed on soils other than Keswick Clay. This was achieved by referring to Table 5.2, which shows the depth to Keswick Clay below the ground surface at each CPT sounding. Table 5.2 was obtained by interpolation with respect to the nine measured depths (shown in bold) by means of the commercial contouring package, *Surfer*® [24]. Generally, the depths used were slightly in excess of those shown in Table 5.2, so as to account for local depth variations due to gilgais and interpolation errors. In this way a Keswick Clay CPT file was created.

[24] *Surfer* is a registered trademark of Golden Software, Inc., P.O. Box 281, Golden, Colorado, 80402.

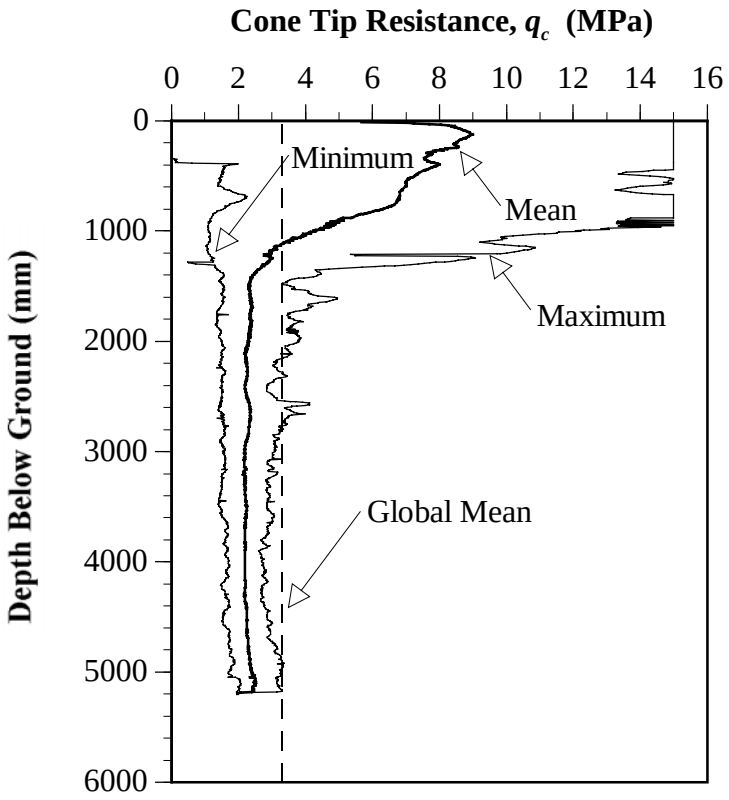

Figure 5.5 Envelope of maxima and minima of measurements of q_c from CPTs CD1 to CD50 performed at the South Parklands site.

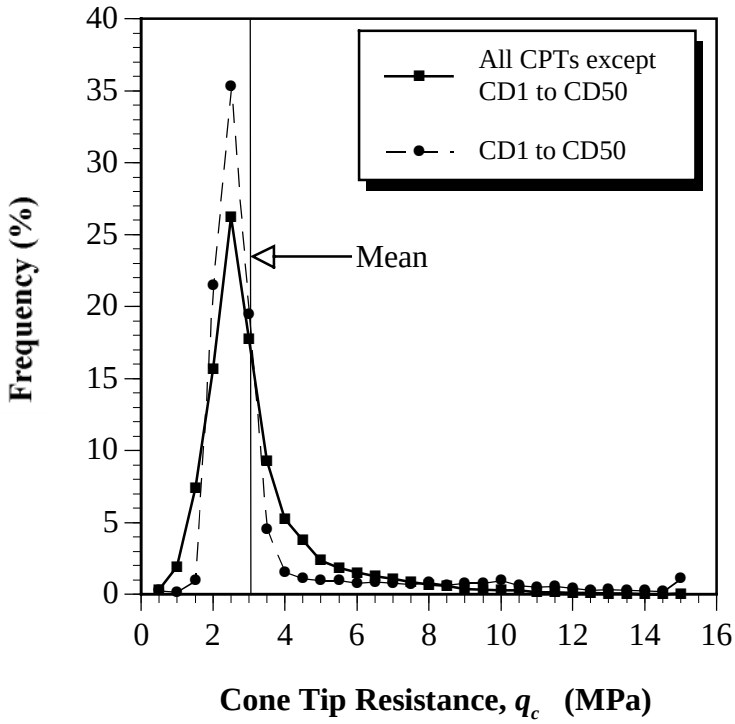

Figure 5.6 Histograms of measurements of q_c from all CPTs performed at the South Parklands site.

Table 5.2 Interpolated depths below ground to the surface of the Keswick Clay, relevant to the CPTs performed at the South Parklands Site.

Ref	0	1	2	3	4	5	6	7	8	9	10
A	**2.30**	2.29	2.26	2.22	2.16	2.08	2.00	1.99	2.23	2.95	**3.40**
B	2.29	2.28	2.28	2.23	2.14	2.01	1.84	1.61	1.55	2.24	2.95
C	2.28	2.28	**2.30**	2.25	2.11	1.95	1.74	1.39	**1.10**	1.54	2.23
D	2.27	2.27	2.26	2.18	2.01	1.87	1.76	1.54	1.39	1.61	1.98
E	2.28	2.25	2.19	2.07	1.86	1.73	1.75	1.75	1.73	1.82	1.97
F	2.33	2.27	2.19	2.03	1.76	**1.60**	1.72	1.85	1.91	1.96	2.03
G	2.41	2.35	2.28	2.13	1.90	1.76	1.84	1.97	2.04	2.06	2.08
H	2.52	2.43	2.38	2.30	2.12	2.01	2.02	2.11	2.15	2.13	2.11
I	2.70	2.49	**2.40**	2.38	2.26	2.16	2.13	2.17	**2.20**	2.16	2.10
J	3.07	2.76	2.49	2.43	2.33	2.23	2.17	2.16	2.16	2.10	2.04
K	**3.30**	3.07	2.70	2.51	2.38	2.28	2.20	2.16	2.12	2.04	**2.00**

Note: Measured depths are shown in **bold**.

2. The Keswick Clay CPT file was loaded into *SemiAuto* and the depths were then rationalised, to enable the sleeve friction to be shifted and also to account for missing depths. In addition, depth rationalisation allows the semivariogram, the auto-correlation and partial autocorrelation functions to be evaluated correctly, as well as reducing their calculation times.

3. Trend functions were evaluated using the method of ordinary least squares (OLS) and, in each case, a quadratic trend was subtracted from the q_c data.

4. The residuals were then examined for stationarity by the processes of eyeballing, examination of the sample ACF and experimental semivariograms, and by performing the runs test and Kendall's τ test, as described in §2.5.1.4. In all but one case, the residuals were found to be stationary after the removal of a quadratic trend.

5. The sample autocorrelation function (ACF) was calculated in accordance with Equation (2.27).

6. Vanmarcke's simple exponential and squared exponential models (Table 2.9) were fitted to the ACF using the method of OLS.

7. Bartlett's limits were calculated using: $|r_k| = \frac{2}{\sqrt{n}}\left(1 + 2\sum_{i=1}^{k-1} r_i^2\right)^{1/2} \approx \pm\frac{1.96}{\sqrt{n}}$, as described in §2.5.1.2(iii).

8. The scale of fluctuation, δ_v, was evaluated using the relationships shown in Table 2.9.

9. The semivariogram was calculated in accordance with Equation (2.49).

10. A model semivariogram was fitted using *SemiAuto*, which allows the user to adjust the model by eye, as recommended by Journel and Huijbregts (1978) and Clark (1979). In every case an appropriate spherical model was found to fit the experimental semivariogram.

The results of the random field theory and geostatistical analyses are treated separately below.

5.3.1.1 Random Field Theory Analyses

In order to illustrate the evaluation process indicated in the previous section, a typical CPT sounding, C8, is used. The measurements of q_c plotted against depth below the ground surface are shown in Figure 5.7. As indicated by the continuous core sample (Figure 4.7), and in Table 5.2, the surface of the Keswick Clay was encountered at a depth of 1,100 mm below the ground surface. Hence, the upper 1,100 mm of q_c measurements is removed from the data set, the result of which is shown in Figure 5.8.

The CPT data, measured within the Keswick Clay for sounding C8, are then loaded into *SemiAuto*, the depths are rationalised, and a series of trends are calculated using the method of OLS. The resulting quadratic trend, as shown in Figure 5.8, is found to exhibit strong correlation with the measured q_c data, with a coefficient of determination, r^2 = 0.719. The OLS linear trend, on the other hand, exhibits weak correlation, since r^2 = 0.088. The presence of the quadratic trend suggests that the data are non-stationary and should, therefore, be removed. It was shown in Chapter 2, and it will be further observed in the following chapter, that the Keswick Clay is overconsolidated as a result of desiccation. Overconsolidated soils generally exhibit a quadratic variation of s_u with depth and, as a consequence, it is entirely appropriate to remove such a trend. Hence, the resulting OLS quadratic trend, shown in Equation (5.1), is subtracted from the measured data set, as shown in Equation (5.2). The resulting, detrended data set, also known as the *residuals*, R_{q_c}, is shown in Figure 5.9.

$$\overline{q}_c = 3.12 - 1.16\times10^{-3}y + 2.01\times10^{-7}y^2 \qquad (5.1)$$

where: $\overline{q}_c$ is the OLS best fit, quadratic function of cone tip resistance in MPa;
y is the vertical distance in mm.

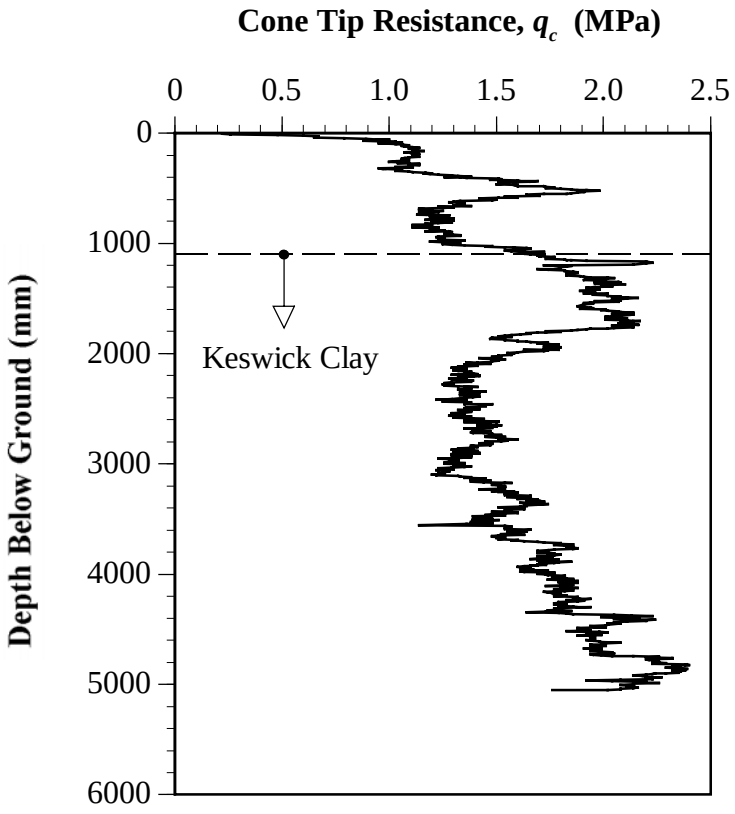

Figure 5.7 Measured cone tip resistance, q_c, for sounding C8.

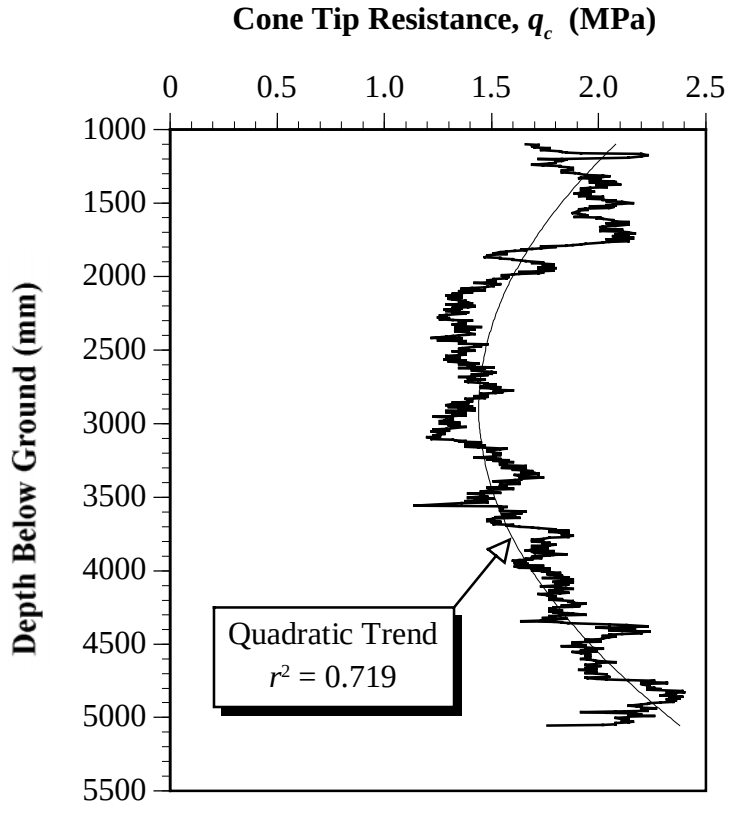

Figure 5.8 Measured cone tip resistance, q_c, within Keswick Clay for sounding C8.

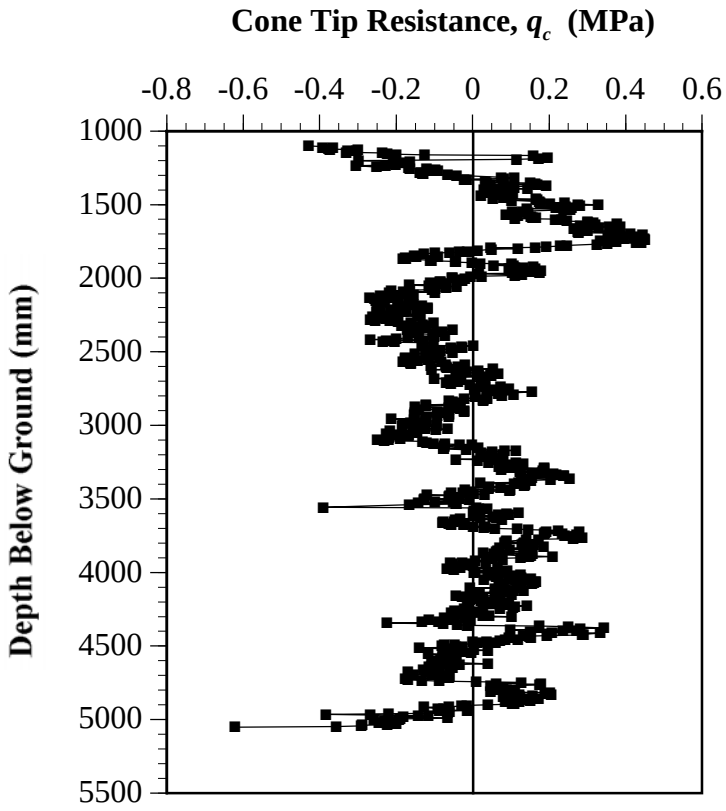

Figure 5.9 Residuals of q_c, for sounding C8, after removing the quadratic trend.

$$R_{q_c} = q_c - \left(3.12 - 1.16\times10^{-3}y + 2.01\times10^{-7}y^2\right) \tag{5.2}$$

As can be seen from Figure 5.9, the data set of the residuals appears to be stationary since there is no apparent trend with depth, and there are no obvious indications that variance is a function of depth. As a check, the detrended data are subjected to the runs test and Kendall's τ test, with the following results being obtained:

- Runs test: $n_1 = 378$; $n_2 = 400$; $n_3 = 0$; $R = 69$ and $z_R = -23.03$ $\therefore$ Fail;
- Kendall's τ test: $S = 13{,}175$; $\tau = 0.044$; $c = 1.091$ and $z_\tau = 1.820$ $\therefore$ Pass.

As is evident from Figure 5.9, the residuals are consistently over or under the mean and, as a consequence, in this case, the runs test may be an inappropriate measure of data stationarity. In contrast, the data set passes Kendall's τ test and, as will be seen later, the sample ACF and the experimental semivariogram also suggest that the data are stationary. Before proceeding, however, it is worth noting that by removing an nth order trend, lower order trends, that is $n-1$, $n-2$, …, 1, are also removed. For example, by eliminating a quadratic trend, a linear drift is also removed, such that the remaining residuals have a mean of zero.

The sample ACF obtained by substituting the residuals, shown in Figure 5.9, into Equation (2.27), is shown in Figure 5.10. Superimposed on the sample ACF in Figure 5.10, are models suggested by Vanmarcke (1977a, 1983), as given previously in Table 2.9.

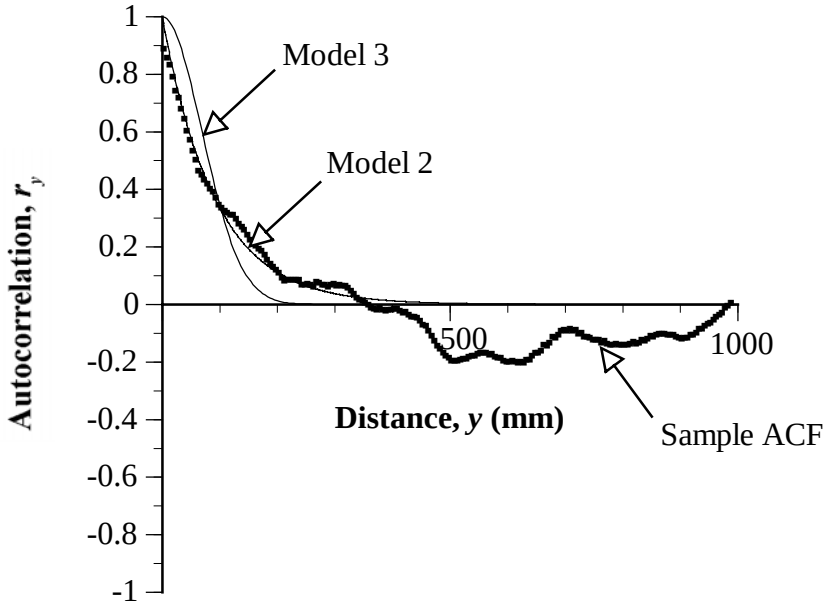

Figure 5.10 Sample and model ACFs obtained from the residuals of q_c for C8.

The models are fitted using the method of OLS, from which the following parameters were obtained:

Model 2: $$\rho_y = e^{-|y|/b} \quad \text{where: } b = 91.4 \text{ mm} \tag{5.3}$$

Model 3: $$\rho_y = e^{-(|y|/c)^2} \quad \text{where: } c = 96.7 \text{ mm} \tag{5.4}$$

The scale of fluctuation, δ_V, is then calculated, for each model, by substituting each parameter into the relevant relationship, as given in Table 2.9. That is:

Model 2: $$\delta_{V_2} = 2b = 182.7 \text{ mm} \tag{5.5}$$

Model 3: $$\delta_{V_3} = \sqrt{\pi}\, c = 171.4 \text{ mm} \tag{5.6}$$

In addition, *Bartlett's limits* are determined as:

$$\text{Bartlett's limit} = \pm 1.96/\sqrt{n} = \pm 1.96/\sqrt{769} = \pm 0.071 \tag{5.7}$$

By superimposing Bartlett's limits onto the sample ACF, the distance termed *Bartlett's distance*, r_B, over which the samples are autocorrelated is determined and is shown in Figure 5.11.

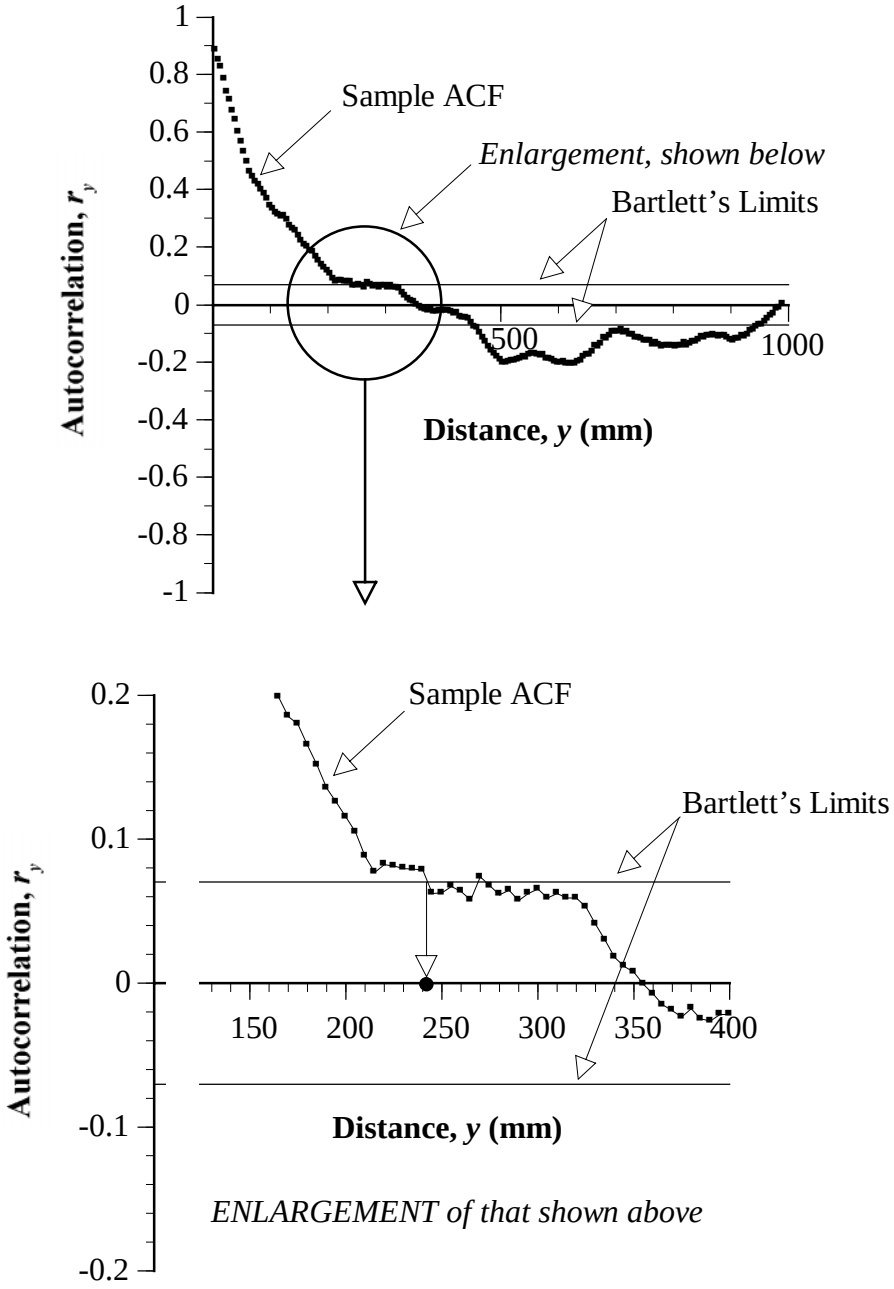

Figure 5.11 Sample ACF, showing Bartlett's limits, obtained from the residuals of q_c for sounding C8, and used to evaluate Bartlett's distance.

It is evident from Figure 5.11 that the sample ACF intersects Bartlett's limits at a distance of approximately 240 mm. Hence r_B = 240 mm.

The process described above was used in each of the detailed analyses performed on the 30 vertical CPTs[25], the results of which are summarised in Table 5.3. As shown in this table, the vertical scale of fluctuation, δ_V, varies between 63 mm and 255 mm, with a mean of 151.5 mm and a coefficient of variation equal to 30.3%. Bartlett's distance, on the other hand, varies between 60 and 240 mm, has a mean of 147.8 mm and a coefficient of variation of 33.4%. One would have confidence in the estimates of δ_V and r_B, as they are based on populations with a large number of data points, as indicated in Table 5.3. The similarity in the results obtained for δ_V and r_B begs the question of the actual relationship between these two parameters. Figure 5.12 shows a plot of δ_V against r_B for the 30 CPTs examined in detail. Figure 5.12 shows a strong correlation between these two parameters. In fact, the OLS line of best fit has properties of r^2 = 0.893, and is expressed by the following function:

$$\delta_V = 0.939 r_B + 14.05 \tag{5.8}$$

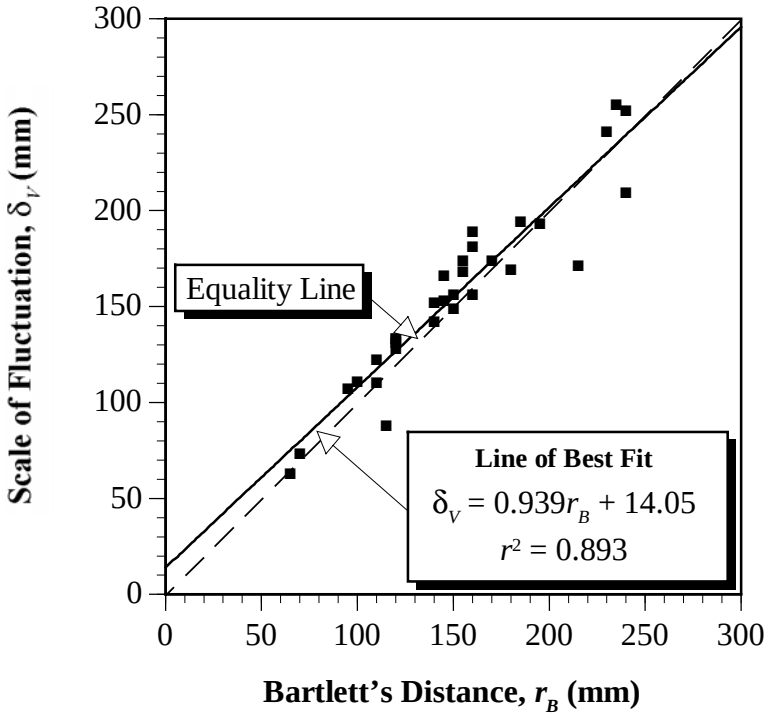

Figure 5.12 Relationship between the scale of fluctuation, δ_V, and Bartlett's distance, r_B.

[25] The measured values of q_c, f_s and F_R for each of the 30 CPTs are shown graphically in Appendix A. In addition, the complete CPT data for C8 are included in Appendix A.

Table 5.3 Results of random field theory analyses on detrended residuals of q_c measurements obtained from 30 of the 222 vertical CPTs at the South Parklands site.

CPT No.	Depth (mm)		No. of Data	Autocorrelation Function			
	Min.	Max.		r_B (mm)	r_1	δ_{V_2} (mm)	δ_{V_3} (mm)
A0	2305	5045	546	195	0.908	172	193
A1	2500	5105	517	150	0.903	126	156
A2	3000	5095	416	150	0.809	168	149
A4	2500	5245	545	145	0.964	141	166
A6	2500	5135	525	160	0.984	166	189
A8	3000	5040	405	65	0.785	71	63
A10	3400	5055	327	185	0.890	170	194
B1	2600	5090	494	70	0.802	63	73
B5	2300	5130	564	120	0.895	116	133
B8	2500	5045	505	110	0.779	100	110
C0	2300	5035	542	100	0.924	104	111
C4	2200	5020	560	120	0.938	126	128
C8	1100	5055	783	240	0.884	183	171
C10	2700	5050	466	120	0.954	122	133
CD1	2500	5020	501	230	0.980	216	241
CD30	3000	5015	400	95	0.954	96	107
D5	2500	4945	488	155	0.887	150	168
D8	2400	5045	525	140	0.892	124	152
E1	2200	5125	581	155	0.982	171	174
E7	2205	5030	560	170	0.863	166	174
G0	2000	5035	603	120	0.966	160	131
G5	2000	5025	602	240	0.904	245	252
G10	2200	5005	557	160	0.964	161	181
H7	2200	5045	564	110	0.956	120	122
H10	2300	5120	559	160	0946	131	156
I1	2100	5150	605	240	0.960	186	209
I9	2200	5120	579	180	0.904	154	169
J8	2200	5025	560	115	0.753	92	88
K0	3305	5275	393	145	0.981	143	153
K10	2005	5020	599	235	0.950	244	255
Average				**152.8**	**0.909**	**146.2**	**156.7**
Standard Deviation				**49.4**	**0.07**	**44.1**	**47.4**
Coefficient of Variation				**32.3%**	**7.2%**	**30.2%**	**30.3%**

Note: The measured data associated with each of the 30 CPTs are shown graphically in Appendix A.

An explanation of each of the following parameters is given later in this section.

r_B *Bartlett's distance* - the distance at which the sample ACF intersects the limit obtained from Bartlett's formula;

r_1 the autocorrelation coefficient at lag 1. These values will be discussed in §5.5;

δ_{V_2}; δ_{V_3} scale of fluctuation obtained by fitting Vanmarcke's *simple exponential* and *squared exponential* models, respectively, to the sample ACF (Models 2 and 3 in Table 2.9).

As can be seen, Equation (5.8) is close to the equality line and, hence for all practical purposes, one can assume that r_B expresses the same quantity as that given by the scale of fluctuation, δ_v. This is significant since it is more straightforward to evaluate Bartlett's distance than δ_v. Hence, as Bartlett's distance expresses the extent over which a parameter exhibits autocorrelation, the scale of fluctuation may also be defined as such. This suggests that the term *correlation distance*, assigned previously to the parameter v_o by Vanmarcke and Fuleihan (1975), may be an inappropriate use of this term, since both r_B and δ_v are essentially expressions of the *correlation distance*, whereas v_o is not the same as δ_v or r_B, as indicated previously in §2.5.2.1. For the remainder of this thesis the term "*correlation distance*" will refer to the extent over which samples exhibit strong autocorrelation, which is synonymous with the definition of δ_v and r_B, and will *not* refer to the explanation given by Vanmarcke and Fuleihan (1975).

The results of tests to assess the stationarity of the residual data, that is, the runs test and Kendall's τ test, are shown in Table 5.4. It can be seen from this table that all 30 detrended data sets failed the runs test, yet all but K10 passed Kendall's τ test. In addition, all 30 of the detrended data sets passed the eyeball test and, inspection of the sample ACF and experimental semivariogram. In addition, when each of the 30 data sets were first-, or second-differenced, none of the transformed data sets passed the runs test. This is contrary to the other four tests which indicated data stationarity. It is evident from this, that the runs test may be a poor indicator of data stationarity for large values of n_1 and n_2.

As a result of the foregoing analyses, within the Keswick Clay, the vertical extent over which the cone tip resistance is autocorrelated (that is, the correlation distance in the vertical direction) is of the order of 150 mm, and varies between 60 mm and 240 mm, as shown in Table 5.3.

The next section presents the results of the geostatistical analyses performed on the same 30 CPTs, and allows comparisons to be made between δ_V, r_B and the range of influence, a.

5.3.1.2 Geostatistical Analyses

Again using sounding C8 for illustrative purposes, and the process detailed in §5.3.1, the experimental semivariogram was evaluated using *SemiAuto*, and the results are shown in Figure 5.13. A model semivariogram is then fitted by eye. Figure 5.13 shows a spherical model superimposed on the experimental semivariogram, and which is expressed by the following equation:

Table 5.4 Results of the runs tests and Kendall's τ tests performed on detrended residuals of q_c measurements obtained from 30 of the 222 vertical CPTs at the South Parklands site.

CPT	Runs Test					Kendall's τ Test				
No.	n_1	n_2	R	z_R		S	τ	z_τ	c	
A0	275	271	72	–17.31	×	863	0.006	0.203	1.012	✓
A1	245	272	87	–15.71	×	–6166	–0.046	–1.571	0.912	✓
A2	212	204	82	–12.47	×	–1482	–0.017	–0.523	0.966	✓
A4	305	240	52	–18.93	×	5830	0.039	1.373	1.082	✓
A6	234	291	31	–20.28	×	6464	0.047	1.610	1.099	✓
A8	203	202	60	–14.28	×	2686	0.033	0.987	1.068	✓
A10	185	142	43	–13.38	×	2685	0.050	1.359	1.106	✓
B1	259	235	116	–11.87	×	–1251	–0.010	–0.341	0.980	✓
B5	299	265	89	–16.33	×	–7726	–0.049	–1.730	0.907	✓
B8	257	247	82	–15.25	×	84	0.001	0.022	1.001	✓
C0	267	275	40	–19.95	×	–331	–0.002	–0.079	0.995	✓
C4	271	289	29	–21.31	×	2782	0.018	0.629	1.036	✓
C8	378	400	69	–23.03	×	13175	0.044	1.820	1.091	✓
C10	234	231	65	–15.64	×	3306	0.031	0.988	1.063	✓
CD1	262	239	20	–20.70	×	548	0.004	0.146	1.009	✓
CD30	178	222	31	–16.99	×	–196	–0.002	–0.073	0.995	✓
D5	222	266	79	–14.99	×	–3936	–0.033	–1.094	0.936	✓
D8	234	291	67	–17.10	×	6720	0.049	1.674	1.103	✓
E1	316	265	12	–23.20	×	862	0.005	0.184	1.010	✓
E7	268	292	89	–16.23	×	4510	0.029	1.020	1.059	✓
G0	322	281	25	–22.61	×	3975	0.022	0.804	1.045	✓
G5	261	341	77	–18.24	×	1671	0.009	0.339	1.019	✓
G10	256	301	28	–21.32	×	7024	0.045	1.601	1.095	✓
H7	296	267	41	–20.37	×	2099	0.013	0.471	1.027	✓
H10	293	267	49	–19.62	×	2012	0.013	0.455	1.026	✓
I1	318	287	25	–22.66	×	–7090	–0.039	–1.428	0.925	✓
I9	268	310	77	–17.70	×	–5123	–0.031	–1.105	0.940	✓
J8	269	291	139	–11.99	×	–7666	–0.049	–1.733	0.907	✓
K0	215	178	25	–17.40	×	2174	0.028	0.836	1.058	✓
K10	256	343	41	–21.15	×	11653	0.065	2.382	1.139	×

Note: The measured data associated with each of the 30 CPTs are shown graphically in Appendix A.
In all of the 30 cases, the number of ties, T, and $n_3 = 0$.

✓ Passed the test;

× Failed the test.

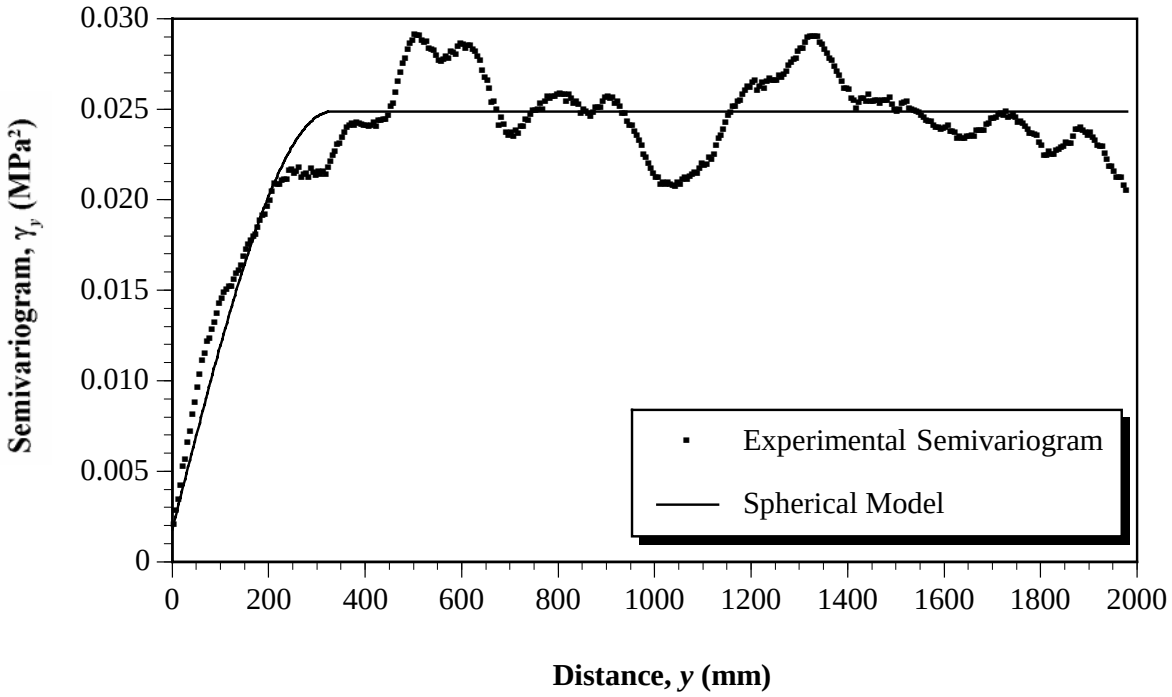

Figure 5.13 Experimental and model semivariograms of residual q_c data from C8.

$$\gamma_y = C\left(\frac{3y}{2a} - \frac{y^3}{2a^3}\right) + C_0 \quad \text{when} \quad y \le a$$
$$\gamma_y = C + C_0 \quad \text{when} \quad y \ge a \tag{5.9}$$

where: a = 330 mm;
C = 0.0231 MPa²;
C_0 = 0.0018 MPa².

As can be seen clearly from Figure 5.13, there is justification for inclusion of a nugget, C_0, within the spherical model. As discussed previously in §2.5.1.3(i), C_0 accounts for microstructures within the geological material, sampling or statistical errors, and random measurement errors. The nugget effect will be discussed in greater detail in §5.5.

The results of the geostatistical analyses performed on the 30 vertical CPTs from the South Parklands are shown in Table 5.5. In each case an appropriate spherical model was found to fit the experimental semivariogram. Three examples of experimental semivariograms, and their associated spherical models, are shown in Figures 5.14 to 5.16. They are included to indicate the variation in how well the spherical model fits the experimental semivariograms obtained. Figure 5.14 shows an example of an *excellent* fit between the spherical model and the experimental semivariogram, whereas Figure 5.15 shows an

Table 5.5 Results of geostatistical analyses performed on measurements of q_c obtained from 30 of the 222 vertical CPTs at the South Parklands site.

CPT No.	Depth (mm)		No. of Data	Semivariogram				
	Min.	Max.		a (mm)	C_0 (MPa²)	C (MPa²)	$C_0/(C+C_0)$	Fit
A0	2305	5045	546	320	1.06×10^{-3}	2.66×10^{-2}	3.8%	G
A1	2500	5105	517	295	1.28×10^{-3}	2.69×10^{-2}	4.5%	G
A2	3000	5095	416	380	6.40×10^{-3}	4.35×10^{-2}	12.8%	G
A4	2500	5245	545	285	2.01×10^{-3}	1.02×10^{-1}	1.9%	G
A6	2500	5135	525	340	0	4.00×10^{-1}	0.0%	G
A8	3000	5040	405	100	1.59×10^{-3}	6.97×10^{-3}	18.6%	Ex
A10	3400	5055	327	375	1.06×10^{-3}	2.86×10^{-2}	3.6%	G
B1	2600	5090	494	125	1.50×10^{-3}	9.19×10^{-3}	14.0%	G
B5	2300	5130	564	210	7.11×10^{-3}	9.43×10^{-2}	7.0%	G
B8	2500	5045	505	215	2.62×10^{-3}	1.52×10^{-2}	14.7%	VG
C0	2300	5035	542	180	1.61×10^{-4}	6.45×10^{-3}	2.4%	F
C4	2200	5020	560	180	1.30×10^{-3}	2.70×10^{-2}	4.6%	VG
C8	1100	5055	783	330	1.77×10^{-3}	2.31×10^{-2}	7.1%	Ex
C10	2700	5050	466	275	1.45×10^{-3}	7.47×10^{-2}	1.9%	F
CD1	2500	5020	501	575	0	9.47×10^{-2}	0.0%	F
CD30	3000	5015	400	175	2.42×10^{-4}	9.80×10^{-3}	2.4%	G
D5	2500	4945	488	330	4.05×10^{-3}	5.43×10^{-2}	6.9%	P
D8	2400	5045	525	315	1.67×10^{-3}	2.03×10^{-2}	7.6%	G
E1	2200	5125	581	265	0	1.94×10^{-1}	0.0%	VG
E7	2205	5030	560	240	1.81×10^{-3}	1.51×10^{-2}	10.7%	F
G0	2000	5035	603	160	2.74×10^{-4}	1.37×10^{-2}	2.0%	G
G5	2000	5025	602	450	3.30×10^{-3}	4.53×10^{-2}	6.8%	Ex
G10	2200	5005	557	345	1.23×10^{-3}	6.43×10^{-2}	1.9%	F
H7	2200	5045	564	200	1.05×10^{-3}	4.70×10^{-2}	2.2%	VG
H10	2300	5120	559	300	1.67×10^{-3}	3.97×10^{-2}	4.0%	VG
I1	2100	5150	605	535	4.55×10^{-4}	2.34×10^{-2}	1.9%	F
I9	2200	5120	579	340	1.15×10^{-3}	1.97×10^{-2}	5.5%	G
J8	2200	5025	560	175	1.39×10^{-3}	4.77×10^{-3}	22.6%	VG
K0	3305	5275	393	240	0	2.15×10^{-2}	0.0%	G
K10	2005	5020	599	430	9.42×10^{-4}	7.01×10^{-2}	1.3%	VG
Average				**289.5**	$\mathbf{1.62\times10^{-3}}$	$\mathbf{5.41\times10^{-2}}$	**5.8%**	-
Standard Deviation				**113.2**	$\mathbf{1.69\times10^{-3}}$	$\mathbf{7.65\times10^{-2}}$	**5.8%**	-
Coefficient of Variation				**39.1%**	**104.4%**	**141.5%**	**99.5%**	-

Note: **The measured data associated with each of the 30 CPTs are shown graphically in Appendix A.**
Fit refers to a subjective assessment of how well the spherical model fits the experimental semivariogram. (Ex: excellent; VG: very good; G: good; F: fair and P: poor).

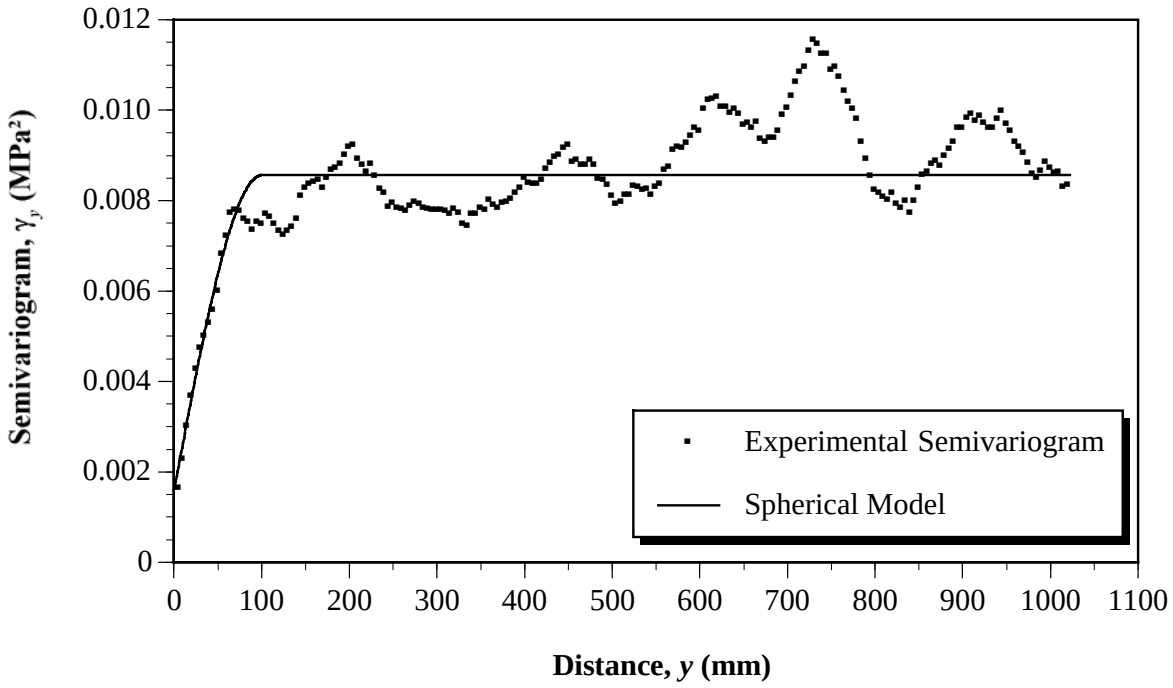

Figure 5.14 Experimental and model semivariograms of residual q_c data from A8 - an example of an *excellent fit*.

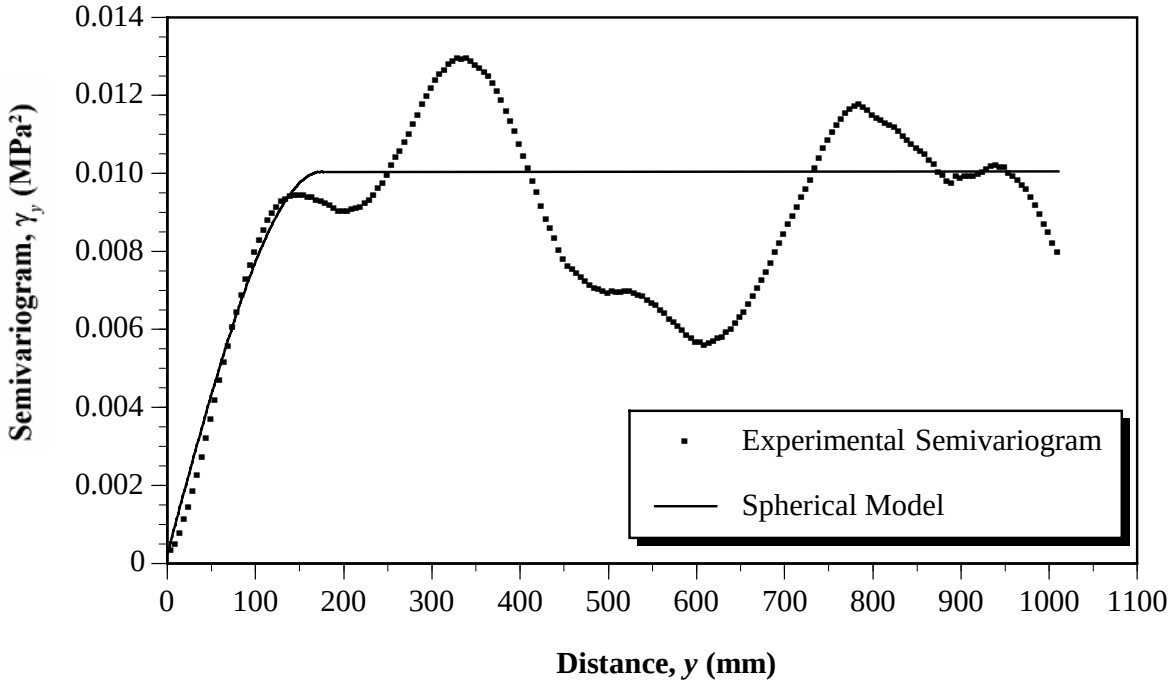

Figure 5.15 Experimental and model semivariograms of residual q_c data from CD30 - an example of a *good fit*.

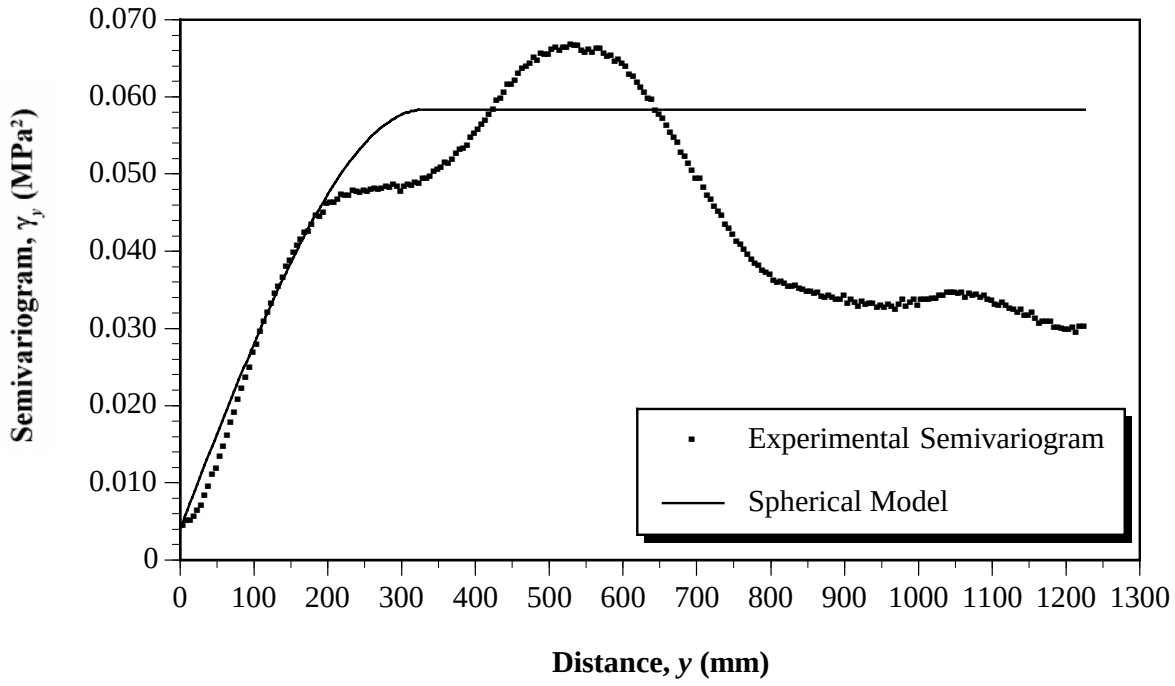

Figure 5.16 Experimental and model semivariograms of residual q_c data from D5 - an example of a *poor fit*.

example of a *good* fit, and Figure 5.16 an example of a *poor* fit. As is evident from these figures, while the experimental semivariogram fluctuates about the sill of the spherical model, that is $C + C_0$, one has confidence that the range, a, and the nugget effect, C_0, are accurately modelled. Furthermore, it can be clearly seen from these figures that the experimental semivariograms are highly regular, that is, there is minimal significant fluctuation between adjacent points. This suggests some degree of confidence with respect to the form of the resulting experimental semivariograms.

Referring to Table 5.5, the range of influence, a, associated with the spherical models varies between 100 mm and 575 mm, with a mean of 289.5 mm and a coefficient of variation, *CV*, of 39.1%. As defined in §2.5.1.3(i), the parameter, a, measures the distance over which samples are correlated. Hence, one would expect the values of a to resemble closely those of δ_V and r_B. While the values of a are similar and within the same order of magnitude as δ_V and r_B, there is some variation between a and the parameters obtained from random field theory analyses. The relationships between a, δ_V and r_B will be examined further, in §5.3.3.

Since the nugget, C_0, and the parameter, C, vary considerably with respect to one another, it is best to examine the ratio between these two variables; that is, the *relative nugget*, $C_0/(C+C_0)$. As shown in Table 5.5, this ratio varies between 0% and 22.6%, with a mean

of 5.8%, and a *CV* of 99.5%. As is evident from the high *CV*, the ratio of C_0 with respect to $C + C_0$ varies considerably. However, an important conclusion is that the nugget effect was evident in 26, or 87%, of the 30 CPTs investigated.

Before concluding this treatment of the vertical spatial variability of the Keswick Clay, it will be necessary, in the following chapters, to combine the small-scale variability model with the large-scale model obtained from measurements of s_u, based on the results of unconsolidated undrained triaxial tests. In order to achieve this, it will be necessary to derive a model based on observations of s_u, rather than on measurements of q_c, as was the case in the preceding analyses. The following section compares the various spatial variability parameters obtained from random field theory and geostatistics, using measurements of q_c, as compared with those obtained using derived values of s_u, via the relationship given previously in Equation (2.5).

5.3.1.3 Spatial Variability Models Derived From s_u Compared With q_c

In Chapter 2, it was shown that the undrained shear strength, s_u, of a clay soil can be determined from the CPT by the following expression, (given previously in Equation (2.5)):

$$s_u = \frac{q_c - \sigma_{v0}}{N_k} \tag{5.10}$$

In Chapter 4, several relationships were examined which yielded estimates for the cone factor, N_k, and it was concluded that no unique and reliable estimate for N_k could be obtained. As a result of this, it was decided to base the spatial variability analyses on measurements of q_c, rather than on derived values of s_u. As a precursor to later analyses, however, it is necessary to examine the effect that varying N_k has on the various random field theory and geostatistical parameters.

Again using CPT C8 as an example, the measurements of q_c within the Keswick Clay, shown previously in Figure 5.8, were converted to values of s_u, via Equation (5.10), by letting N_k = 20 and 40, respectively. The values of σ_{v0} were obtained using:

$$\sigma_{v0} = \gamma z \tag{5.11}$$

where: γ is the bulk unit weight of the clay, which was set at 18 kN/m^3 (Cox, 1970);
z is the depth below ground (m).

In order to satisfy stationarity, the OLS quadratic trend was removed prior to calculating the ACF and semivariogram. Figure 5.17 shows the sample and model ACFs given by N_k = 20 and 40 (the plots are identical), whereas Figures 5.18 and 5.19 show the experimental and model semivariograms given by N_k = 20 and 40, respectively. Since the sample ACF for N_k = 20 is identical to that for N_k = 40, the model ACF, and hence the scale of fluctuation, is independent of N_k. Furthermore, the sample ACFs given by N_k = 20 and 40, are identical to the sample ACF obtained by using the residuals of q_c, shown previously in Figure 5.10. Figures 5.18 and 5.19, on the other hand, indicate that the experimental semivariogram for N_k = 20 is identical to that for N_k = 40, except for the scale of the *y*-axis, or γ_y. In other words, the ranges of influence, *a*, are identical, and only *C* and C_0 depend on the value of N_k.

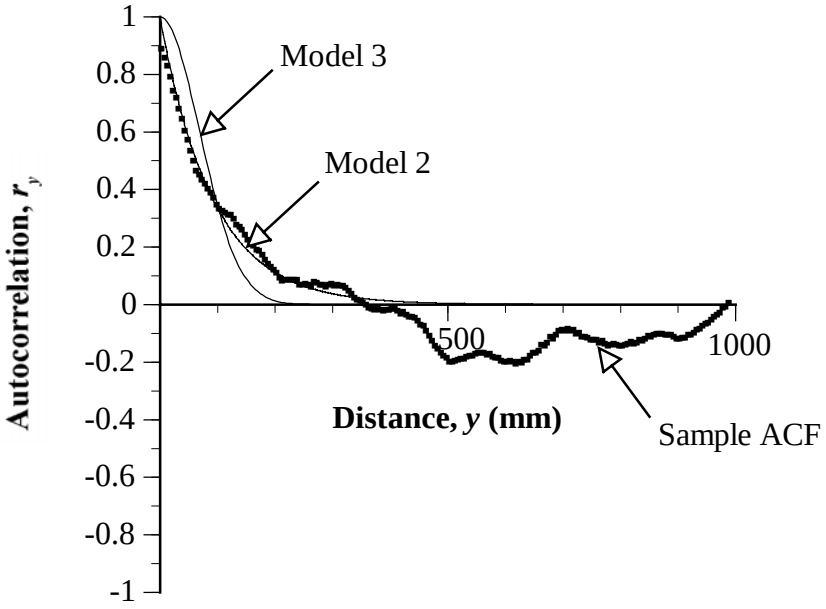

Figure 5.17 Sample and model ACFs of the residuals of s_u, for C8, obtained by converting measurements of q_c using N_k = 20, and 40.

Hence, both the scale of fluctuation, δ_v, and the range of influence, *a*, are independent of N_k. This is an important outcome, which will be used later when developing a general horizontal spatial variability model.

While the analyses, thus far, have been concerned with evaluating the vertical spatial variability of the Keswick Clay, the following two sections deal with quantifying the horizontal spatial variability of this clay.

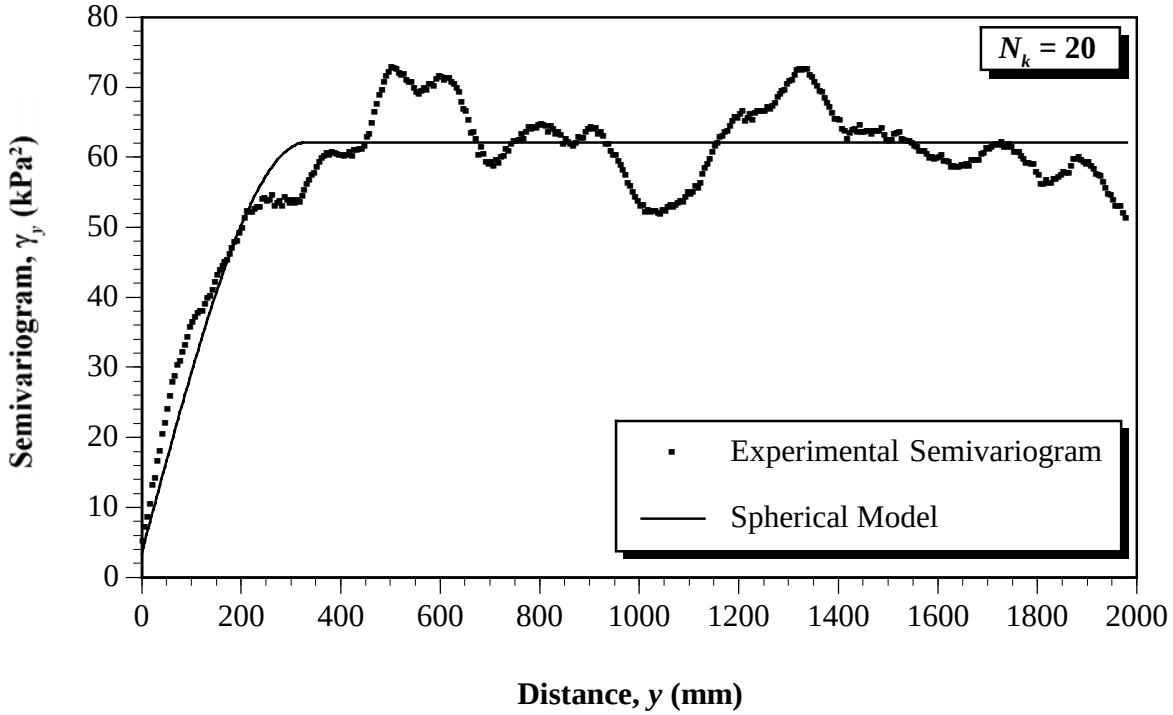

Figure 5.18 Experimental and model semivariograms of the residuals of s_u, for C8, obtained by converting measurements of q_c using N_k = 20.

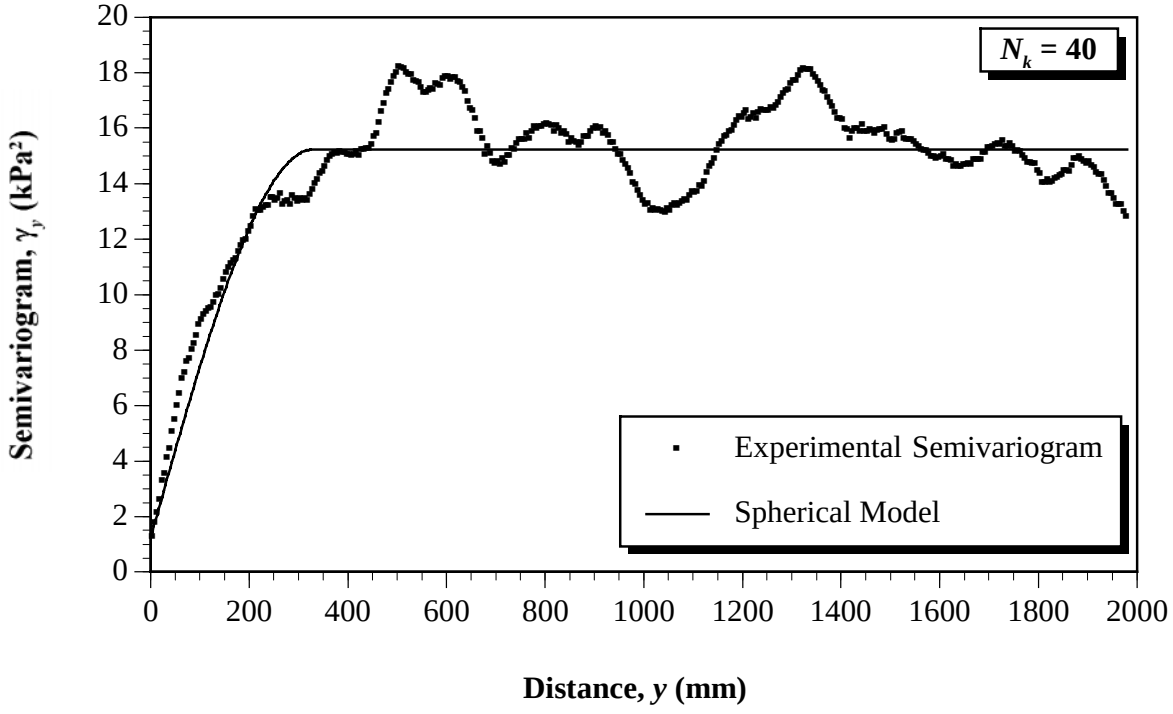

Figure 5.19 Experimental and model semivariograms of the residuals of s_u, for C8, obtained by converting measurements of q_c using N_k = 40.

5.3.2 Horizontal Spatial Variability

The horizontal spatial variability of the Keswick Clay was examined at two sites: the South Parklands site and the Keswick site. The spatial variability analyses associated with each of these sites are treated separately, below.

5.3.2.1 South Parklands Site

The data for the horizontal spatial variability analyses were obtained by examining the measurements of q_c, at a particular depth below the ground surface, for each of the 51 CPTs located along a single line. Only the line consisting of CPTs A5 to K5 was examined, as the F0 to K10 transect contained many unsuccessful soundings and, therefore, contained too much missing information, as indicated in Figure 4.7. Each of the 51 CPTs along the line A5 to K5 were first rationalised so that consistent depths, spaced at 5 mm increments, could be established for each of the soundings. Once this was achieved, the 51 CPTs were combined to form a single data file so that adjacent CPTs were placed in neighbouring columns, as shown in Table 5.6. For example, for a depth of 4,250 mm below the ground, the horizontal spatial variability data consisted of the following values: 3.3, 2.7, 2.9, 3.4, 2.64, 2.96, 2.57, 2.33, 2.68, … , 1.8, 1.7, 2.2, as highlighted in Table 5.6; with each of these data being spaced at one metre intervals.

In order to guarantee that only Keswick Clay data were used to analyse the horizontal spatial variability, measurements of q_c at depths of 3.5, 3.75, 4.0 and 4.25 metres below the ground surface were investigated. These data sets are shown in Figure 5.20.

It is evident from Figure 5.20 that each of the data sets appear to be non-stationary. This is verified by the fact that each of the data sets failed the runs test and Kendall's τ test. However, once the OLS quadratic trend was removed, each of the four data sets satisfied the stationarity constraint. The sample ACFs and experimental semivariograms of the residuals of each data set are shown in Figures 5.21 and 5.22, respectively. Bartlett's distances, r_B, were calculated using the technique detailed previously, and the parameters, a, C_0 and C, were obtained by fitting appropriate spherical models to the experimental semivariograms, an example of which is shown in Figure 5.23. Table 5.7 provides a summary of these parameters.

Table 5.6 Measurements of q_c from vertical CPTs A5 to K5 used to generate horizontal spatial variability data.

Depth	Measured Cone Tip Resistance, q_c (MPa)												
(mm)	A5	A51	A52	A53	A54	B5	B51	B52	B53	...	J53	J54	K5
5	0.7	1.9	1.4	1.28	0.45	0.69	0.92	1.39	1.39	...	0	0	N/A
10	0.7	1.9	1.4	1.39	0.69	0.81	0.92	0.92	1.39	...	0	0	N/A
15	0.5	1.4	0.9	1.16	0.45	0.45	1.39	1.39	1.39	...	0	0	N/A
20	0.8	1.9	1.4	1.39	0.69	0.45	1.39	1.39	1.39	...	N/A	0	N/A
25	0.9	1.9	1.4	1.39	0.45	0.92	1.39	1.39	1.39	...	0.1	0	N/A
30	1	1.9	1.6	1.39	0.45	0.69	1.39	1.39	1.39	...	0.3	0.1	N/A
35	1.1	1.9	1.9	1.63	0.69	0.81	1.39	1.39	1.39	...	0.6	0.2	N/A
40	1.1	1.9	1.9	1.39	0.69	0.92	1.39	1.39	1.39	...	0.8	0.3	N/A
45	1.3	1.9	1.9	1.63	0.45	0.92	1.39	1.39	1.39	...	1	0.5	N/A
50	1.3	1.9	1.9	1.63	0.69	0.92	1.39	1.39	1.39		1.1	0.7	N/A
⋮	⋮	⋮	⋮	⋮	⋮	⋮	⋮	⋮	⋮	⋮	⋮	⋮	⋮
4250	3.3	2.7	2.9	3.4	2.64	2.96	2.57	2.33	2.68	...	1.8	1.7	2.2
4255	3.2	2.8	2.9	3.4	2.65	3.08	2.62	2.32	2.67	...	1.9	1.8	2.2
4260	3.2	2.6	2.9	3.4	2.74	3.01	2.68	2.23	2.65	...	1.9	1.8	2.2

Note: N/A refers to missing data.

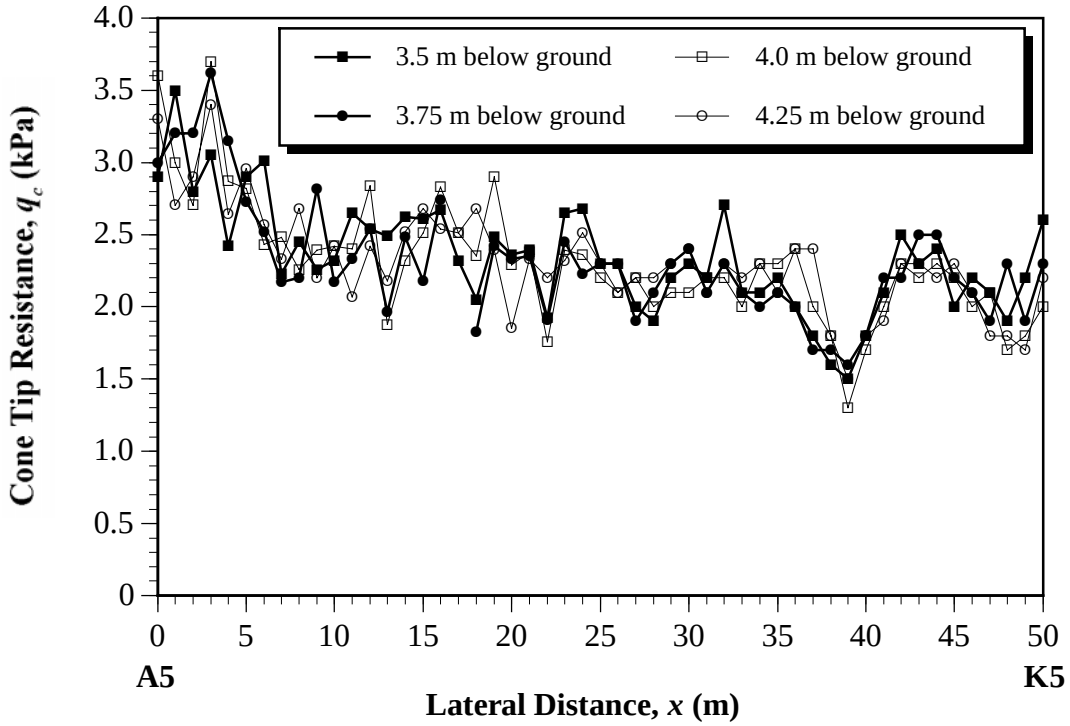

Figure 5.20 Horizontal spatial variability data along transect A5 to K5.

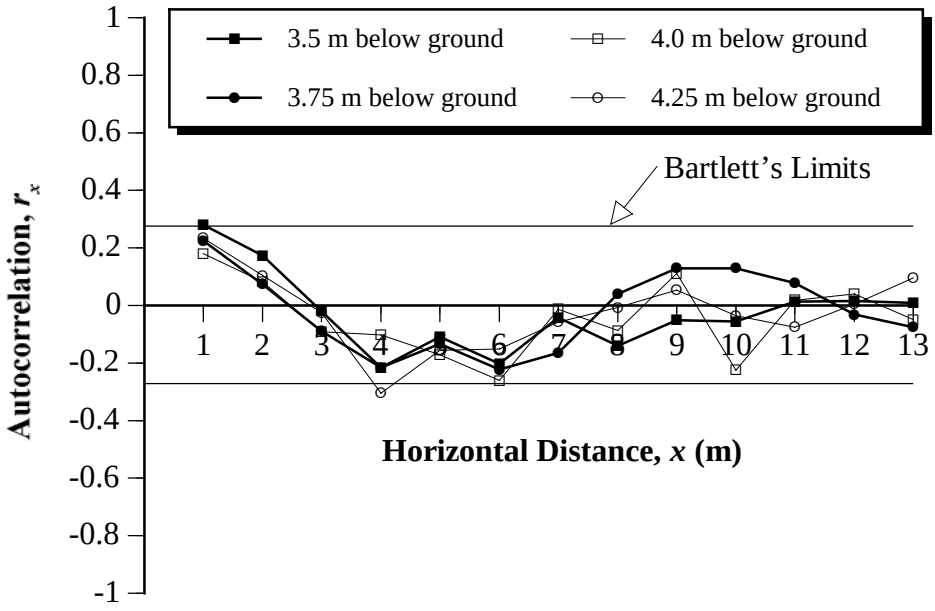

Figure 5.21 Sample ACFs of the residuals of the horizontal spatial variability data for transect A5 to K5.

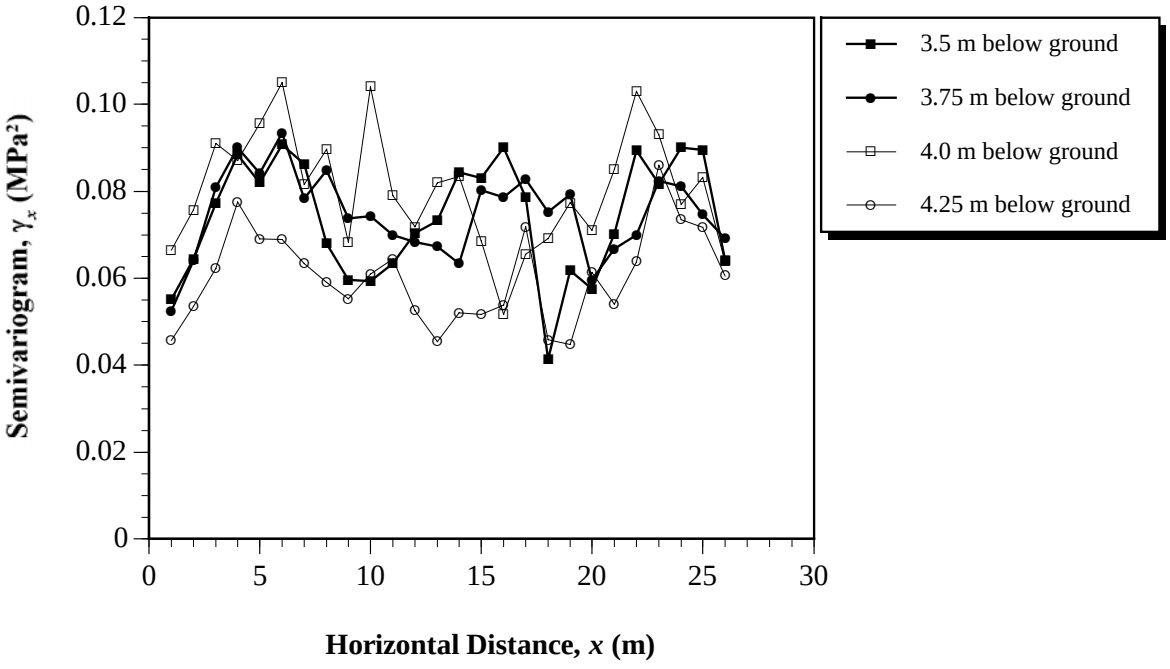

Figure 5.22 Experimental semivariograms of the residuals of the horizontal spatial variability data for transect A5 to K5.

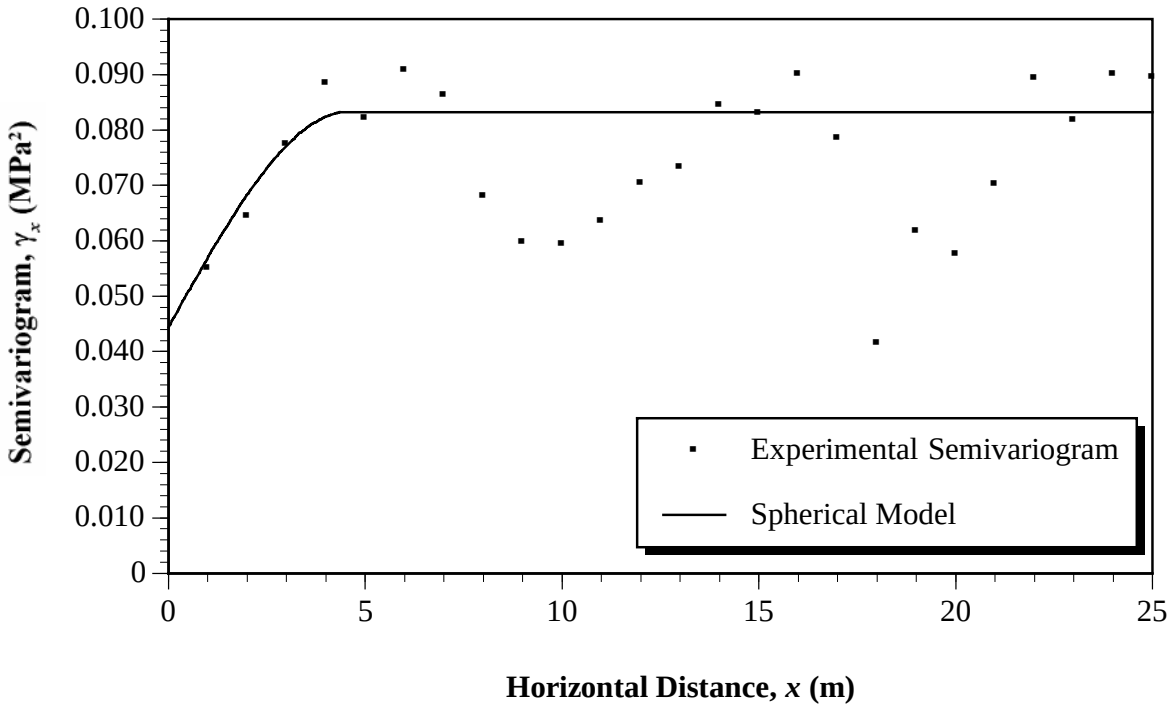

Figure 5.23 Experimental semivariogram of the residuals of transect A5 to K5, at a depth of 3.5 metres.

Table 5.7 Results of random field theory and geostatistical analyses of horizontal spatial variability data, from transect A5 to K5, at various depths.

Depth (m)	ACF	Semivariogram			
	r_B (m)	a (m)	C_0 (MPa²)	C (MPa²)	$C_0/(C+C_0)$
3.5	0.9	4.6	4.44×10^{-2}	3.89×10^{-2}	53%
3.75	1.0	4.2	3.72×10^{-2}	4.40×10^{-2}	46%
4.0	0.9	4.5	5.16×10^{-2}	4.44×10^{-2}	54%
4.25	0.9	4.6	3.61×10^{-2}	3.14×10^{-2}	53%
Average	**0.9**	**4.5**	$\mathbf{4.23 \times 10^{-2}}$	$\mathbf{3.97 \times 10^{-2}}$	**52%**

It is evident from Figures 5.21 and 5.22, and Table 5.7, that:

- the value of r_B is approximately equal to, or slightly less than, the spacing between the cone penetration tests;

- at least 3 points define the descending limb of the sample ACFs and the ascending limb of the experimental semivariograms;

- the relative nugget values are comparatively large, suggesting a substantial random component which is difficult to quantify reliably at this scale of testing.

While appropriate models may be fitted to the sample ACFs and the experimental semivariograms shown in Figures 5.21 and 5.22, the reliability of these models may be questionable. As a consequence, it is desirable to obtain measurements of q_c at lateral spacings closer than one metre.

As described in §4.3.2, in order to better model the lateral variability of the Keswick Clay, a further 50 CPTs were drilled at the South Parklands site; with each CPT spaced at 0.5 metre lateral intervals, which is about the closest practical spacing for drilling vertical CPTs. These 50 CPTs, CD1 to CD50, shown previously in Figure 4.7, were treated in the same way as the data from CPTs A5 to K5, detailed above. Again, q_c measurements from four separate depths were analysed; that is, 3.5, 4.0, 4.5 and 5.0 metres below the ground surface[26]. These data were generated using the same procedure detailed above, and the results are shown in Figure 5.24.

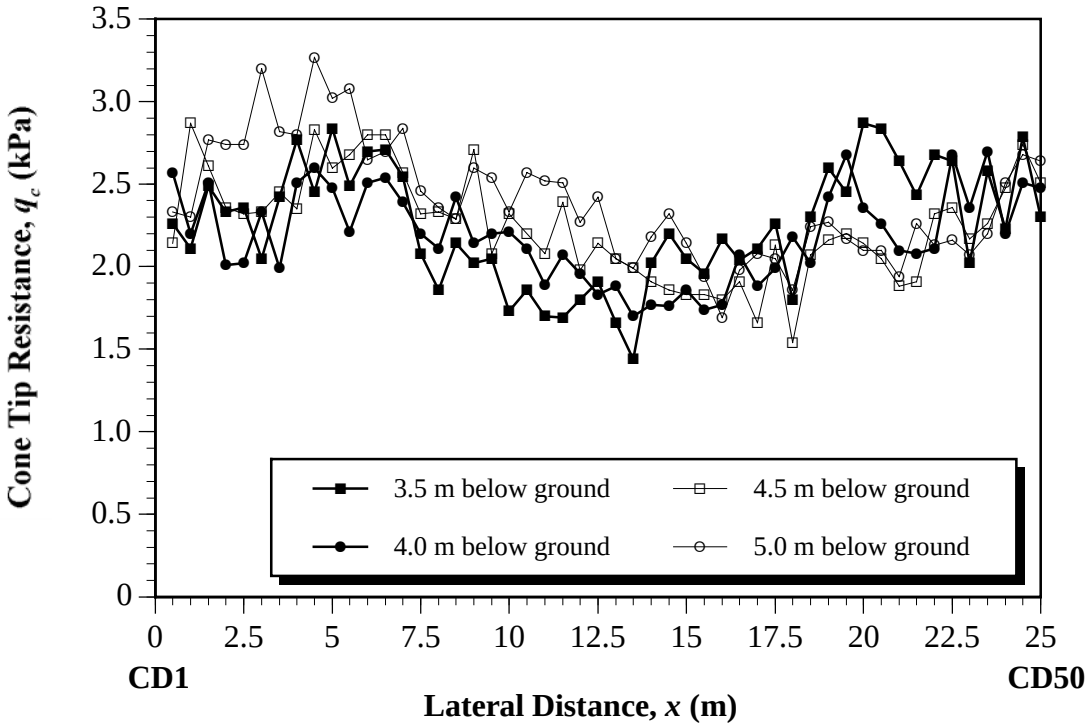

Figure 5.24 Horizontal spatial variability data along transect CD1 to CD50.

[26] It should be noted that different depths were used for the CD1 to CD50 transects to those of the A5 to K5 transects. This is due to missing data at some of the depths along the transects, as well as the variation of the surface of the Keswick Clay across the South Parklands site.

Again, in order to satisfy the requirement of stationarity, the OLS quadratic trends for each data set were evaluated. Interestingly, Kendall's τ test indicated stationarity with no trend removal, whereas the other tests suggested that the untransformed data were non-stationary. This result seems to indicate that at reasonably low values of n, say less than 50, Kendall's τ test may, in some cases, fail to reject non-stationary data. This highlights the point made by Brockwell and Davis (1991) that no single stationarity test should be used in isolation.

The sample ACFs and the experimental semivariograms for each of the four de-trended data sets are shown in Figures 5.25 and 5.26, respectively. Table 5.8 presents a summary of r_B, a, C_0 and C values pertaining to the sample ACFs and the experimental semivariograms. The values of a, C_0 and C were obtained by fitting appropriate spherical models to the experimental semivariograms, an example of which is shown in Figure 5.27.

Table 5.8 Results of random field theory and geostatistical analyses of horizontal spatial variability data, from transect CD1 to CD50, at various depths.

Depth (m)	ACF	Semivariogram			
	r_B (m)	a (m)	C_0 (MPa^2)	C (MPa^2)	$C_0/(C+C_0)$
3.5	1.8	5.2	3.27×10^{-2}	8.25×10^{-2}	28%
4.0	1.3	5.5	2.25×10^{-2}	4.01×10^{-2}	36%
4.5	1.5	6.3	2.65×10^{-2}	4.63×10^{-2}	36%
5.0	1.0	5.3	1.92×10^{-2}	5.82×10^{-2}	25%
Average	**1.38**	**5.6**	$\mathbf{2.52 \times 10^{-2}}$	$\mathbf{5.68 \times 10^{-2}}$	**31%**

It is evident from Figures 5.25 and 5.26, and Table 5.8, that the data from CD1 to CD50 yield relatively reliable estimates of r_B, a, C_0 and C, and these results compare well with those obtained from the one metre spaced data, as shown in Table 5.7. Furthermore, the relative nugget values have decreased, which is likely to be caused by the difference in location between transects CD1 to CD50 and A5 to K5, rather than due to the reduced sample spacing.

It is worth noting that some of the experimental semivariograms, given in Figure 5.26, describe a structural function which is sometimes monotonically *decreasing*. Such an example is shown in Figure 5.27. Generally, one would expect a semivariogram to be monotonically increasing, and in the case of transitive models, to asymptote towards the sill, as the separation distance increases. This behaviour expresses the notion that adjacent samples are more closely related than samples separated by greater distances. The semivariogram given in Figure 5.27 suggests that, for example, samples separated by a

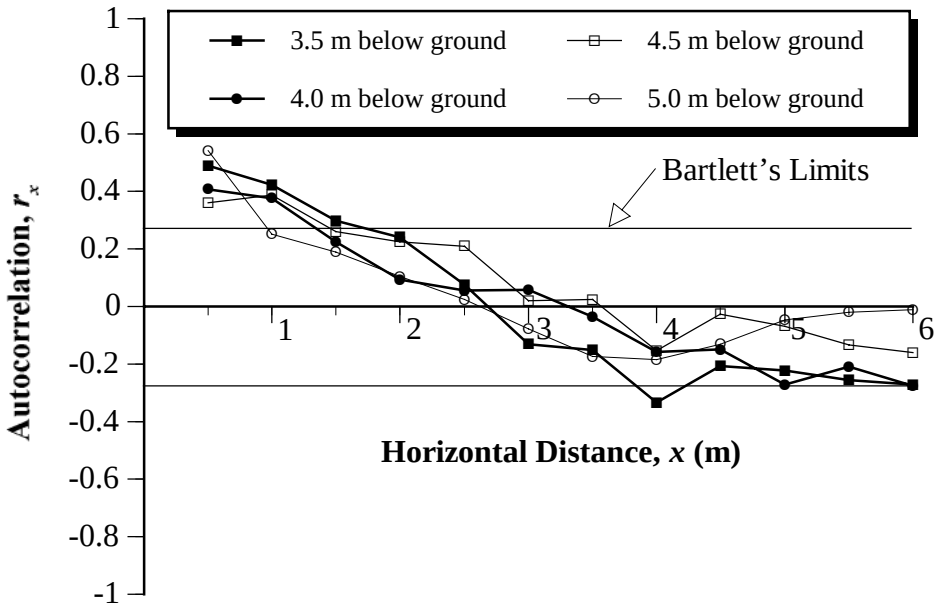

Figure 5.25 Sample ACFs of the residuals of the horizontal spatial variability data for transect CD1 to CD50.

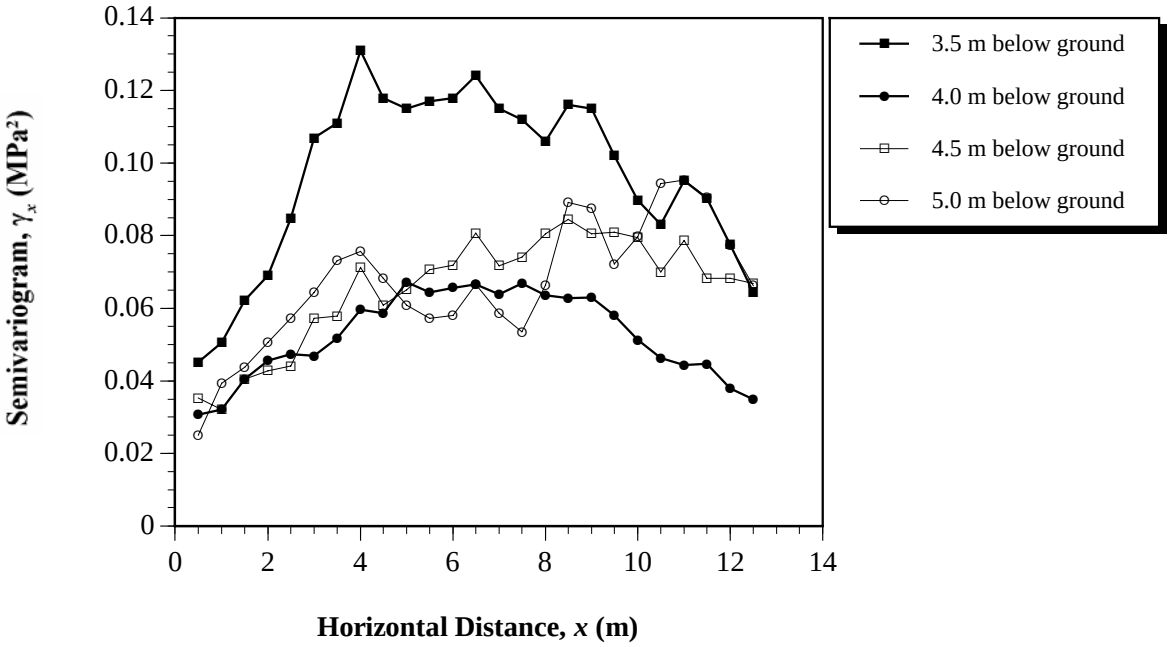

Figure 5.26 Experimental semivariograms of the residuals of the horizontal spatial variability data for transect CD1 to CD50.

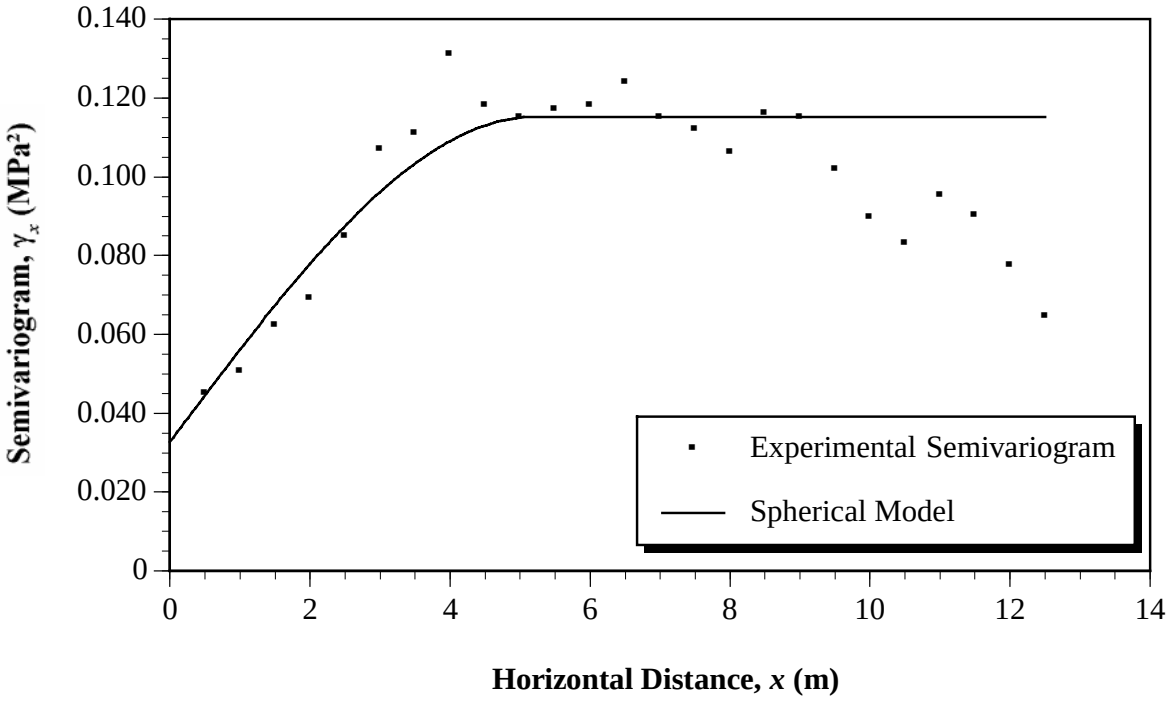

Figure 5.27 Experimental semivariogram of the residuals of transect CD1 to CD50 at a depth of 3.5 metres.

distance of 12 metres exhibit greater correlation than samples separated by a distance of 4 metres. However, as pointed out in §2.5.1.3(i), the reliability of the semivariogram, γ_h, is related to the number of pairs, which decreases as the separation distance, h, increases. Journel and Huijbregts (1978) suggested that a minimum of 30 data pairs should be used to determine the experimental semivariogram. With reference to Figure 5.27, at separation distances of $x > 9.5$ metres, the number of data pairs, $N \leq 30$. Hence, semivariogram values at separation distances, x, in excess of 9.5 metres should be neglected. As a result, the remaining experimental semivariogram does not exhibit monotonically decreasing behaviour.

It should be noted that the data sets used in the preceding analyses were obtained by taking a series of horizontal slices, 5 mm in thickness and, either, 25 or 50 metres in length. Since the ground surface is not level, as shown by Figures 4.17 and 4.18, the horizontal slices are not planar sections, but thin strips which follow the topography of the ground surface. Using these thin strips neglects the influence of macro-structures within the clay mass, such as gilgais, as well as the influence of variations in the ground surface. Perhaps a more appropriate technique is to average the values of q_c with depth, and analyse the resulting data set. Such *spatial averaging* would even out local depositional and structural fluctuations, and may actually give a better representation of the 'true' nature of the horizontal spatial variability of the Keswick Clay. Figure 5.28 shows measurements of q_c,

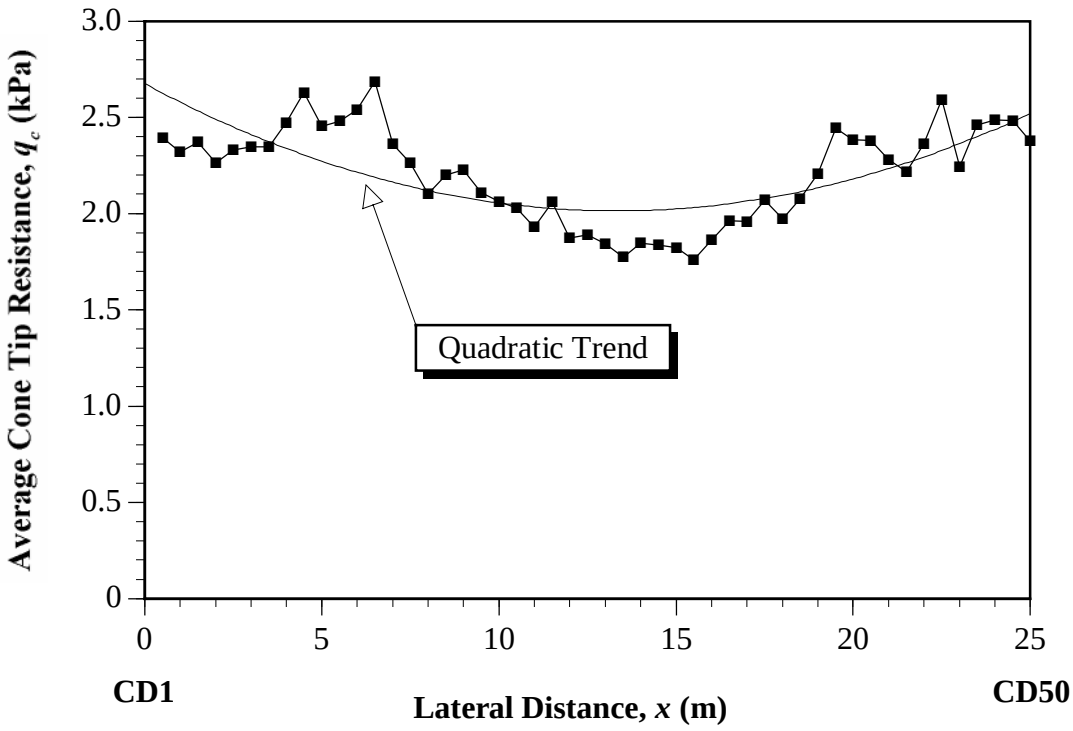

Figure 5.28 Horizontal spatial variability data, along transect CD1 to CD50, averaged over depths 3.5 m to 4.5 m below the ground surface.

for each of the CPTs from CD1 to CD50, averaged between depths of 3.5 and 4.5 metres below ground. Again, a quadratic trend, shown in Figure 5.28, was removed from the data in order to satisfy the stationarity constraint. The sample ACF and experimental semivariogram were calculated as before, and the results are shown in Figures 5.29 and 5.30.

From Figure 5.29, r_B was found to equal 2.3 metres. By fitting a suitable spherical model to the experimental semivariogram in Figure 5.30, the following parameters were obtained:

$$a = 6.1 \text{ metres};$$
$$C = 4.12 \times 10^{-2} \text{ MPa}^2;$$
$$C_0 = 2.25 \times 10^{-3} \text{ MPa}^2.$$

These results compare well with those given previously. However, as one would expect, the spatial averaging process results in greater continuity in the random field. This is observed by the values of r_B and a being slightly greater than the values obtained in Tables 5.7 and 5.8. In addition, as suggested by Vanmarcke (1977a), the variance of the spatially averaged data is lower than that of the point values, as indicated by the respective values of C and C_0. Again, the experimental semivariogram values at separation distances in excess of 9.5 metres were obtained using less than 30 data pairs and, as a result, should be ignored.

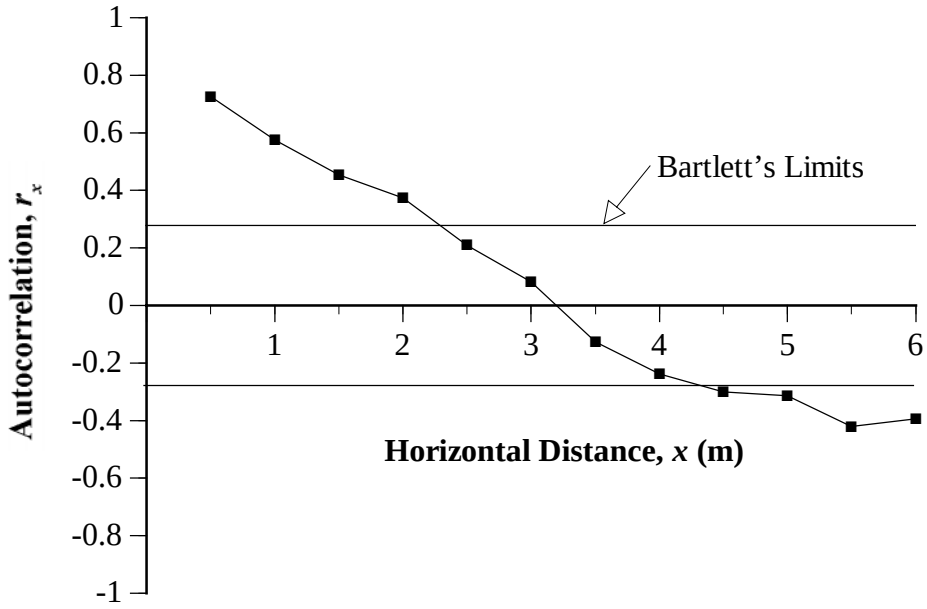

Figure 5.29 Sample ACF of the residuals of the data, for transect CD1 to CD50, averaged over depths 3.5 m to 4.5 m below the ground surface.

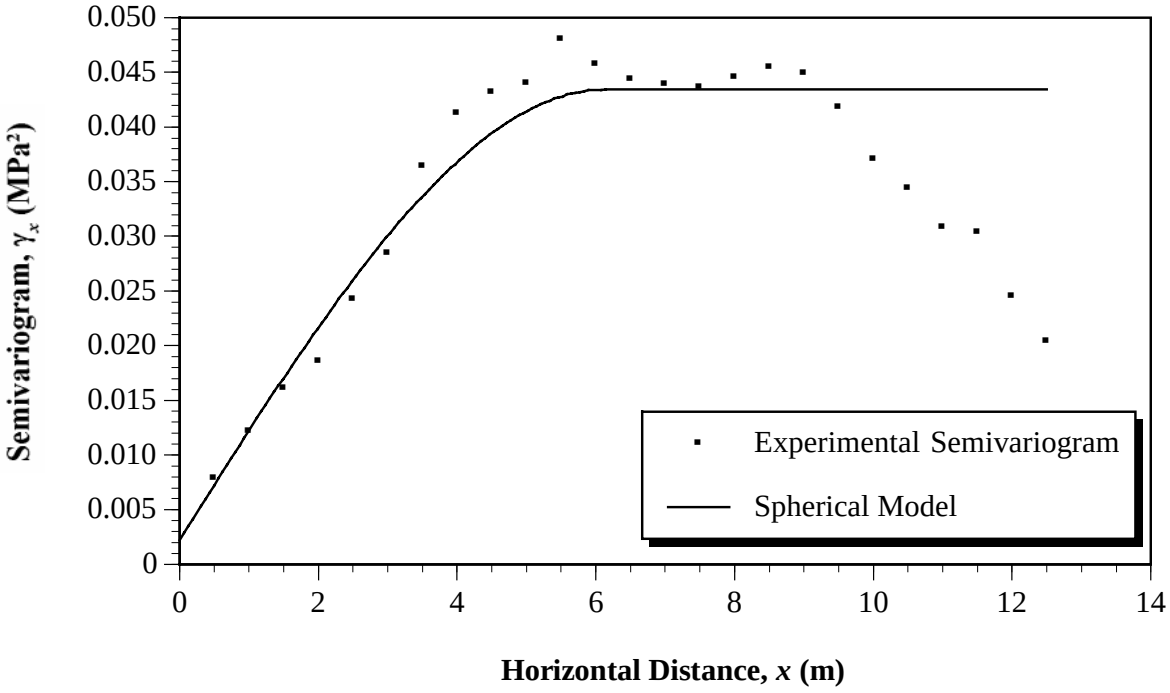

Figure 5.30 Experimental semivariogram of the residuals of the data, for transect CD1 to CD50, averaged over depths 3.5 m to 4.5 m below the ground surface.

It appears from the analyses presented in this section, that the horizontal correlation distance of the Keswick Clay, obtained from the sample ACF, is between 1 and 2 metres, and the range, *a*, obtained from the experimental semivariogram, is between 5 and 6 metres. These results are, however, based on a limited number of data, obtained from a series of vertical CPTs spaced at lateral intervals of between 0.5 and 1 metre. As discussed in §4.4, the physical limitations of drilling closely-spaced vertical boreholes, as well as the limited population size, prompted the drilling of a horizontal cone penetration test at the Keswick site. The results of this test are examined in the following section.

5.3.2.2 Keswick Site

As detailed previously in §4.4.2, only one horizontal CPT could be performed within the imposed time and financial constraints at the Keswick site. Figure 5.31 shows the measured values of q_c plotted against the horizontal penetration distance for the CPT. The first two metres of data have been removed from the data set, as these measurements are likely to have been influenced by weathering and movements adjacent to the face of the embankment. In addition, Figure 5.31 shows a quadratic trend, indicated by Equation (5.12), fitted to the data by the method of OLS regression.

$$q_c = -4.44\times10^{-8}x^2 + 4.66\times10^{-4}x + 1.37 \qquad (5.12)$$

where: x is the horizontal distance of penetration in mm.

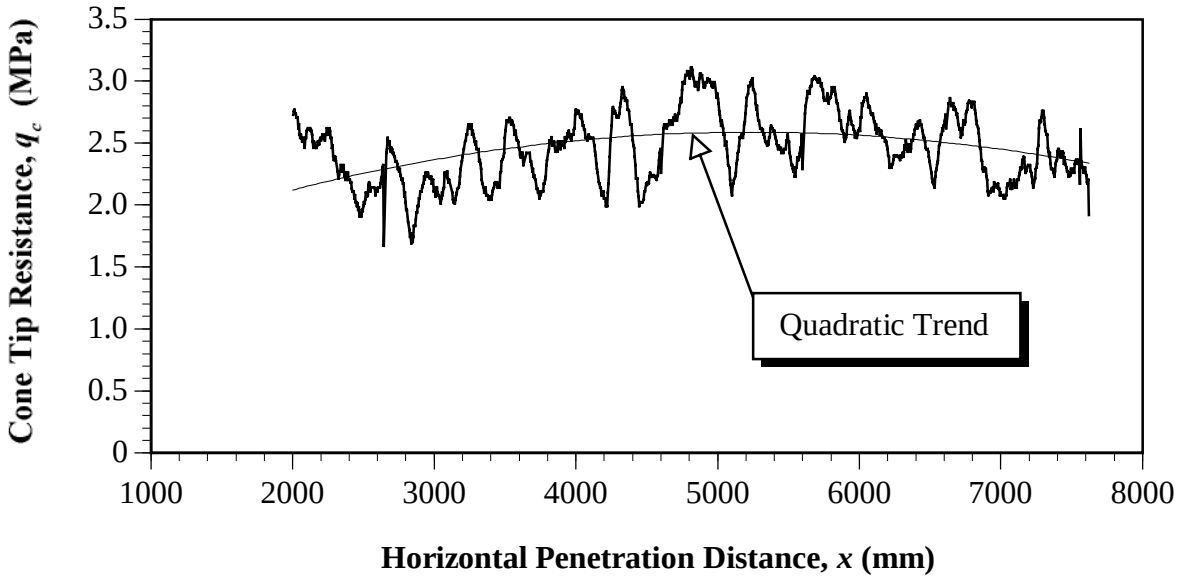

Figure 5.31 Horizontal CPT data with quadratic trend function.

The statistics for the horizontal q_c data set are: mean, m = 2.46 MPa; standard deviation, σ = 0.284 MPa; coefficient of variation, CV = 11.53%; skewness = 0.106 MPa^3; kurtosis = 2.38 MPa^4; and the number of values, N = 1,106.

Figure 5.32 shows the residuals after the quadratic trend has been removed. As can be seen from this figure, the data set appears to be stationary, which is supported by the fact that Kendall's τ test was passed.

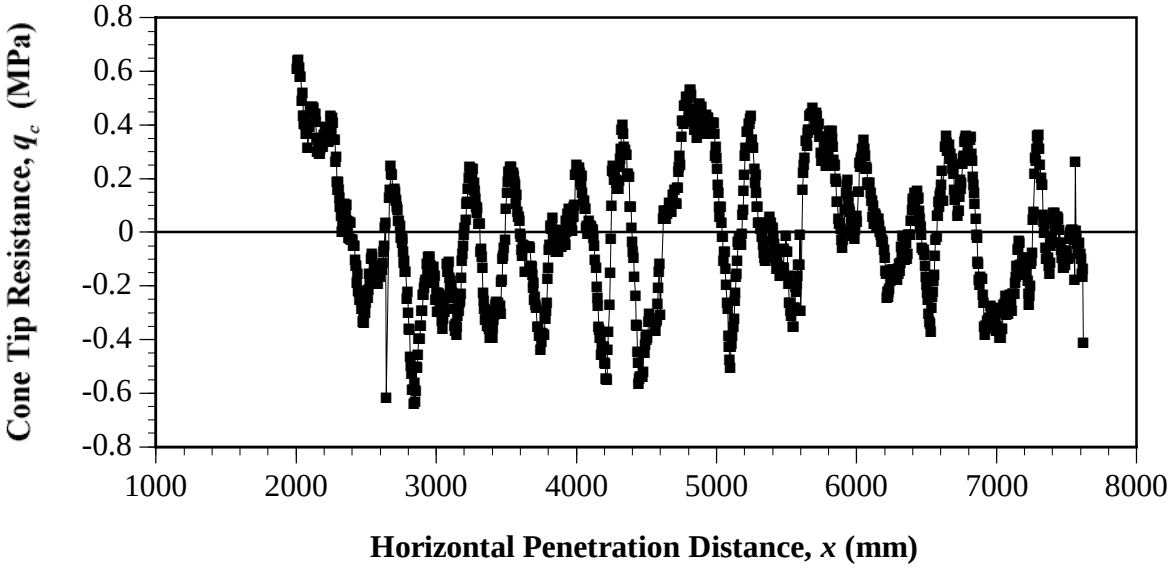

Figure 5.32 Residuals of the horizontal CPT data after quadratic trend removal.

The sample ACF of the residual data set is shown in Figure 5.33. Models 2, 3 and 4 were fitted by means of OLS regression to the sample ACF, two of which are shown in Figure 5.33. A summary of these models, their parameters and their associated horizontal scales of fluctuation, δ_H, is given in Table 5.9.

Table 5.9 Summary of random field theory analyses, performed on the residuals of the horizontal CPT data, obtained from the Keswick site.

Model No.	Model ACF	Parameters	Scale of Fluctuation, δ_H
2	$\rho_x = e^{-\lvert x\rvert/b}$	b = 71 mm	142 mm
3	$\rho_x = e^{-(\lvert x\rvert/c)^2}$	c = 80 mm	142 mm
4	$\rho_x = e^{-\lvert x\rvert/d}\left(1+\frac{\lvert x\rvert}{d}\right)$	d = 35.6 mm	142 mm

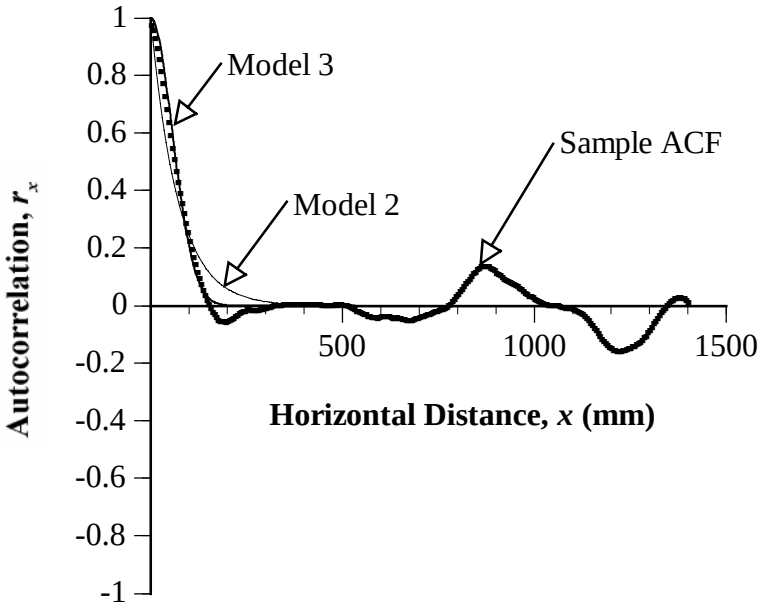

Figure 5.33 Sample and model autocorrelation functions of the de-trended horizontal CPT data.

As can be seen from Figure 5.33 and Table 5.9: the model ACFs fit the sample ACF very well; the resulting horizontal scales of fluctuation, δ_H = 142 mm; and the values of δ_H are identical for each model.

The value of δ_H, obtained above, can be compared with Bartlett's distance, r_B. Bartlett's limits are equal to ± 0.060, which intersects the sample ACF at a lag of 28, or a distance of 140 mm. Hence, Bartlett's distance, r_B, is equal to 140 mm, which is almost identical to the 142 mm obtained for δ_H. This gives further weight to the conclusion made in §5.3.1.1, that r_B is equal to the scale of fluctuation, δ_v.

The experimental semivariogram of the residual data set is shown in Figure 5.34. Again, the spherical model was found to satisfactorily describe the experimental semivariogram. The model is represented by the following equation:

$$\begin{aligned} \gamma_x &= C\left(\frac{3x}{2a} - \frac{x^3}{2a^3}\right) + C_0 \quad \text{when} \quad x \le a \\ \gamma_x &= C + C_0 \qquad\qquad\qquad\quad \text{when} \quad x \ge a \end{aligned} \tag{5.13}$$

where: a = 190 mm;
C = 6.80×10^{-2} MPa^2;
C_0 = 0 MPa^2.

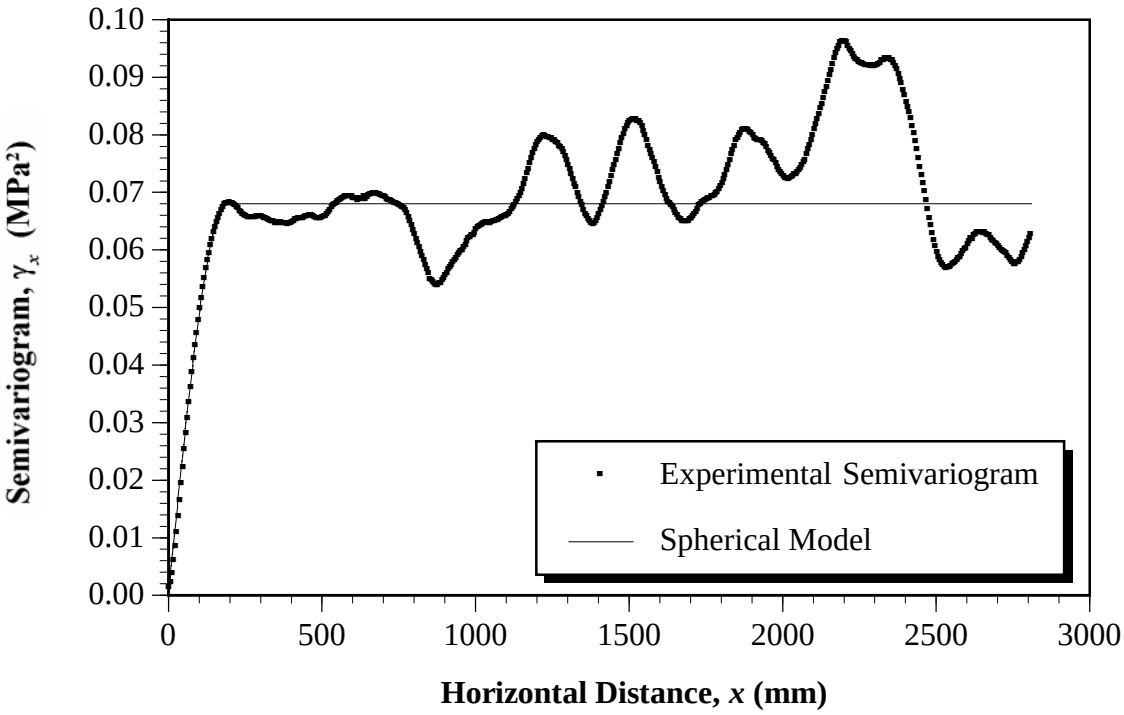

Figure 5.34 Experimental and model semivariograms of the de-trended horizontal CPT data.

As can be seen from Figure 5.34, the spherical model fits the experimental semivariogram very well, especially for values of x between 0 and the range, a. The range of 190 mm is comparable to the value of δ_H of 140 mm, obtained earlier.

5.3.2.3 Discussion of Horizontal Spatial Variability Results

The results obtained from the horizontal spatial variability analyses, performed on the South Parklands data, suggest that the Keswick Clay has a horizontal correlation distance of between 1 and 2 metres, and a range of influence, a, of between 5 and 6 metres. On the other hand, the results of similar analyses performed on data from the Keswick site, suggest that the same clay has a horizontal correlation distance of 140 mm and a range of 190 mm. While these results appear to contradict one another, they do, however, provide evidence of *nested structures* within the Keswick Clay. Nested structures are sources, or structures, of variability which come into play simultaneously for all distances h, and which are influenced by the scale of observation (Journel and Huijbregts, 1978).

Vanmarcke (1978) recognised that the scale of spatial variability modelling may vary greatly, depending upon the type of problem considered. With reference to Figure 5.35,

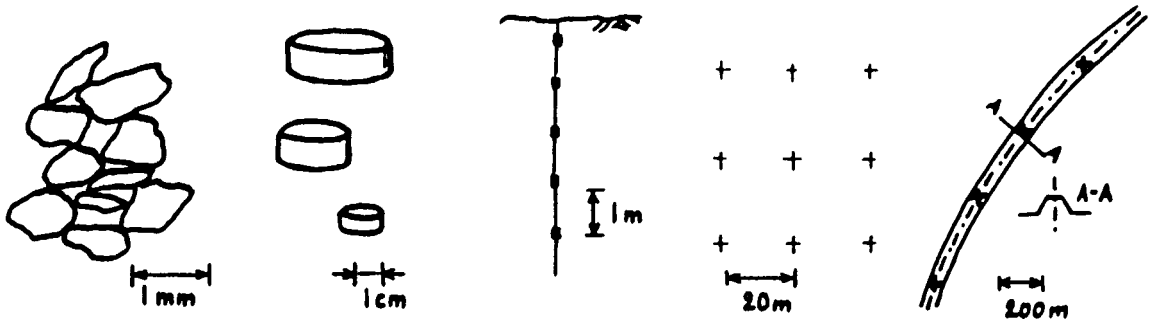

(a) **(b)** **(c)** **(d)** **(e)**

Figure 5.35 Scales of spatial variability modelling in geotechnical engineering. ***(After Vanmarcke, 1978).***

Vanmarcke (1978) suggested that the dimensions may include any of the following:

(a) sizes of soil particles;
(b) sizes of laboratory specimens;
(c) vertical sampling distances;
(d) lateral distances between borings;
(e) horizontal intervals measured along the centreline of long linear facilities.

As a consequence of this, Vanmarcke (1978) suggested that geotechnical properties may exhibit two, or more, superimposed scales of fluctuation, depending on the modelling scale. As mentioned previously, the results of the horizontal CPT were obtained by sampling at 5 mm intervals, over a lateral extent of 7.62 metres. The results obtained from the horizontal spatial variability analyses of the South Parklands data were obtained by sampling at intervals of 0.5 and 1 metre, over a maximum distance of 50 metres. It is not surprising, therefore, that two quite distinct scales of fluctuation (δ_1 = 150 mm and δ_2 = 2 metres) were observed. Vanmarcke (1978) proposed a framework for incorporating these superimposed variabilities within random field theory. For the one-dimensional case, Vanmarcke suggested that, if a geotechnical property, $v(\Delta z)$, is actually the sum of two independent contributions, $v_1(\Delta z)$ and $v_2(\Delta z)$, then the mean, $\bar{v}$, and variance, σ_v^2, of $v(\Delta z)$ may be expressed as:

$$\begin{aligned} \bar{v} &= \bar{v}_1 + \bar{v}_2 \\ \sigma_v^2 &= \sigma_{v_1}^2 + \sigma_{v_2}^2 = \left(a_1 + a_2\right)\sigma_v^2 \end{aligned} \tag{5.14}$$

where: $a_1 = \dfrac{\sigma_{v_1}^2}{\sigma_v}$; $a_2 = \dfrac{\sigma_{v_2}^2}{\sigma_v}$; and $a_1 + a_2 = 1$.

Vanmarcke (1978) proposed that the ACF, $\rho_v(\Delta z)$, and the variance function, $\Gamma_v^2(\Delta z)$, of $v(\Delta z)$ could then be expressed as:

$$\begin{aligned} \rho_v(\Delta z) &= a_1 \rho_{v_1}(\Delta z) + a_2 \rho_{v_2}(\Delta z) \\ \Gamma_v^2(\Delta z) &= a_1 \Gamma_{v_1}^2(\Delta z) + a_2 \Gamma_{v_2}^2(\Delta z) \end{aligned} \tag{5.15}$$

Since Vanmarcke proposed this *nested structure model*, there appears to be no indication of its use in the geotechnical engineering literature; probably because, until now, there has been little experimental evidence of geotechnical properties exhibiting the presence of such structures. Journel and Huijbregts (1978) also provided a similar theoretical setting for incorporating nested structures. However, their framework was based on the theory of geostatistics. For example, the semivariogram function, γ_h, may be expressed as the linear combination of several separate semivariograms:

$$\gamma_h = \gamma_{h_1} + \gamma_{h_2} + \gamma_{h_3} + \ \ldots \ + \gamma_{h_n} \tag{5.16}$$

In §5.3.2.1, a number of horizontal semivariogram models were suggested by the measurements of q_c, obtained from the South Parklands site. These models may be summarised by the following spherical model:

$$\begin{aligned} \gamma_x &= 0.06\left(\frac{3x}{2a} - \frac{x^3}{2a^3}\right) + 0.03 \quad \text{when} \quad x \le a \\ \gamma_x &= 0.09 \quad \text{when} \quad x \ge a \end{aligned} \tag{5.17}$$

where: a = 6 metres.

In §5.3.2.2, a horizontal semivariogram model was proposed by the measurements of q_c, obtained from the Keswick site. For comparative purposes, this model is restated here in the following equation:

$$\begin{aligned} \gamma_x &= 0.07\left(\frac{3x}{2a} - \frac{x^3}{2a^3}\right) + 0 \quad \text{when} \quad x \le a \\ \gamma_x &= 0.07 \quad \text{when} \quad x \ge a \end{aligned} \tag{5.18}$$

where: a = 0.2 metres.

While these models describe the spatial variability of the undrained shear strength of the Keswick Clay, they are, however, based on measurements of q_c. As mentioned previously, in order to combine both the small-scale and the large-scale spatial variability models, it is imperative that they be derived from the same parameter. Therefore, it is necessary to convert the measurements of q_c to estimates of s_u, in order to maintain consistency with the

data which will be used to derive the large-scale model, as will be presented in Chapter 6. It was shown in §5.3.1.3, that the scale of fluctuation and the range of influence are independent of the value of N_k, which is used to convert measurements of q_c to values of s_u. Only the scale of the *y*-axis of the semivariogram, and hence C_0 and C, are dependent on N_k. In Chapter 2, several relationships were presented for the estimation of N_k. It was concluded in §4.5, that the expression proposed by Baligh (1975), given in Equation (2.7), yielded the best estimates of the undrained shear strength of the Keswick Clay from measurements of q_c, when compared with observations of s_u derived from triaxial tests. Furthermore, Table 4.4 presented a summary of values of N_k which were obtained by comparing measurements of q_c from CPTs, with measurements of s_u from triaxial tests. Taking an average of the estimates of N_k, derived from the relationship proposed by Baligh (1975), yields $\overline{N}_k$ = 17.2. This value of N_k was then substituted into Equation (5.10), in order to convert the measurements of q_c to estimates of s_u. It should be noted that since the measurements of q_c were obtained from horizontal transects, the value of the overburden pressure, σ_{v0}, is constant for each data set. As a consequence, σ_{v0} may be neglected, since its inclusion simply results in a small, uniform translation of s_u, whose influence is nullified by the removal of the trend.

The experimental semivariograms for the Keswick data (described previously in §5.3.2.2) and for South Parklands data (given in §5.3.2.1) were obtained by: first converting the measurements of q_c to values of s_u, using N_k = 17.2; and then removing the OLS quadratic trend in order to achieve stationarity. Appropriate spherical models were then fitted to the resulting experimental semivariograms, these models being described in Equations (5.19) and (5.20), and shown graphically in Figure 5.36.

- ***Keswick Site:***

$$\gamma_1 = 230\left(\frac{3x}{2a} - \frac{x^3}{2a^3}\right) + 0 \quad \text{when} \quad x \le a \tag{5.19}$$

$$\gamma_1 = 230 \quad \text{when} \quad x \ge a$$

where: a = 0.2 metres.

- ***South Parklands Site:***

$$\gamma_x = 290\left(\frac{3x}{2a} - \frac{x^3}{2a^3}\right) + 100 \quad \text{when} \quad x \le a \tag{5.20}$$

$$\gamma_x = 390 \quad \text{when} \quad x \ge a$$

where: a = 6 metres.

It is evident from Figure 5.36, that the two spherical models appear to be appropriate since, as the range increases, so too does the level of the sill, as one would expect. Furthermore, since the model obtained from the Keswick site, γ_1, was measured over a total lateral extent of 7.62 metres (§4.4.2), the model semivariogram is appropriate over a region of

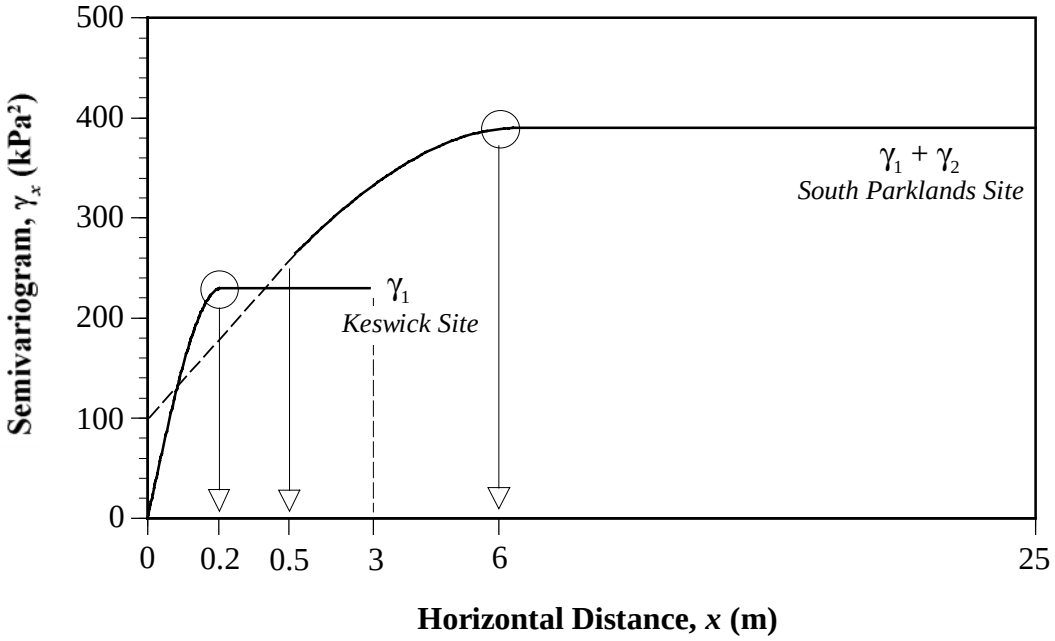

Figure 5.36 The two spherical semivariogram models used to describe the horizontal spatial variability of the Keswick Clay.

(Note: x-axis is not drawn to scale).

half this distance, say 3 metres. In contrast, the model obtained from the South Parklands site is appropriate over a lateral distance of 25 metres.

One would normally have expected that the nugget associated with the South Parklands model would be greater than the level of the sill of the Keswick site model. It is apparent from Figure 5.36 that this is not the case. The nugget associated with the South Parklands model is 100 kPa^2, whereas the sill level of the Keswick site model is 230 kPa^2. It is likely that this apparent discrepancy is due to the fact that these two models are based on testing performed at two different locations within the Adelaide city area. Since a lateral spatial variability model will be used in Chapter 7 to predict estimates of undrained shear strength at untested locations, a model based on testing at various sites within the Adelaide city area is entirely appropriate.

Combining these two models into a single, nested semivariogram, yields the following relationship, which is shown graphically in Figure 5.37.

$$\gamma_x = 0 + 230\left(\frac{3x}{2a_1} - \frac{x^3}{2a_1^3}\right) + 160\left(\frac{3x}{2a_2} - \frac{x^3}{2a_2^3}\right) \qquad (5.21)$$

where: a_1 = 0.2 metres;
a_2 = 6 metres.

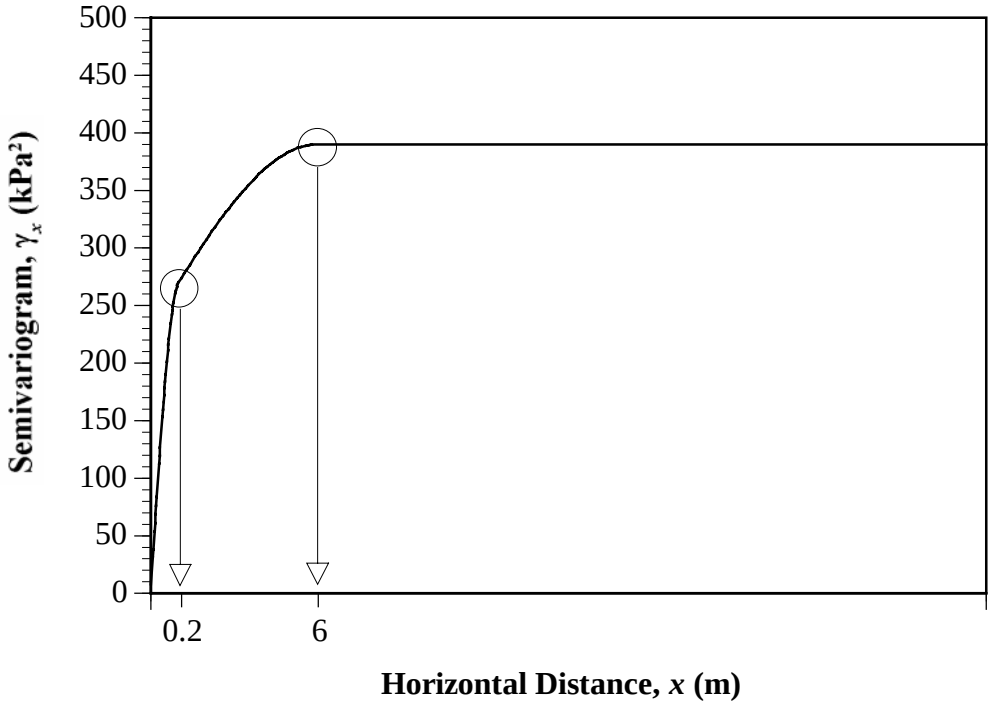

Figure 5.37 Nested horizontal spatial variability model for Keswick Clay.

(Note: x-axis is not drawn to scale).

The genesis of the two horizontal spatial variability structures is unknown. It is possible, though, that micro-fissuring within the Keswick Clay contributes to the small-scale variability structure (a_1 = 0.2 metres); whereas the larger structure (a_2 = 6 metres) may be influenced by gilgais and/or jointing within the soil mass (Marsland and Quarterman, 1982). Unfortunately, it is not possible to determine the 'true' origin of the variability structures without far more extensive testing and investigation, which is beyond the scope of this study.

Since the study of the horizontal spatial variability of the undrained shear strength of the Keswick Clay was confined to a lateral distance of 50 metres, it is possible that additional nested structures may exist beyond this distance. The following chapter will detail data used to quantify the large-scale variability of the Keswick Clay, and Chapter 7 will analyse these data to determine whether additional nested structures exist beyond distances of 50 metres.

It was found in §5.3.1.1 that the scale of fluctuation, δ_v, is comparable to Bartlett's distance, r_B. In addition, though δ_v, r_B and the range of influence, a, are defined as each measuring the correlation distance, it was observed that values of a are somewhat different to those of both δ_v and r_B. The following section examines the empirical relationship between these three parameters.

5.3.3 Relationship Between δ_v, r_B and a

Figure 5.38 shows the relationship between δ_v and a, and superimposed on the data is the OLS line of best fit. The line fits the data reasonably well, as indicated by the value of $r^2 = 0.783$. However, one would expect the range of influence to equal zero when δ_v equals zero; which is not the case with the OLS linear function. Figure 5.39 shows the same graph, but with a power function, obtained by the method of OLS, superimposed on the data. It is evident from the regression coefficients ($r^2 = 0.829$), that the power function better fits the data, and also passes through the origin.

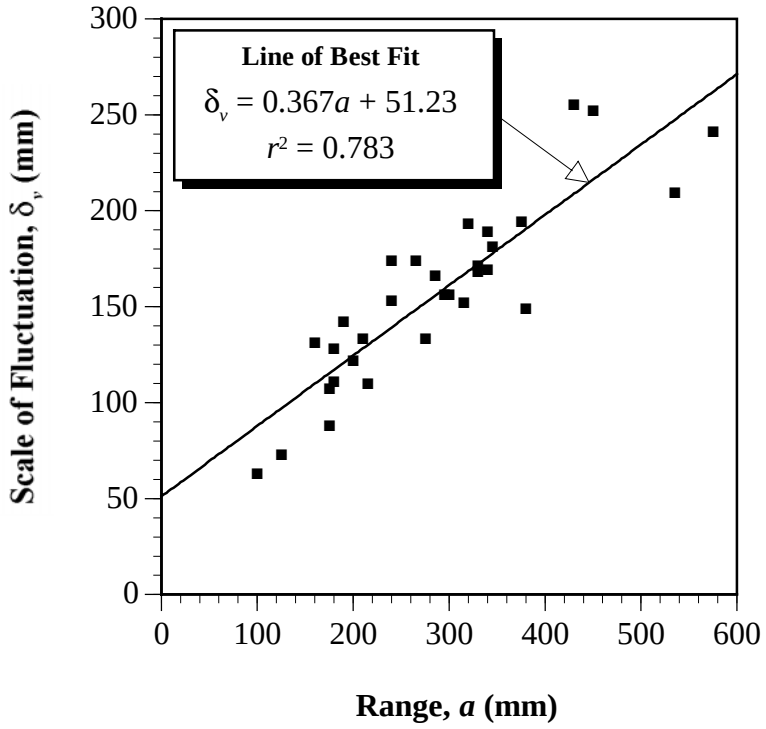

Figure 5.38 Relationship between δ_v and a, OLS best fit linear function.

Figure 5.40 shows the relationship between Bartlett's distance, r_B, and the range of influence, a. Superimposed on the data in Figure 5.40 is the OLS best fit power function. The regression coefficient ($r^2 = 0.959$) indicates that this relationship is slightly better than that obtained for δ_v and a.

Based on the regression analyses of δ_v, r_B and a, and shown in Figures 5.39 and 5.40, the following relationships are proposed:

$$\delta_v = 2.559a^{0.728} \tag{5.22}$$

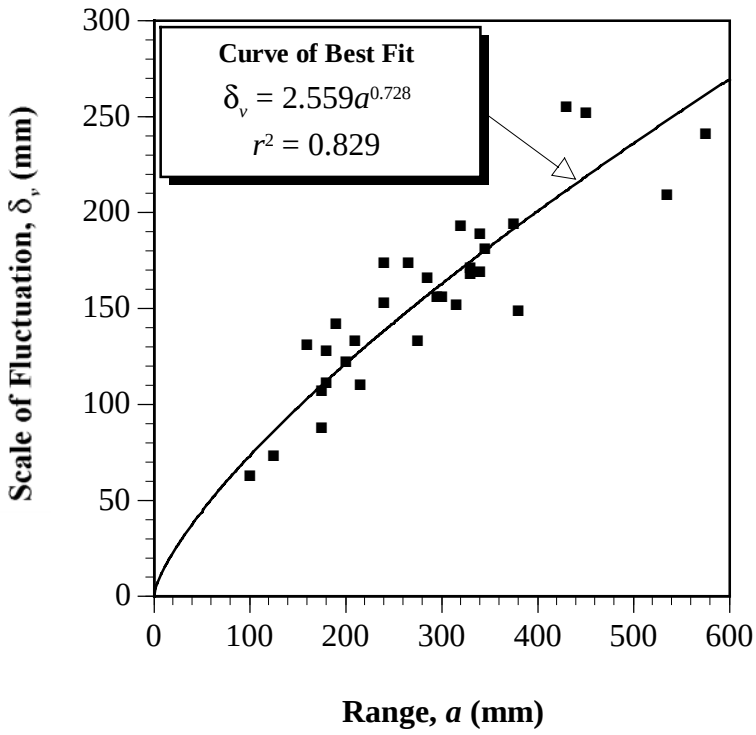

Figure 5.39 Relationship between δ_v and a, OLS best fit power function.

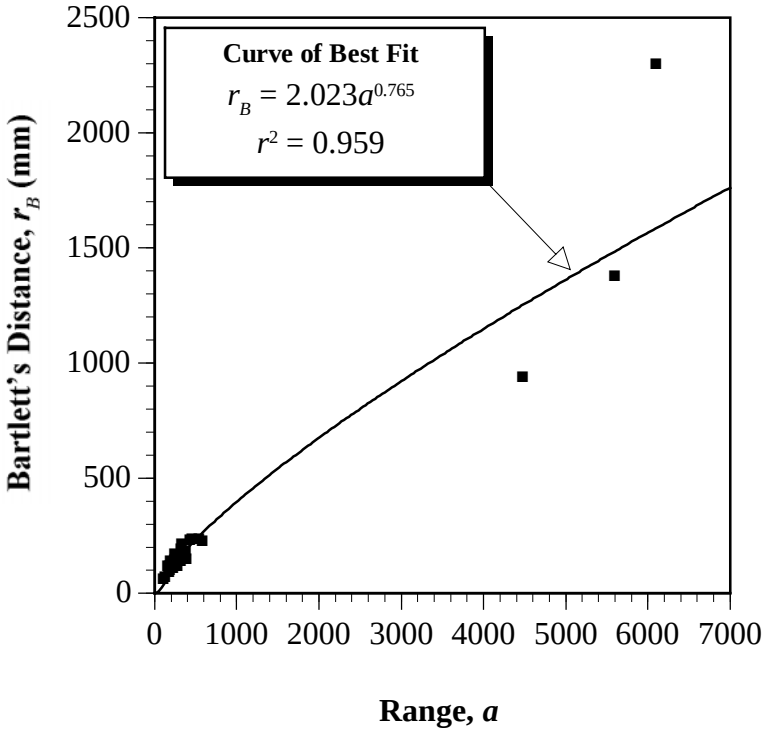

Figure 5.40 Relationship between r_B and a, OLS best fit power function.

$$r_B = 2.023a^{0.765} \tag{5.23}$$

where: δ_v, r_B and a are expressed in mm.

As a consequence of their respective definitions, one would expect the values obtained for δ_v and a to be identical, or at least closely related to one another. While the latter was observed, a non trivial difference was also found to exist between these two parameters. The processes of evaluating δ_v and a are substantially different, and this may explain, to some degree, the observed discrepancy.

To this point, each of the preceding analyses has been confined to the treatment of measurements of the cone tip resistance, q_c. The following section examines measurements of sleeve friction, f_s.

5.3.4 Analysis of Sleeve Friction Measurements

Unlike the measurements of q_c, the measurements of f_s are complicated by a phenomenon that appears to be associated with rebound of the Keswick Clay, and is termed the *rebound phenomenon*. Figure 5.41 shows the measurements of f_s for the CPT sounding A0. Immediately below the depth at which penetration of the cone was temporarily suspended to allow the addition of further drilling rods, the values of f_s have increased significantly above the measurements that were obtained prior to the test being suspended. This can be seen more clearly by examining the CPT results, obtained from the horizontal CPT performed at the Keswick site. The measurements of f_s from this CPT are shown in Figure 5.42. This CPT was carried out using an hydraulic ram that provided a maximum stroke of one metre, as described previously in §4.4.2. Hence further drilling rods were added at penetration intervals of one metre. As is evident from Figure 5.42, this rebound phenomenon occurs at each point in the CPT where the test is temporarily halted, to allow additional rods to be added, and recommenced after some short period of time. This is more evident in Figures 5.43 and 5.44, which show an enlargement of the CPT A0 and the horizontal CPT performed at the Keswick site.

This phenomenon has been observed in each of the CPTs performed at the South Parklands site, as well as CPTs carried out at other locations throughout the Adelaide city area within the Keswick Clay. In contrast, however, this phenomenon has *not* been observed in similar tests performed in other soils. Figure 5.45 shows the measurements of f_s obtained from CPTs carried out in Red-Brown Earth, and Estuarine Sands and Clays. As can be seen from this figure, no rebound phenomenon is evident in either of the two CPTs.

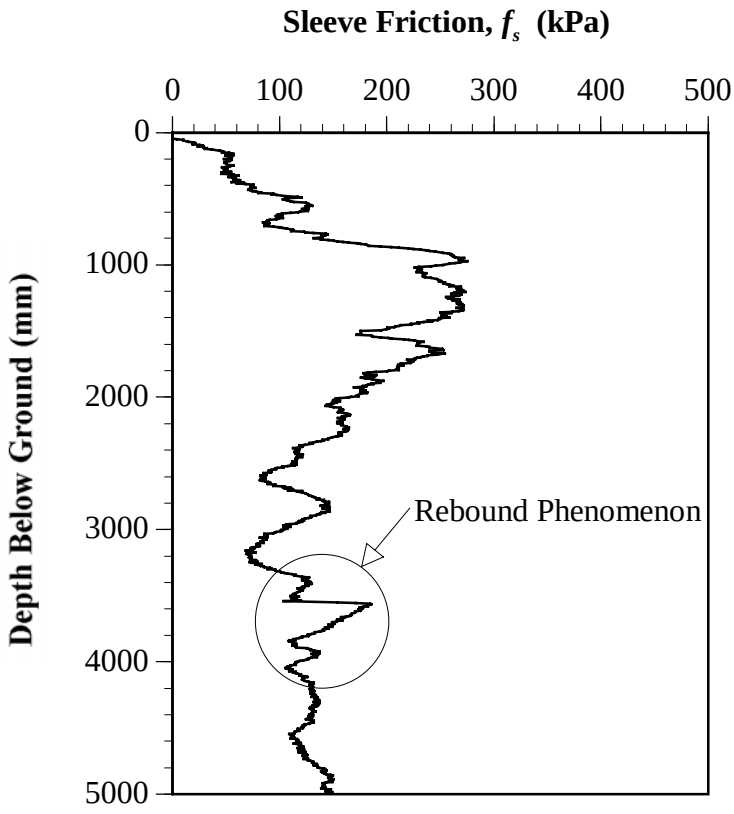

Figure 5.41 Sleeve friction measurements from A0.

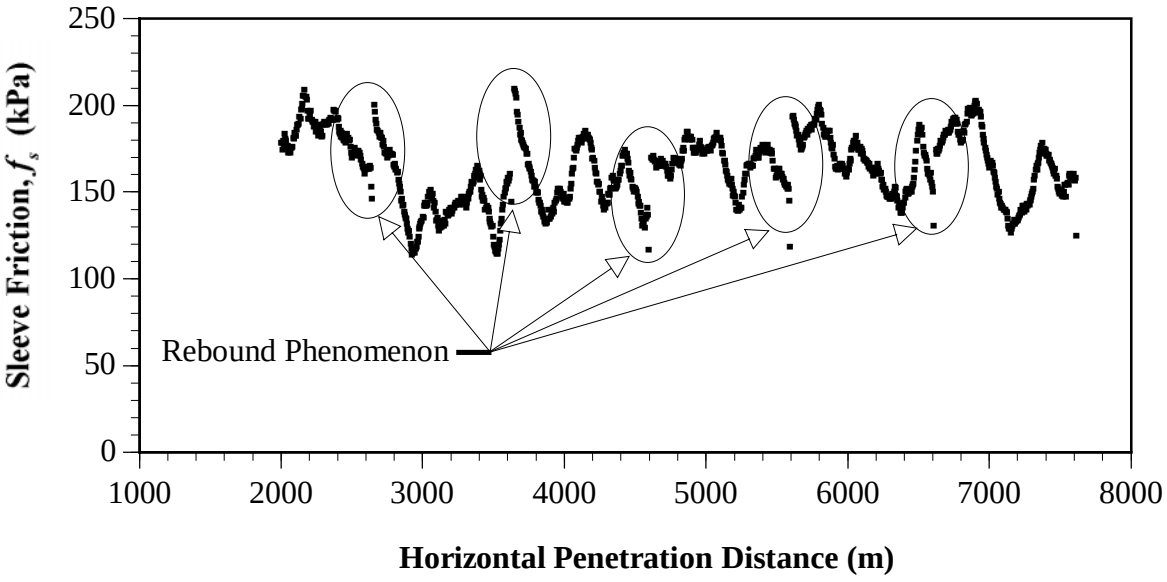

Figure 5.42 Sleeve friction measurements from horizontal CPT performed at the Keswick site.

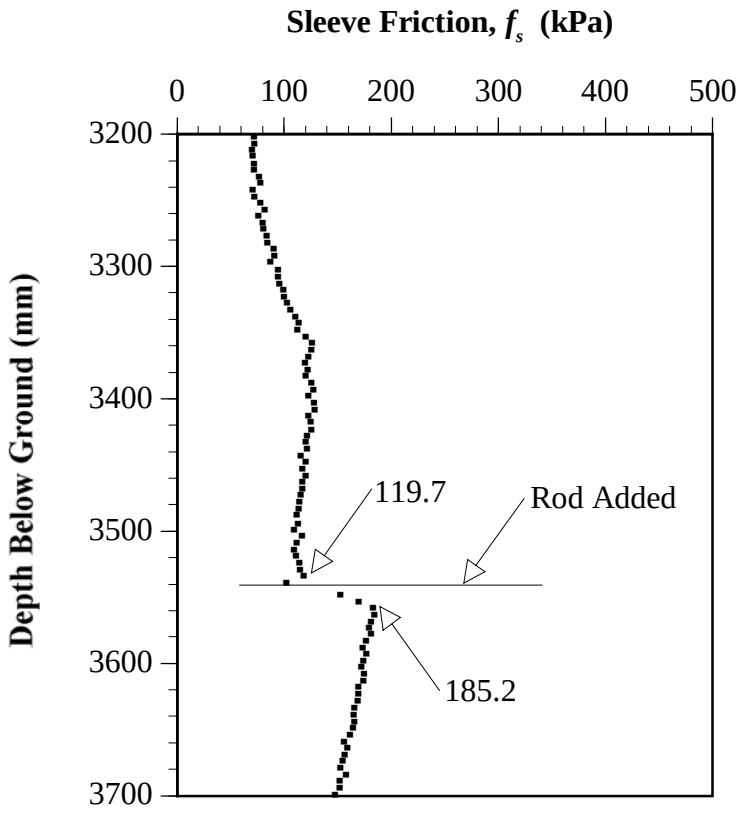

Figure 5.43 Rebound phenomenon from A0.

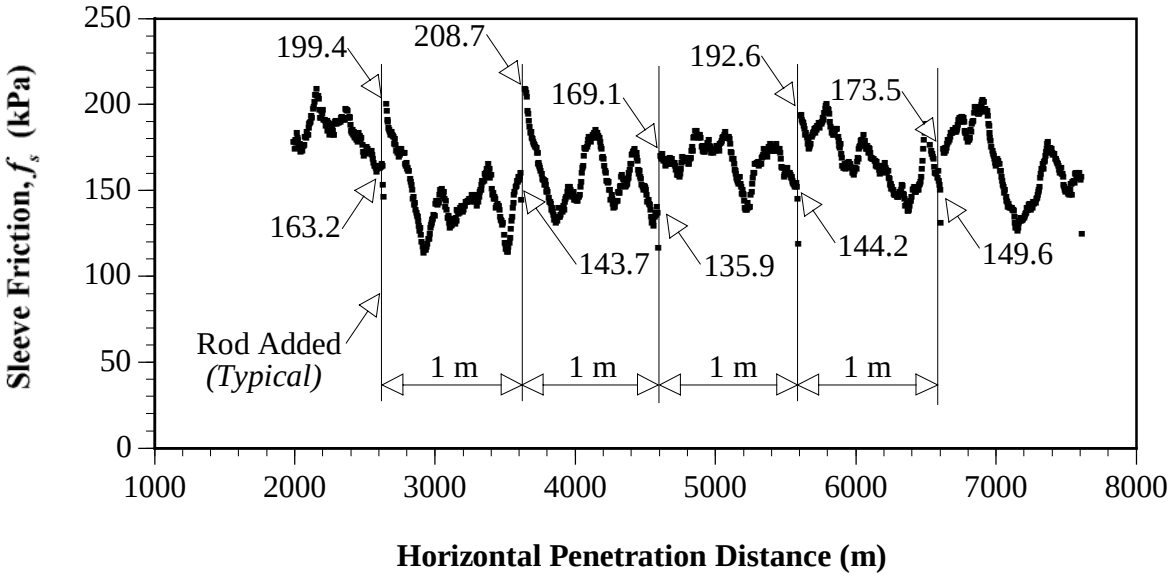

Figure 5.44 Rebound phenomenon from the horizontal CPT from the Keswick site.

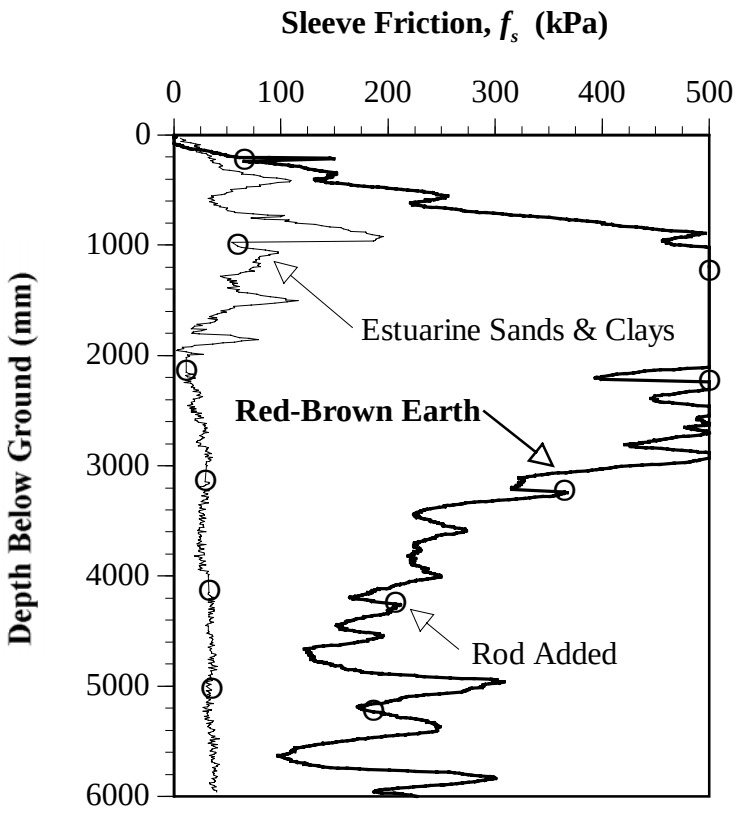

Figure 5.45 Sleeve friction measurements from CPTs performed in red-brown earth and estuarine sands and clays.

Since the Keswick Clay is overconsolidated as a result of desiccation, as described previously in §2.3.2.1(i), it is proposed that the rebound phenomenon is a consequence of rebound of the Keswick Clay. As a result of this rebound phenomenon, the profile of f_s measurements is unreliable and does not reflect the 'true' distribution of f_s within the Keswick Clay at that particular location. Use can only be made of f_s measurements obtained from the first stage of penetration; that is, from the ground surface to the depth at which the first drilling rod was added.

The CPT I1 is one of the few CPTs performed, either at the South Parklands or the Keswick sites, that provides a reasonable amount of f_s data within the Keswick Clay, as shown in Figure 5.46. As can be seen from this graph, since the likely surface of the Keswick Clay is encountered at a depth of approximately 2.1 metres below ground, and the first rod was added at a depth of 3.18 metres, little over one metre of f_s data are available for analysis. As before, the OLS quadratic trend was removed from these data in order to create a stationary data set, as indicated by Figure 5.47. This plot suggests that the data appear to be stationary (which is supported by the fact that Kendall's τ test was passed), although the data may be heteroscedastic. There are too few data, however, to justify any variance transformations.

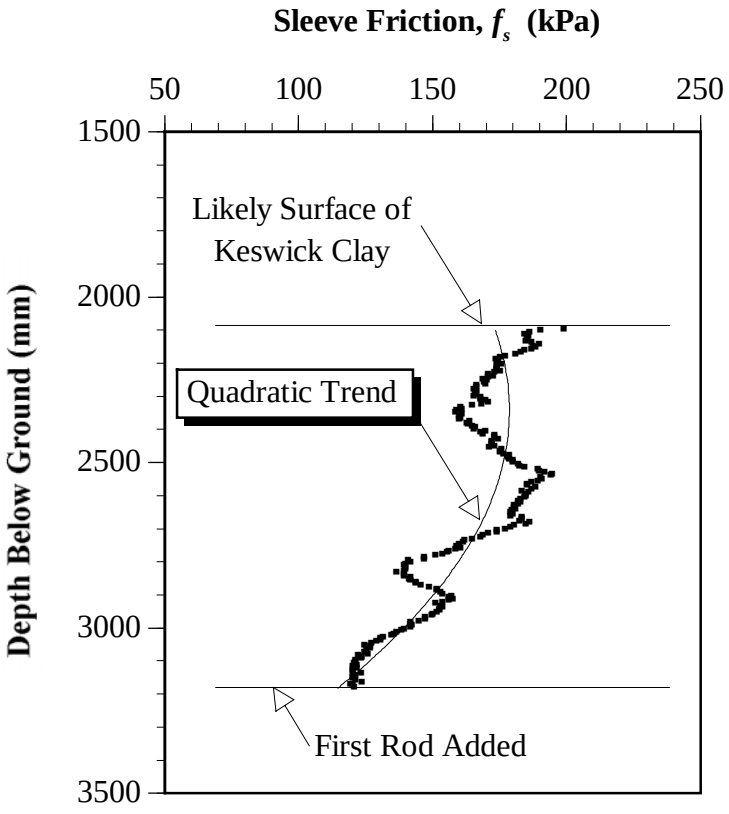

Figure 5.46 Sleeve friction measurements from I1.

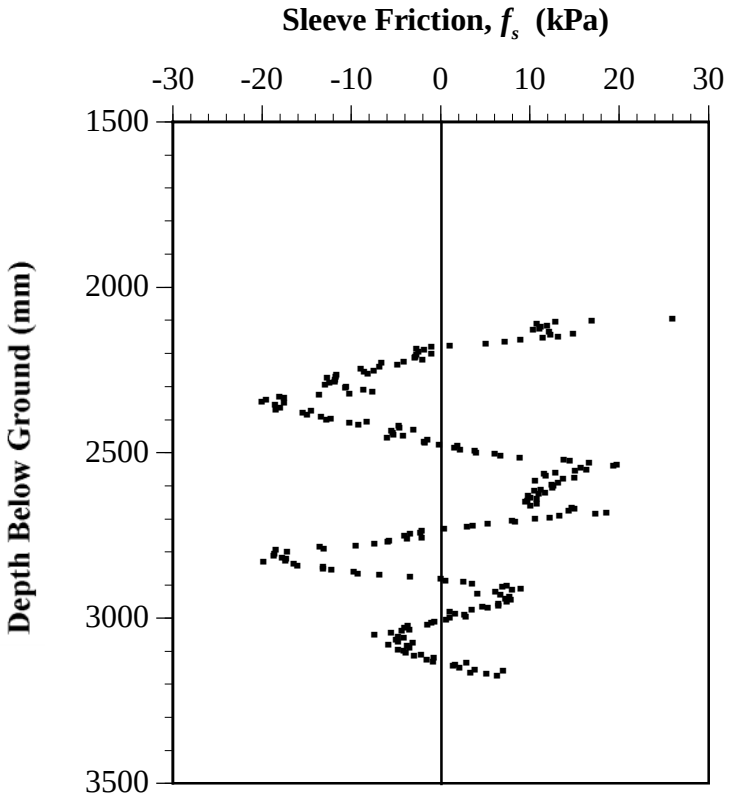

Figure 5.47 Residuals of sleeve friction measurements from I1.

Again, the sample ACF and the experimental semivariogram were evaluated, and the results are shown in Figures 5.48 and 5.49, respectively. The simple exponential and the squared exponential models, proposed by Vanmarcke (1977a, 1983), were fitted to the sample ACF by means of OLS regression, the results of which are given below.

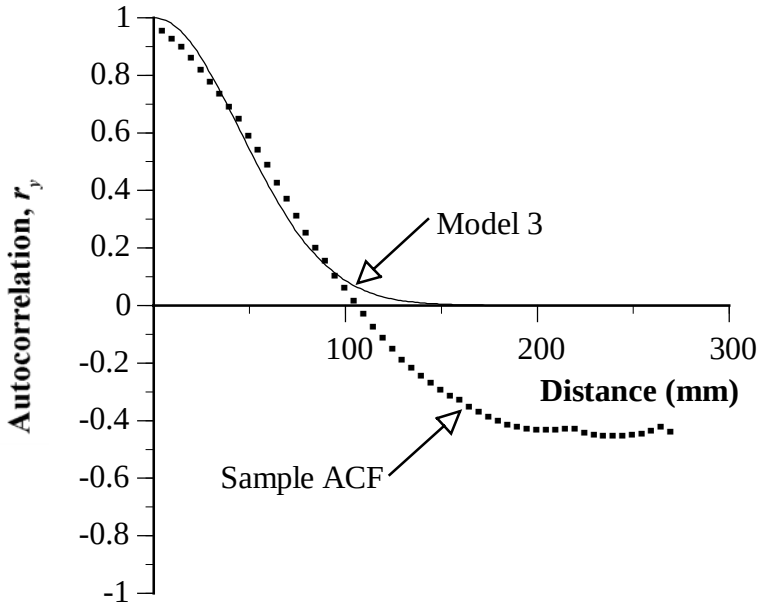

Figure 5.48 Sample autocorrelation function and model obtained from residuals of f_s measurements from I1.

(i) Model 2:
$$\rho_y = e^{-|y|/b} \quad \text{where: } b = 52.2 \text{ mm} \tag{5.24}$$
$$\delta_{V_2} = 2b = 104.4 \text{ mm} \tag{5.25}$$

(ii) Model 3:
$$\rho_y = e^{-(|y|/c)^2} \quad \text{where: } c = 63.8 \text{ mm} \tag{5.26}$$
$$\delta_{V_3} = \sqrt{\pi}\, c = 113.1 \text{ mm} \tag{5.27}$$

(iii) Bartlett's distance, r_B, was found to equal 95 mm.

Again, the scale of fluctuation, δ_v, is very close to r_B. An appropriate spherical model was fitted to the experimental semivariogram, and the parameters were found to be:

a = 240 mm;
C = 0.0173 MPa^2;
C_0 = 0 MPa^2.

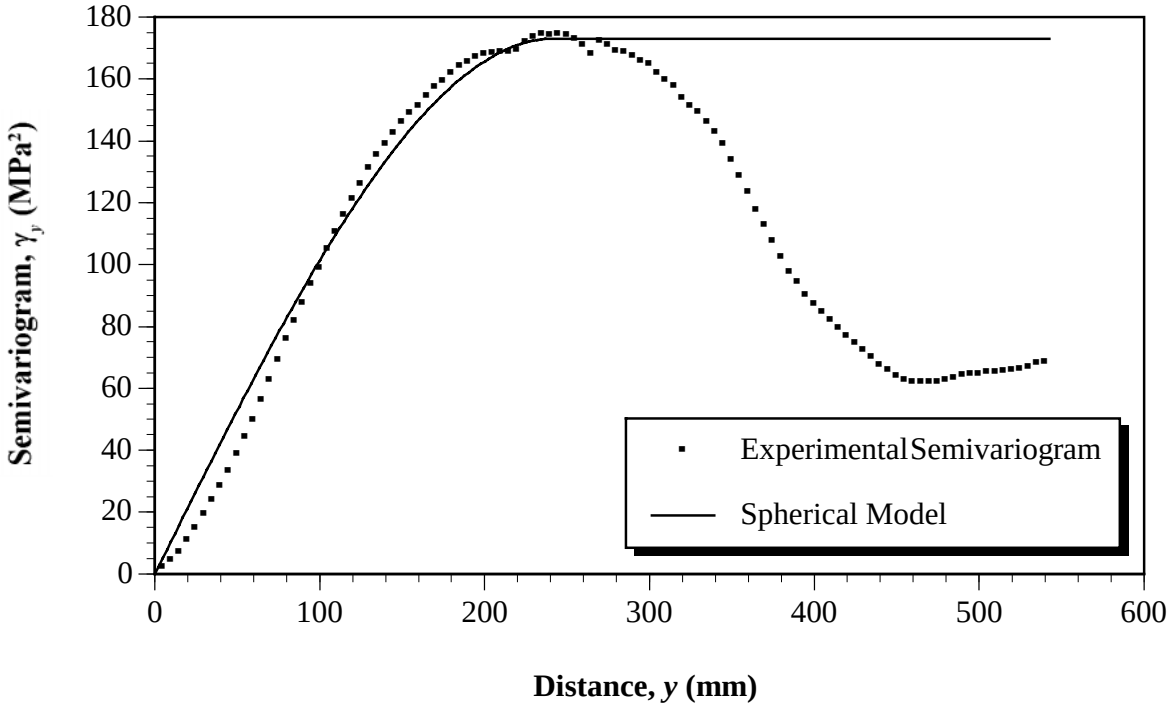

Figure 5.49 Experimental semivariogram and spherical model obtained from residuals of f_s measurements from I1.

It is evident from Figure 5.49, that beyond the range, a = 240 mm, the experimental semivariogram exhibits a monotonically *decreasing* behaviour. Since, in this case, there is a sufficient number of data pairs associated with each of the experimental semivariogram values ($N_{\min}$ = 108 at y = 540 mm), this monotonically decreasing behaviour must be associated with some other phenomenon. Journel and Huijbregts (1978) suggested that a semivariogram which displays a growth which is not monotonic is said to exhibit a *hole effect*. The genesis of hole effects are periodicities within the random field, which may result from the interception of layer boundaries whose elevation fluctuates with lateral distance (Journel and Huijbregts, 1978; Hohn, 1988). It is possible that the hole effect may be the result of variations caused by gilgai structures within the Keswick Clay. However, it is difficult to confirm this, since a large number of sampling boreholes would be required to determine the extent of gilgais within the site. Journel and Huijbregts (1978) suggested that, for estimation purposes, an experimental hole effect that is open to a doubtful interpretation, or is not very marked, can simply be ignored. Should one wish to model a hole effect, however, it is possible to do so using the *hole effect semivariogram model* (Journel and Huijbregts, 1978; Olea, 1991):

$$\gamma_h = C\left(1-\frac{\sin(ah)}{ah}\right)+C_0 \tag{5.28}$$

As a verification of the relationship between δ_v and a, substituting a = 240 mm into Equation (5.22) yields an estimate of δ_v equal to 138.5 mm, which is slightly higher than the 110 mm determined above.

The results of this one analysis, concerning the spatial variability of measurements of f_s within the Keswick Clay, indicate that the values of δ_v, r_B and a are within the ranges of those found earlier. Because of the relatively small number of reliable measurements of f_s, subsequent spatial variability analyses will be confined to measurements of q_c, alone. The sleeve friction data, nevertheless, will be used in the next section to investigate the most appropriate value for the shift distance, by means of cross-correlation analyses.

5.3.5 Cross-Correlation Analysis: q_c and f_s

Several researchers and codes of practice (Standards Association of Australia, 1977; Campanella et al., 1983; American Society of Testing and Materials, 1986; Schmertmann, 1978; De Beer et al., 1988) suggest that, when interpreting or presenting CPT results, attention should be given to the fact that measurements of q_c and f_s do not correspond to the same depth. Schmertmann (1978) suggested that if attention is not given to this depth anomaly, errors can result from the interpretation of CPT measurements, such as the calculation of the *friction ratio*, F_R. Generally, this is achieved by shifting the f_s values back by the *shift distance*; usually 75 mm. However, it is difficult to know the 'true' shift distance, as it is a complex variable which involves the extent of the zones of soil contributing to the measurements of q_c and f_s, and the distance between these zones. The evaluation of the shift distance is made more difficult because the extent of these zones is a function of the soil type, as mentioned in §2.4.6.

Campanella et al. (1983) suggested that, for heavily interbedded soils and relatively stiff soils, the shift distance may be significantly greater than the standard shift distance, in their case equal to 100 mm. The authors developed a data presentation program which enables the user to input any value for the shift distance and, in addition, provides a facility for the evaluation of the shift distance, whereby the peaks and troughs of the q_c and f_s profiles may be matched by means of the graphical capabilities of a computer.

Alternatively, the cross-correlation function (CCF) provides a statistical technique for determining this shift distance. The recorded values of f_s measured from CPT I1 within the Keswick Clay, and shown previously in Figure 5.46, were combined with the measurements of q_c at the same depths, and substituted into Equations (2.46) and (2.47), via *SemiAuto*. The resulting sample CCF is shown in Figure 5.50.

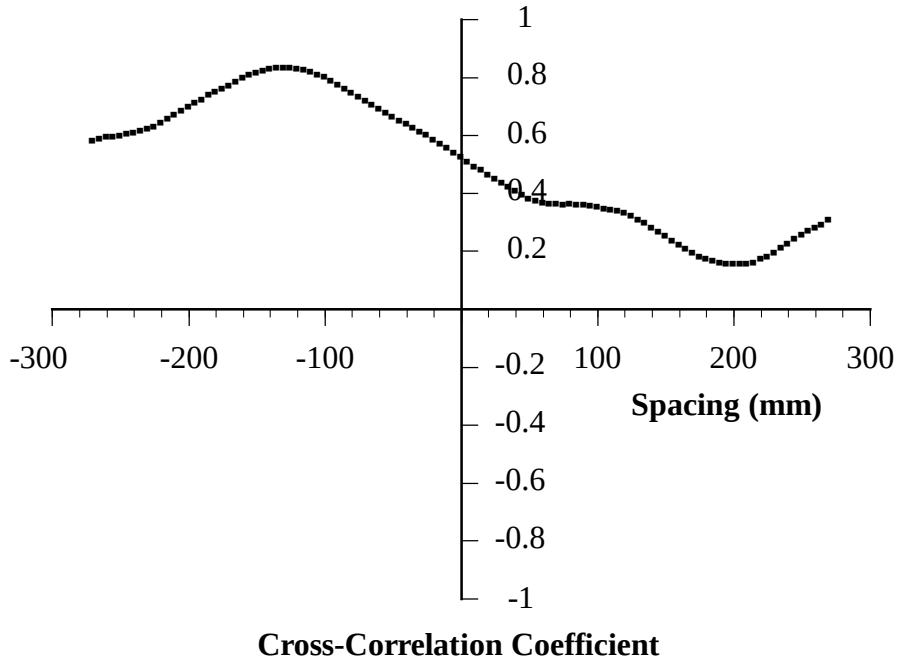

Figure 5.50 Sample cross-correlation function of cone tip resistance and sleeve friction measurements, from within the Keswick Clay, from CPT I1.

It can be seen clearly from Figure 5.50 that the maximum value of the cross-correlation coefficient, $r_{k_{XY}}$, occurs at a spacing of −125 mm[27]. This implies that the optimal shift distance is 125 mm, somewhat higher than the actual physical spacing of 75 mm.

While the CCF shown in Figure 5.50 was derived from sleeve friction data free from the influence of rebound, as discussed previously, there are extremely limited sleeve friction data, measured from within the Keswick Clay, which fit this criterion. As a consequence, in order to derive a reliable CCF based on a large population size, it is preferable to use the entire q_c and f_s measurements of each CPT. In order to evaluate an appropriate shift distance for the Keswick Clay, of the 222 vertical CPTs performed in the South Parklands site, 77 were chosen, effectively at random, for the purpose of cross-correlation analyses. Of the 77 examined, 60 yielded sensible results, and these are summarised in Table 5.10; whereas the remaining 17 produced inappropriate, or ambiguous, shift distances. The results given in Table 5.10, provide a range of shift distances varying from −70 to −165 mm, with a mean of −112.7 mm, standard deviation of 22.56 mm and a coefficient of variation of 20.0%.

[27] For each of the cross-correlation analyses referred to in this section, a negative value of spacing implies that the sleeve friction measurements are shifted *upwards* relative to the cone tip resistance values.

Table 5.10 Results of cross-correlation analyses performed on measurements of q_c and f_s, from 60 of the 222 vertical CPTs, from the South Parklands site.

CPT No.	Shift Distance (mm)	Maximum $r_{k_{XY}}$	CPT No.	Shift Distance (mm)	Maximum $r_{k_{XY}}$
A0	−135	0.853	**CD20**	−135	0.917
A2	−120	0.957	**CD24**	−125	0.948
A3	−110	0.916	**D4**	−75	0.856
A4	−105	0.861	**D8**	−115	0.763
A5	−145	0.858	**D10**	−95	0.942
A8	−105	0.967	**E4**	−80	0.877
A10	−95	0.911	**E53**	−130	0.926
B7	−80	0.879	**E7**	−115	0.568
B8	−125	0.585	**F13**	−70	0.929
B10	−125	0.896	**F33**	−150	0.939
C0	−90	0.705	**F42**	−125	0.926
C8	−130	0.773	**F6**	−105	0.939
CD1	−95	0.826	**F64**	−115	0.583
CD2	−105	0.824	**F8**	−80	0.587
CD3	−90	0.733	**F94**	−105	0.617
CD4	−135	0.772	**G0**	−105	0.945
CD5	−110	0.832	**G4**	−110	0.949
CD6	−105	0.852	**G9**	−125	0.883
CD7	−80	0.862	**G10**	−110	0.755
CD8	−90	0.913	**H0**	−120	0.881
CD9	−70	0.895	**H5**	−100	0.952
CD11	−135	0.946	**I1**	−110	0.721
CD12	−165	0.922	**I7**	−145	0.926
CD13	−130	0.953	**I10**	−160	0.731
CD14	−130	0.875	**J0**	−75	0.842
CD15	−140	0.683	**J1**	−90	0.877
CD16	−95	0.565	**J6**	−110	0.890
CD17	−155	0.983	**K0**	−135	0.871
CD18	−100	0.961	**K4**	−120	0.861
CD19	−115	0.820	**K8**	−110	0.875

The majority of the CPT data yielded CCFs that enabled a relatively straightforward and unambiguous value of the shift distance to be determined. Two such examples are given in Figures 5.51 and 5.52. As can be seen from these figures, a single and/or relatively obvious maximum value for the correlation coefficient is given, which can readily be associated with an appropriate shift distance. For example, Figure 5.51 yields a maximum value of 0.916 for the correlation coefficient, which occurs at a distance of −110 mm,

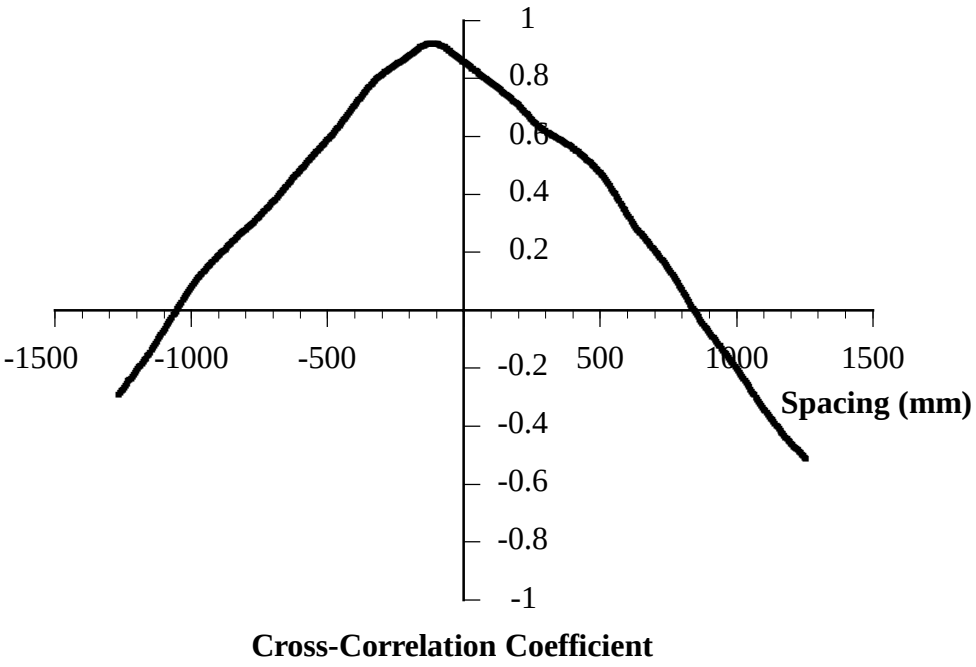

Figure 5.51 Sample CCF of q_c and f_s measurements from CPT A3.

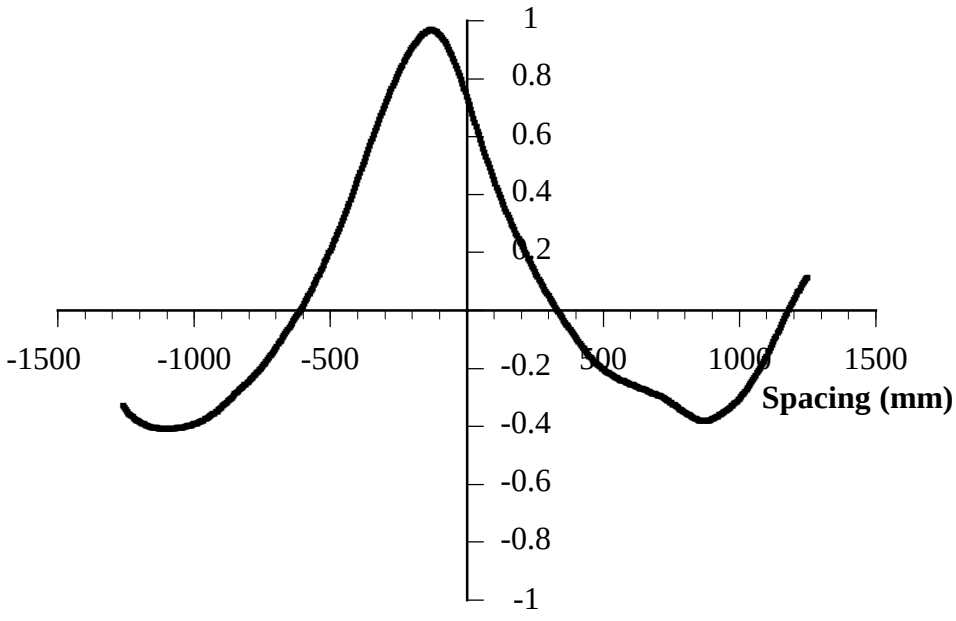

Figure 5.52 Sample CCF of q_c and f_s measurements from CPT B10.

whereas Figure 5.52 produces a maximum value of 0.963 at a shift distance of −125 mm. Occasionally, however, the cross-correlation analyses yielded CCFs that indicated inappropriate shift distances. Two such examples are given in Figure 5.53. As is evident from these plots, the global maximum value of the cross-correlation coefficient, for both CPTs A1 and CD40, yield unrealistic values for the shift distance. In the majority of cases the occurrence of a 'poor' CCF, as shown in Figure 5.53, can be explained by the presence of one or more relatively large rebound phenomena, contained within the sleeve friction data. However, not every poor CCF can be attributed to this. The CPT CD40 is a good example. As shown in Appendix A, where the complete CPT profile of CD40 is given, this cone penetration test does not appear to have any obvious data irregularities, nor rebound phenomena, that one would expect would cause poor cross-correlation results. In addition, since each of the CPTs, including CD40, contain measurements of q_c and f_s from soils other than the Keswick Clay, it is possible that these values contribute, in some way, to the poor cross-correlation results. Yet, Figure 5.53, clearly demonstrates that *local* maxima occur at shift distances consistent with those given in Table 5.10. In fact, each of the 17 cases which resulted in poor CCFs, yielded local maxima which compare well with those in Table 5.10.

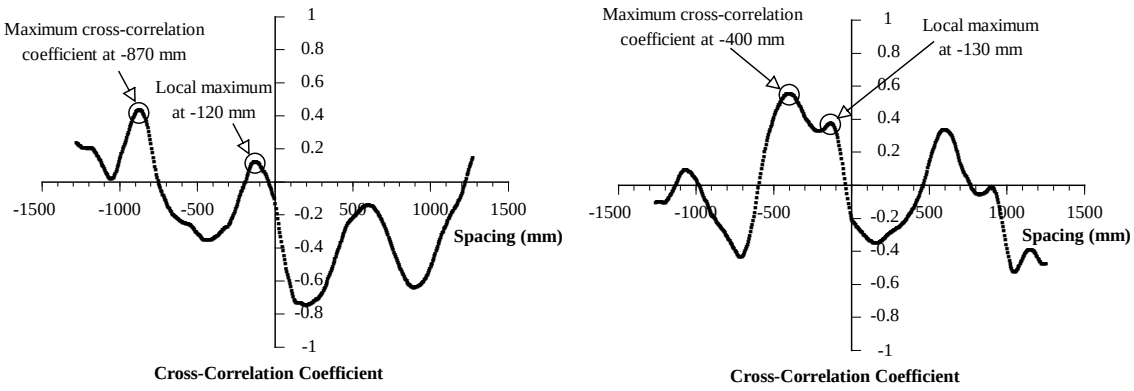

Figure 5.53 Sample CCF of q_c and f_s measurements from CPT: (a) A1 and (b) CD40.

The measurements of q_c and f_s, obtained from the horizontal CPT and performed at the Keswick site, were also used to generate the sample CCF, the results of which are shown in Figure 5.54. As can be seen from this figure, the maximum cross-correlation coefficient, of magnitude 0.607, occurs at a shift distance of −120 mm, which is consistent with the results given in Table 5.10.

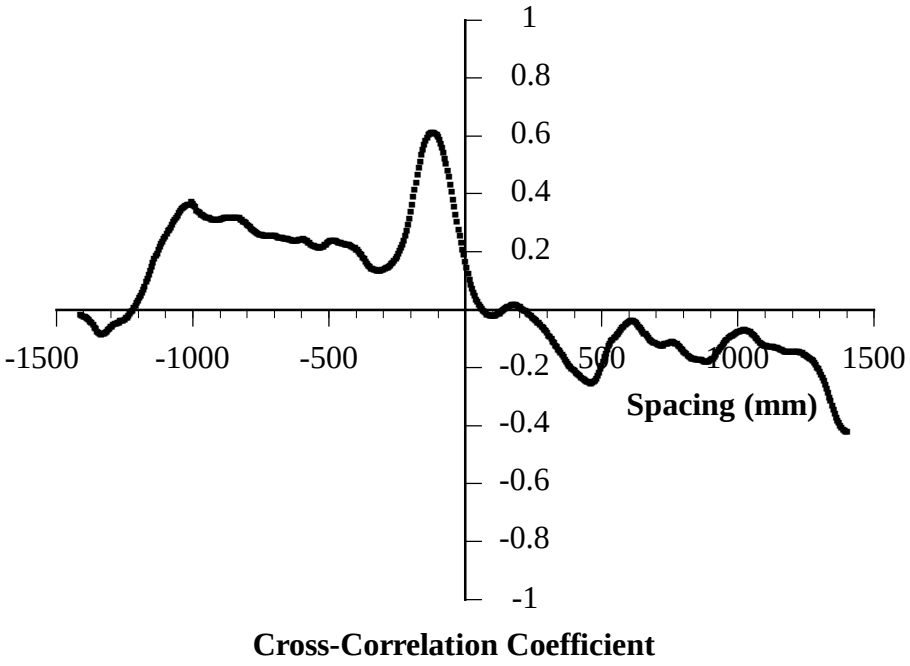

Figure 5.54 Sample CCF of q_c and f_s measurements from the horizontal CPT performed at the Keswick site.

In summary, the cross-correlation analyses presented in this section suggest that, statistically, the most appropriate shift distance associated with CPTs performed in the Keswick Clay varies between −70 and −165 mm, with a mean of −112.7 mm, standard deviation of 22.56 mm and a coefficient of variation of 20.0%.

5.3.6 Discussion of Spatial Variability Results

Throughout the course of the analyses presented in this chapter, it has been found that the distance indicated by the intersection of the sample ACF and the $+2/\sqrt{N}$ line, presently referred to as Bartlett's distance, r_B, yields almost identical values to those of the scale of fluctuation, δ_v. Since δ_v is evaluated by fitting one of Vanmarcke's ACF models to the sample ACF by means of ordinary least squares (OLS), it is computationally more efficient to evaluate r_B, instead. While it has been shown, in each of the relevant analyses performed in this chapter, that r_B yielded excellent estimations of δ_v, it remains to be demonstrated whether such a relationship will be observed in other soil types.

The results presented in this section have been obtained using the classical decomposition technique for the transformation of non-stationary data. While the process of differencing is a valid and useful technique for transforming non-stationary data to the state of stationarity, it is known that such a process completely destroys the continuity of the

original data, which is an undesirable outcome when quantifying the correlation distance of a soil (Campanella et al., 1987). In fact, the sample ACF of the residuals, after first- or subsequent differencing, yields essentially a white noise process, or at best, a significant peak up to a lag of perhaps 3. In addition, the experimental semivariogram of the differenced residuals also demonstrates a white noise process, as indicated by a pure nugget model. This would imply an extremely small correlation distance and range of influence, which is in conflict with the results obtained from classical decomposition, as well as those published in the literature. While the technique of differencing is used extensively in random field theory, particularly in the Box-Jenkins methodology, it is not used at all in the field of geostatistics. As a consequence of this, the transformation process of differencing has not been used to assess the correlation distance, nor the range of influence of the Keswick Clay, but will be used in the next section to determine the usefulness of ARIMA models as estimators of the spatial variability of these soils.

The vertical correlation distance of the undrained shear strength of the Keswick Clay has been found to lie within the range 60 to 240 mm, with a mean of 150 mm and a *CV* of 30%. Table 5.11 presents a summary of vertical and horizontal correlation distances ($\equiv \delta_v$) for s_u, q_c and f_s of clay soils published in the literature. (These results were given previously in Table 2.10). It is evident, from Table 5.11, that the vertical correlation distance varies between 0.13 and 8.6 metres. While the vertical correlation distance obtained for the Keswick Clay of 0.15 metres lies at the lower end of the range reported by others, it is in general agreement with the results presented by Campanella et al. (1987), Li and Lee (1991), and Wickremesinghe and Campanella (1993). From observations of the vertical experimental semivariograms, it is possible that a larger-scale nested structure exists within the Keswick Clay. The maximum layer thickness of the clay is approximately 7 metres and, in this study, its spatial variability has been examined over the upper 4 metres of this soil. As a consequence, any larger-scale nested structure, if one exists, must have a vertical correlation distance greater than 4 metres. In this investigation, since the extent of cone penetration testing has been confined to a maximum depth of 5 metres, the presence of a vertical correlation distance greater than 0.15 metres cannot be discounted.

Investigation of the horizontal spatial variability of the undrained shear strength of the Keswick Clay has indicated that a nested structure exists within this soil. At the micro-scale, the clay has been shown to exhibit a horizontal correlation distance of 0.15 metres and a range, *a*, of 0.19 metres. At a larger-scale, the clay manifested a horizontal correlation distance of 1 to 2 metres and a range, *a*, of between 5 and 6 metres. To date, no researcher has investigated the horizontal spatial variability of soil properties at closely-spaced, lateral intervals. Perhaps as a consequence of this, the geotechnical engineering

Table 5.11 Summary of vertical and horizontal correlation distances ($\equiv \delta_v$) of s_u, q_c and f_s of clay soils published in the literature.

Soil Type	Geotech. Property	Direction (H: Horiz., V: Vert.)	Scale of Fluctuation δ_v (m)	Sampling Interval Δz_0 (m)	Researcher(s)
Marine Clay, Hong Kong	s_u	V	6.0	0.3	Lumb (1974)
Chicago Clay	s_u	V	8.6	?	Wu (1974)
Marine Clay, Japan	s_u	V	1.3 - 2.7	1.0 - 7.7	Matsuo (1976)
New Liskeard Varved Clay, Canada	s_u	V	5	≈ 1.5	Vanmarcke (1977b)
	s_u	H	46	≈ 25	
Seabed Deposits, Nth. Sea	q_c	H	53	> 20	Tang (1979)
Soft Clay, New York	s_u	V	2.4	1.0 - 3.3	Asaoka and A-Grivas (1982)
	s_u	V	6.2	3.0 - 4.8	
Deltaic Soils, Canada	q_c	V	0.13 - 0.71	0.025	Campanella et al. (1987)
Silty Clay, California	q_c	V	0.68	0.1	Spry et al. (1988)
Silty Clay	q_c	V	0.2	0.020	Li & Lee (1991)
Deltaic Soils, Canada	q_c	V	0.24 - 0.32	0.025	Wickremesinghe and Campanella (1993)
	f_s	V	0.35 - 0.40	0.025	

literature suggests that soils exhibit horizontal correlation distances of the order of 50 metres (Vanmarcke, 1977b; Tang, 1979).

Furthermore, with respect to correlation distances, by the very nature of the CPT, one would expect soils to exhibit correlation over some finite distance. Figure 5.55 shows the failure zone associated with a vertical CPT performed in the Keswick Clay. It was shown in Table 4.4 that, for the Keswick Clay, the rigidity index, I_r, was found to vary between 15.0 and 116.5, with a mean of 67.4. Using the relationships given by Teh and Houlsby (1991), shown in Figure 2.10, with a_c = 17.9 mm, $\beta = 60°$ and I_r = 67.4, the parameters z_p and r_p, were found to equal 65 mm and 122 mm, respectively, as shown in Figure 5.55. It can be seen from this figure that as the CPT progresses, the failure zone 'front' follows the cone penetrometer with an offset equal to z_p, or 65 mm. As a consequence, the measurements of q_c and f_s are spatially averaged values within this failure zone. Therefore, one would expect, as a minimum, soils located within a depth of 38 mm (I_r = 15.0) to 90 mm (I_r = 116.5), to exhibit correlation as a result of this soil failure zone.

The cross-correlation results, presented in §5.3.5, indicated that, statistically, the most appropriate value for the shift distance for the Keswick Clay is approximately 120 mm,

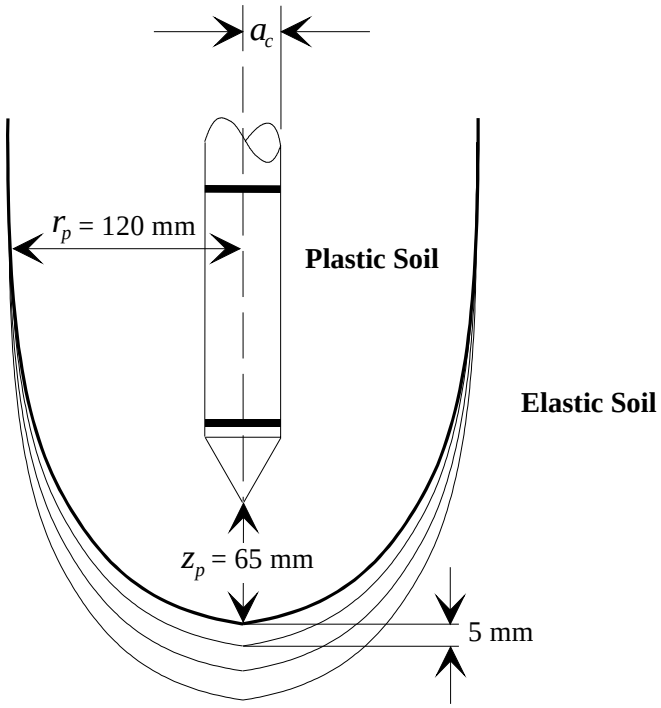

Figure 5.55 Extent of the failure zone of the CPT in Keswick Clay. (a = 17.9 mm, β = 60° and I_r = 67.4)

both vertically and horizontally. One would expect the value to be slightly greater than the physical distance separating the cone tip and sleeve friction load cells, that is, approximately 75 mm. This is because the centroid of the soil contributing to the measurement of q_c is below the cone tip, as shown in Figure 5.55. Consequently, the distance between this centroid and the centre of the friction sleeve is greater than 75 mm, and depends on the extent of the failure zone.

5.3.7 Summary

In summary, the analyses presented in this section have yielded the following results:

- Using random field theory analyses, the vertical correlation distance of the cone tip resistance, q_c, of the Keswick Clay (and hence s_u) has been found to be in the range of 60 to 240 mm, with a mean of approximately 150 mm and a *CV* of 30%. Using geostatistics, the vertical range of influence of q_c of the Keswick Clay (and hence s_u) was found to be between 100 to 575 mm, with a mean of approximately 290 mm and a *CV* of 40%.

- Using geostatistics, the lateral spatial variation of the undrained shear strength of the Keswick Clay has been found to exhibit a nested structure, which is satisfactorily modelled using the following nested spherical model:

$$\gamma_x = 0 + 230\left(\frac{3x}{2a_1} - \frac{x^3}{2a_1^3}\right) + 160\left(\frac{3x}{2a_2} - \frac{x^3}{2a_2^3}\right)$$

where: a_1 = 0.2 metres;
a_2 = 6 metres.

- The vertical correlation distance of the sleeve friction, f_s, of the Keswick Clay was found to be 95 mm, and the range of influence, a, of f_s was found to equal 240 mm. Both of these values lie within the ranges observed for q_c.

The following section makes use of these results to develop random field theory and geostatistical models, to stochastically describe the spatial variability of the undrained shear strength of the Keswick Clay.

5.4 MODEL FORMULATION, PARAMETER ESTIMATION, FORECASTING AND DATA SIMULATION

The results of the analyses, presented in §5.3, provide a framework for the formulation of spatial variability models that stochastically describe the measured CPT data. They also enable measurements, at yet untested locations, to be estimated. This section details the process of formulating, both random field and geostatistical models. For the analysis of random fields, as shown in Figure 2.14, the process of defining a model involves the estimation of its parameters and diagnostic checking. Once the model has been formulated, forecasts can then be obtained. For geostatistics, on the other hand, the model is defined by the model semivariogram, and forecasts, or estimates, are obtained by the process of kriging. In addition, with the relevant model defined, it is possible to generate an infinite number of simulated data sets. Both random field theory and geostatistics provide frameworks whereby such simulated data may be generated. Data simulations are particularly useful in reliability and risk analyses. These processes of model formulation, parameter estimation, forecasting and data simulation, for both random field theory and geostatistics, are treated separately below.

5.4.1 Random Field Theory

Before examining the random field models associated with the 30 CPTs studied in the previous section, by means of introduction, and also to verify the calculations, it is worth looking briefly at the analyses presented by Ravi (1992).

5.4.1.1 Re-examination of Ravi's (1992) Analysis

As discussed in §2.5.2.1, Ravi (1992) re-examined the data presented by Asaoka and A-Grivas (1982) and used standard time series techniques to fit ARMA models to the 5 separate sets of data. One such data set, from borehole A-1, is given in Figure 5.56 and Table 5.12. Using their method, described previously in §2.5.2.1, Asaoka and A-Grivas (1982) proposed the following model for the A-1 data set:

$$\bar{s}_u = \frac{\beta_0}{1-\beta_1} z = \frac{1.401}{1-0.437} z = 2.488z \qquad (5.29)$$

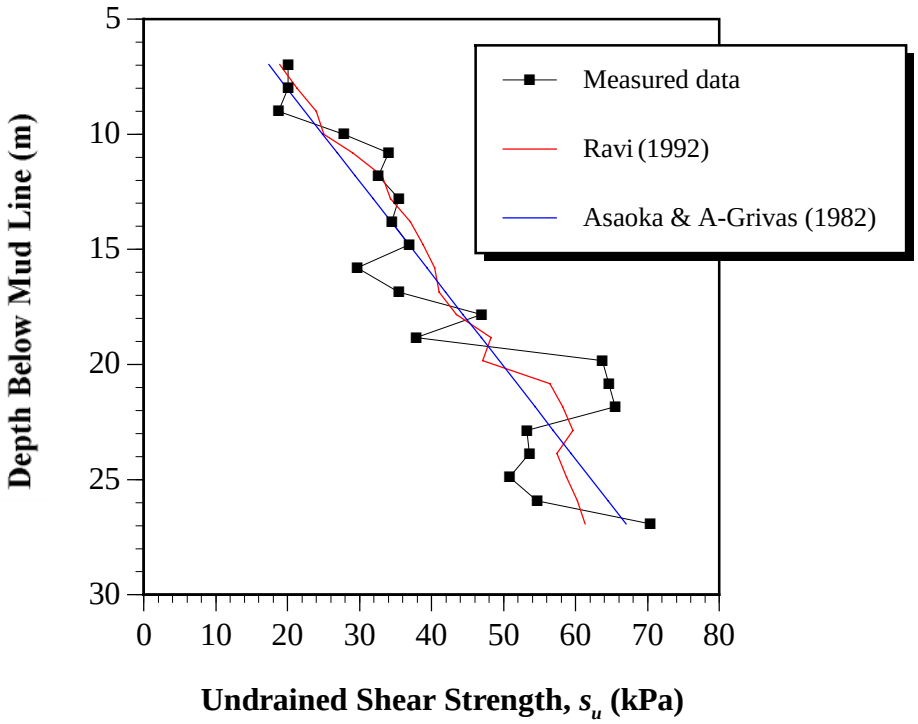

Figure 5.56 Data from borehole A-1 with models proposed by Asaoka and A-Grivas (1982) and Ravi (1992).

Table 5.12 Undrained shear strength data from borehole A-1 presented by Asaoka and A-Grivas (1982) and re-examined by Ravi (1992).

Depth Below Mud Line (m)	Undrained Shear Strength (kPa)	Depth Below Mud Line (m)	Undrained Shear Strength (kPa)
6.98	20.1	17.83	46.9
7.99	20.1	18.84	37.8
8.99	18.7	19.84	63.7
10.00	27.8	20.85	64.6
10.82	34.0	21.85	65.5
11.80	32.6	22.86	53.2
12.80	35.4	23.87	53.6
13.81	34.5	24.90	50.8
14.81	36.9	25.91	54.6
15.82	29.7	26.91	70.4
16.86	35.4		

Ravi (1992), after removing the OLS linear and quadratic trends from the data, fitted an AR(1) model to the measurements of undrained shear strength. A summary of the model presented by Ravi is given below.

$$Z_t = 0.33Z_{t-1} + a_t \tag{5.30}$$

where: a_t has a mean of zero and a variance of 45.1.

The models proposed by Asaoka and A-Grivas (1982) and Ravi (1992) are shown graphically in Figure 5.56, along with the original data. It is common practice in the assessment of models, to measure the sum of the squared differences, *SSD*, between the measured data, *Y*, and the model estimate, Y^*, as shown in the following equation:

$$SSD = \sum_{i=1}^{n} \left(Y_i - Y_i^* \right)^2 \tag{5.31}$$

where: Y_i is the *i*th measurement;
Y_i^* is the model estimate of the *i*th element;
n is the number of data.

Ravi (1992) calculated the sum of the squared differences, *SSD*, for both his AR(1) model and that proposed by Asaoka and A-Grivas (1982), and found that the *SSD*s equalled 950.9 and 1103.0, respectively. While the difference between the two *SSD*s is relatively small, the difference calculated for the other 4 data sets was more marked. As a result, Ravi

argued that traditional time series modelling yielded better estimates than the technique proposed by Asaoka and A-Grivas (1982). The measurements of s_u obtained from borehole A-1, given previously in Table 5.12, were input into *PEST* (Brockwell and Davis, 1991), a one-dimensional, time series analysis and computer modelling package. As can be seen from Figure 5.56, a strong trend exists between s_u and the depth below the mud line. In addition, these data failed both the runs test and Kendall's τ test and, as a consequence, the untransformed data are non-stationary. As Ravi (1992) suggested, the OLS quadratic trend was removed from these data. Such a transformation yields a stationary data set, as indicated by the fact that the runs test and Kendall's τ test were both passed. Ravi suggested that the most appropriate ARMA model for each of the 5 data sets is a first-order autoregressive process; that is, an ARMA(1,0), or simply an AR(1). After entering this model, as well as the detrended data into the software package, *PEST* yielded the following parameter estimates by means of the maximum likelihood method:

$$Z_t = 0.314 Z_{t-1} + a_t \tag{5.32}$$

where: a_t has a mean of zero and a variance, σ_a^2, of 45.10.

As described in §2.5.1.2(v), the adequacy of a model is assessed by examining the residuals. Brockwell and Davis (1987, 1991) suggested the use of residuals, $\hat{W}_t$, which are one-step prediction errors and are given by the following relationship:

$$\hat{W}_t = \frac{\left(Y_t - \hat{Y}_t\right)}{\sqrt{\mathrm{E}\left[Y_t - \hat{Y}_t\right]^2 / \sigma_a^2}} \tag{5.33}$$

where: Y_t is the random field, or time series, data;

$\hat{Y}_t$ is the best linear mean-square predictor of Y_t, based on the observations up to distance, $t - 1$;

σ_a^2 is the white noise variance of the fitted model.

These residuals are then rescaled as follows:

$$\hat{W}_t^{(r)} = \frac{\sqrt{n}\,\hat{W}_t}{\sum_{j=1}^{n} \hat{W}_t^2} \tag{5.34}$$

As suggested by Brockwell and Davis (1991), these rescaled residuals were then examined for autocorrelation. Inspection of the ACF of the residuals, as well as the portmanteau test, indicated that the residuals were in fact uncorrelated, suggesting that the AR(1) model and its estimated parameters were appropriate. Interestingly, if these rescaled residuals are

recombined with the original OLS quadratic trend and superimposed on to the measured data, as shown in Figure 5.57, a slightly better fit is obtained than by the models proposed by both Ravi (1992) and Asaoka and A-Grivas (1982). In fact, the sum of the squared differences, *SSD*, was found to be 946.8, a slight improvement on the model proposed by Ravi (1992) which was quoted as having an *SSD* equal to 950.9. However, examination of Figures 5.56 and 5.57 suggest that, while the model proposed by Ravi (1992) is a significant improvement of that proposed by Asaoka and A-Grivas (1982), it falls far short of adequately modelling the spatial variability of the data.

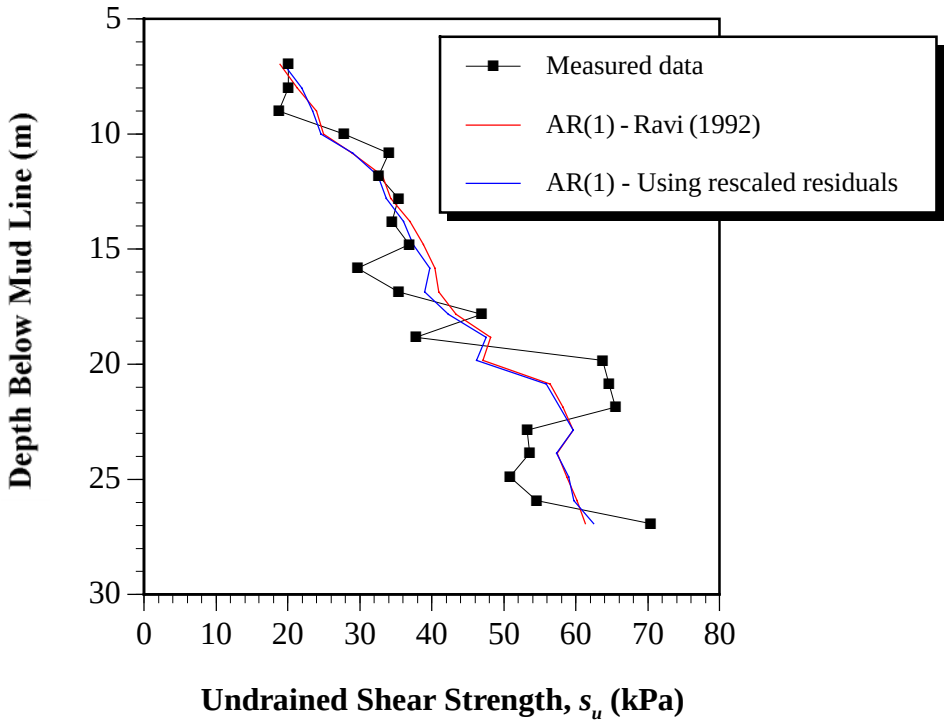

Figure 5.57 Data from borehole A-1 with the model proposed by Ravi (1992) and that obtained by using rescaled residuals.

The analyses presented in this section have shown that the random field theory model formulation, parameter estimation, and forecasting calculations, are equivalent to those performed by other researchers. The following section analyses the CPT data presented earlier in this chapter.

5.4.2 Random Field Analyses of Keswick Clay

Before forecasts of values of q_c for the Keswick Clay can be generated, it is first necessary to formulate random field models and estimate their parameters. The following section summarises the analyses performed in each of these stages.

5.4.2.1 Model Formulation and Parameter Estimation

Firstly, in order to introduce the calculations involved in the process of model formulation and parameter estimation, a typical CPT, C8, is examined in some detail. The measurements of q_c within the Keswick Clay, for CPT C8, were given previously in Figures 5.8 to 5.10, and are included in Figures A.13 to A.26 in Appendix A. The sample PACF of the residual q_c data, from C8, is shown in Figure 5.58.

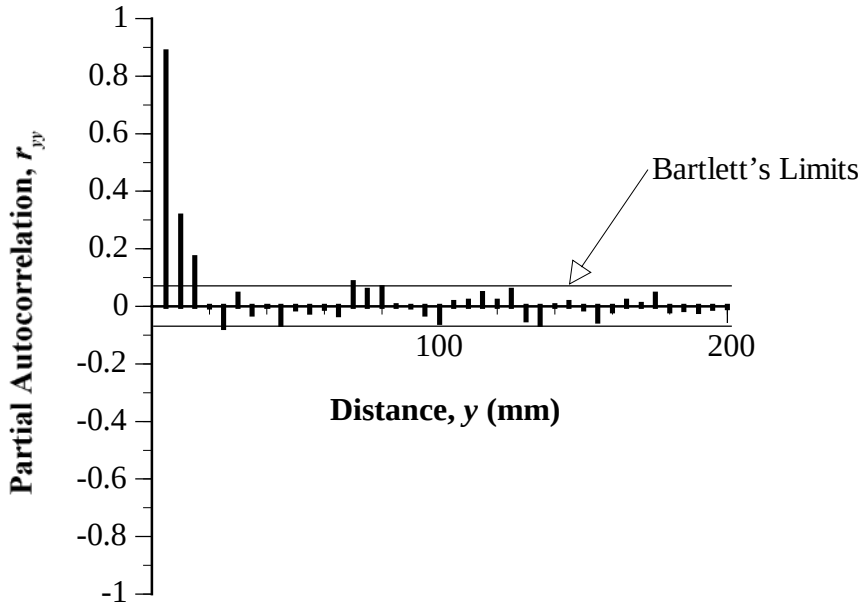

Figure 5.58 Sample PACF obtained from the residuals of q_c for C8 after classical transformation, that is, removal of the OLS quadratic trend.

It can be seen from Figure 5.58 that the sample PACF cuts off after a distance of 15 mm, or lag 3. This, together with the fact that the sample ACF decays in an exponential fashion (Figure 5.10), indicates that the appropriate model is an autoregressive process of order 3; that is, an AR(3). Preliminary estimates of the AR parameters are obtained from *PEST* and

are: $\phi_1 = 0.669$; $\phi_2 = 0.152$; and $\phi_3 = 0.111$. These parameters are then optimised by means of the maximum likelihood method and the resulting AR(3) model is:

$$Z_t = 0.672Z_{t-1} + 0.154Z_{t-2} + 0.114Z_{t-3} + a_t \tag{5.35}$$

where: a_t has a mean of zero and a variance, σ_a^2, of 0.0372.

Diagnostic tests performed on the rescaled residuals yielded the following results:

- Portmanteau test: For $K = 20$, $Q = 24.04$. $\chi_5^2(17) = 27.59$ ∴ Pass;
- Test based on turning points: 535. Asymptotically normal = 520.7 ∴ Pass;
- Difference-sign test: 385. Asymptotically normal = 391 ∴ Pass;
- Rank test: 149,169. Asymptotically normal = 153,077 ∴ Pass.

The rescaled residuals are shown in Figure 5.59 and the ACF of the rescaled residuals is given in Figure 5.60. As is evident from these figures, the residuals give no indication of non-stationarity, nor autocorrelation. Furthermore, since each of the 4 diagnostic tests were passed, as well as the test for normality (performed within *PEST*), then the AR(3) model satisfactorily describes the underlying process of the spatial variability of q_c for the CPT sounding C8.

In order to assess the suitability of a model, one approach is to superimpose the model estimates on to the original data, as was done previously in Figure 5.57. Another technique, which will be examined later in §5.4.2.2, is to compare the forecasts obtained from the model with measured data at the forecast locations. Since the rescaled residuals are actually prediction errors, the model estimates are obtained by simply adding the rescaled residuals to the original measurements. Figure 5.61 shows the estimates obtained from the AR(3) model superimposed on to the measured C8 data. As can be seen from the figure, the model estimates provide an excellent representation of the spatial variability of the q_c measurements. The sum of the squared differences, *SSD*, between the model estimates and the original q_c data, was evaluated and found to equal 2.82 MPa^2. This relatively low value of the *SSD* is a further indication that the AR(3) model is an excellent descriptor of the spatial variability of the q_c measurements.

An alternative to the classical transformation approach is to use differencing, as detailed previously in §2.5.1.2(ii). The measurements of q_c for sounding C8, shown previously in Figure 5.8, were differenced at lag 1, that is, first-differenced; the residuals of which are given in Figure 5.62. Performing Kendall's τ test on the first-differenced data, yielded $\tau = 0.0019$, $z_\tau = 0.080$ and $c = 1.004$, which indicates that the transformed data are stationary. Inspection of the scatterplot (Figure 5.62), the sample ACF (Figure 5.63)

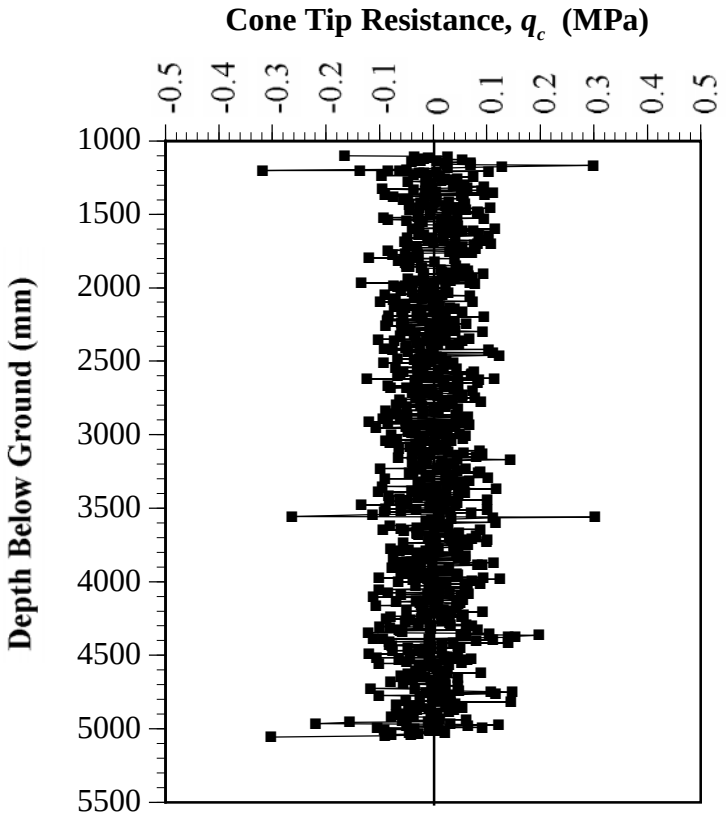

Figure 5.59 Rescaled residuals after fitting an AR(3) model to the classically transformed measurements of q_c for sounding C8.

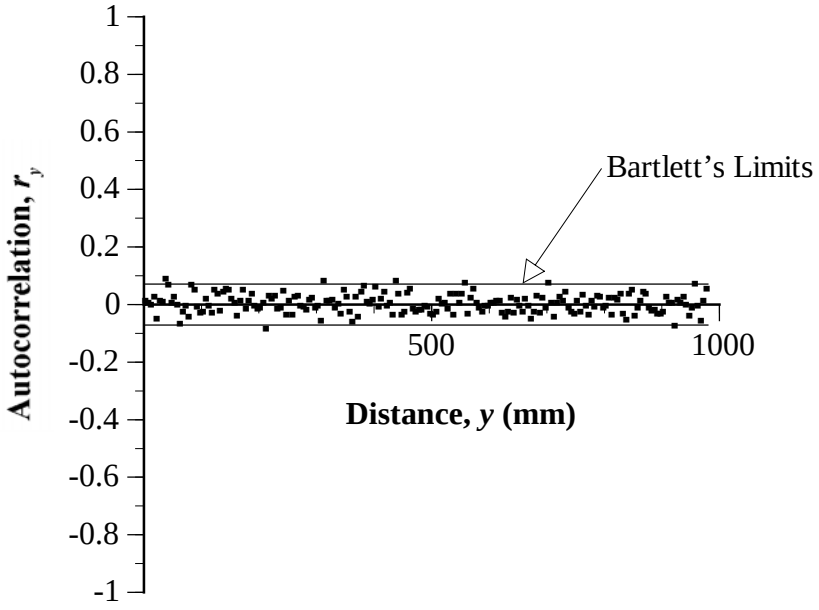

Figure 5.60 ACF of the rescaled residuals of q_c for C8 after fitting an AR(3) model.

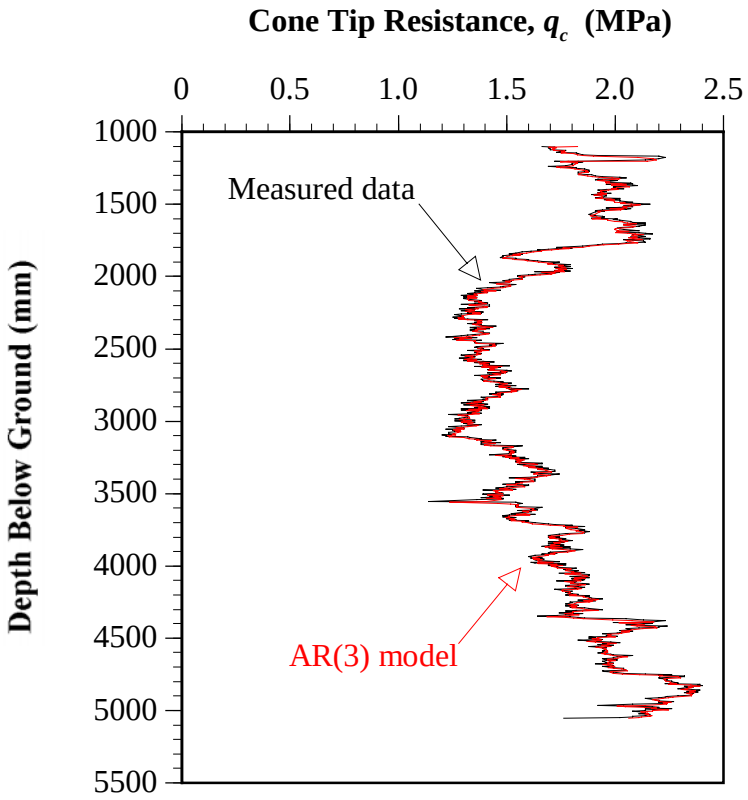

Figure 5.61 Measured q_c data from C8 with the AR(3) model obtained by using rescaled residuals.

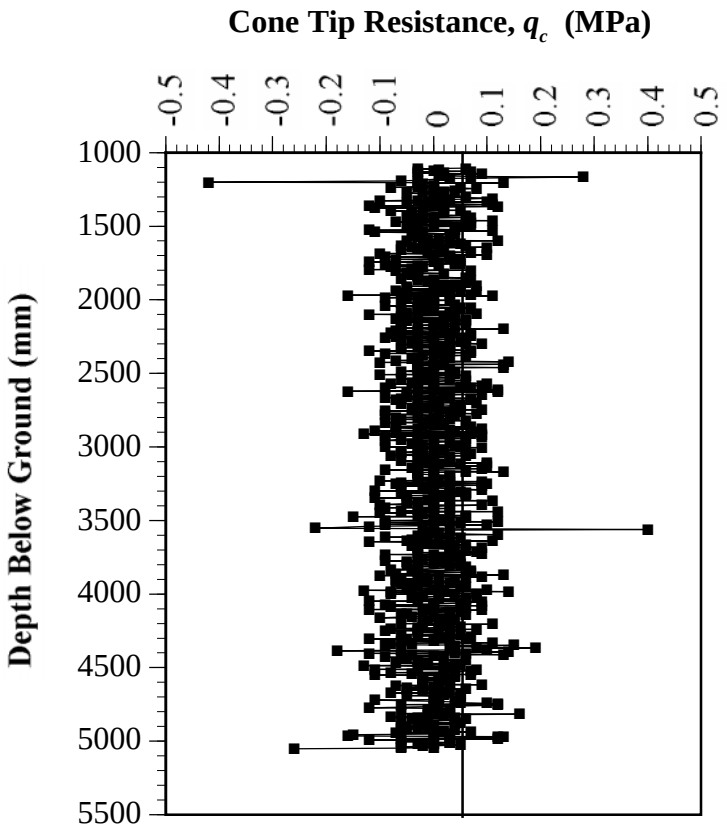

Figure 5.62 Residuals of q_c, for sounding C8, after first-differencing.

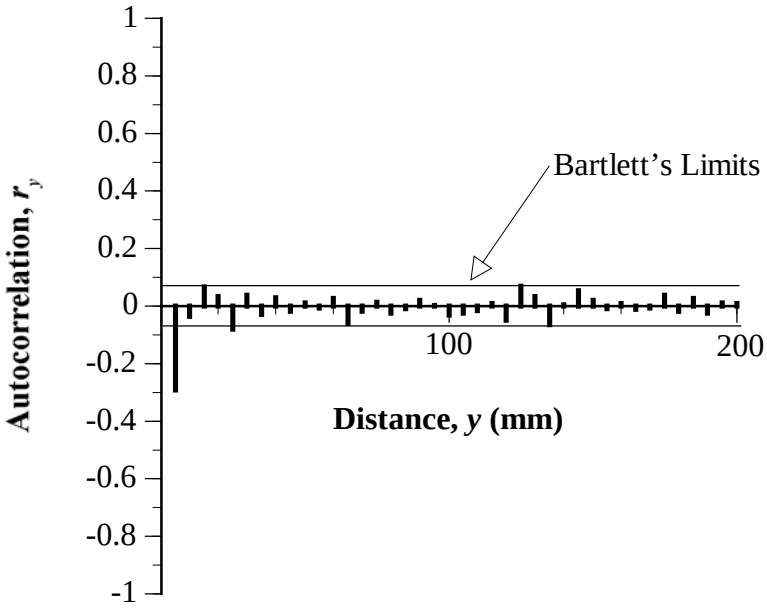

Figure 5.63 Sample ACF obtained from the residuals of q_c, for sounding C8, after first-differencing.

and the experimental semivariogram (Figure 5.64), confirm the conclusion of stationarity. The runs test, on the other hand, yielded R = 462 and z_R = 5.484, which suggests that the data are non-stationary. This, again, supports the conclusion that the runs test may be an inappropriate assessor of stationarity, either when the data fluctuates relatively slowly about the mean, as is the case with the measurements of q_c from C8, or when the number of data is large, say greater than 50. The sample ACF and PACF of the first-differenced data are given in Figures 5.63 and 5.65. It can be clearly seen from these figures that the sample ACF cuts-off after lag 1 (a distance of 5 mm) and the sample PACF cuts-off after lag 2 (a distance of 10 mm). This suggests that an integrated moving average process of order 1, or IMA(1,1), is an appropriate model. A preliminary estimate of the IMA parameter is obtained from *PEST* and is: $\theta_1 = -0.299$. This parameter is then optimised by means of the maximum likelihood method and the resulting IMA(1,1) model is:

$$Z_t = a_t - 0.321a_{t-1} \tag{5.36}$$

where: a_t has a mean of zero and a variance, σ_a^2, of 0.0375.

Diagnostic tests performed on the rescaled residuals yielded the following results:

- Portmanteau test: For K = 20, Q = 26.79. $\chi_5^2(19) = 30.14$ ∴ Pass;
- Test based on turning points: 528. Asymptotically normal = 520 ∴ Pass;
- Difference-sign test: 382. Asymptotically normal = 391 ∴ Pass;
- Rank test: 153,340. Asymptotically normal = 152,686 ∴ Pass.

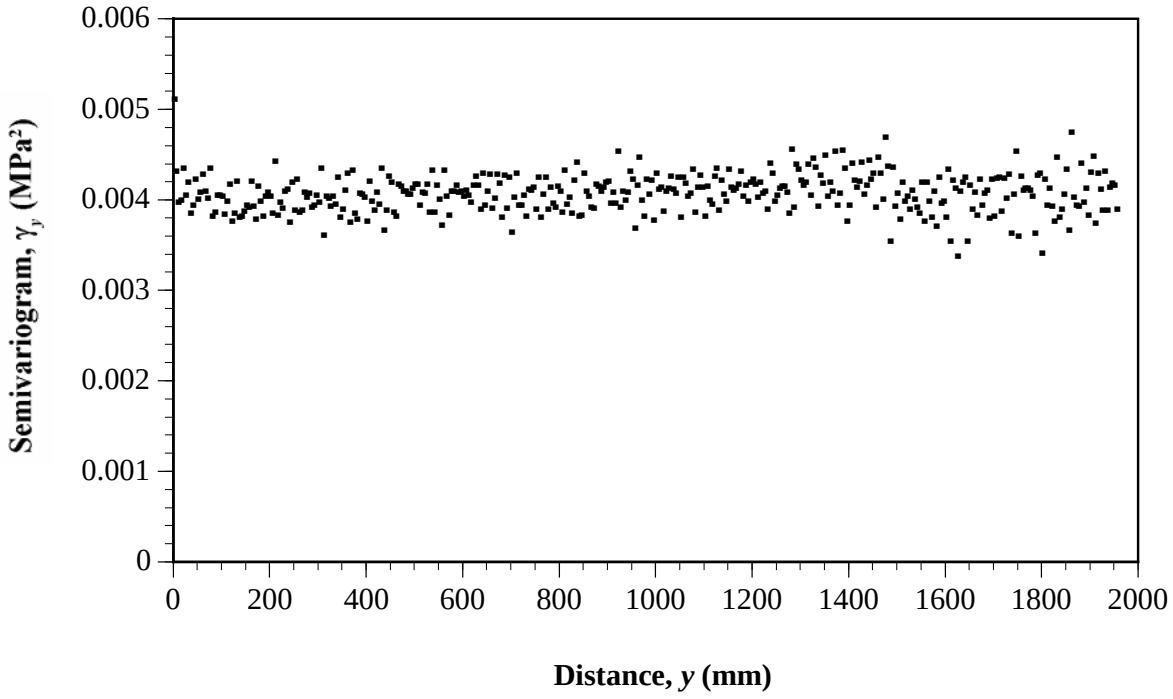

Figure 5.64 Experimental semivariogram obtained from the residuals of q_c, for sounding C8, after first-differencing.

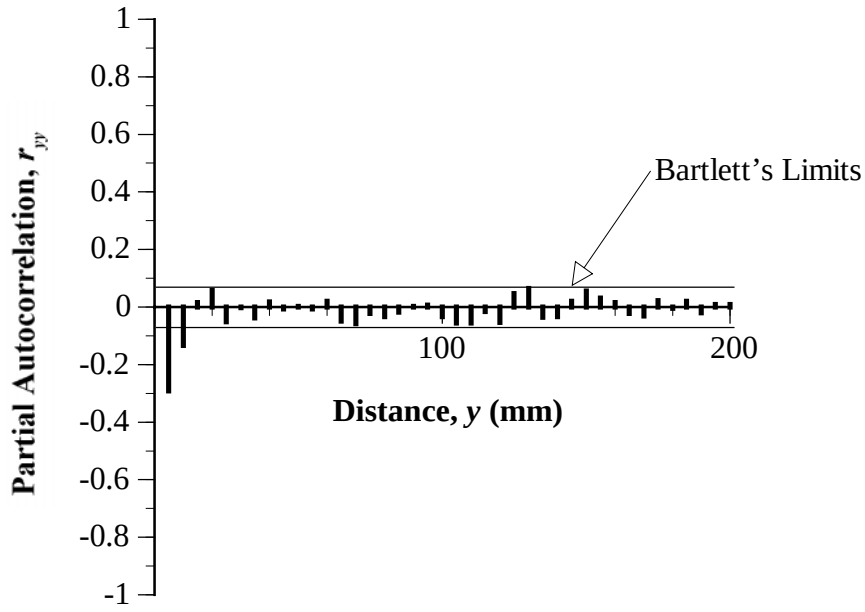

Figure 5.65 Sample PACF obtained from the residuals of q_c, for sounding C8, after first-differencing.

The rescaled residuals are shown in Figure 5.66 and the ACF of the rescaled residuals is given in Figure 5.67. As is evident from these figures, the residuals give no indication of non-stationarity, nor autocorrelation, and, since each of the diagnostic tests were passed, the IMA(1,1) model satisfactorily describes the underlying process of the spatial variability of q_c, for the CPT sounding C8.

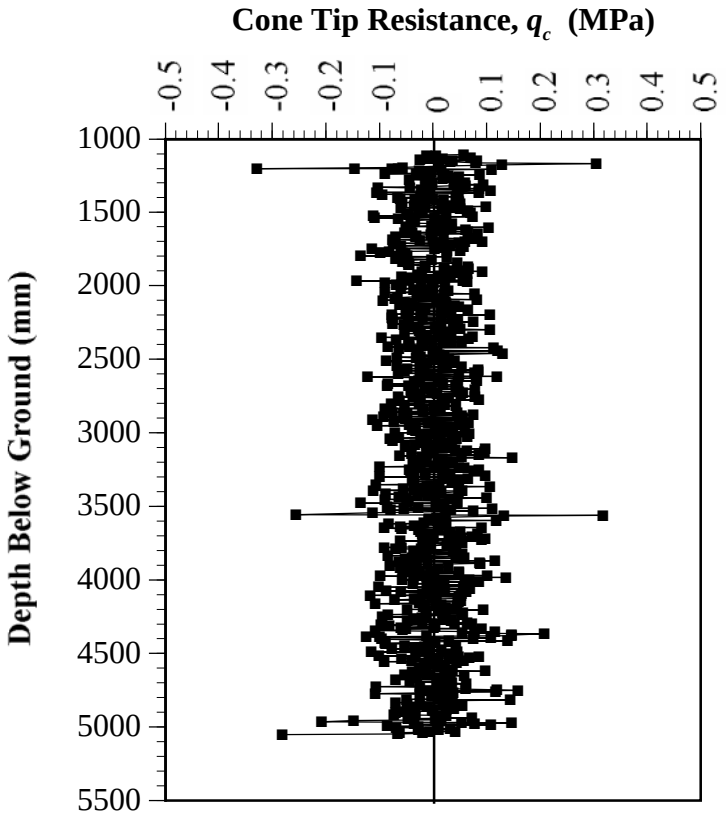

Figure 5.66 Rescaled residuals, after fitting an IMA(1,1) model to the first-differenced measurements of q_c, for sounding C8.

Again, in order to assess the suitability of the proposed IMA(1,1) model, the estimates are superimposed onto the original data, as shown in Figure 5.68. The model estimates were obtained by *undifferencing* the rescaled residuals, shown previously in Figure 5.66, with the original q_c measurements. Undifferencing is achieved by reversing the differencing process, that is:

$$Y_t = \nabla Y_t + Y_{t-1} \tag{5.37}$$

where: ∇Y_t is the rescaled residual at location, t;

Y_{t-1} is the original q_c measurement at location, $t-1$.

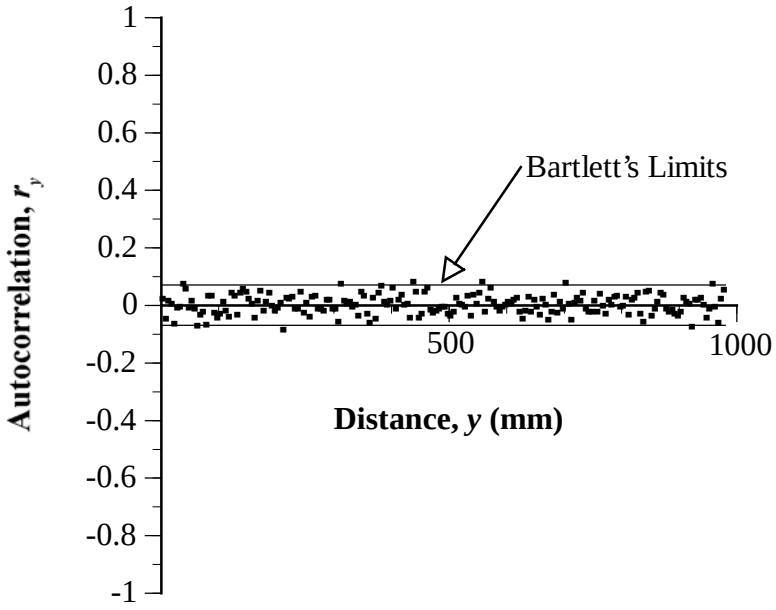

Figure 5.67 ACF of the rescaled residuals of q_c for C8 after fitting an IMA(1,1) model.

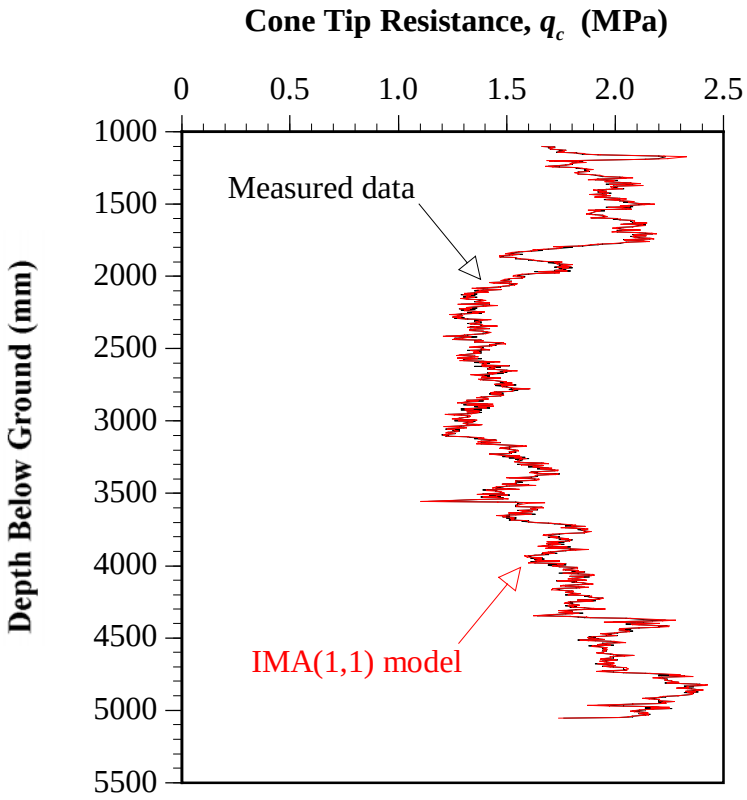

Figure 5.68 Measured q_c data from C8 with the IMA(1,1) model obtained by using rescaled residuals.

As can be seen from Figure 5.68, the IMA(1,1) model is an excellent representation of the spatial variability of the q_c measurements. The sum of the squared differences, *SSD*, between the model estimates and the original q_c data, was found to equal 0.29 MPa^2. Again, this extremely low *SSD* gives further confirmation that the IMA(1,1) model is an excellent descriptor of the spatial variability of the q_c measurements, and that it is slightly superior to the AR(3) model (*SSD* = 2.82 MPa^2) given by classical transformation.

Based on the approach given above, the same 30 vertical CPTs from the South Parklands, which were examined previously in §5.3.1 and Table 5.3, were entered into the program, *PEST*, in order to determine the parameters of the most appropriate ARIMA model. The results of these analyses are summarised in Tables 5.13 and 5.14: Table 5.13 giving the results which refer to classically transformed data; and Table 5.14 giving the results which refer to differenced data. In addition, Tables 5.13 and 5.14 present the variance, σ_a^2, of the white noise component, a_t, of the ARMA and ARIMA models; as well as the sum of the squared differences, *SSD*, between the original measured data and the model estimates. In obtaining the results presented in Tables 5.13 and 5.14 the following steps were performed:

1. The values of q_c measured within the Keswick Clay, for each of the 30 CPT data sets, were, first, separately entered into *SemiAuto*. The data were then rationalised, in accordance with §3.4.3.2, to account for missing data. Each of the 30 data sets were transformed, either by classical transformation, or by first-differencing. Kendall's τ tests, performed previously on the classically transformed data (refer to Table 5.4), supported the hypothesis that the residuals are stationary; whereas, each of the first-differenced data sets also passed Kendall's τ test, suggesting that these data are also stationary.

2. The sample ACF, and the sample PACF, were calculated for each of the stationary data sets. The sample ACF and PACF were used to provide a preliminary estimate of the appropriate ARMA or ARIMA model, using the rules given in §2.5.1.2(v).

3. The transformed q_c data for each of the 30 CPTs were then input separately into *PEST*, where, in addition to the sample ACF and PACF, preliminary ARMA and ARIMA models were proposed and preliminary estimates of the autoregressive ϕ parameters and the moving average θ parameters, were obtained by means of relationships similar to those given in §2.5.1.2(v).

4. The preliminary estimates of the ϕ and θ parameters were optimised within *PEST*, by means of the maximum likelihood method.

Table 5.13 Results of random field analyses performed on classically transformed residuals of q_c measurements obtained from 30 of the 222 vertical CPTs performed at the South Parklands site.

CPT No.	No. of Data	ARMA Model	ARMA Parameters	σ_a^2 (MPa^2)	*SSD* (MPa^2)
A0	546	AR(3)	0.433, 0.312, 0.219	0.0272	1.49
A1	517	AR(3)	0.536, 0.250, 0.178	0.0261	1.35
A2	416	AR(3)	0.592, –0.136, 0.468	0.0853	3.55
A4	545	AR(8)	0.634, 0.208, 0.036, –0.067 0.262, 0.039, –0.054, –0.093	0.0031	1.68
A6	525	AR(5)	0.929, 0.162, 0.090, –0.092, –0.106	0.0319	2.78
A8	405	AR(2)	0.640, 0.222	0.0289	1.17
A10	327	AR(3)	0.482, 0.280, 0.191	0.0352	1.15
B1	494	AR(2)	0.425, 0.479	0.0243	1.20
B5	564	AR(8)	0.449, 0.258, 0.156, 0.236, 0, 0, 0, –0.160	0.112	6.34
B8	505	AR(3)	0.437, 0.321, 0.158	0.0438	2.21
C0	542	AR(2)	0.747, 0.225	0.0055	0.30
C4	560	AR(8)	0.726, 0.189, 0.177, 0, 0, –0.161, 0.123, –0.106	0.0221	1.24
C8	783	AR(3)	0.672, 0.154, 0.114	0.0372	2.82
C10	466	AR(7)	0.732, 0.332, 0, 0, 0, 0, –0.098	0.0343	1.60
CD1	501	AR(6)	0.804, 0.347, –0.032, 0, –0.015, –0.122	0.0111	0.56
CD30	400	AR(4)	0.756, 0.392, 0, –0.188	0.0053	0.23
D5	488	AR(9)	0.365, 0.182, 0.258, 0.162, 0.127, 0, 0, 0, –0.148	0.0586	3.00
D8	525	AR(3)	0.435, 0.275, 0.243	0.0278	1.46
E1	581	AR(5)	0.933, 0.150, 0.034, 0, –0.130	0.0304	1.77
E7	560	AR(3)	0.459, 0.311, 0.171	0.0327	1.83
G0	603	AR(6)	0.804, 0.333, 0.015, –.028, –0.076, –0.080	0.0052	0.31
G5	602	AR(7)	0.302, 0.368, 0.241, 0.184, 0, 0, –0.134	0.050	2.99
G10	557	AR(6)	0.710, 0.304, 0.090, 0, 0, –0.131	0.0180	1.00
H7	564	AR(6)	0.690, 0.335, 0.105, 0.031, –0.102, –0.106	0.0267	1.51
H10	559	AR(6)	0.541, 0.232, 0, 0.376, 0, –0.188	0.0210	1.18
I1	605	AR(5)	0.610, 0.413, 0.156, –0.071, –0.136	0.0097	0.59
I9	579	AR(8)	0.531, 0.127, 0.088, 0.020, 0.277, –0.019, 0.050, –0.129	0.0219	1.27
J8	560	AR(3)	0.457, 0.211, 0.198	0.0230	1.29
K0	393	AR(4)	0.930, 0.340, –0.059, –0.232	0.0043	0.17
K10	599	AR(6)	0.560, 0.341, 0.146, 0.107, –0.054, –0.131	0.0043	2.54

Note: AR parameters are given in the numerical order, that is, ϕ_1, ϕ_2, ... , ϕ_p;
SSD refers to the sum of the squared differences between the original data and the model estimates.

Table 5.14 Results of random field analyses performed on first-differenced residuals of q_c measurements obtained from 30 of the 222 vertical CPTs performed at the South Parklands site.

CPT No.	No. of Data	ARIMA Model	Mean	ARIMA Parameters	σ_a^2 (MPa^2)	*SSD* (MPa^2)
A0	545	IMA(1,1)	0.00112	–0.506	0.0279	0.39
A1	516	IMA(1,1)	0.00072	–0.433	0.0268	0.26
A2	415	IMA(1,5)	–0.00152	–0.423, –0.352, 0.222, 0.149, –0.154	0.0873	1.44
A4	544	IMA(1,5)	–0.00092	–0.343, 0.040, 0.137, 0.060, 0.119	0.0319	4.30
A6	524	No ARIMA model could be fitted to the first–differenced data				
A8	404	IMA(1,1)	–0.00136	0.309	0.0309	0.11
A10	326	IMA(1,1)	–0.00095	–0.478	0.0361	0.26
B1	493	IMA(1,2)	0.00032	–0.571, 0.246	0.0249	0.48
B5	563	IMA(1,4)	–0.00275	–0.580, 0, 0, 0.202	0.114	2.38
B8	504	IMA(1,1)	–.00012	–0.513	0.0447	0.57
C0	541	IMA(1,1)	0.00065	–0.157	0.0055	0.01
C4	559	No ARIMA model could be fitted to the first–differenced data				
C8	782	IMA(1,1)	0.00013	–0.321	0.0375	0.29
C10	465	IMA(1,6)	–0.00202	–0.342, 0.126, 0, 0, 0, 0.155	0.0347	0.25
CD1	500	No ARIMA model could be fitted to the first–differenced data				
CD30	399	IMA(1,5)	–0.00008	–0.246, 0.218, 0, 0, 0.136	0.0054	0.03
D5	487	ARIMA(2,1,2)	–0.00099	0.631, –0.257, *–1.175, 0.513*	0.0609	0.91
D8	524	IMA(1,1)	0	–0.482	0.0288	0.30
E1	580	ARIMA(5,1,5)	–0.00266	–0.154, 0.868, 0.679, –0.397, –0.176 *0, –0.748, –0.399, 0.507, 0*	0.0295	0.22
E7	559	IMA(1,1)	0.00098	–0.535	0.0327	0.51
G0	602	No ARIMA model could be fitted to the first–differenced data				
G5	601	IMA(1,3)	–0.00150	–0.711, 0.159, 0.113	0.507	1.64
G10	556	IMA(1,2)	–0.00095	–0.279, 0.115	0.0188	0.09
H7	563	IMA(1,4)	–0.00263	–0.277, 0.124, 0.079, 0.101	0.0279	0.17
H10	558	IMA(1,5)	–0.00183	–0.400, 0.118, 0.145, 0, 0.106	0.0215	0.24
I1	604	IMA(1,3)	0.00098	–0.386, 0.159, 0.114	0.0099	0.10
I9	578	IMA(1,1)	–0.00064	–0.412	0.0228	0.22
J8	559	IMA(1,1)	0.00045	–0.562	0.0235	0.38
K0	392	IMA(1,3)	0.00112	–0.106, 0.317, 0.235	0.0043	0.03
K10	598	IMA(1,1)	0.00035	–0.385	0.0448	0.39

Note: Parameters shown in *italics* are moving average parameters, i.e. θ_i, whereas the autoregressive parameters are shown normally;
IMA(d,q), the *integrated moving average* process, is equivalent to the ARIMA(0,d,q) process;
ARIMA parameters are given in the numerical order, that is, ϕ_1, ϕ_2, ... , ϕ_p, θ_1, θ_2, ... , θ_q;
SSD refers to the sum of the squared differences between the original data and the model estimates.

5. Finally, diagnostic tests were performed on the rescaled residuals. These diagnostic tests: the portmanteau test; the test based on turning points; the difference-sign test; and the rank test, examine the hypothesis that the residuals are observations from an independent and identically distributed sequence (Brockwell and Davis, 1991). In addition, the ACF of the rescaled residuals was inspected, and the rescaled residuals were tested for normality by examining the histogram of the residuals. Each of these tests assesses whether the proposed ARMA or ARIMA process satisfactorily models the underlying behaviour of the random field, bearing in mind that neither of these tests is foolproof in all situations (Brockwell and Davis, 1991). Each of the ARMA and ARIMA models presented in Tables 5.13 and 5.14 passed these 4 diagnostic tests, as well as the test for independence, as indicated by the ACF of the residuals and the test for normality.

It is evident from Tables 5.13 and 5.14 that an autoregressive (AR) process, usually of order 3, though occasionally as high as order 8 or 9, satisfactorily describes the classically transformed data. In contrast, the integrated moving average (IMA) process, usually of order 1, though occasionally as high as order 5 or 6, satisfactorily models the differenced data. In addition, Table 5.14 shows that 2 of the differenced data sets were best modelled by combined ARIMA processes. Furthermore, it is evident from the *SSD*s, given in Tables 5.13 and 5.14, that the IMA process provides a slightly better representation of the spatial variability of the measured data. However, this is not always the case, as shown in Table 5.14, since no ARIMA model could be satisfactorily fitted to 4 of the 30 CPTs examined.

Following the procedure detailed above for sounding C8, the measurements of q_c obtained from the horizontal CPT, performed at the Keswick site, were also examined. Firstly, the classically transformed data indicated an exponentially decaying sample ACF and a sample PACF which cut-off at a distance of 30 mm, or lag 6. As a consequence, an AR(6) model was investigated. After preliminary estimation of the parameters, by means of the program, *PEST*, the parameters were optimised using the maximum likelihood method, which yielded the following model:

$$Z_t = 0.769Z_{t-1} + 0.346Z_{t-2} + 0.051Z_{t-3} - 0.051Z_{t-4} + 0.071Z_{t-5} + 0.077Z_{t-6} + a_t \quad (5.38)$$

where: a_t has a mean of zero and a variance of 0.0282.

Diagnostic tests performed on the rescaled residuals suggested that the AR(6) model is a valid representation of the data. This is supported by Figure 5.69 which shows the AR(6) model superimposed on the original q_c measurements. As can be seen clearly from this

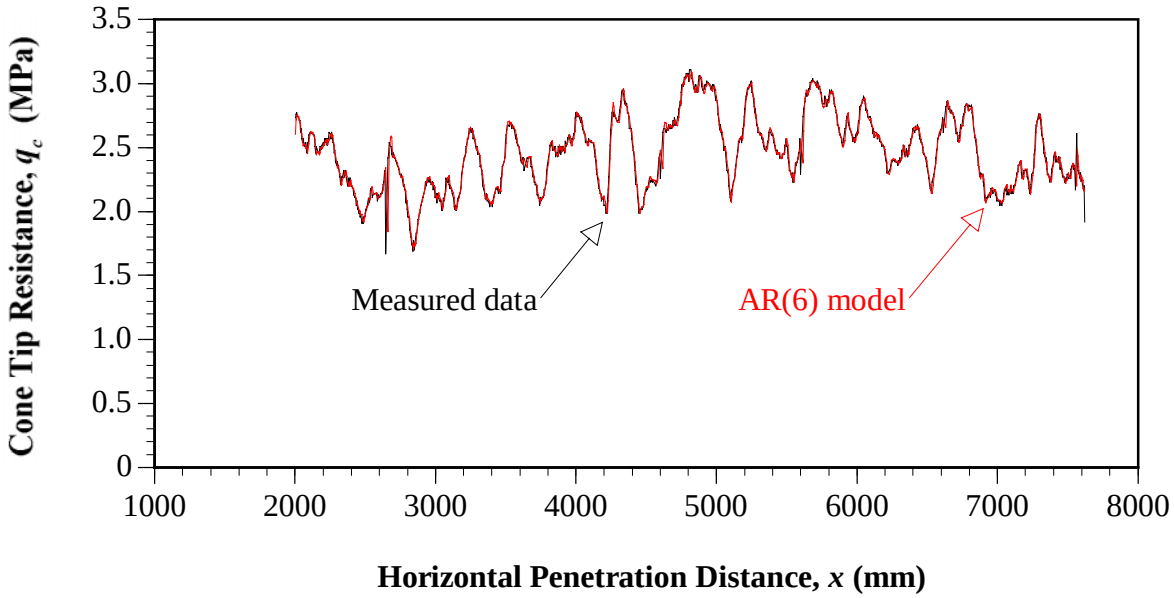

Figure 5.69 Measured q_c data from horizontal CPT, from the Keswick site, with the AR(6) model obtained by using rescaled residuals.

figure, as well as the relatively low value of *SSD* (3.12 MPa^2), the AR(6) model is an excellent representation of the spatial variability of the q_c measurements, obtained from the horizontal CPT within the Keswick Clay.

The sample ACF and PACF, of the first-differenced data, indicated that both cut-off at a lag of 3. As a consequence, an ARIMA(3,1,3) model was investigated. Again, preliminary estimates of the parameters were obtained by the program, *PEST*, and these parameters were subsequently optimised using the maximum likelihood method. The ARIMA model obtained is given in the following equation:

$$Z_t = -0.287Z_{t-1} - 0.171Z_{t-2} + 0.102Z_{t-3} + a_t + 0.058a_{t-1} + 0.401a_{t-2} + 0.122a_{t-3} \quad (5.39)$$

where: a_t has a mean of zero and a variance of 0.0288.

Again, diagnostic tests were performed on the rescaled residuals, which suggested that the ARIMA(3,1,3) model is a valid representation of the data. Figure 5.70 shows this model superimposed on the original q_c measurements. This figure clearly demonstrates that the ARIMA(3,1,3) model is an excellent representation of the spatial variability of the q_c measurements, obtained from the horizontal CPT within the Keswick Clay. This conclusion is again supported by the low value of *SSD*, which was found to equal 0.44 MPa^2.

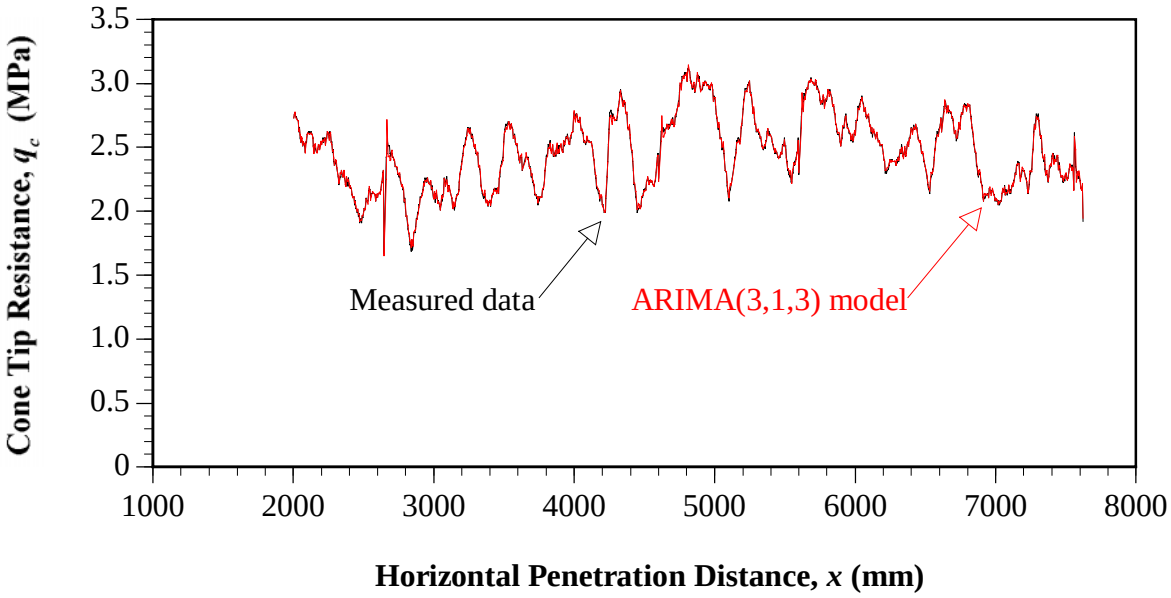

Figure 5.70 Measured q_c data from horizontal CPT, from the Keswick site, with the ARIMA(3,1,3) model obtained by using rescaled residuals.

It has been demonstrated in the foregoing discussion, and the results presented, that random field theory provides a useful framework for modelling the spatial variability of geotechnical properties. The following section extends these models, so that forecasts may be obtained at locations yet to be tested.

5.4.2.2 Forecasting

As detailed in §2.5.1.2(v), the field of time series analysis and, in particular, the Box-Jenkins methodology, provides a framework whereby forecasts, or predictions, may be generated at unsampled locations. Again, the vertical CPT sounding, C8, and the horizontal CPT performed at the Keswick site, will be examined in some detail. The program, *PEST*, allows forecasts to be made up to 52 lags into the future, or up to a distance of 52 times the sample spacing. In order to assess the success, or otherwise, of the application of random field theory to forecasting measurements of q_c at untested locations, the lower 30 values were removed from the C8 data set, and then input into *PEST*. The data were transformed either by: (i) removing the OLS quadratic trend; or (ii) first-differencing. Then, for each of these data sets, the appropriate ARIMA model, as given previously in Tables 5.13 and 5.14, was entered into *PEST* and forecasts were then obtained for the lower 30 depths, that is, from 4,905 mm to 5,050 mm. The results of these analyses are summarised in Figure 5.71, where the AR(3) model refers to the classically transformed data set, and the IMA(1,1) model refers to the first-differenced data. The sum

of the squared differences for the AR(3) and IMA(1,1) models, over the forecast depth range 4,905 mm to 5,050 mm, are 2.03 and 1.10 MPa^2, respectively. Table 5.15 summarises the first 10 forecasts for both the AR(3) and IMA(1,1) models. It is relatively obvious from Figure 5.71, Table 5.15 and the values of *SSD*, that neither the AR(3) nor the IMA(1,1) model provide satisfactory forecasts of q_c. Furthermore, both of the models failed to predict the direction of the q_c measurements.

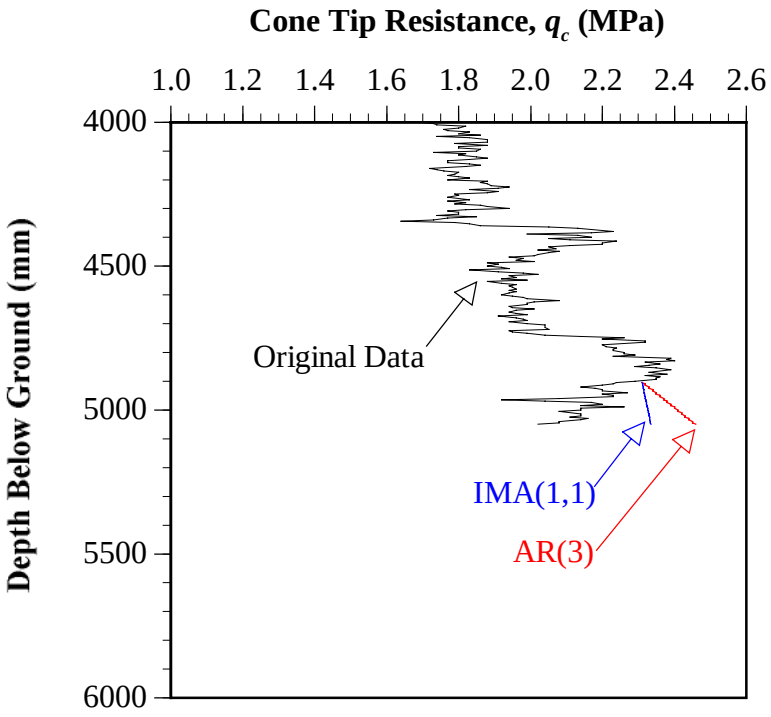

Figure 5.71 Forecasts of q_c measurements obtained from classically transformed data, AR(3), and first-differenced data, IMA(1,1), for C8.

Table 5.15 First 10 forecasts of q_c (MPa) for CPT C8.

Depth (mm)	Measured Data	AR(3)	IMA(1,1)
4,905	2.24	2.31	2.31
4,910	2.23	2.32	2.31
4,915	2.20	2.32	2.31
4,920	2.14	2.33	2.31
4,925	2.18	2.33	2.31
4,930	2.20	2.34	2.31
4,935	2.2	2.34	2.32
4,940	2.27	2.35	2.32
4,945	2.20	2.35	2.32
4,950	2.23	2.36	2.32

The same procedure was adopted for the measurements of q_c obtained from the horizontal CPT, performed at the Keswick site. In this case, the last 44 values of q_c were removed and, again, the classically transformed data set (the AR(6) model) and the first-differenced data set (the ARIMA(3,1,3) model) were used by *PEST* to generate forecasts. The 44 forecasts for each of the models, as well as the original measurements, are shown in Figure 5.72. The *SSD* for the AR(6) model, and the ARIMA(3,1,3) model, was calculated to be 1.01 and 1.03 MPa^2, respectively. Figure 5.72 and the calculated values of the *SSD*, again, suggest that the random field models fail to accurately predict the spatial variability of the q_c measurements. Table 5.16 presents the first 10 of the 44 forecasts generated for the horizontal CPT. It is evident, from this table, that these first 10 forecasts are reasonable estimates of q_c. On the whole, however, it can be concluded that the random field models, examined here, fail to satisfactorily forecast measurements of q_c at unsampled locations.

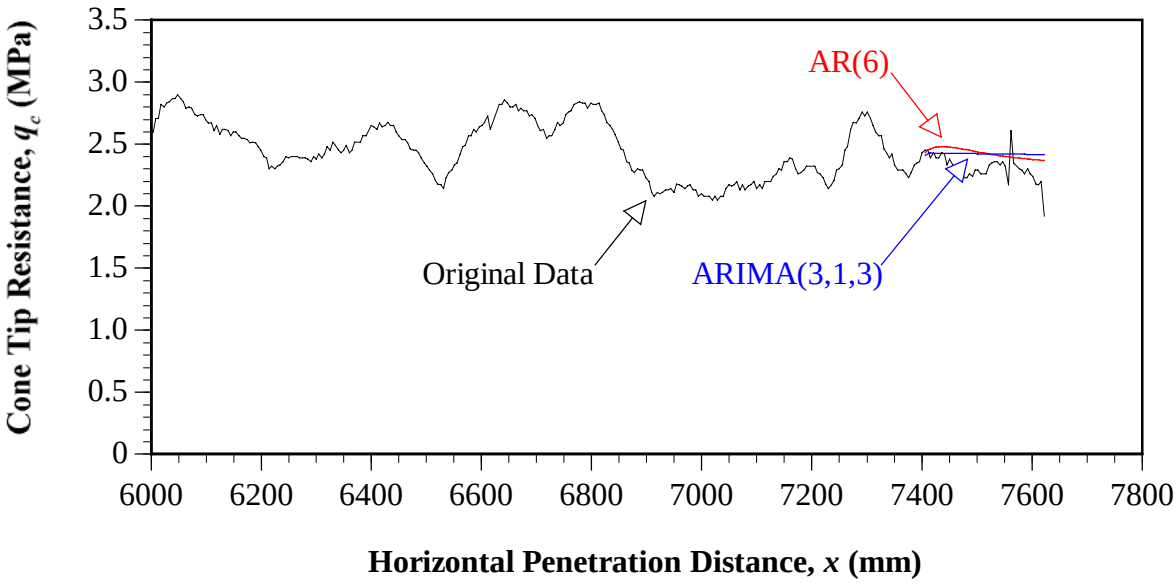

Figure 5.72 Forecasts of q_c measurements obtained from classically transformed data, AR(6), and first-differenced data, ARIMA(3,1,3), for the horizontal CPT.

Another aspect associated with models which characterise the spatial variability of geotechnical properties, is that of data simulation. This aspect is treated in the next section.

5.4.2.3 Data Simulation

Once a random field model has been formulated, which characterises the spatial variability of some geotechnical property in question, it is possible to generate an infinite number of

Table 5.16 First 10 forecasts of q_c (MPa) for the horizontal CPT from the Keswick site.

Depth (mm)	Measured Data	AR(6)	ARIMA(3,1,3)
7,405	2.45	2.43	2.41
7,410	2.45	2.45	2.42
7,415	2.39	2.46	2.43
7,420	2.43	2.47	2.42
7,425	2.39	2.48	2.43
7,430	2.39	2.48	2.43
7,435	2.43	2.48	2.43
7,440	2.42	2.48	2.43
7,445	2.33	2.48	2.43
7,450	2.38	2.48	2.42

random realisations of measurements of this property. For example, consider again the AR(3) model generated for the classically transformed data of CPT C8:

$$Z_t = 0.672Z_{t-1} + 0.154Z_{t-2} + 0.114Z_{t-3} + a_t \tag{5.40}$$

where: a_t has a mean of zero and a variance, σ_a^2, of 0.0372.

Recall that, by definition, a_t is a purely random process, also known as a white noise process, for which each member of the population is independently and normally distributed, and has a mean of zero and a constant variance, σ_a^2. By randomly generating a series of values for a_t and substituting these into Equation (5.40), it is possible to generate a realisation of q_c measurements which will have the properties of the AR(3) model, given in Equation (5.40). While it is extremely unlikely that any given realisation will be identical to that measured at the location C8, it is, nevertheless, a valid representation of the process generating that CPT, which, it can be argued, *may* have been measured under slightly different site conditions. For example, such a realisation may have been measured at a location very near to C8, or may have been obtained had the test been performed on a different day, or had the subsurface moisture regime been slightly different, and so on. By generating a sufficiently large number of such realisations, it is possible to examine the reliability of some geotechnical system in question. For example, the probability of failure of an embankment with some particular geometry, and under some particular loading configuration, can be examined by evaluating the stability of the embankment for a large number of possible ground situations. Once this has been achieved, it is then possible to

calculate the likelihood, or probability, of embankment failure. Such a case study will be examined in Chapter 8.

The Monte Carlo Method enables such realisations of data to be performed, essentially following the procedure given above. The program *Monte*, discussed previously in §5.2.2, was used to generate five random realisations of the AR(3) process, given in Equation (5.40), for CPT C8, and these are shown in Figure 5.73. As can be seen from this figure, while none of the 5 realisations are identical to the values of q_c measured at location C8, they appear to be valid representations of the underlying process. *Monte* was subsequently used to generate 1,000 such realisations, the envelope of which is given in Figure 5.74. It is evident from this envelope that the AR(3) process seems to satisfactorily model the spatial variability of q_c at location C8.

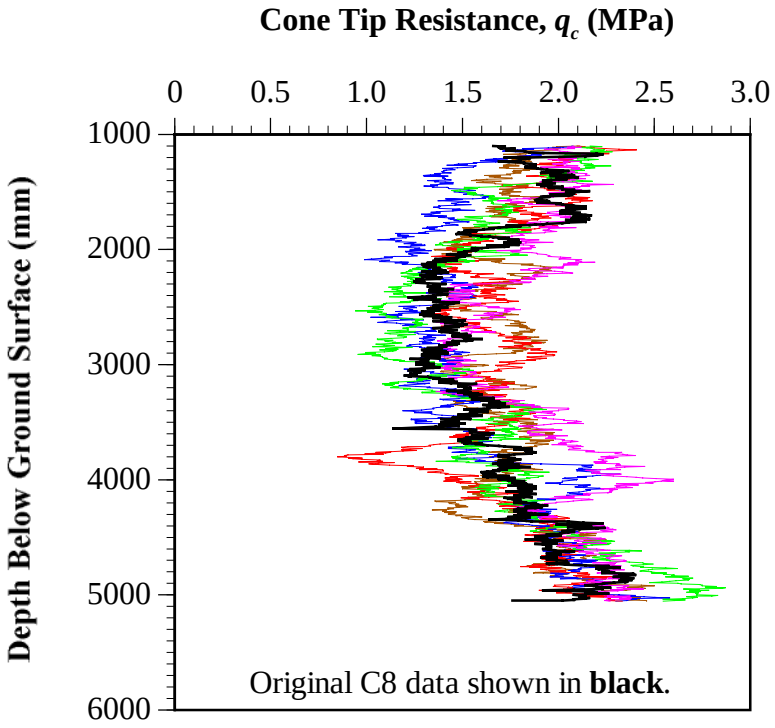

Figure 5.73 Five random realisations of the AR(3) process for CPT C8 obtained from *Monte*.

The program, *Monte*, was also used to obtain an envelope of 1,000 realisations of the IMA(1,1) model, which represents the first-differenced C8 data. This envelope is given in Figure 5.75. As can be seen clearly from this figure, the envelope is extremely large, the minimum locus of which even extends well into the negative region, which is unrealistic for the CPT. As a consequence of the large extent of the IMA(1,1) envelope, as well as the fact that a number of the realisations extend into the negative q_c region, it is concluded that

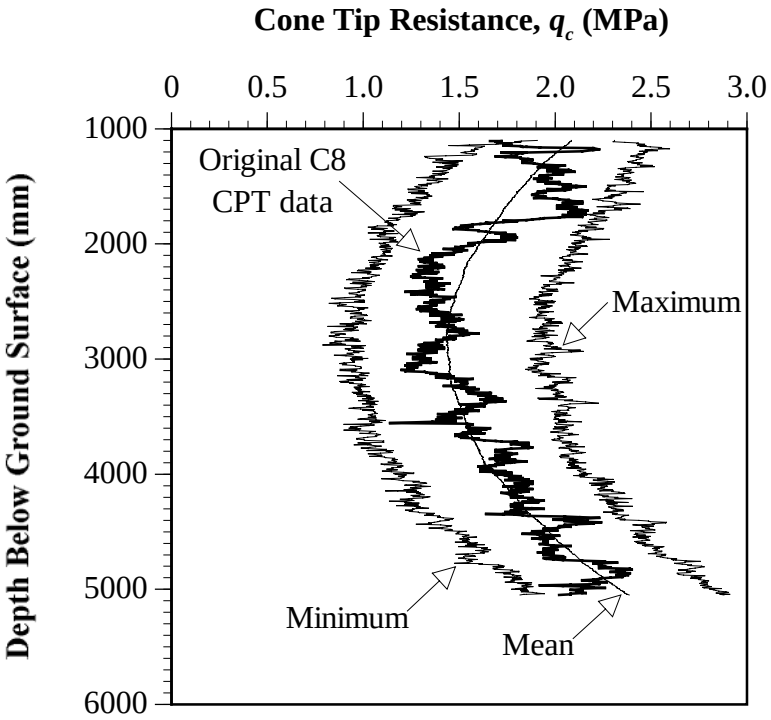

Figure 5.74 Envelope of 1,000 realisations of the AR(3) process, for CPT C8, obtained from *Monte*.

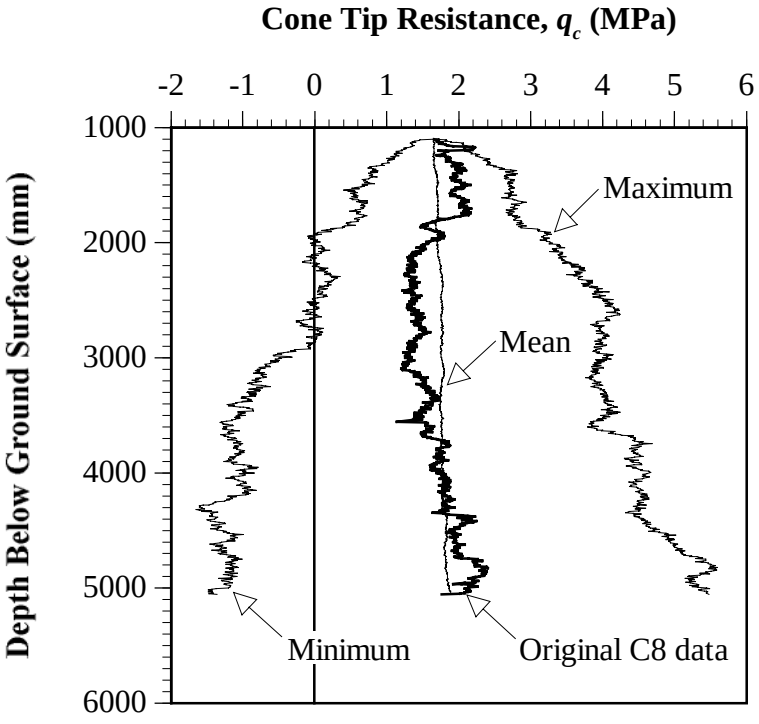

Figure 5.75 Envelope of 1,000 realisations of the IMA(1,1) process, for CPT C8, obtained from *Monte*.

the IMA(1,1) model is an inappropriate representation of the spatial variability of q_c for CPT C8, with respect to data simulation.

Figures 5.76 and 5.77 present the minimum and maximum envelopes of the AR(6) and the ARIMA(3,1,3) models, respectively, for the horizontal CPT performed at the Keswick site. The envelopes were again obtained by entering the respective models into the program, *Monte*, and subsequently performing 1,000 realisations. As was observed with the C8 data, the classically decomposed model (the AR(6) process) provides a valid representation for the spatial variability of the CPT data. On the other hand, the first-differenced model (the ARIMA(3,1,3) process), again, fails to adequately represent the data, since many of the realisations yielded negative values of q_c.

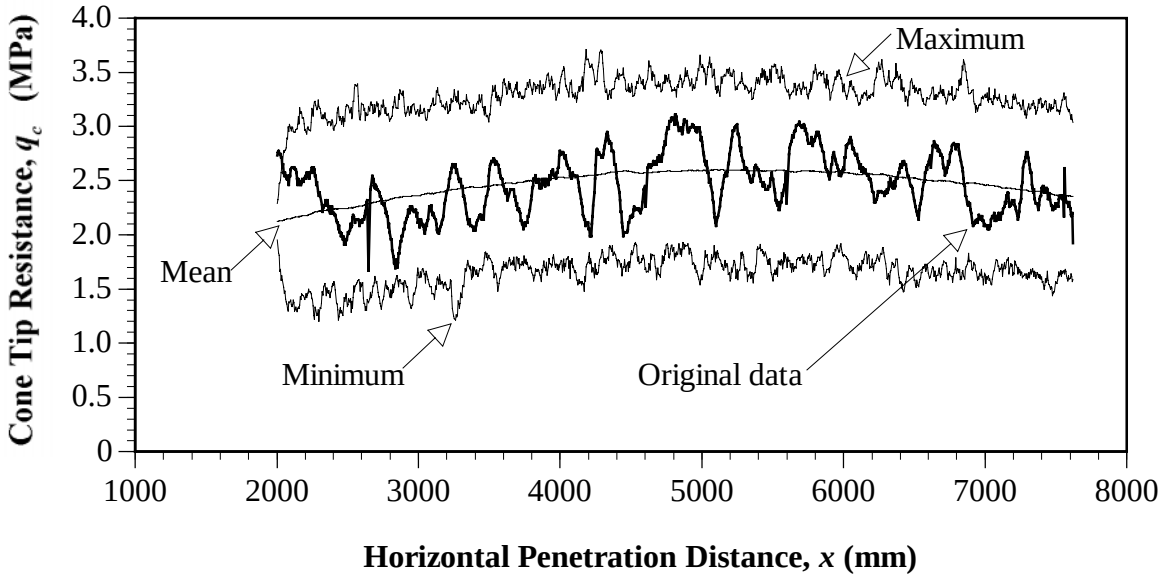

Figure 5.76 Envelope of 1,000 realisations of the AR(6) process, for the horizontal CPT, obtained from *Monte*.

In summary, while the models which were derived using the Box-Jenkins method of differencing, that is the ARIMA processes, yielded somewhat better representations of the measured data, as was shown in §5.4.2.1, these models failed to provide robust estimates when derived from simulation. In contrast, the models obtained from classical decomposition provided better estimates than the ARIMA models, when used in data simulation. However, neither the ARIMA models, nor the ARMA models, provided reasonable forecasts of measurements at untested locations. In conclusion, therefore, the AR models obtained from classical decomposition yielded, overall, far more robust estimates than those obtained from the Box-Jenkins method of differencing.

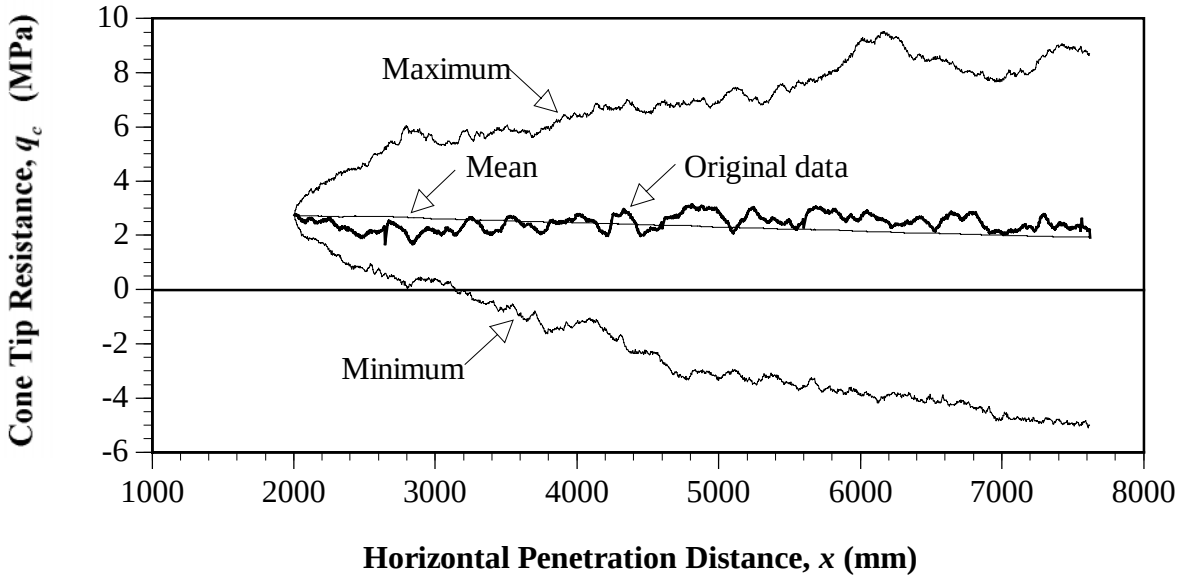

Figure 5.77 Envelope of 1,000 realisations of the ARIMA(3,1,3) process, for the horizontal CPT, obtained from *Monte*.

The following section deals with the same aspects of data estimation, although, in this case, based on the framework of geostatistics.

5.4.3 Geostatistical Analyses

In geostatistics, forecasts are obtained by, firstly calculating the experimental semivariogram, fitting a model semivariogram to it and, lastly, by using the process of kriging to obtain the forecasts. As a consequence, the model formulation stage, with respect to geostatistics, consists essentially of fitting a model semivariogram to the experimental semivariogram, as was undertaken previously in §5.3.1.2 and §5.3.2. The following section uses these geostatistical models to obtain forecasts at unsampled locations and compares these results with those obtained from random field analyses, given in the previous sections.

5.4.3.1 Forecasting

In §5.4.2.1, random field analyses were used to generate estimates of the measured quantity using the proposed ARIMA model. The validity of the model was assessed by comparing these estimates with the actual measured values, an example of which was given previously in Figure 5.61. Geostatistics, on the other hand, provides no direct means whereby such estimates of the measured quantity can be generated from the model. However, it is

possible to compare the geostatistical model with its random field counterpart, by using kriging. The estimated quantities, given previously in §5.4.2.1, were essentially *one-step ahead forecasts*; that is, at the following 5 mm depth interval. In geostatistics, by using kriging, it is also possible to generate similar one-step ahead forecasts. For example, if every second measurement is removed from the data set, it is possible to use kriging to estimate these 'deleted' measurements. While these values are 'estimates' of the measured data, they are in fact forecasts and, hence, are not the same as the estimates derived from random field analyses. They will, nevertheless, suffice for comparison purposes.

Again, the vertical CPT sounding C8, and the horizontal CPT from the Keswick site, will be examined so that the results can be compared with those given in §5.4.2.1 and §5.4.2.2. In order to allow one-step ahead forecasts to be generated, each of the data sets were first detrended by removing the OLS quadratic trend, using *SemiAuto*, and the residuals were then manipulated using the program, *CPTSpace*, detailed previously in §5.2.3. Kriging was then carried out using the computer program, *OKB2D*, which is part of the *GSLIB* package (Deutsch and Journel, 1991) and which performs two-dimensional ordinary, block or point kriging of user specified data. The program, *OKB2D*, was written in standard Fortran 77 and was used on an IBM-PC platform. Lastly, the kriged estimates were recombined with the OLS quadratic trend to produce final estimates of q_c.

While *OKB2D* enables two-dimensional block kriging to be performed, the program was used to carry out one-dimensional *point* kriging. This was achieved by entering a dummy y variable, so that each measurement of q_c had an associated depth in millimetres and a y value of unity, and by specifying values of 1 for both the x and y block discretisation parameters. The results of the one-step ahead forecasts for C8 and the horizontal CPT, obtained by ordinary kriging from *OKB2D*, are shown in Table 5.17, and Figures 5.78 and 5.79, respectively.

Table 5.17 Results of one-step ahead ordinary kriging from *OKB2D*.

CPT No.	No. of Data	Spacing of Data (mm)	*SSD* (MPa^2)	Range of kriging variance, σ_k^2, (MPa^2)
C8	389	10	1.18	0.003 - 0.004
Horizontal	553	10	1.03	0.003 - 0.010

The ordinary kriged point estimates, shown in Figures 5.78 and 5.79, were obtained by setting: the grid spacing to 5 mm in the depth direction; the maximum number of points used in the kriging process to 20; the *search radius* to 2,000 mm, that is, the maximum

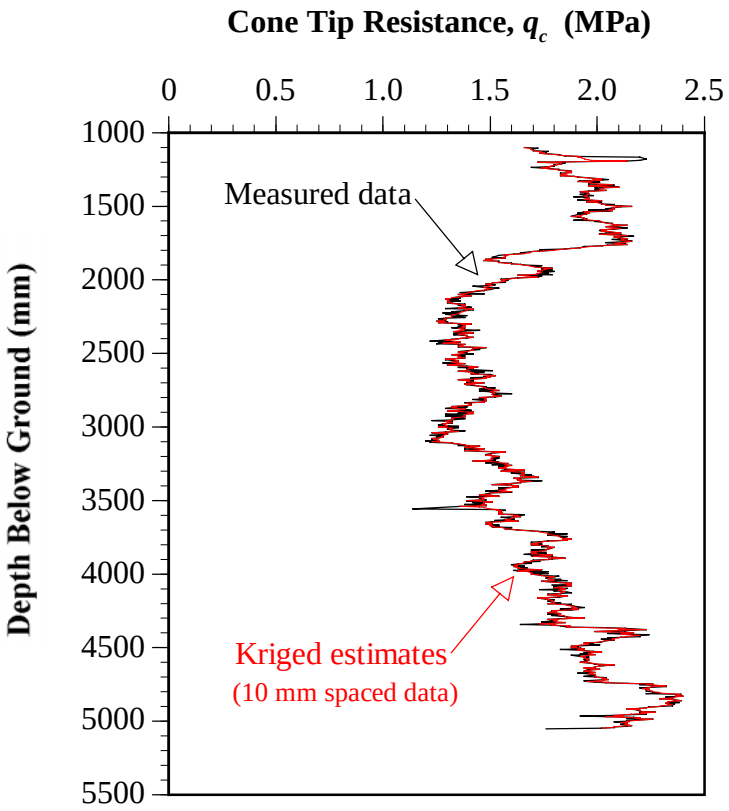

Figure 5.78 Results of one-step ahead ordinary kriging of C8 from *OKB2D*.

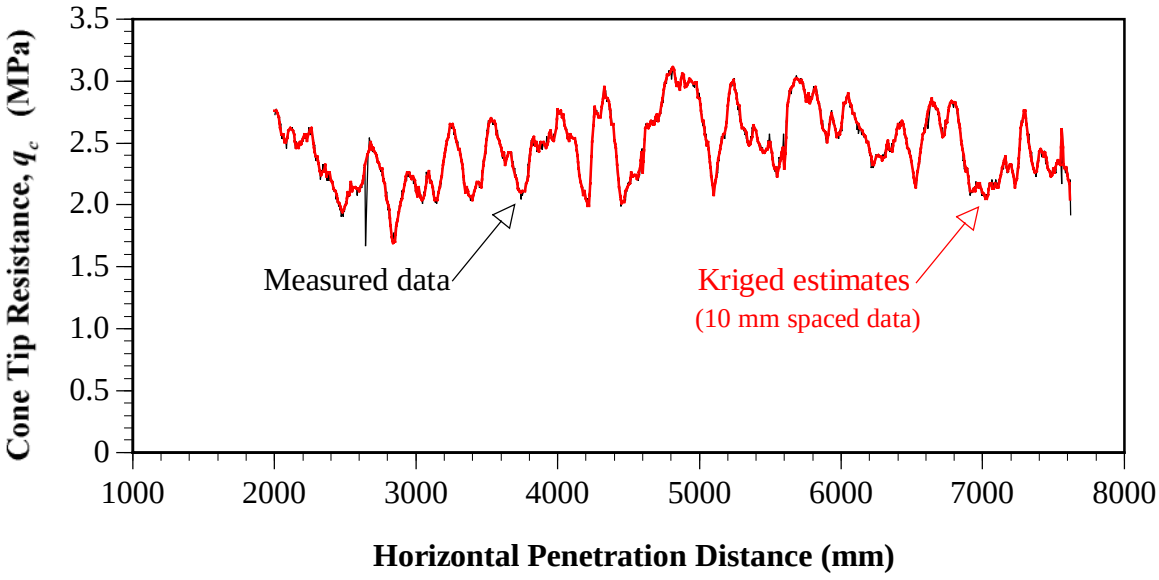

Figure 5.79 Results of one-step ahead ordinary kriging of the horizontal CPT using *OKB2D*.

isotropic distance over which *OKB2D* searches for points; the model semivariogram to a spherical model (*it* = 1), with parameters a = 330 mm, C_0 = 0.0018, C = 0.0231 (*cc*), for C8, and a = 270 mm, C_0 = 0, C = 0.0901, for the horizontal CPT, which are consistent with the models derived previously.

As is evident from Figures 5.78 and 5.79, and the sum of the squared differences, *SSD*, given in Table 5.17, the one-step ahead forecasts provide very good predictions of the 'deleted' data. This is justified by comparing the values of *SSD*, for each of the random field models, with the values obtained from kriging, as shown in Table 5.18. While the first-differenced models (the ARIMA processes) yield the lowest *SSD*s, it has been shown in §5.4.2.3 that these models are not robust, since they fail to provide adequate descriptions of the spatial variability of the q_c measurements. The kriged one-step forecasts, on the other hand, yield lower *SSD*s than the classically transformed autoregressive processes.

Table 5.18 Results of one-step ahead ordinary kriging from *OKB2D*, compared with those obtained from random field analyses.

	Random Field Analysis				**Geostatistics**
CPT	**Classically Transformed**		**First-Differenced**		**Kriged**
No.	**Model**	***SSD***	**Model**	***SSD***	***SSD***
C8	AR(3)	2.82	IMA(1,1)	0.29	1.18
Horizontal	AR(6)	3.12	ARIMA(3,1,3)	0.44	1.03

By examining the output file given by *OKB2D*, it is possible to inspect the kriging weights obtained by the ordinary point kriging process. For C8, the estimates were obtained by using 6 points. For example, data point 722, that is, at a depth of 4,705 mm, the ordinary kriged point estimate was obtained by the following equation:

$$\begin{aligned} q_c(4705) &= q_c(4680)\times 0.055 + q_c(4690)\times 0.120 + q_c(4700)\times 0.325 \\ &\quad + q_c(4710)\times 0.325 + q_c(4720)\times 0.120 + q_c(4730)\times 0.055 + \text{OLS trend} \\ &= (-0.120)\times 0.055 + (-0.100)\times 0.120 + (-0.110)\times 0.325 \\ &\quad + (-0.070)\times 0.325 + (-0.060)\times 0.120 + (-0.170)\times 0.055 + \text{OLS trend} \\ &= -0.0937 + \text{OLS trend} = \mathbf{2.008\ MPa} \end{aligned} \tag{5.41}$$

where: $q_c(4705)$ is the value of q_c at a depth of 4705 mm.

The values of 0.055, 0.120 and 0.325, are the kriging weights, w_i, discussed previously in §2.5.1.3(ii). Notice that the 6 weights sum to unity, a requirement of the kriging process; the weights are symmetrical about the estimate, since the spacing of the 6 points is constant; and the weights decrease away from the location of the estimate, as one would expect. The kriged estimate of –0.0937, when recombined with the OLS quadratic trend, yields an estimate of q_c of 2.008 MPa, which compares well with the measured value of 2.04 MPa. This represents an estimation error of 1.6%, which lies within the 5.4% kriging error limits given by *OKB2D*. The vast majority of the kriged estimates consisted of these 6 kriging weights of 0.055, 0.120, 0.325, 0.325, 0.120 and 0.055. However, while this example demonstrated symmetrical kriging weights, this was not always the case. Unsymmetrical weights are obtained when missing data are encountered, or when extrapolation is performed. Data number 736, that is, at a depth of 4,775 mm, is an example of a situation where unsymmetrical weights were obtained, as shown below.

$$\begin{aligned} q_c(4775) &= q_c(4740)\times 0.037 + q_c(4750)\times 0.081 + q_c(4760)\times 0.221 \\ &\quad + q_c(4780)\times 0.429 + q_c(4790)\times 0.159 + q_c(4800)\times 0.073 + \text{OLS trend} \\ &= (-0.090)\times 0.037 + (0.130)\times 0.081 + (0.180)\times 0.221 \\ &\quad + (0.050)\times 0.429 + (0.070)\times 0.159 + (0.090)\times 0.073 + \text{OLS trend} \\ &= 0.0861 + \text{OLS trend} = \mathbf{2.239\ MPa} \end{aligned} \tag{5.42}$$

Notice that $q_c(4770)$ is a missing depth and, hence, the data values are not symmetrical about the depth 4,775 mm and, as a result, neither are the kriging weights. The kriged estimate of 0.0861 MPa, when recombined with the OLS quadratic trend, yields an estimate of q_c of 2.239 MPa. This compares well with the measured value of 2.20 MPa and represents an estimation error of 1.8%, which lies within the 5.0% kriging error limits given by *OKB2D*.

For the horizontal CPT performed at the Keswick site, similar estimates were obtained. While in many cases the kriged estimates consisted of 6 points, the vast majority of estimates used only 2 points. Examples of each are given below.

$$\begin{aligned} q_c(6715) &= q_c(6680)\times -0.001 + q_c(6690)\times 0.000 + q_c(6700)\times 0.250 \\ &\quad + q_c(6720)\times 0.751 + q_c(6730)\times 0.000 + q_c(6740)\times -0.001 + \text{OLS trend} \\ &= (0.268)\times -0.001 + (0.240)\times 0.000 + (0.151)\times 0.250 \\ &\quad + (0.054)\times 0.751 + (0.075)\times 0.000 + (0.186)\times -0.001 + \text{OLS trend} \\ &= 0.0777 + \text{OLS trend} = \mathbf{2.575\ MPa} \end{aligned} \tag{5.43}$$

$$q_c(7175) = q_c(7170) \times 0.500 + q_c(7180) \times 0.500$$

$$= (-0.129) \times 0.500 + (-0.157) \times 0.500 + \text{OLS trend} \qquad (5.44)$$

$$= -0.1430 + \text{OLS trend} = \mathbf{2.285\ MPa}$$

It was observed from the *OKB2D* output file that 6 points were used in the kriged estimate only when a missing depth was encountered. This is the case in Equation (5.43) where 6710 is a missing depth and, consequently, has no associated measurement of q_c. The kriged estimate of 0.0777, when recombined with the OLS quadratic trend, yielded an estimate for q_c at a depth of 6,715 mm, of 2.575 MPa, which compares reasonably well with the measured value of 2.62 MPa. This value represents an estimation error of 1.7%, which lies within the 4.3% kriging error limits suggested by *OKB2D*. Equation (5.44), on the other hand, contains no missing depths and, consequently, as can be seen, only 2 points were used. Since the kriging weights are equal to 0.5 and only two points were used, this estimate represents a linear prediction; that is, the interpolated estimate is a simple average of the two end points. In this way, the kriged estimate was found to be equal to –0.1430 and, when recombined with the trend, yielded an estimate of q_c of 2.285 MPa. This compares favourably with the measured value of 2.26 MPa and represents an estimation error of 1.1%, which lies within the 4.6% kriging error limits given by *OKB2D*.

A sensitivity study was undertaken to examine the influence of using a greater number of data points in the kriging process. Up to 20 points were used in both the C8 and horizontal CPT data sets and it was found, by examining the *SSD*s, that no better estimates were obtained than by using the 6 data points, as detailed above. In fact, in some instances, the estimates produced by using a greater number of data points yielded slightly poorer results.

The examples given above, referred to one-step ahead forecasts, so that the results of random field analyses could be compared with those obtained from geostatistics. However, kriging allows far greater flexibility, with respect to estimation, than does random field theory. The program, *OKB2D*, was used to generate estimates at 5 mm intervals based on: input data at 20, 50, 100, 200 and 300 mm spacings; and the spherical semivariogram model originally derived from the 5 mm spaced data. These analyses are similar to those performed by Brooker (1977) and the results are summarised in Table 5.19.

Figures 5.80 and 5.81 show examples of the kriged estimates for C8 and the horizontal CPT, respectively, using input data at 200 mm spacings. In other words, the program, *OKB2D*, generated estimates of q_c at 5 mm spacings based on measured data spaced at 200 mm, as shown in Figures 5.80 and 5.81. It is evident from these figures that the kriged estimates are ‘smoothed’ approximations of the measured data. In fact, the process of

Table 5.19 Results of forecasts at 5 mm spacings obtained by ordinary kriging using *OKB2D*.

CPT No.	No. of Data	Spacing of Data (mm)	*SSD* (MPa^2)	Range of kriging variance, σ_k^2, (MPa^2)
C8	194	20	2.27	0.003 - 0.005
	79	50	3.77	0.004 - 0.005
	40	100	6.34	0.004 - 0.014
	20	200	8.31	0.004 - 0.027
	14	300	13.30	0.005 - 0.020
Horizontal	277	20	1.55	0.004 - 0.020
	110	50	4.39	0.005 - 0.049
	55	100	15.50	0.005 - 0.085
	28	200	41.82	0.005 - 0.118
	17	300	63.02	0.005 - 0.120

kriging is equivalent to fitting spline functions to the measured data using a specific model for the covariance (Olea, 1991) and, as a result, are, by their very nature, smoothed representations of the data. It is appears from Figures 5.80 and 5.81, that the kriged estimates are simply linear interpolations of the input data. However, closer examination of the estimates, reveal that they are, in fact, curvilinear approximations, which yield somewhat better estimates than those given by linear interpolation, as shown in Table 5.20.

Table 5.20 Comparison of the sum of the squared differences, *SSD*, (MPa^2) between linear interpolation and ordinary kriging of C8 and the horizontal CPT.

CPT No.	*All Estimates (inc. extrapolated)*		*Interpolated Values Only*	
	Linear Interpolation	Kriging	Linear Interpolation	Kriging
C8	11.21	8.31	8.77	8.09
Horizontal	42.37	41.82	41.52	39.91

A significant feature of geostatistics is that the error associated with the kriged estimate, that is, the kriging variance, σ_k^2, is readily available, as mentioned previously. By superimposing the 95% confidence limits ($\pm 2\sigma$) of the kriged estimates onto the original measured data, it is possible to assess the validity of the kriging process. Figures 5.82 and 5.83 show the ordinary kriged estimates obtained from *OKB2D*, using 200 mm spaced input data, shown previously in Figures 5.80 and 5.81, as well as the 95% confidence limits

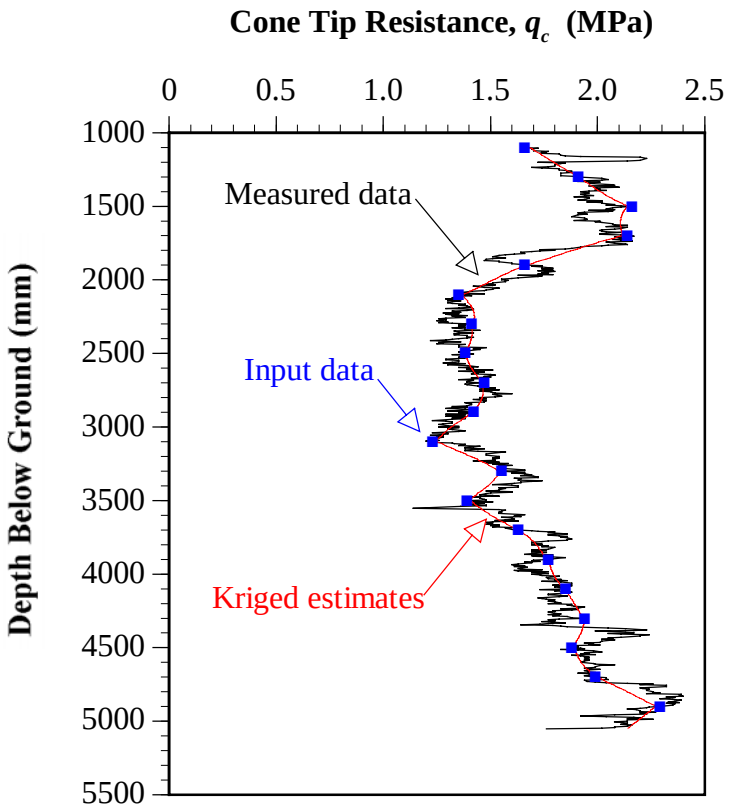

Figure 5.80 Results of ordinary kriging using 200 mm spaced input data from C8.

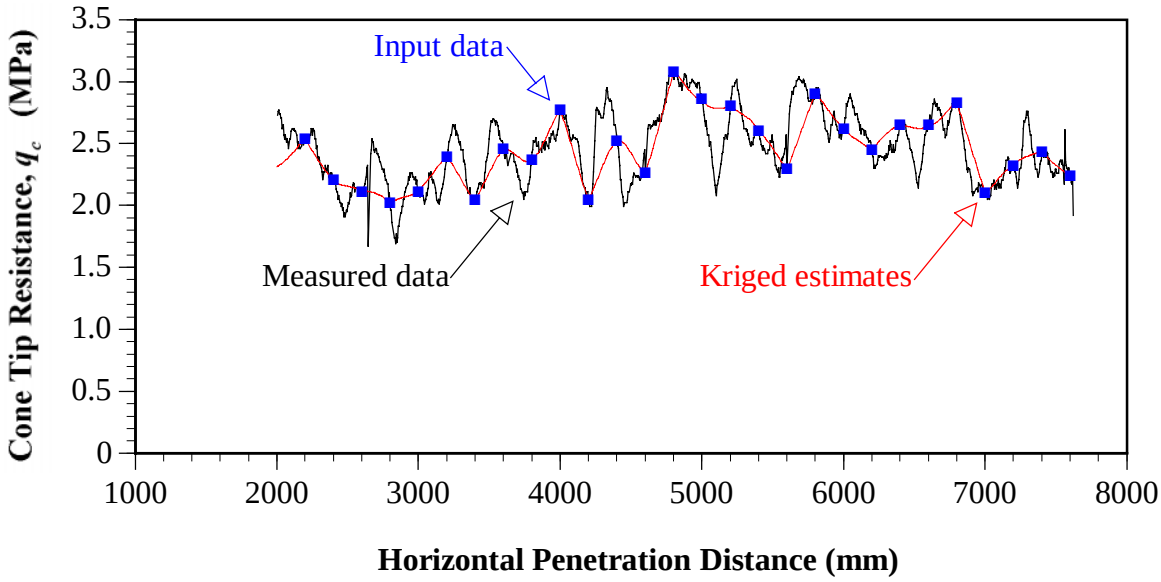

Figure 5.81 Results of ordinary kriging using 200 mm spaced input data from the horizontal CPT.

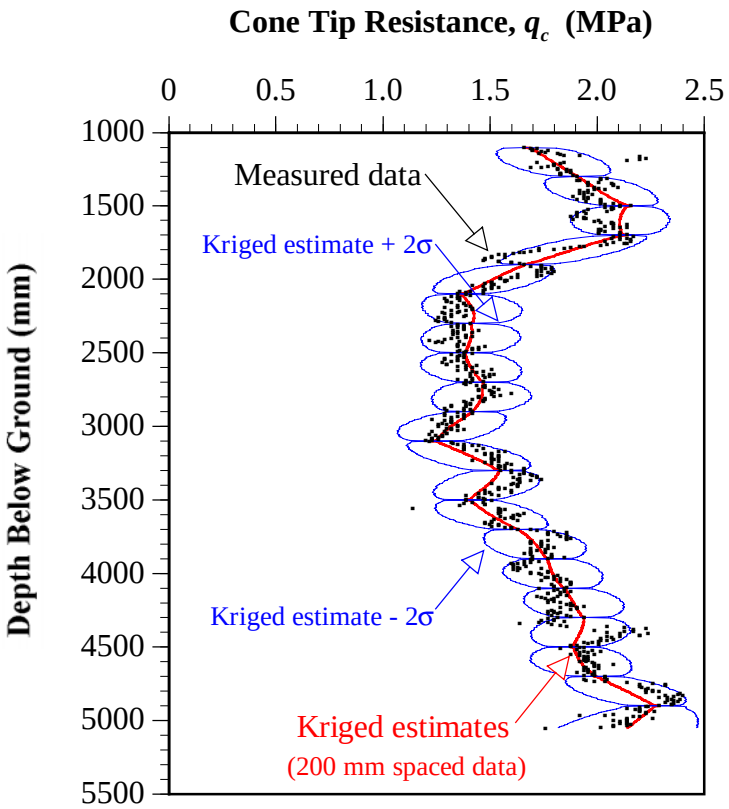

Figure 5.82 Ordinary kriged estimates and the 95% confidence limits (±2σ) using 200 mm spaced input data from C8.

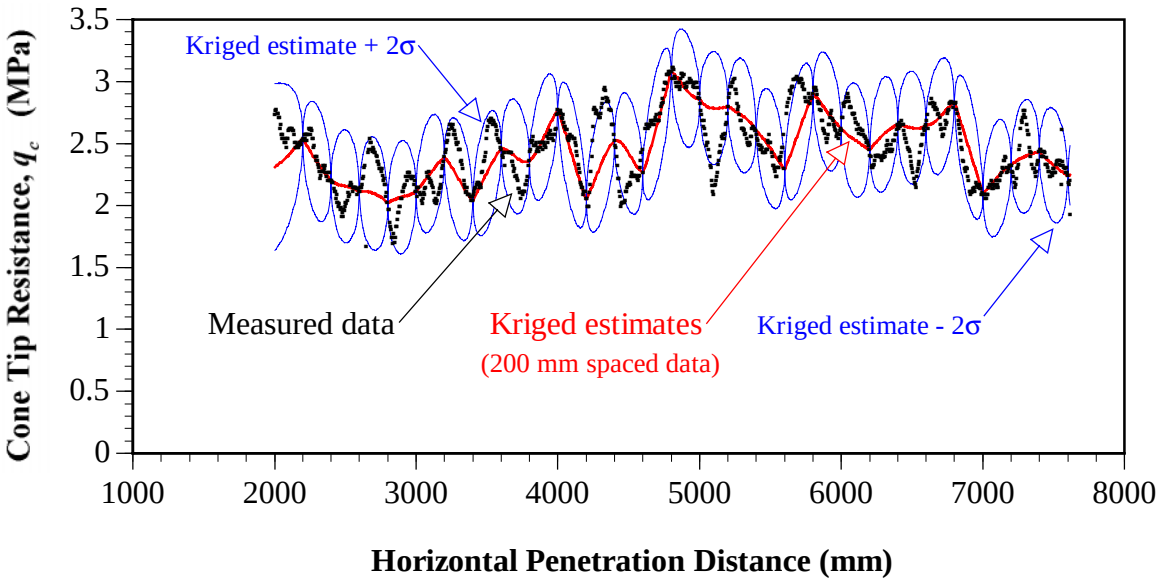

Figure 5.83 Ordinary kriged estimates and the 95% confidence limits (±2σ) using 200 mm spaced input data from the horizontal CPT.

and the original measured data for C8 and the horizontal CPT, respectively. As can be seen clearly from these figures, the 2σ envelope encloses the majority of the measured data. In fact, for C8, 39 out of the 791 values, or 4.9%, lie outside this envelope and, for the horizontal CPT, 62 out of the 1124 values, or 5.5%, lie outside. These results support the fact that these bounds are actually 95% confidence limits, since 95% of the data are included within its envelope. As a consequence, the geostatistical models adequately define the spatial variability of the q_c measurements of the Keswick Clay.

Interestingly, if the original q_c data are kriged without detrending, practically identical forecasts are obtained. This holds true for interpolation situations, but not for extrapolation. Journel and Rossi (1989) also reported similar findings when they compared the results of ordinary kriging, with those of universal kriging. The observation that almost identical forecasts are obtained whether the trend is removed or not, implies that a sizeable amount of computational effort may be saved by not first detrending the data and, subsequently recombining the trend with the kriged estimates.

To this point, kriging has been used primarily to provide forecasts at untested locations, essentially in an interpolation setting. Just as the random field ARIMA models were used to provide forecasts beyond the measured data, as in §5.4.2.2, kriging may also be used to generate such extrapolated forecasts. By inputting the same data as in §5.4.2.2 (that is, measurements of q_c at 5 mm spacings, between 1,100 and 4,900 mm for C8, and between 2,000 and 7,400 mm for the horizontal CPT), *OKB2D* was used to krige extrapolated forecasts at 5 mm intervals (between 4,905 and 5,050 mm for C8, and between 7,405 and 7,620 mm for the horizontal CPT). The ordinary kriged forecasts for C8 and the horizontal CPT are shown in Figures 5.84 and 5.85. The *SSD*s for each of the kriged forecasts are given in Table 5.21, as well as those evaluated for the ARIMA models, given previously in §5.4.2.2.

Table 5.21 Results of forecasts obtained by ordinary kriging, using *OKB2D*, compared with those obtained from random field theory.

	Random Field Theory				**Geostatistics**
CPT	**Classically Transformed**		**First-Differenced**		**Kriged**
No.	**Model**	***SSD***	**Model**	***SSD***	***SSD***
C8	AR(3)	2.03	IMA(1,1)	1.10	1.96
Horizontal	AR(6)	1.01	ARIMA(3,1,3)	1.03	0.56

It is evident from Table 5.21 that the process of kriging produces forecasts as good, or better than, those given by random field theory. However, examination of Figures 5.84 and

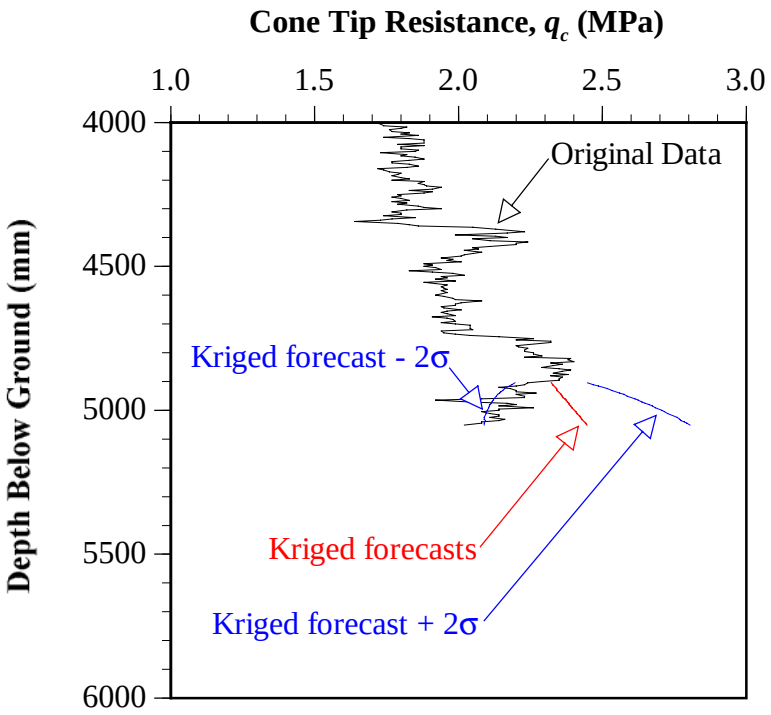

Figure 5.84 Ordinary kriged forecasts at 5 mm intervals for C8.

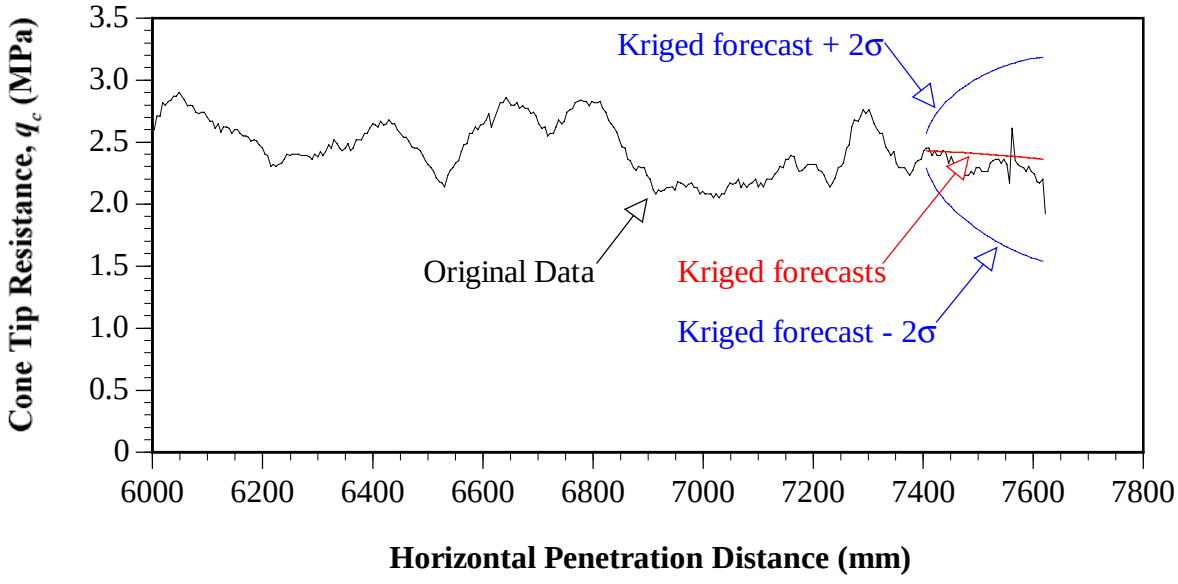

Figure 5.85 Ordinary kriged forecasts at 5 mm intervals for the horizontal CPT.

5.85 indicates that the kriged forecasts, while being smoothed representations of the variability of q_c, lack much of its detail. As a result, it would appear that, while the forecasts produced by random field theory and geostatistics look reasonable, models more complex than simple linear estimators are necessary to generate predictions which closely match the variability indicated by measurements.

While geostatistics also provides a framework for data simulation, unlike random field theory, its implementation is far more complex. As a consequence, while geostatistical data simulation will not be addressed in this chapter, various geostatistical simulation techniques will be discussed and implemented in Chapter 8.

5.4.4 Summary of Random Field and Geostatistical Modelling of Keswick Clay

In summary:

1. For each of the data sets examined, the removal of the OLS quadratic trend was sufficient to satisfy the stationarity criterion.

2. The differencing method, while useful in the estimation and forecasting process, causes the continuity of the data to be lost. As a consequence, it is not recommended as a valid transformation procedure when the correlation distance of the geotechnical parameter is being examined.

3. By the application of random field theory, classically transformed CPT data follow an autoregressive, AR, process, with up to 8 parameters; whereas first-differenced CPT data generally follow an integrated moving average, IMA, process, with up to 5 parameters. While the IMA models tended to fit the measured data better than their *AR* counterparts, in a small number of cases, no IMA, nor ARIMA, model was found to fit the CPT data. When used in a forecasting mode, both the AR and IMA models produced overly smoothed representations of the measured data. In addition, it has been shown that, by use of the random field models, it is possible to generate any number of random realisations of the CPT data which exhibit the same statistical behaviour. It has been observed that, while the IMA models yielded valid simulated data, in many instances the measurements of q_c fell below zero, an impossible outcome in a standard CPT. The AR models, on the other hand, yielded more robust estimates, the envelope of which, tended to follow the OLS quadratic trend.

4. It has been observed that geostatistics provides a more flexible framework for the prediction, or forecasting, of values at yet-to-be tested locations, than does random field theory. It has been shown that the process of kriging provides estimates which are similar to curve fitting using spline functions and, as a result, provide smoothed representations of the actual measured data. In a one-dimensional forecasting sense, kriging has been shown to provide as good predictions as those given by random field theory and, in some cases, the forecasts were significantly better.

To this point, the CPT data used to establish models describing the spatial variability of the undrained shear strength of the Keswick and Hindmarsh Clays, have been assumed to be adequate representations of the 'true' strength of these soils. The following section examines the accuracy of these measured data and the factors which may influence results obtained from them.

5.5 ASSESSMENT OF ACCURACY OF MEASURED DATA

It was shown previously in §2.4.7 that the CPT has been reported to have the lowest total measurement error of any in situ test in current practice. The assessments of the accuracy of the CPT, reported in the literature, were based on an analysis procedure, proposed by Baecher (1982), and treated in §2.5.2.1. This procedure separates the scatter observed in geotechnical data into its two component sources: (i) the spatial variability of the material; and (ii) the random measurement error associated with the test itself. Several other authors (Tang, 1984; Filippas et al., 1988; Spry et al., 1988; Kay, 1990; Kay et al., 1991; DeGroot and Baecher, 1993; Christian et al., 1994) have used this method, or results based on it, to postulate various aspects relating to geotechnical uncertainty and reliability. However, before the accuracy of the CPT data is considered, the limitations of Baecher's technique are first examined.

5.5.1 Inadequacies of Baecher's Method

While Baecher's approach focuses on the tools associated with random field analyses, treated in §2.5.1.2, three important factors in geostatistics have highlighted inadequacies with the current method. These factors: the nugget effect; the spacing between samples; and the degree of trend removed from the data, greatly influence the random measurement error obtained by the procedure proposed by Baecher (1982), and are each discussed below.

5.5.1.1 Nugget Effect

It has long been appreciated in geostatistics that many ore bodies exhibit erratic behaviour at lags close to zero. This erratic behaviour, known as the nugget effect, C_0, manifests itself as an apparent non-zero value of the semivariogram at zero lag. As discussed previously in §2.5.1.3, the nugget effect is the combination of three separate phenomena:

1. *microstructures within the geological material*;
2. *sampling, or statistical, errors*;
3. *measurement errors*.

Baecher's procedure, in essence, attributes the nugget effect solely to measurement error and ignores microstructure variabilities and sampling errors. These two effects must be accounted for before conclusions can be made regarding the extent of random measurement error associated with a particular test.

At this point, it is necessary to define a new parameter, the *ACF nugget*, R_0, which is the difference between unity and the value of the autocorrelation coefficient at lag zero, r_0, obtained by extrapolating the sample ACF back to lag zero, as shown in Equation (5.45). The ACF nugget, like the nugget effect from geostatistics, accounts for the micro-variability of the geological material, sampling errors and random measurement errors; but is determined from the sample ACF, rather than from the semivariogram.

$$R_0 = 1 - r_0 \tag{5.45}$$

5.5.1.2 Sample Spacing

As mentioned in the previous section, another important factor is the effect of the sample spacing on the observed nugget. In fact, the nugget effect that is obtained from the experimental semivariogram, depends greatly on the physical distance between the individual samples that form the data set. As the sampling distance decreases, it is possible to obtain a better estimate of C_0. However, while one is able to reduce the sampling interval to a very small distance, the cost of the exploration programme increases dramatically. As a result, it is often unreasonable, and in fact unnecessary, to reduce the sample spacing below some nominal minimum value. Unfortunately, this minimum sampling distance is dependent on the geological material being examined and cannot be known prior to investigation. Common practice is to begin sampling with a relatively

coarse grid and then to in fill with a repeatedly finer grid, as discussed in Chapter 4, until the sample spacing no longer influences the resultant experimental semivariogram.

In §5.5.2, two case studies will be used to demonstrate the effect of sample spacing on the observed nugget.

5.5.1.3 Trend Removal from Data

The applications of the theories of both random fields and geostatistics are greatly simplified by stationary data. The ACF, ACVF and the semivariogram are each dependent on the stationarity of the data set and, as a result, so too is the nugget effect and, hence, the random measurement error, obtained from each.

As detailed in §2.5.1.2, in both random field analysis and geostatistics, it is common practice to transform a non-stationary data set to a stationary one by removing a low-order polynomial trend, which is usually estimated by means of the method of ordinary least squares (OLS). Agterberg (1970) asserted that OLS assumes that the data are random and uncorrelated, which is inconsistent with spatial variability analyses which, having removed some trend determined by OLS, subsequently examine the correlation structure of the residuals. Li (1991) suggested that a technique based on *generalised least squares* (GLS) should be used as an alternative to OLS and the more complex methods suggested by Matheron (1973) and Delfiner (1976). Kulatilake (1991) stated that, while in general agreement with Li (1991), the GLS technique has significant drawbacks when applied in a practical sense. Furthermore, Ripley (1981) found that the trend produced by GLS varied only slightly from that produced by OLS.

Regardless of which method is used to evaluate the trend component within a non-stationary data set, the nugget effect is significantly influenced by the stationarity of the data, as will be seen in the following section.

5.5.2 Case Studies

The following two case studies examine the influence of trend removal and sample spacing on the nugget effect, as well as their effect on the spatial variability parameters r_B, a, C_0 and C. The first case uses vertical CPT data from sounding C8 and measured at the South Parklands site, whereas the second case examines horizontal CPT data obtained from the Keswick site.

5.5.2.1 Sensitivity of Vertical Spatial Variability

(i) Effect of Trend Removal

Firstly, the effect of trend removal is examined by removing a series of polynomial trends from the measurements of q_c from CPT C8, which were shown previously in Figure 5.8. The results of the random field and geostatistical analyses performed on the original data, as well as each of the detrended data sets, are summarised in Table 5.22; as are the results of Kendall's τ tests performed on each of the data sets. As detailed in §2.5.1.1, the coefficient of determination, r^2, is a measure of how well the regressed curve fits the data. The sample ACF, which pertains to the original data set with no trend removed, and the sample ACF, obtained by removing the OLS linear trend, are shown in Figure 5.86. The sample ACF, obtained after removing the OLS quadratic trend, was given previously in Figure 5.10.

As shown by the results in Table 5.22, the ACF nugget, R_0, determined using Baecher's approach, varies substantially, from 5% to 22% and, as a result, depends greatly on the degree of trend removed from the data. In fact, all of the parameters, r_B, r_1, R_0, a, C_0 and C, are sensitive to the level of trend removed from the data, particularly so when the data are non-stationary as indicated by Kendall's τ test. As one would expect, as the degree of polynomial trend increases, the corresponding values of r_B and a decrease. This is due to the fact that as the regressed polynomial trend better fits the data, as indicated by r^2, the characteristics of the residual noise component change and the correlation distance decreases. Hence, the correlation distance is dependent on the degree of polynomial trend removed from the data, as well as the extent of differencing. Therefore, it is particularly important that this be included in the definition of the correlation distance. While the literature is not specific in this regard, due mainly to the scant data on which the evaluation of the correlation distance is based, it would appear that the correlation distance should be defined as: *the distance, given by the sample ACF, which is derived from data transformed by the* ***lowest*** *degree of polynomial trend that satisfies data stationarity and, in particular, Kendall's τ test.* This is in general agreement with Kulatilake and Ghosh (1988), who suggested that the lowest order polynomial be used to detrend the data, such that the residuals satisfy the stationarity assumption. It can be seen from Table 5.22 that, for the C8 data, the lowest polynomial trend that satisfies data stationarity is of degree 2. Accordingly, the correlation distance is 240 mm.

Table 5.22 Summary of data stationarity analyses (vertical spatial variability - C8).

Random Field Theory

Degree of Polynomial Trend Removed from Data	Kendall's τ Test	Degree of Fit, r^2	r_B (mm)	r_1	r_0	ACF Nugget, R_0
None	×	-	765	0.95	0.95	5%
1	×	0.088	680	0.94	0.94	6%
2	✓	0.719	240	0.88	0.88	12%
3	✓	0.730	190	0.88	0.88	12%
4	✓	0.774	190	0.87	0.87	13%
5	✓	0.818	110	0.86	0.86	14%
6	✓	0.846	85	0.78	0.78	22%

Geostatistics

Degree of Polynomial Trend Removed from Data	Kendall's τ Test	Degree of Fit, r^2	a (mm)	C_0 (MPa^2)	C (MPa^2)	$C_0/(C+C_0)$
None	×	-	*	0	*	*
1	×	0.088	*	0	*	*
2	✓	0.719	285	1.77×10^{-3}	2.25×10^{-2}	7.3%
3	✓	0.730	300	1.56×10^{-3}	2.25×10^{-2}	6.5%
4	✓	0.774	300	1.56×10^{-3}	1.94×10^{-2}	7.4%
5	✓	0.818	170	1.14×10^{-3}	1.53×10^{-2}	6.9%
6	✓	0.846	145	1.38×10^{-3}	1.33×10^{-2}	9.4%

Note: * The *linear* model, $\gamma_y = 0.00045y$, best fits the experimental semivariogram;
× Failed Kendall's τ test;
✓ Passed Kendall's τ test.

(ii) Effect of Sample Spacing

In order to test the sensitivity of the nugget with respect to sample spacing, the original data set of q_c measurements, sampled at 5 mm, was modified to provide sets of data at different sample spacings. Data sets at different sample spacings were obtained by removing intervening rows of data. For example, to obtain a data set with q_c measurements at 10 mm spacings, every second row was removed. This provided two data sets of measurements spaced at 10 mm intervals - one from 1,100 mm and the other starting from 1,105 mm to 5,055 mm. This process of removing intervening rows was used to provide several data sets of q_c measurements at spacings of 10, 20, 50, 100 and 200 mm. The generation of each of the data sets was simplified by the use of the computer program, *CPTSpace*,

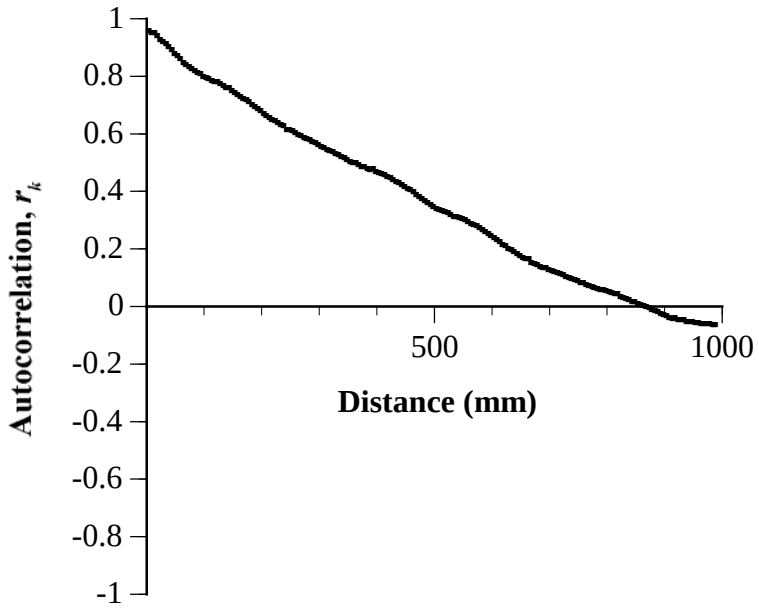

(a)

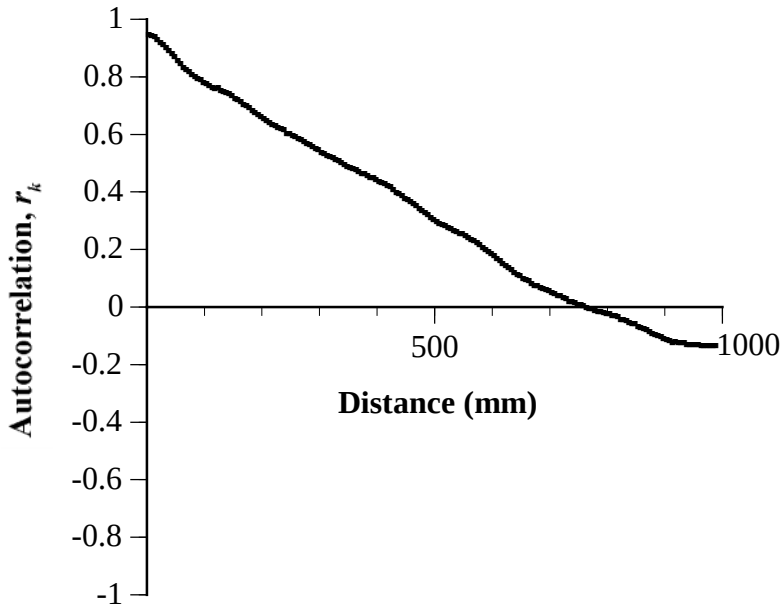

(b)

Figure 5.86 Sample ACFs after: (a) no trend removal; and (b) a linear trend removal.

discussed previously in §5.2.3. By removing the quadratic trend from each of these data sets, the residuals were obtained in order to determine the sample ACFs. Each of the detrended data sets passed Kendall's τ test. Again using the procedure proposed by Baecher (1982), the ACF nugget was evaluated by extrapolating the sample ACF back to lag, $k = 0$. The results for each of the data sets are summarised in Table 5.23. Examples of two sample ACFs are shown in Figure 5.87.

Table 5.23 Summary of sample spacing analyses (vertical spatial variability - C8).

Random Field Theory

Sample Spacing (mm)	r_B (mm)	r_1	r_0	ACF Nugget, R_0
5	240(1)	0.90(1)	0.90	10%
10	200, 205(2)	0.84, 0.86	0.89, 0.90	10% to 11%
20	180 to 190(4)	0.76 to 0.81	0.93 to 0.95	5% to 7%
50	135 to 175(5)	0.48 to 0.64	0.76 to 0.97	3% to 24%
100	90 to 170(5)	0.26 to 0.49	0.40 to 0.82	18% to 60%
200	100 to 160(5)	–0.03* to 0.29	0.38 to 0.97	3% to 62%

Note: $^{(n)}$ Separate data sets examined;
* Not possible to sensibly extrapolate R_0 when $r_1 < 0$.

Geostatistics

Sample Spacing (mm)	a (mm)	C_0 (MPa^2)	C (MPa^2)	$C_0/(C+C_0)$
5	330	1.77×10^{-3}	2.31×10^{-2}	7.1%
10	260, 335(2)	1.96×10^{-3}	2.02, 2.23×10^{-2}	8.1%, 8.8%
20	310 to 325(4)	1.92×10^{-3}	2.26 - 2.37×10^{-2}	7.5% to 7.8%
50	335 to 485(5)	0.96 - 8.35×10^{-3}	1.91 - 2.74×10^{-2}	3.4% to 30.3%
100	500 to 655(5)	4.35 - 13.2×10^{-3}	1.03 - 2.58×10^{-2}	14.4 to 56.2%
200	375 to 750(5)	0 - 1.91×10^{-3}	* - 4.53×10^{-2}	0% to 100%

Note: $^{(n)}$ Separate data sets examined;
* One of the cases yielded a pure nugget model, with $C_0 = 1.91 \times 10^{-3}$.

It can be seen from Table 5.23, that the calculated ACF nugget obtained from vertical spatial variability analyses is significantly dependent on the spacing of the samples and can vary between 3% and 62%. In addition, the spatial variability parameters r_B, a, C_0 and C, appear to be somewhat insensitive to sample spacing when the spacing is less than the correlation distance. However, once the sampling interval is equal to, or greater than, the correlation distance of the material, the values of a, C_0 and C vary substantially, as one

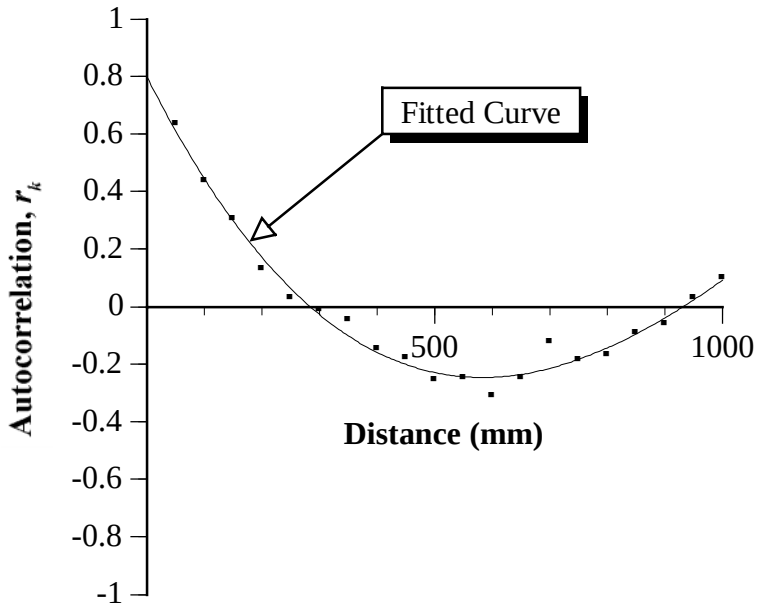

(a)

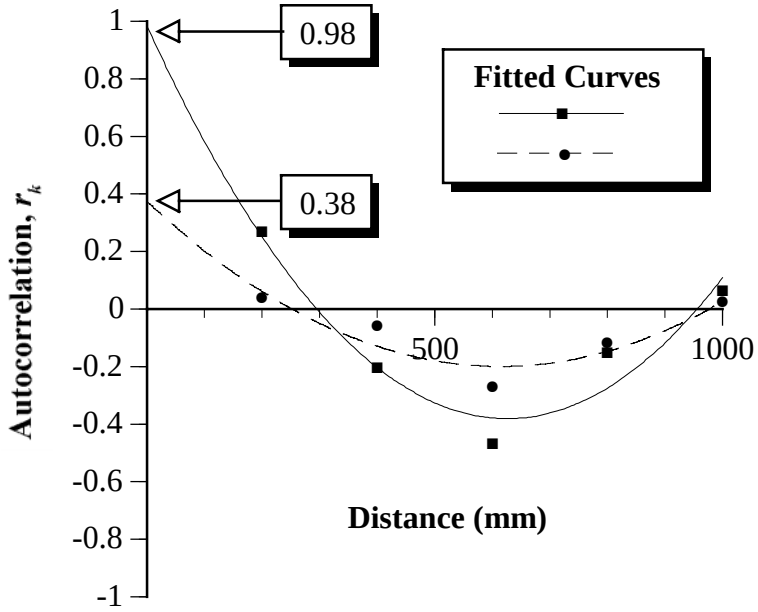

(b)

Figure 5.87 Sample ACFs for: (a) 50 mm spaced data set; and (b) 200 mm spaced data set.

would expect. The parameter r_B, on the other hand, appears to be more robust than a in this regard. Furthermore, it should be noted that as the sample spacing increases, the reliability of the sample ACF and experimental semivariograms decreases because of the reduction in the number of samples. This factor also affects the parameters r_B, a, C_0 and C.

5.5.2.2 Sensitivity of Horizontal Spatial Variability

In order to investigate the sensitivity of the horizontal spatial variability of soils, with respect to the factors described in §5.5.1, data from the horizontal CPT performed at the Keswick site, were analysed. Firstly, the effect of trend removal is examined by subtracting a series of polynomial trends from the measurements of q_c, which were shown previously in Figure 5.31. Secondly, the influence of sample spacing is also examined.

(i) Effect of Trend Removal

The results of the random field and geostatistical analyses performed on the original and, each of the detrended data sets, are summarised in Table 5.24. The sample ACF obtained after removing the OLS quadratic trend was shown previously in Figure 5.33.

Table 5.24 shows that the value of R_0 determined using Baecher's technique, varies only marginally from 3% to 4%. There is little difference in the value of R_0 obtained by removing the OLS linear trend, as compared to that obtained by removing the OLS quadratic, or higher order trends. The values of r_B are significantly different when no trend, a linear and a quadratic trend are removed from the data. However, there is little difference in the value of r_B when higher than order 2 trends are removed. The values of a, C_0 and C, again appear unaffected by trend removal. This is due mainly to the fact that the polynomials of degree 3 to 6 provide only a marginally better fit to the data, than that provided by the quadratic trend. Hence the characteristics of the residual noise component appear to remain the same. Had the higher orders of polynomial trends provided significantly better fits, one would have expected to obtain results similar to those obtained in the vertical spatial variability example, given in the previous section.

(ii) Effect of Sample Spacing

Again, in order to test the sensitivity of the calculated ACF nugget with respect to sample spacing, the original horizontal CPT data, which were sampled at 5 mm intervals, were

Table 5.24 Summary of data stationarity analyses (horizontal spatial variability).

Random Field Theory

Degree of Polynomial Trend Removed from Data	Kendall's τ Test	Degree of Fit, r^2	r_B (mm)	r_1	r_0	ACF Nugget, R_0
None	×	-	1,075	0.97	0.97	3%
1	✓	0.047	655	0.97	0.97	3%
2	✓	0.184	135	0.97	0.97	3%
3	✓	0.297	110	0.97	0.97	3%
4	✓	0.379	100	0.96	0.96	4%
5	✓	0.384	100	0.96	0.96	4%
6	✓	0.394	95	0.96	0.96	4%

Geostatistics

Degree of Polynomial Trend Removed from Data	Kendall's τ Test	Degree of Fit, r^2	a (mm)	C_0 (MPa^2)	C (MPa^2)	$C_0/(C+C_0)$
None	×	-	190	0.001	0.068	1.5%
1	✓	0.047	190	0.001	0.068	1.5%
2	✓	0.184	190	0.001	0.068	1.5%
3	✓	0.297	190	0.001	0.068	1.5%
4	✓	0.379	190	0.001	0.065	1.5%
5	✓	0.384	190	0.001	0.065	1.5%
6	✓	0.394	190	0.001	0.065	1.5%

Note: × Failed Kendall's τ test;
✓ Passed Kendall's τ test.

modified to provide data sets with spacings of 10, 20, 50, 100 and 200 mm between adjacent measurements of q_c, in the same way as for the vertical spatial variability case, described previously. By removing the quadratic trend from each of these data sets by the method of OLS, the residuals were obtained and the sample ACFs determined. Two such sample ACFs are shown in Figure 5.88.

Again, using Baecher's procedure, the ACF nugget is determined by extrapolating the sample ACF back to lag, $k = 0$. The results of a number of the horizontal CPT data sets are summarised in Table 5.25. As is indicated by the results shown in this table, the calculated ACF nugget varies significantly, from 3% to 50%, and again indicates that the ACF nugget depends greatly on the sample spacing of the data. Furthermore, for a spacing of 200 mm, 3 of the 5 data sets examined, yielded values of r_1 less than zero, making it impossible to

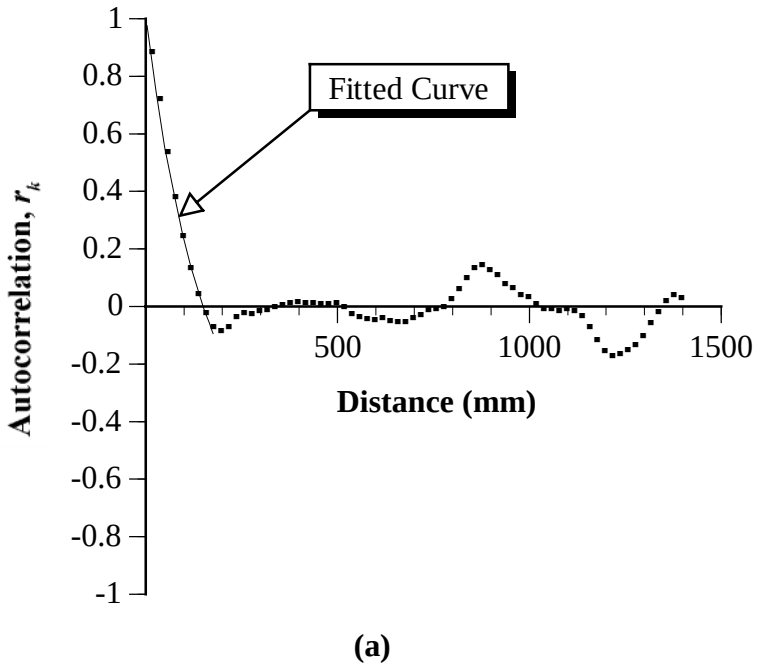

(a)

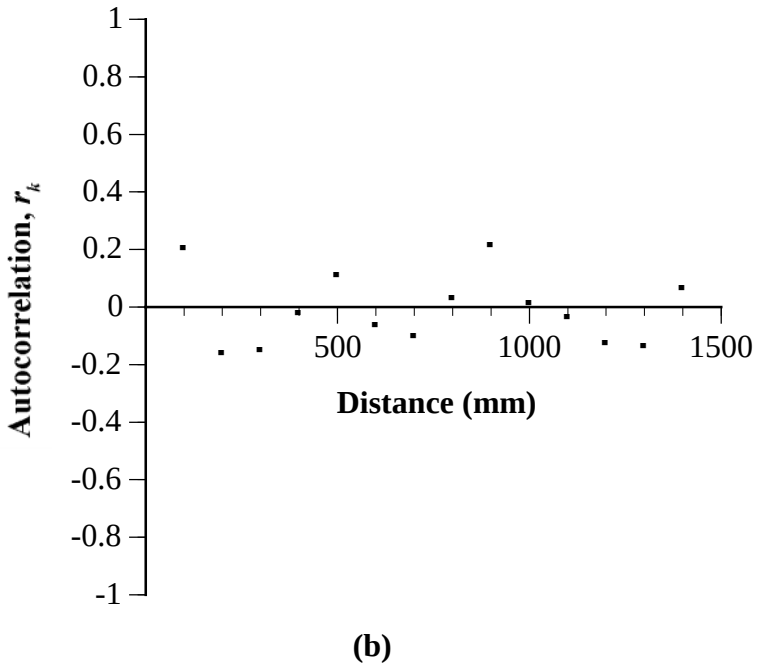

(b)

Figure 5.88 Sample ACFs for: (a) 20 mm spaced data set; and (b) 100 mm spaced data set.

Table 5.25 Summary of sample spacing analyses (horizontal spatial variability).

Random Field Theory

Sample Spacing (mm)	r_B (mm)	r_1	r_0	ACF Nugget, R_0
5	140[(1)]	0.97	0.97	3%
10	130, 135[(2)]	0.95, 0.95	0.97, 0.97	3%
20	120 to 130[(4)]	0.88 to 0.90	0.95	5%
50	110 to 115[(5)]	0.62 to 0.64	0.90 to 0.92	8 to 10%
100	100 to 110[(5)]	0.20 to 0.29	0.50 to 0.67	33 to 50%
200	100 to 160[(5)]	-0.28* to 0.20	? to 0.82	18% to ?

[(n)] : Separate data sets examined;
* : Not possible to sensibly extrapolate R_0 when $r_1 < 0$;
? : Unknown value of R_0 since $r_1 < 0$.

Geostatistics

Sample Spacing (mm)	a (mm)	C_0 (MPa^2)	C (MPa^2)	$C_0/(C+C_0)$
5	190[(1)]	0	6.80×10^{-2}	0%
10	195, 205[(2)]	0	6.68, 6.78×10^{-2}	0%
20	190 to 195[(4)]	0	6.64 - 6.90×10^{-2}	0%
50	195 to 210[(5)]	0	6.22 - 7.06×10^{-2}	0%
100	*[(5)]	4.35 - 13.2×10^{-3}	*	100%
200	*[(5)]	5.64 - 6.64×10^{-3}	*	100%

[(n)] : Separate data sets examined;
* : Only possible to fit a pure nugget model to the experimental semivariogram.

extrapolate a positive value of R_0. In addition, as indicated in Table 5.25, the spatial variability parameters r_B, a, C_0 and C, are relatively insensitive to sample spacing. When the sampling interval is equal to, or greater than, the correlation distance of the geological material, the values of a, C_0 and C, obtained by fitting a model to the experimental semivariogram, vary substantially, as one would expect. As was evident with the previous case study, the parameter r_B appears to be more robust than a with respect to sample spacing. Again, as in §5.5.2.1((ii)), at large sample spacings there are insufficient data to adequately define the ACF and semivariogram models.

5.5.3 Conclusions

This section has examined the sensitivity of the method proposed by Baecher (1982) for separating the spatial variability component of the geotechnical material from the random measurement error of the test, as well as the sensitivity of the spatial variability parameters r_B, a, C_0 and C, with respect to the influence of trend removal and sample spacing. The conclusions which relate to each, are given below.

1. Baecher's Method

It has been shown that conclusions made, regarding the random measurement error associated with a particular test, depend greatly on: (i) the spacing of the samples in the data set; and (ii) the stationarity of the data. In fact, the *ACF nugget*, R_0, is a combination of: random measurement error; small-scale variability of the soil; sampling errors; and non-stationarity errors. It is not solely random measurement errors associated with the particular test, as several authors have incorrectly assumed.

Several sample ACFs were obtained by removing no trend, as well as a series of OLS polynomial trends, from vertical and horizontal CPT data sets. Examination of these ACFs indicated that the calculated ACF nugget in Keswick Clay can vary by as much as 3% to 22% depending on which, if any, trend is removed. These results imply that the ACF nugget is significantly dependent on the degree of trend removed from the data. In addition, it appears that once stationarity has been achieved, as indicated by Kendall's τ test, R_0 is less sensitive to the degree of polynomial trend removed from the data.

By varying only the sample spacing of a data set, in increments of 5 mm up to 200 mm, it has been shown that the calculated ACF nugget can vary between 3% and 62% for vertical spatial variability, and between 3% and 50% for horizontal spatial variability. Since the majority of the information published, regarding random measurement errors associated with various tests, has been based on ACFs derived from samples taken at spacings well in excess of 200 mm, one must question the validity of their conclusions.

As a result of the data and analyses presented in this section, it is likely that the random measurement error associated with the cone penetration test is less than, or equal to, 3%. Table 5.3 presented the results of random field analyses performed on 30 of the 222 vertical CPTs obtained at the South Parklands site. The values of r_1 for each of these 30 CPTs were given in this table and, as shown, r_1 varies between 0.753 and 0.984, with a mean of 0.909 and CV = 7.2%. Hence, R_0 varies between 1.6% and 24.7%, with a mean of

9.1% and *CV* of 7.2%. Unfortunately, as stated by Soulié et al. (1990), it is extremely difficult to separate random measurement error from the micro-variabilities of the material being tested. As a consequence, it is not possible to separate R_0 into its component parts of random measurement error and soil micro-variability. However, since the minimum value of R_0 was found to be 1.6%, it is likely that the random measurement error associated with the CPT is less than, or equal to, 1.6%. This result compares well with the conclusion made by Campanella et al. (1987), that the random measurement error of the CPT may be as low as 1%.

2. Spatial Variability Parameters

It has been shown in this section that the spatial variability parameters, r_B, a, C_0 and C, are influenced by data stationarity; particularly so when the data are non-stationary, as indicated by Kendall's τ test. In addition, it has been seen that r_B, a, C_0 and C are relatively insensitive to sample spacing. However, when the spacing is greater than or equal to the correlation distance of the material, a, C_0 and C vary substantially, as one would expect. The parameter r_B, on the other hand, appears to be more robust than a in this regard.

5.6 SUMMARY

In summary:

1. It has been shown in this chapter that both random field theory and geostatistics provide adequate models for describing the spatial variability of the cone tip resistance of the Keswick Clay. Using these models it is possible to: estimate measured values; predict, or forecast, values at unsampled locations; and generate any number of simulated data. It has been shown that, while these models produce adequate descriptions of the spatial variability of the undrained shear strength of the Keswick Clay, much of the detail fails to be satisfactorily modelled. This is a limitation of using simple linear estimators and can only be rectified by using more complex models and estimation procedures. Such models and techniques have yet to be developed fully. This aspect is discussed in greater detail in Chapter 9.

2. In general, the technique of geostatistics has a number of advantages over random field theory. Geostatistics: provides a framework for 2D and 3D estimation; allows volumes of variable size to be estimated; enables interpolation forecasts to be performed; and allows missing data to be readily included in the modelling and estimation procedures.

While 2D and 3D forecasting regimes for random fields have been established theoretically (Vanmarcke, 1983), their use in the geotechnical engineering community has been extremely limited.

3. It has been shown in this chapter, that, in general, the spatial variability parameters of δ_v, r_B, a, C_0 and C, are dependent on the stationarity of the data, as well as the spacing of the samples. Furthermore, it has been observed that this dependence is associated with the relationship between the sample spacing and the correlation distance of the material under investigation. As a consequence, it is paramount that data used to assess the spatial variability of geotechnical materials be obtained at sample spacings *less than* the correlation distance of the material. Since the correlation distance is often unknown prior to testing and is often the subject of investigation itself, the data acquisition process may involve testing at two different stages, using two separate sampling intervals. Otherwise, data from published research can be used to give an indication of preliminary correlation distances, which will enable the sample spacing to be chosen.

4. The random measurement error associated the CPT has been found to be less than, or equal to, 1.6% and, as a consequence, the CPT provides a high level of reliability.

5. As a consequence of the analyses presented in this chapter, it is suggested that the correlation distance be defined as "the distance given by the sample ACF, δ_v, r_B or a, which is derived from data transformed by the *lowest* degree of polynomial trend that satisfies data stationarity and, in particular, Kendall's τ test."

6. In addition, it has been observed that the scale of fluctuation, δ_v, as originally defined by Vanmarcke (1977a, 1983), is equivalent to the correlation distance, that is, the distance over which the property in question exhibits strong correlation. This contradicts the definition of correlation distance as proposed by Diaz Padilla and Vanmarcke (1974) and Vanmarcke and Fuleihan (1975), who suggested that the correlation distance is the distance at which the ACF is equal to e^{-1} (0.3679).

7. Finally, the assessment of data stationarity is often a subjective one. A number of quantitative tests have been proposed in the literature, however, none of these have been entirely successful on their own. The most useful appears to be Kendall's τ test, though, it has been found that, in some instances, the test fails to reject apparently non-stationary data. This has been observed in only a few of the data sets examined; in particular, when n was approximately equal to 50. The runs test was also examined for its suitability in detecting non-stationary data and it appears that the test may be an inappropriate measure of the stationarity of CPT data, particularly when n_1 and n_2 are large, say greater than 50. Used in conjunction with other more subjective methods, for

example; eyeballing the data scatterplot, and examination of the sample ACF and the experimental semivariogram; Kendall's τ test; and the runs test, can provide additional information regarding the assessment of the stationarity of a data set. It must, however, be emphasised that none of these techniques should be used in isolation.

The following chapter discusses the development of a data base, *KESWICK*, which was compiled in order to provide data for the quantification of the large-scale spatial variability of the Keswick and Hindmarsh Clays.

Chapter Six

Compilation of a Data Base of Geotechnical Properties of the Keswick and Hindmarsh Clays

6.1 INTRODUCTION

In order to model both the small and large-scale spatial variability of geotechnical materials, a large volume of data is required, as mentioned in Chapter 2. The acquisition of such a large quantity of geotechnical information requires a significant outlay of both resources and time. A large body of geotechnical information, with respect to the Keswick and Hindmarsh Clays, already exists as a result of many site investigations, performed in Adelaide, for numerous and varied developments. The majority of these test results are unpublished and reside in the archives of the offices and laboratories of the geotechnical engineering consultants and Government instrumentalities of Adelaide. It was decided that, in order to enable a model for the large-scale variability of the Keswick and Hindmarsh Clays to be derived, a data base of existing geotechnical test results be compiled from these consulting and government bodies. This chapter discusses this compiled data base, known as *KESWICK*, compares it with other data bases discussed in the literature, and presents results derived from it.

6.2 GEOTECHNICAL DATA BASES DISCUSSED IN THE LITERATURE

GEOSHARE (Wood, 1980; Wood et al., 1982; Wood et al., 1983; Day et al., 1983) is a data base compiled in Britain to address a desire by the Construction Industry Research and Information Association (CIRIA) to disseminate information stored in site investigation reports (Tuckwell and Sadgrove, 1977). In addition, *GEOSHARE* was compiled to:

investigate the feasibility of developing a computer dedicated storage system, which was seen as being an economically efficient means of storing large quantities of factual site investigation information; and to investigate the geology of estuarine deposits in the Thames Basin (Wood et al., 1982). The information stored in *GEOSHARE* is summarised in Table 6.1.

Table 6.1 Information stored in *GEOSHARE*.
(Adapted from Wood et al., 1983 and Day et al., 1983).

Data type	**Numeric data**
Borehole reference data	Grid reference (National grid) Ground surface height (with respect to an assumed datum) Date of drilling Borehole diameter Casing limits
Sample and test data	Depths of strata In situ test results Sample recovery Laboratory test results Water level data
	Descriptive data
Soil descriptions	Consistency/compaction Colour Structure and organic content Primary soil type Secondary soil type Formation name/geological origin
General comments	50 characters per borehole

These data were stored on a Commodore PET personal computer with 32 kb of RAM, an extremely modest amount of storage by today's standards. *GEOSHARE* uses a BASIC interpreter to interrogate the information, upon input to the data base, and also to generate output. As an example of its flexibility, Wood et al. (1982) used *GEOSHARE* to plot contours of the surface of the London Clay. While the information stored in the data base is assumed to be a record made in good faith of the soil conditions encountered at that particular location, Wood et al. (1982, 1983) concluded that computer storage of data derived from site investigation reports is an efficient and effective means of data collection. In addition, Wood (1980) and Wood et al. (1982) stated that such a data base provides the facility for improving the planning of future site investigations.

Several authors have used data bases to examine correlations and trends that may exist between various data. From published literature, Mayne (1986) compiled a data base of 42 different sites world-wide, in order to develop a relationship between the *OCR* of clay soils and CPT and piezocone test data. Using the data base, Mayne (1986) concluded that q_c is a useful index for developing profiles of in situ *OCR* with depth, and that the piezocone can be also used to evaluate the degree of preconsolidation. Mayne et al. (1990) collected data from 83 different clay sites tested using the piezocone. By means of this data base, the authors were able to show that porewater pressures, during cone penetration in clay soils, are significantly affected by the position of the porous element, the size of the element and several other factors. Several additional trends and observations were also made by Mayne et al. (1990), by means of the data base. Chen and Kulhawy (1993) developed two data bases to examine correlations and trends that may exist between the undrained shear strength of CIU and UU tests, and from CIU and UC[28] tests. Again, by using data bases, the authors were able to show that good correlations exist between the undrained shear strengths obtained from CIU, UU and UC tests.

More recently, a number of authors have used computer-stored data bases for various aspects of geotechnical engineering. These include: *shallow foundations* (ASCE Shallow Foundations Committee, 1991); *tunnelling* (Hawkes, 1991; Touran and Martinez, 1991); *soil classification using CPT data* (Chan and Tumay, 1991); and *reliability analyses* (Favre et al., 1991). Each of the authors has found that the compilation of data on computer is both an efficient and effective means of data storage and information retrieval. Furthermore, a significant advantage of data bases is that they provide the facility to enable improved planning and decision making (Wood et al., 1982; Touran and Martinez, 1991).

As can be seen from the preceding treatment, data bases and, particularly, computer based data sets, provide valuable tools for the assessment of trends and correlations that may exist between various geotechnical properties. The following section details the formulation of the *KESWICK* data base.

6.3 FORMULATION OF THE *KESWICK* DATA BASE

In order to provide the data necessary for spatial variability analyses of the undrained shear strength of the Keswick and Hindmarsh Clays, a variety of information is needed, which includes:

- Measurement of shear strength;

[28] unconfined compression (triaxial) test

- In situ or laboratory test method used to determine shear strength;
- Location of shear strength measurement - coordinates in three dimensions;
- Soil type or unit to which the shear strength measurement refers;
- Date of sampling for laboratory testing, or date of testing for in situ tests;
- State of the soil - moisture content, dry density, total soil suction;
- Site information - for internal and cross-checking purposes.

To enable three-dimensional modelling of the spatial variability of the undrained shear strength of the Keswick and Hindmarsh Clays, it was necessary to develop a three-dimensional coordinate system for each test location. It was decided to use the standard Australian Map Grid (AMG) coordinates for the plan surface; that is, eastings and northings, and distances above the Australian Height Datum (AHD) for elevations above the plan surface. The AMG is a standard map grid established by the National Mapping Council of Australia and derived from a Transverse Mercator projection of latitudes and longitudes, the coordinates of which, are in metres (National Mapping Council of Australia, 1986). As mentioned in Chapter 4, the AHD is a standard datum surface, adopted by the National Mapping Council, to which all vertical control for mapping is referred. An important and useful outcome of using AMG and AHD coordinates, is that the *KESWICK* data base conforms to standard Australian topographic and cadastral maps. This enables results obtained from the data base to be transferred directly to these maps. In addition, as will be seen in the next section, these topographic and cadastral maps will be used to determine the three-dimensional coordinates for each site and test location.

6.4 DESCRIPTION OF THE *KESWICK* DATA BASE

A number of private consulting practices and Government instrumentalities were approached in order to collate as much data as possible, for the purpose of quantifying the large-scale variability of the Keswick and Hindmarsh Clays. All private consulting practices and Government departments approached responded positively and allowed their files and reports to be inspected, and the data within to be recorded. Seven consulting firms and one Government department participated in this research, each of which are listed below.

- *ACER Wargon Chapman (SA) Pty. Ltd. (formerly Hosking Oborn Freeman and Fox);*
- *Coffey Partners International Pty. Ltd.;*
- *Connell Wagner (SA) Pty. Ltd.;*
- *Golder Associates Pty. Ltd. (formerly Woodburn Fitzhardinge Geotechnical);*
- *Kinhill Engineers Pty. Ltd.;*
- *Koukourou and Partners;*

- *Rust PPK Consultants Pty. Ltd.;*
- *SACON.*

The *KESWICK* data base includes test results from site investigations conducted within the Adelaide city area. The data set consists of approximately 160 site investigations carried out within the Adelaide city area since the early 1960's. In total, *KESWICK* contains approximately 380 separate boreholes and 10,140 measurements. Figure 6.1 shows the locations of the boreholes included in the data base.

Data were compiled over the period December 1989 to October 1991 and the following information was recorded:

- **Subsurface profile data:** Depth to top of Keswick Clay (m);
  Depth to top of Hindmarsh Clay Sand Member (m);
  Depth to top of Hindmarsh Clay Member (m);
  Depth to base of Hindmarsh Clay (m);
  Reduced level of ground surface (m AHD).

  These data enable the thicknesses of the Keswick Clay, Hindmarsh Clay Sand member and Hindmarsh Clay member, and the depths to the surface of each layer, to be determined.

- **State of Clay/Sand:** Moisture content, w (%);
  Dry density, ρ_d (t/m^3);
  Total soil suction, u (pF);
  Instability Index, I_{pt} (%).

  These data provide information regarding the state of the soil from which other parameters can be evaluated, such as: the bulk unit weight, γ; dry unit weight, γ_d; saturated unit weight, γ_{sat}; void ratio, e; porosity, η; and degree of saturation, S_r, of the soil.

- **Test Type:** Cone penetration test (CPT);
  Consolidated drained triaxial test (TCD#) with # stages;
  Consolidated undrained triaxial test (TCU#) with # stages;
  Direct shear test (DST);
  Self-boring pressuremeter test (SBPT);
  Screw plate load test (SPLT);
  Standard penetration test (SPT);

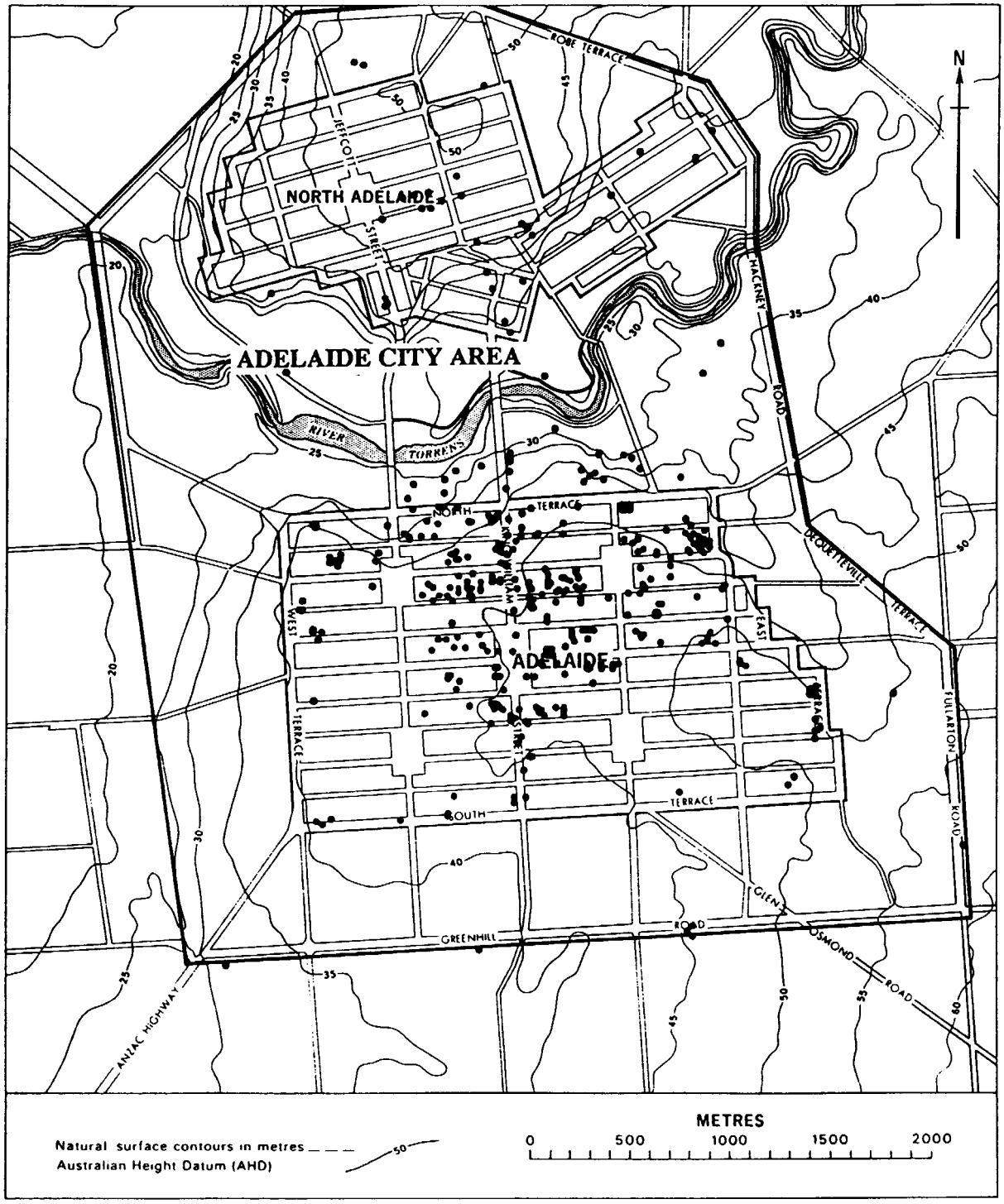

Figure 6.1 Location of boreholes included in *KESWICK*.
(Base plan from Selby and Lindsay, 1982).

Unconfined compression test (TUC);
Unconsolidated undrained triaxial test (TUU#) with # stages.

This information specifies the type of test associated with the shear strength measurement.

- **Test Depth**

  The depth at which an in situ test is carried out, or the depth of the upper surface of a sample obtained for laboratory testing.

- **Geotechnical Properties:** Shear strength, c_u, c' (kPa);
  Internal angle of friction, ϕ_u, ϕ' (degrees);
  Young's modulus of elasticity, E (MPa);
  Confining pressure, σ_3, for triaxial tests (kPa);
  Standard penetration number, N;
  Coefficient of earth pressure at rest, K_0.

  These data define various geotechnical properties associated with the soils tested, in particular, the shear strength, internal angle of friction and Young's modulus of elasticity.

- **Site Information:** Site location;
  Job number;
  Borehole number;
  Borehole location plan;
  Australian Map Grid (AMG) coordinates (m);
  Date of sampling;
  Additional comments.

  This information provides details relevant to the site and its location; the date soil samples were obtained; internal referencing details, such as job number and borehole number; and additional comments relevant to the data recorded in *KESWICK*.

For ease of data storage, manipulation and presentation, the data were prepared in spreadsheet format using Microsoft *Excel* 4.0® [29]. A portion of the *KESWICK* data base, in spreadsheet format, is included in Appendix C.

In order to determine the three-dimensional coordinates for each test location, it was necessary to transfer spatial information from the borehole location plan to 1:2,500 scale

[29] *Excel* is a registered trademark of Microsoft Corporation, One Microsoft Way, Redmond, WA, USA, 98052-6399.

topographic/cadastral maps of the Adelaide city area; 8 in all. Each map has an Australian Map Grid superimposed on it at spacings of 100 metres in both the north and east directions, as well as contours at 2 metre intervals. By referring to the surveying measurements indicated on the original borehole location plan, obtained from the site investigation reports of the consultants, the locations of the boreholes were plotted on the relevant topographic/cadastral maps. For each borehole location, the AMG coordinates were then obtained by scaling from these plans, with reference to the superimposed Australian Map Grid. An example of this procedure is shown in Figure 6.2. Where the reduced levels of the ground surface of the boreholes were not measured by the geotechnical engineer, the elevations were scaled from the plans by interpolating the AHD level from the contours. In this way, each test location was assigned a three-dimensional coordinate as shown in Figure 6.3.

Using the process described above, it is conservatively estimated that the accuracy of the scaled coordinates is:

Eastings and Northings (AMG coordinates)	±10 metres;
Reduced Levels (AHD)	±1 metre.

In terms of generally accepted surveying errors, the uncertainties associated with these coordinates are relatively high. These errors arise from the fact that, in general, most of the site investigations, which are referenced in the data base, contain site information based on relatively elementary surveying measurements, with limited control. However, in order to reduce these errors further, a significant amount of resources would be necessary, and would involve repeating the entire sampling and testing programme of each site investigation referred to in the data base, or conducting one of similar scope from the start. Naturally, such an exercise would be impractical and unwarranted.

In addition, the inherent measurement errors associated with the geotechnical properties and depths to each soil layer, are assumed to be those that could reasonably be expected to be obtained by a competent geotechnical engineer and testing authority, using appropriate standards of practice. This assumption is similar to that made by Wood et al. (1981, 1982) and is an inherent, and often unstated, assumption of all data bases using information obtained from third parties.

As a consequence of the large number of laboratory and in situ test results incorporated within the *KESWICK* data base, several trends and correlations can be established. The following section details the application of the data base to a number of situations, and examines the relationships and trends that can be derived from such applications.

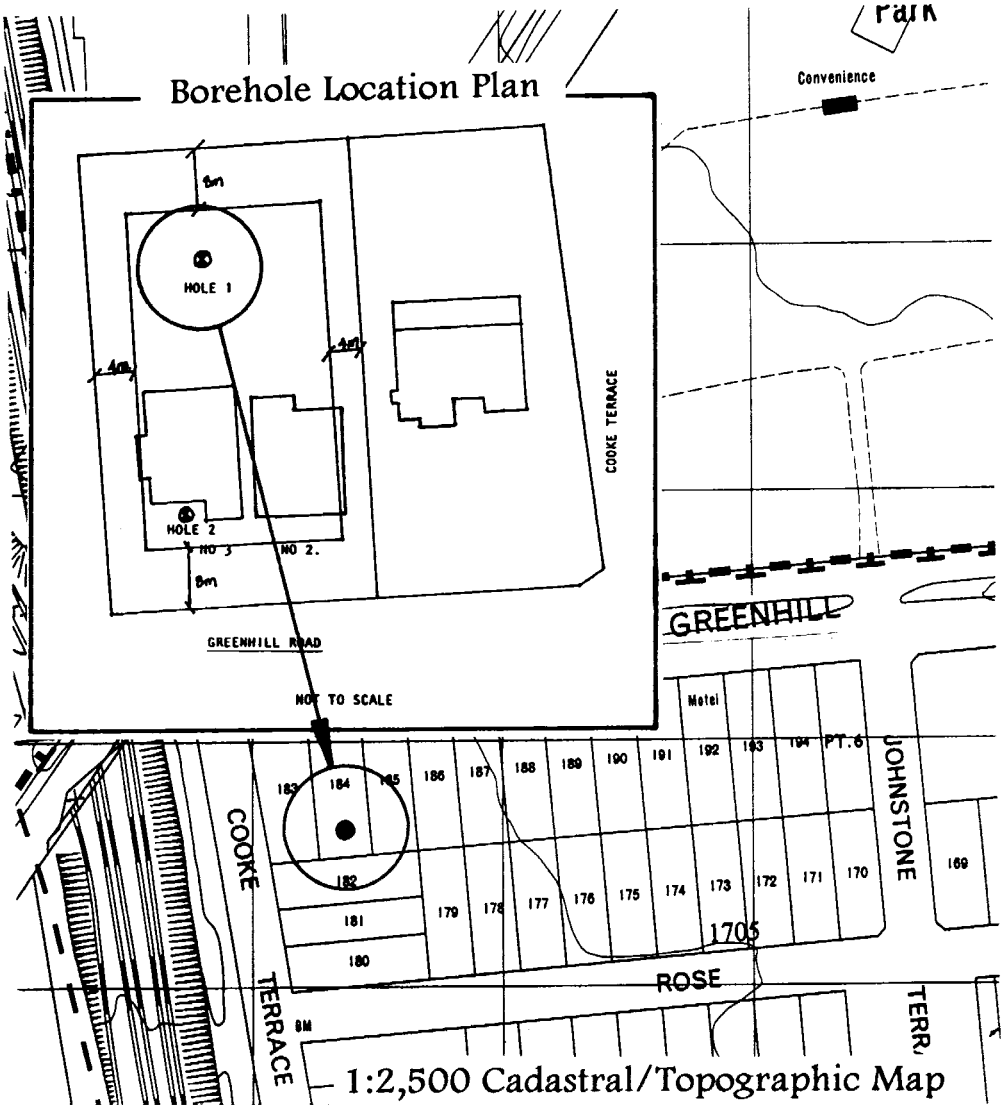

Figure 6.2 Procedure used to determine the three-dimensional coordinates for each test in the *KESWICK* data base.

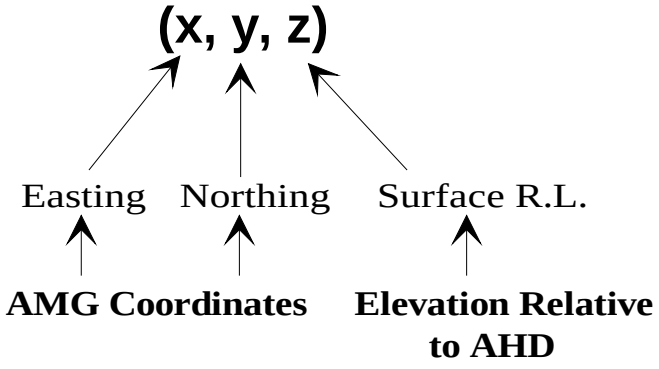

Figure 6.3 Three-dimensional coordinates associated with each test in *KESWICK*.

6.5 APPLICATION OF THE *KESWICK* DATA BASE

This section makes use of the data within the *KESWICK* data base, in order to establish general relationships and trends with respect to: (i) contours of the surface of the Keswick Clay, Hindmarsh Clay Sand Member and the Hindmarsh Clay Layer; (ii) moisture and density variations with depth; (iii) specific gravity and degree of saturation; (iv) shear strength; (v) Young's modulus of elasticity; (vi) SPT number; (vii) soil suction; and (viii) contours of undrained shear strength. Each of these are treated separately below.

6.5.1 Contours of Layer Surfaces

As described in §6.4, the *KESWICK* data base contains information regarding the depth below the ground surface at which the Keswick Clay, Hindmarsh Clay Sand Member and Hindmarsh Clay Layer were encountered in each of the 380 boreholes of the data base. In addition, *KESWICK* also contains the height above mean sea level (AHD) to the ground surface associated with each of these boreholes. As a result, it is possible to plot contours of the depth below ground, as well as the height above the AHD, to which the surface of each of these layers are expected to be encountered, within the Adelaide city area. Figures 6.4, 6.5 and 6.6 show the variation, with the depth below ground, of the surface of the Keswick Clay, Hindmarsh Clay Sand Member and Hindmarsh Clay Layers, respectively, within the Adelaide city area. Figures 6.7, 6.8 and 6.9, on the other hand, show the variation of the surface of the Keswick Clay, Hindmarsh Clay Sand Member and Hindmarsh Clay Layers, respectively, in relation to the AHD. Each of these figures were generated using the *Surfer*® and *DeltaGraph*®[30] graphical presentation packages. Firstly, a series of estimates was generated over a 25×25 grid spanning the Adelaide city area, using *Surfer*'s *GRID* program. The grid estimates were obtained using the inverse distance squared procedure, which is examined in some detail in §7.4.2. Finally, these gridded estimates were then entered into the *DeltaGraph* package, which subsequently created Figures 6.4 to 6.9.

It should be noted at this point, that, since all of *KESWICK*'s boreholes lie within, or on the boundary of, the Adelaide city area, values which lie outside the study region are obtained by extrapolation during the contouring process. As a consequence, these values should be treated with caution and are included only as a guide. Furthermore, the presence of gilgais, particularly within the Keswick Clay, as well as lenses and pockets, which are evident in the Hindmarsh Clay Sand Member, result in considerable depth variation within a

[30] *DeltaGraph* is a registered trademark of DeltaPoint Inc., 2 Harris Court, Suite B-1, Monterey, California, 93940.

particular site, as well as between sites. As a consequence of this, the contours given are a somewhat 'smoothed' version of the true distribution of these soils.

It can be seen from Figures 6.4 and 6.7 that the River Torrens has partially, or completely, removed the Keswick Clay within an erosion valley which extends over a lateral extent much greater than it presently occupies. This supports the conclusions made by Selby and Lindsay (1982).

It is evident from Figures 6.5, 6.6, 6.8 and 6.9 that the Hindmarsh Clay Sand Member and the Hindmarsh Clay Layer have also been partially, or totally, removed by the River Torrens. It appears that both of these soils remain in a wide band which runs in a north-westerly direction from the south-east corner of the Adelaide city area. This conflicts with the direction of elongation suggested by Selby and Lindsay (1982), mentioned previously in §2.3.2.1(ii). This is probably due to the fact that the *KESWICK* data base incorporates a larger number of boreholes which intercept the Hindmarsh Clay Sand Member, as well as including a larger section of the Adelaide city area.

The Hindmarsh Clay Layer may extend over regions not shown in Figures 6.6 and 6.9. This is due to the fact that, when the Hindmarsh Clay Sand Member is absent from the subsurface profile, it is difficult to distinguish between the Keswick Clay and the underlying Hindmarsh Clay Layer. As a result, many of the boreholes may have encountered the Hindmarsh Clay Layer, which was not identified by the logger. Furthermore, many of the boreholes within the *KESWICK* data base may not have extended to a depth large enough to intercept the Hindmarsh Clay or Sand layers. Nevertheless, Figures 6.5 to 6.9 provide useful information for the preliminary design of geotechnical site investigations.

6.5.2 Moisture and Density Relationships with Depth

As mentioned previously, it is useful to establish trends and relationships of various geotechnical parameters, particularly with depth. Figures 6.10 and 6.11 show two such parameters; namely moisture content, w, and dry density, ρ_d, respectively. These are plotted against depth for the Keswick Clay, Hindmarsh Clay Layer and undifferentiated Keswick Clay-Hindmarsh Clay Layer. It can be seen from these figures that, for each soil, no consistent trend exists for either parameter, w nor ρ_d, with depth. On the contrary, both w and ρ_d seem to fluctuate considerably with depth. In addition, it is not possible to support the conclusions made by Cox (1970) that the moisture content of the Hindmarsh Clay Layer is much less than that of the Keswick Clay.

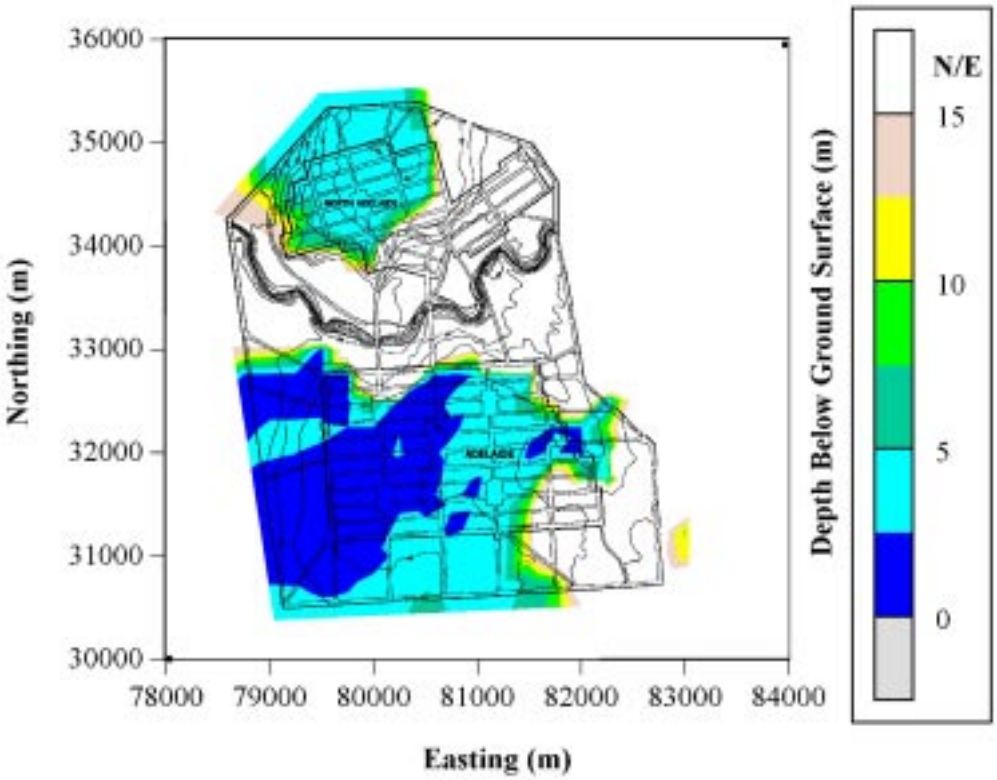

Figure 6.4 Variation of the depth below ground of the surface of the Keswick Clay.

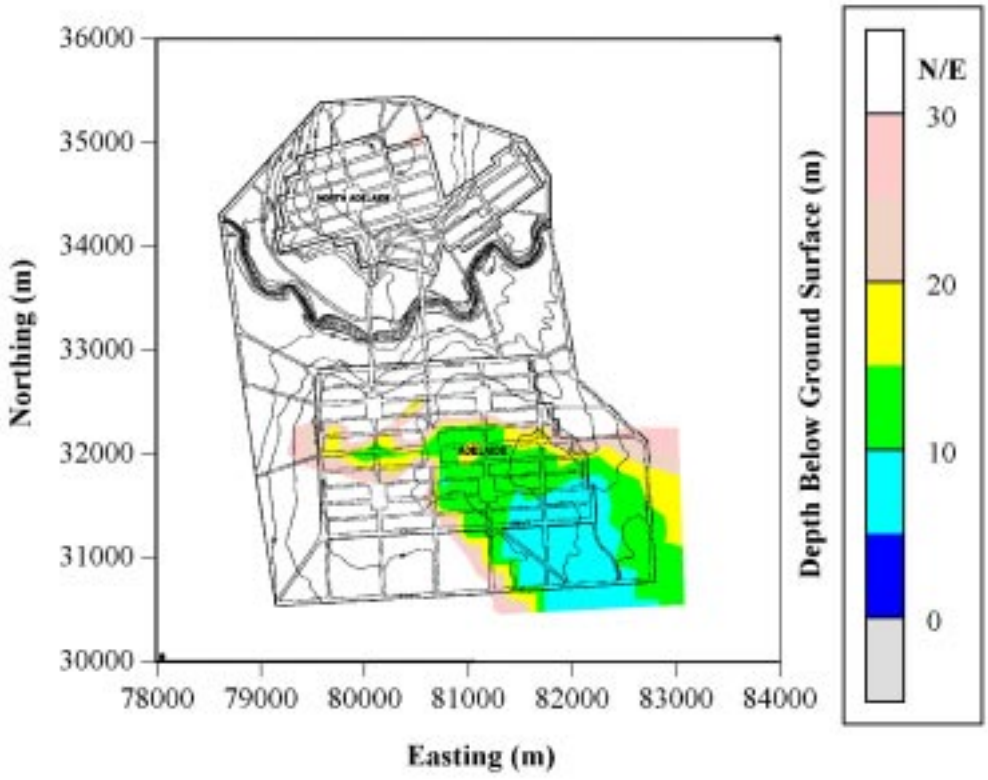

Figure 6.5 Variation of the depth below ground of the surface of the Hindmarsh Clay Sand Member.

INTENTIONALLY BLANK

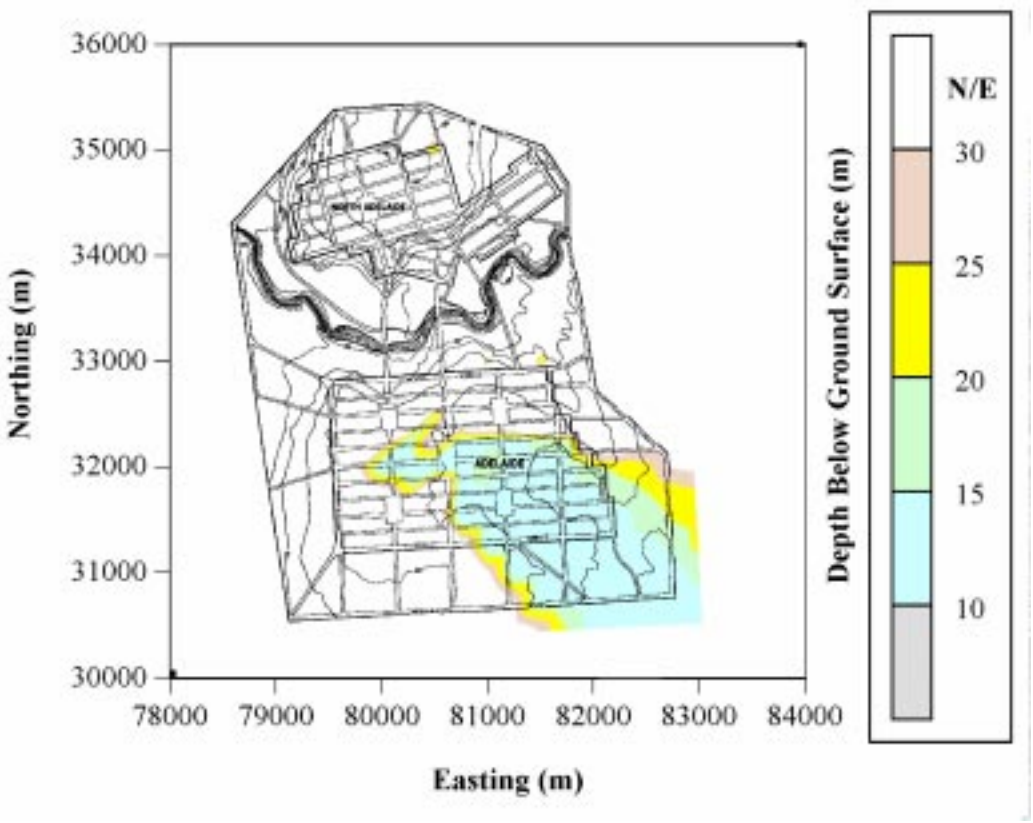

Figure 6.6 Variation of the depth below ground of the surface of the Hindmarsh Clay Layer.

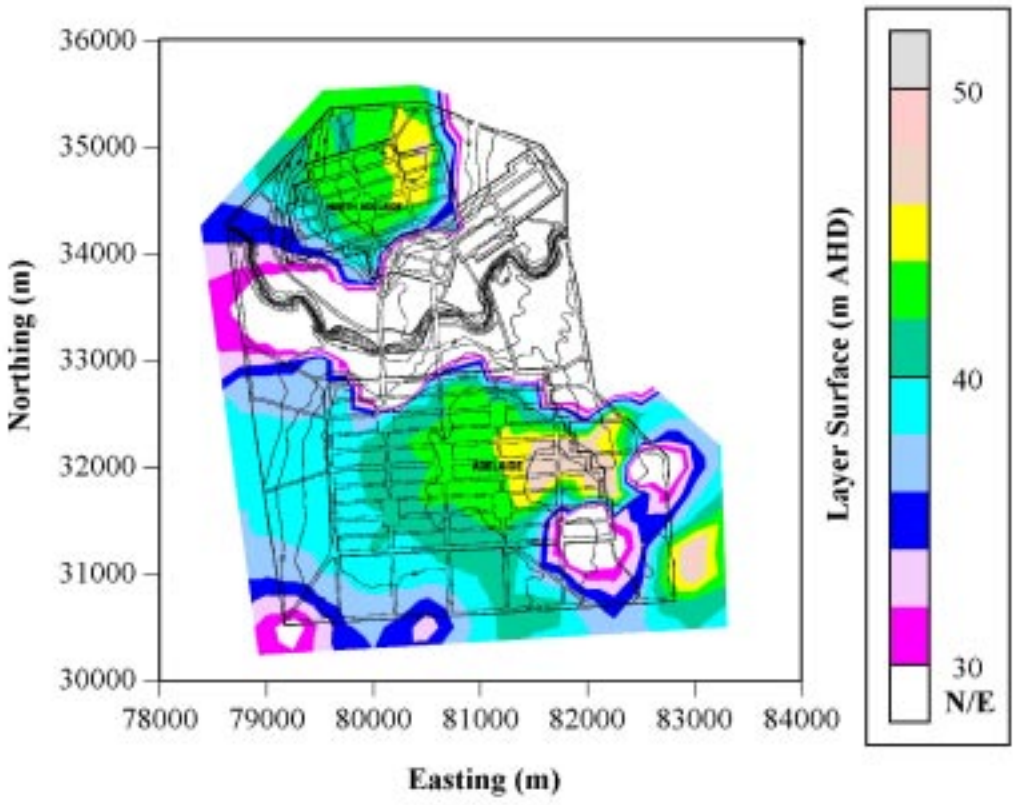

Figure 6.7 Variation of the surface of the Keswick Clay to the AHD.

INTENTIONALLY BLANK

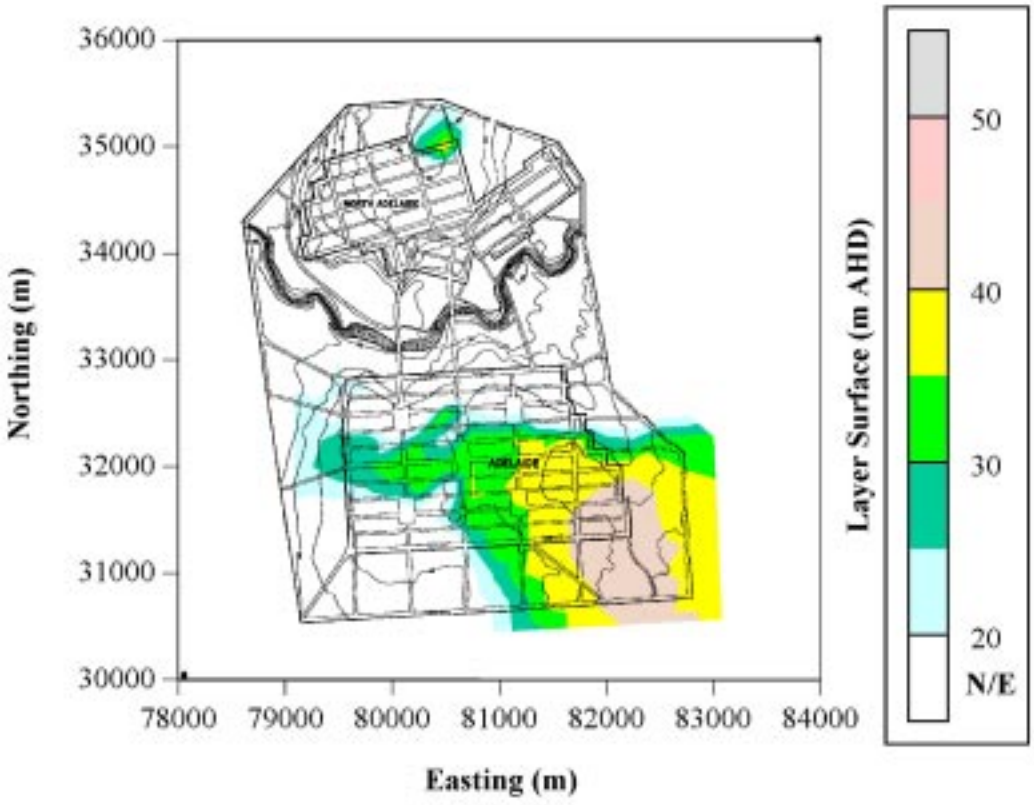

Figure 6.8 Variation of the surface of the Hindmarsh Clay Sand Member to the AHD.

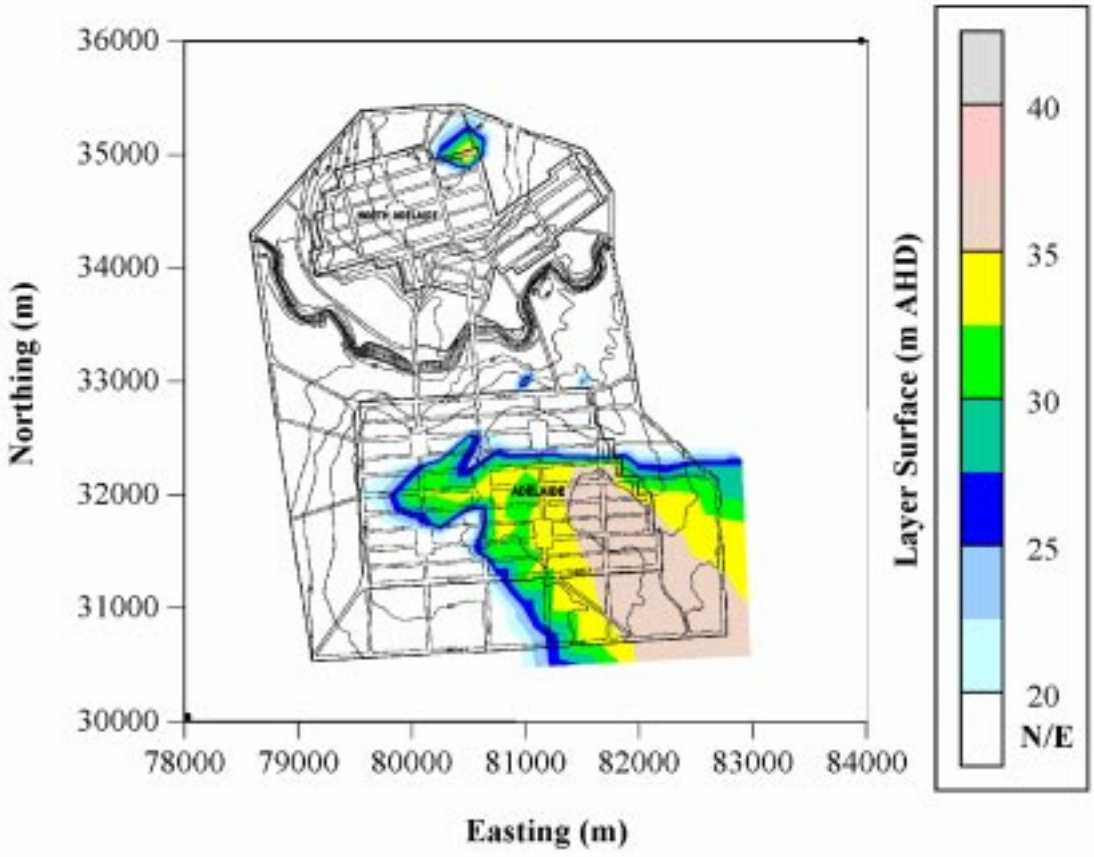

Figure 6.9 Variation of the surface of the Hindmarsh Clay Layer to the AHD.

INTENTIONALLY BLANK

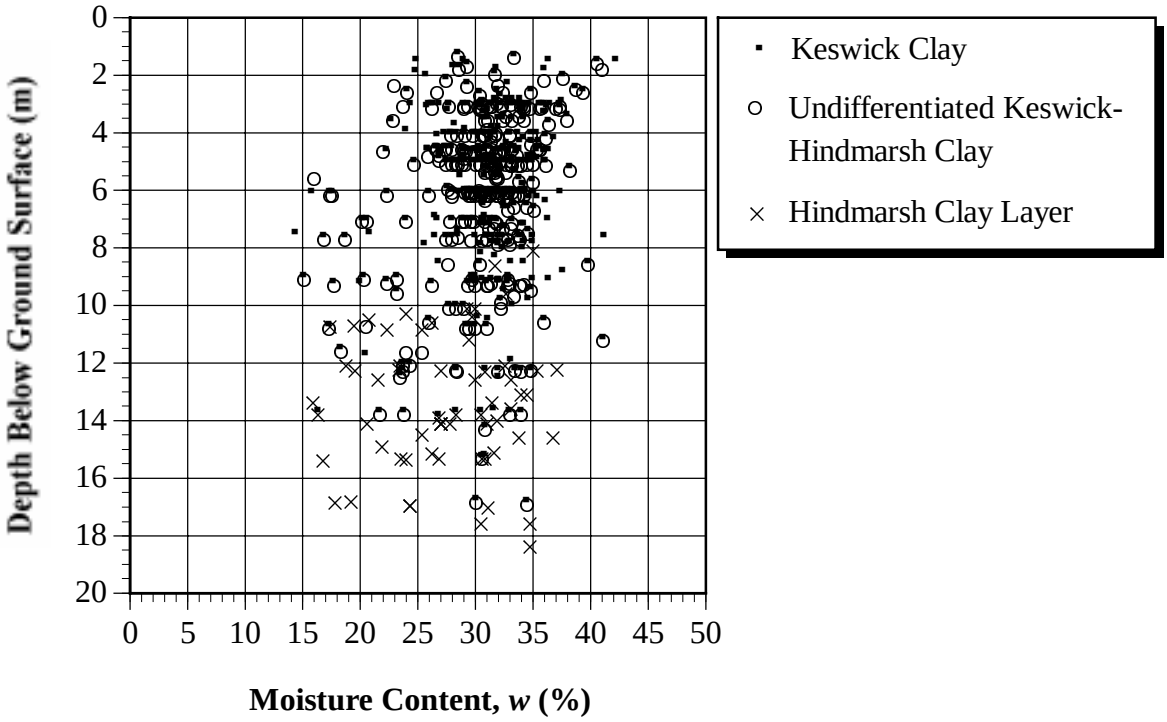

Figure 6.10 Relationship between moisture content and depth below ground for the Keswick Clay, undifferentiated Keswick Clay-Hindmarsh Clay, and the Hindmarsh Clay Layer.

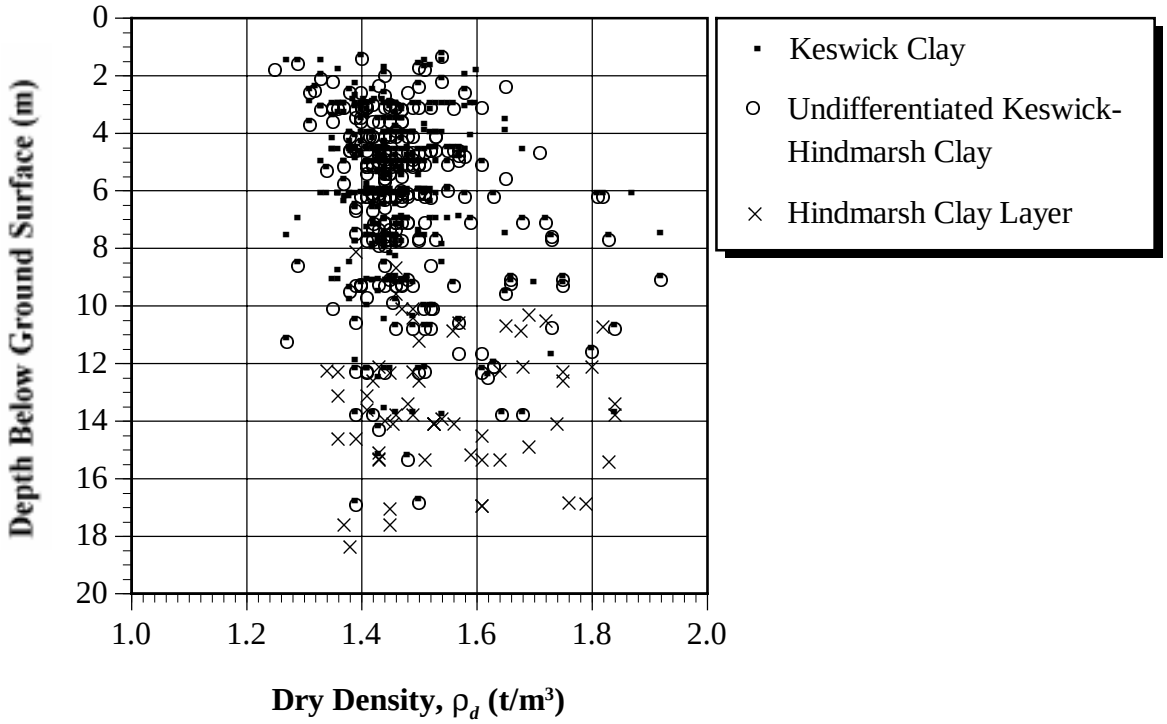

Figure 6.11 Relationship between dry density and depth below ground for the Keswick Clay, undifferentiated Keswick Clay-Hindmarsh Clay, and the Hindmarsh Clay Layer.

Some statistics associated with w and ρ_d, for each of the soil layers contained in the *KESWICK* data base, are given in Table 6.2. It should be noted that the *skewness* (skew.) is a measure of symmetry of the distribution of the data. A skewness of zero suggests a symmetrical distribution, a positive value indicates a right-hand skew, and a negative value implies a left-hand skew. The *kurtosis* (kurt.), on the other hand, is a measure of the 'peakedness' of the data distribution, a normal distribution having a value equal to 3.0. A kurtosis less than 3 indicates a flattened curve, whereas a value above 3, implies a more sharply-peaked curve.

It can be seen from Table 6.2 that the statistics associated with w and ρ_d, for both the Keswick Clay and the undifferentiated Keswick Clay-Hindmarsh Clay Layer, are very similar, implying that much of the undifferentiated material is likely to be Keswick Clay. Table 6.2 and Figures 6.10 and 6.11 are useful in that they provide general information regarding the most likely value for both w and ρ_d, the mean, as well as indicating ranges of values for which each of these parameters are likely to lie within. The recorded moisture content for each of these soils lies in the range of approximately 15% to 45%, which compares well with the 15% - 40% range given by Cox (1970). On the other hand, the dry density lies between 1.2 and 1.9 t/m^3.

Table 6.2 Statistics associated with w and ρ_d of the various soil layers stored in *KESWICK*.

Soil Layer	No. of Data	Min.	Max.	Mean	Std. Dev.	*CV* (%)	Skew.	Kurt.
Moisture Content, w (%)								
Keswick Clay	451	14.4	42.2	30.97	4.10	13.2	–1.13	2.65
Undiff. Keswick Clay-Hind. Clay	271	15.1	41.1	30.45	4.41	14.5	–0.93	1.68
Hindmarsh Clay Sand Member	11	9.0	21.0	14.46	3.86	26.7	0.21	–0.92
Hindmarsh Clay Layer	62	15.9	37.1	27.33	5.65	20.6	–0.33	–0.85
Dry Density, ρ_d (t/m^3)								
Keswick Clay	451	1.27	1.92	1.464	0.094	6.4	1.79	5.23
Undiff. Keswick Clay-Hind. Clay	268	1.25	1.92	1.475	0.101	6.8	1.49	3.25
Hindmarsh Clay Sand Member	11	1.56	1.91	1.794	0.103	5.8	–1.24	1.66
Hindmarsh Clay Layer	62	1.34	1.84	1.550	0.142	9.2	0.57	–0.78

6.5.3 Specific Gravity and Degree of Saturation

It is useful to plot the moisture content, w, of a soil against its dry density, ρ_d. By using Equation (2.1) and assuming a suitable G_s, it is then possible to estimate the degree of saturation of the soil. Figure 6.12 shows one such plot, obtained from 451 separate tests performed on samples of Keswick Clay from various locations throughout the Adelaide city area (shown previously in Figure 6.1), and assuming G_s = 2.70 (Cox, 1970). Superimposed on Figure 6.12 are the 80%, 90% and 100% degree of saturation lines. Of the 451 pairs of w and ρ_d data, 64, or 14%, lie above the zero air voids line, or 100% degree of saturation. This is physically not possible, as a soil is not able to have a volume of water greater than its volume of voids, or a volume of air less than zero. This implies, as a consequence, that either the measured values of w and ρ_d may be in error, or the assumed 'average' value of the soil's G_s may be inappropriate. As a result of this, as well as an estimation based on the mineralogy of the Keswick Clay, Jaksa and Kaggwa (1992) suggested that a more appropriate value for the average G_s of the Keswick Clay would be 2.75 ± 0.02. By assuming a G_s of 2.75, only 13 of the 451 data pairs, or 3%, plot above the 100% degree of saturation line, as shown in Figure 6.13.

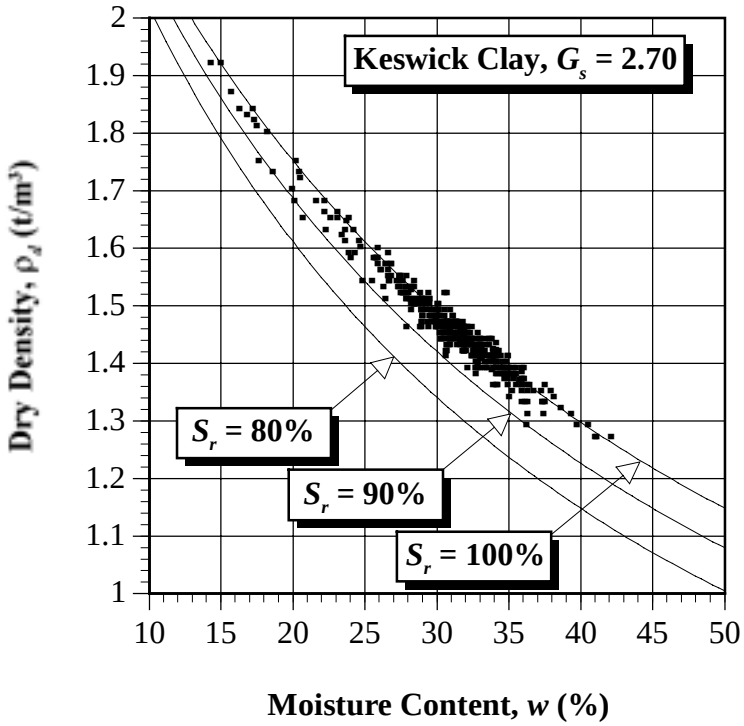

Figure 6.12 Relationship between w, ρ_d, and S_r for Keswick Clay with G_s = 2.70.

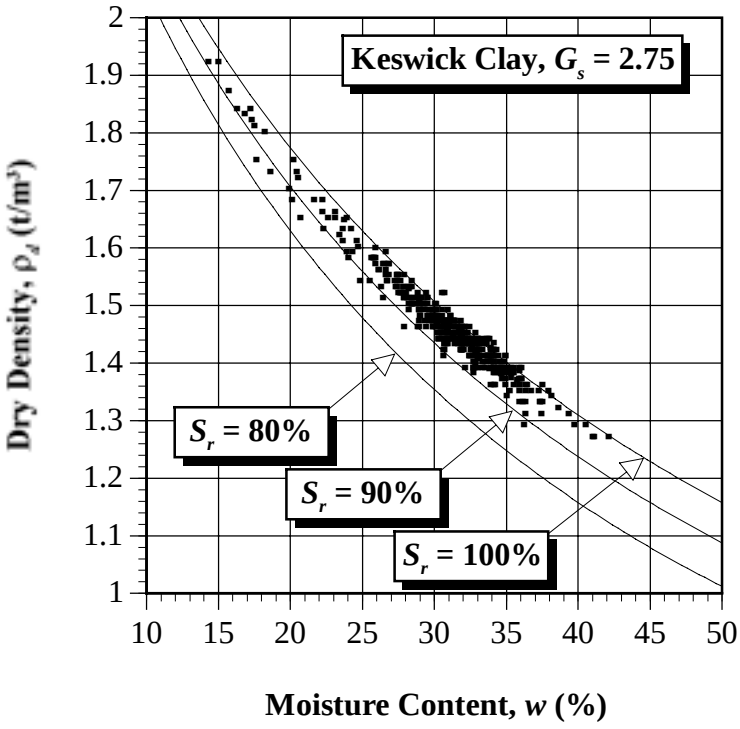

Figure 6.13 Relationship between w, ρ_d, and S_r for Keswick Clay with G_s = 2.75.

Li (1992), in response to Jaksa and Kaggwa (1992), performed a Monte Carlo simulation assuming true values of w = 30%, ρ_d = 1.45 t/m^3, G_s = 2.70 and CV = 2%, implying a very precise level of measurement. After carrying out 1,000 realisations, Li found that approximately 13% of the results yielded degrees of saturation greater than 100%. Li (1992) argued that errors associated with the measurement of w and ρ_d will invariably cause S_r to rise above 100%. This is especially so considering that Lee et al. (1983) reported that the CV associated with the measurement of w may vary by as much as 6% to 63%, and the CV for the measurement of density, between 1% and 10%. However, the values of CV quoted by Lee et al. (1983) contain, not only measurement error, but also the natural, or spatial, variability of the material. As a result, the CVs that account for the measurement errors of each of the tests are expected to be somewhat lower than the values suggested by Lee et al. (1983).

It is apparent, therefore, that errors are inevitably associated with the reported values of w and ρ_d contained in the *KESWICK* data base. It is unrealistic, though, to assume that the average value of G_s accounts for these uncertainties. In reality, the errors associated with the measurement of w and ρ_d, as well as inappropriate values of G_s, contribute to errors in the calculation of S_r. However, as described in §2.3.2.5, tests performed by Islam (1994) indicate that there may be some justification for increasing the 'average' value of the G_s of Keswick Clay. Perhaps a value between 2.73 and 2.75 may be a more reasonable estimate than the value of 2.70 suggested by Cox (1970). In addition, Figures 6.12 and 6.13 show

that the majority of the Keswick Clay is saturated or very close to being saturated, which is in agreement with Cox (1970), Stapledon (1970), and Jaksa and Kaggwa (1992).

Using the methodology suggested by Jaksa and Kaggwa (1992), the relationship between w and ρ_d, for samples of undifferentiated Keswick Clay-Hindmarsh Clay Layer, is shown in Figure 6.14, assuming G_s = 2.75. The relationship for the Hindmarsh Clay Layer, is shown in Figure 6.15, assuming G_s = 2.77. Based on the results shown in these figures, it seems reasonable to assume that the average values of G_s, for undifferentiated Keswick Clay-Hindmarsh Clay Layer and the Hindmarsh Clay Layer, are 2.75 and 2.77, respectively. Again, there is uncertainty associated with these assumed 'average' values, due to the errors inherent in the measurement of w and ρ_d; however, it is difficult, if not impossible, to quantify this uncertainty.

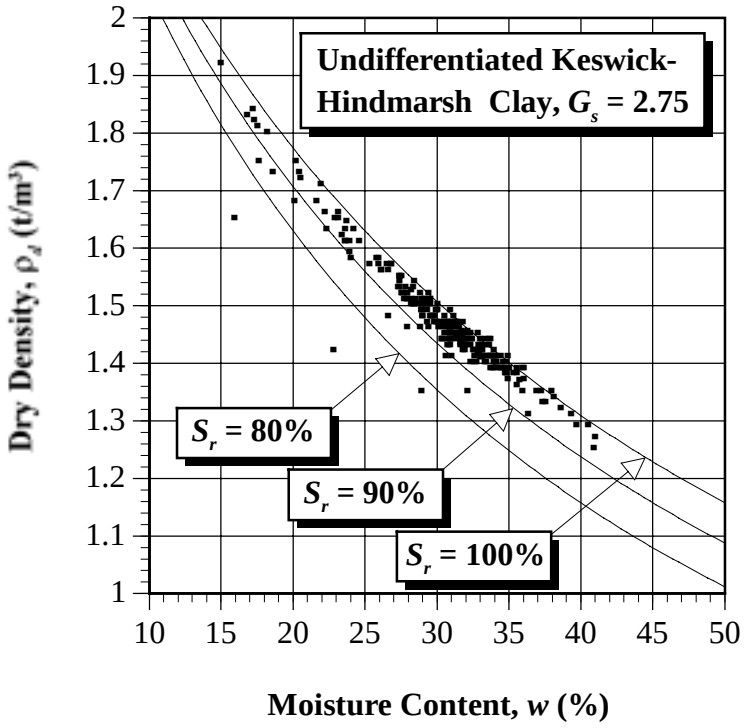

Figure 6.14 Relationship between w, ρ_d, and S_r for undifferentiated Keswick Clay-Hindmarsh Clay with G_s = 2.75.

Figure 6.16 shows the relationship between the degree of saturation of the Keswick Clay and depth below the ground surface. As in the previous section, there appears to be no trend or relationship between S_r and depth.

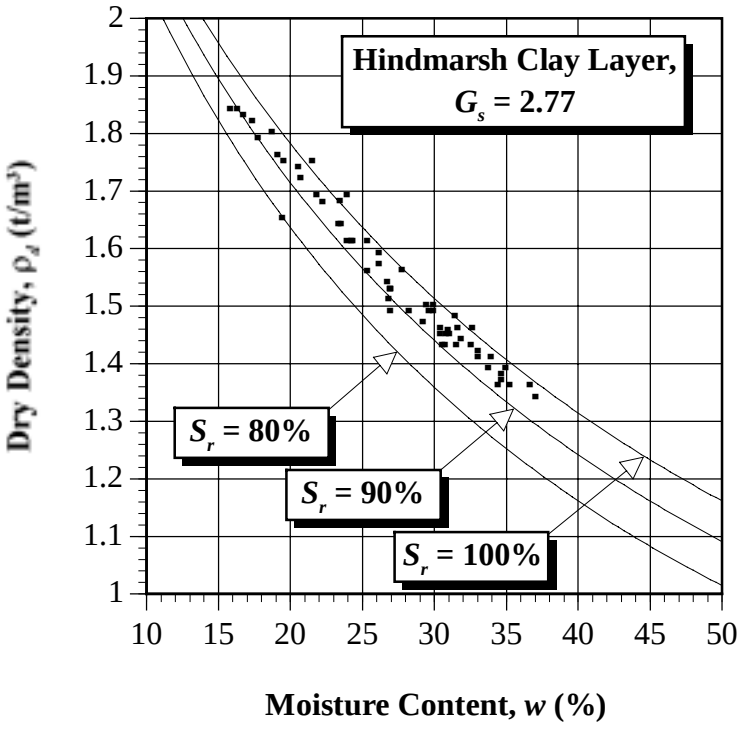

Figure 6.15 Relationship between w, ρ_d, and S_r for the Hindmarsh Clay Layer with G_s = 2.77.

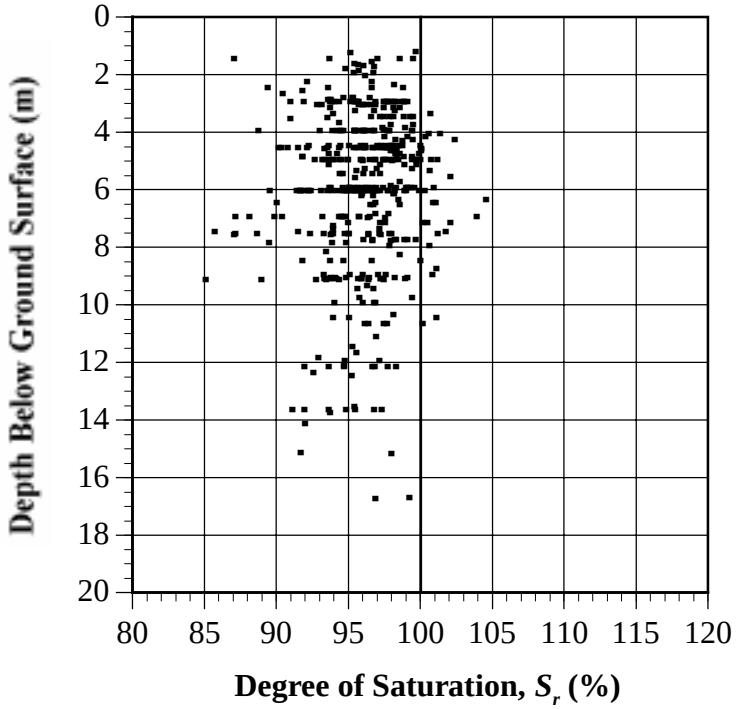

Figure 6.16 Relationship between S_r and depth below ground for the Keswick Clay with G_s = 2.75.

6.5.4 Shear Strength

The main purpose of creating the *KESWICK* data base was to provide information regarding the large-scale spatial distribution of the undrained shear strength of the Keswick and Hindmarsh Clays. As a result, the majority of the data contained within *KESWICK* relates directly to the undrained shear strength, s_u, of these soils. This section examines relationships and trends associated with s_u.

Figures 6.17 to 6.20 show the relationship between s_u, obtained from the first stage of unconsolidated undrained triaxial tests (UU) performed on samples of the Keswick Clay, undifferentiated Keswick Clay-Hindmarsh Clay, Hindmarsh Clay Sand Member and the Hindmarsh Clay Layer, respectively. Superimposed on these graphs are lines representing $s_u = \sigma_{v0}$ and $s_u = 2\sigma_{v0}$. In general, from Figures 6.17, 6.18 and 6.20, the clay soils indicate a trend of s_u increasing with depth, with the majority of each of the s_u values lying between σ_{v0} and $2\sigma_{v0}$. Figure 6.19, on the other hand, suggests that there is no such relationship for the Hindmarsh Clay Sand Member. The small number of data points implies, however, that such a conclusion may be inappropriate. Figures 6.18 and 6.20 indicate that a number of samples of the undifferentiated Keswick Clay-Hindmarsh Clay, and the Hindmarsh Clay Layer, exhibited undrained shear strengths lower than σ_{v0}, as well as values of s_u greater than $2\sigma_{v0}$. The values of s_u which are less than σ_{v0}, are likely to be associated with failures along fissures or joints.

Table 6.3 summarises the statistics associated with the undrained shear strength of the various clay layers contained in the *KESWICK* data base, and Figure 6.21 shows the histograms of s_u for these clay soils.

Table 6.3 Statistics associated with s_u (kPa) obtained from UU tests.

Soil Layer	No. of Data	Min.	Max.	Mean	Std. Dev.	*CV* (%)	Skew.	Kurt.
Keswick Clay	150	50	352	148.9	55.3	37.1	0.78	0.92
Undiff. Keswick Clay-Hindmarsh Clay	229	31	567	163.2	74.8	45.8	1.57	4.12
Hindmarsh Clay Layer	46	50	676	283.9	110.5	38.9	0.88	2.60

Again, it can be seen from Table 6.3 and Figure 6.21 that the statistics and distribution of s_u of the Keswick Clay and the undifferentiated Keswick Clay-Hindmarsh Clay are very similar, further confirming that much of the undifferentiated material is in fact Keswick

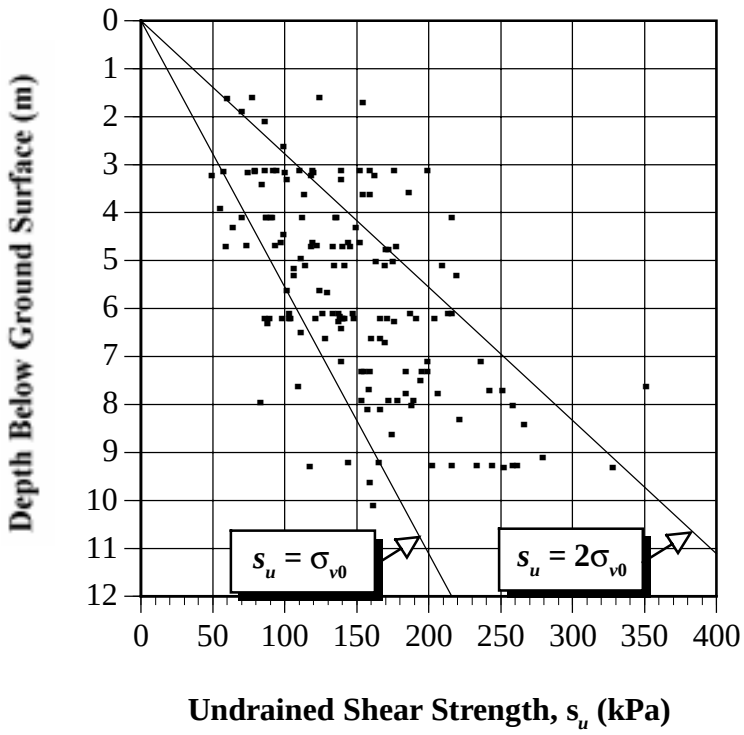

Figure 6.17 Undrained shear strength, s_u, of the Keswick Clay obtained from the first stage of UU tests.

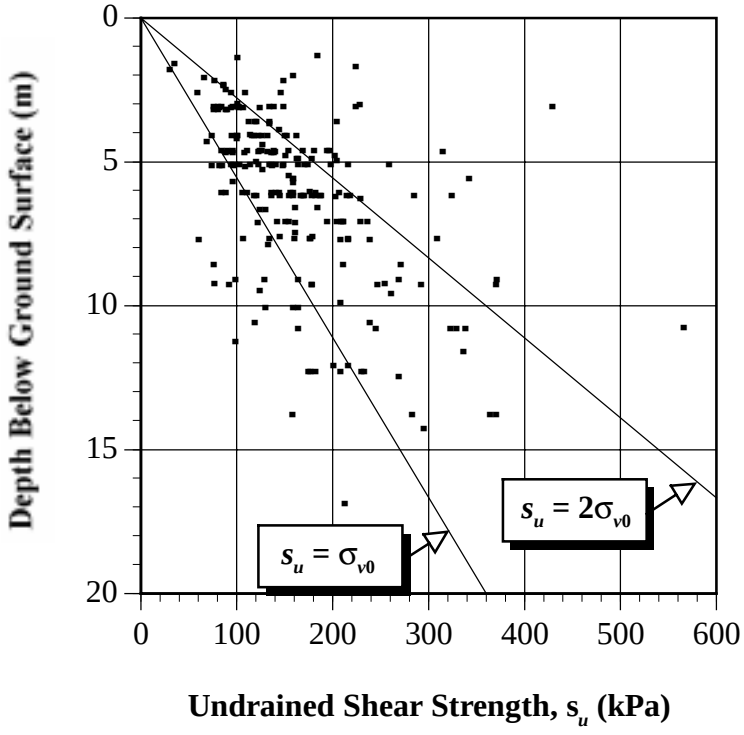

Figure 6.18 Undrained shear strength, s_u, of undifferentiated Keswick Clay-Hindmarsh Clay obtained from the first stage of UU tests.

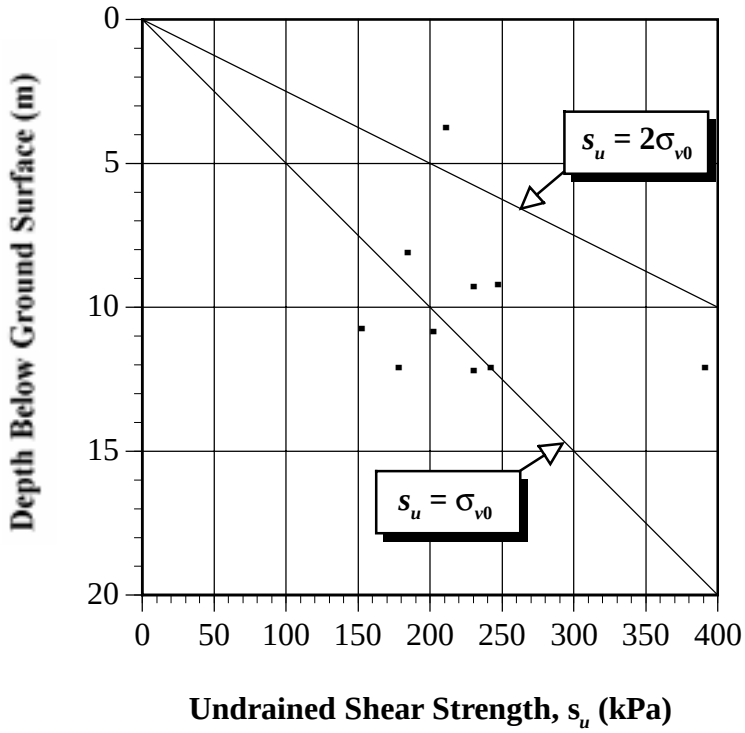

Figure 6.19 Undrained shear strength, s_u, of the Hindmarsh Clay Sand Member obtained from the first stage of UU tests.

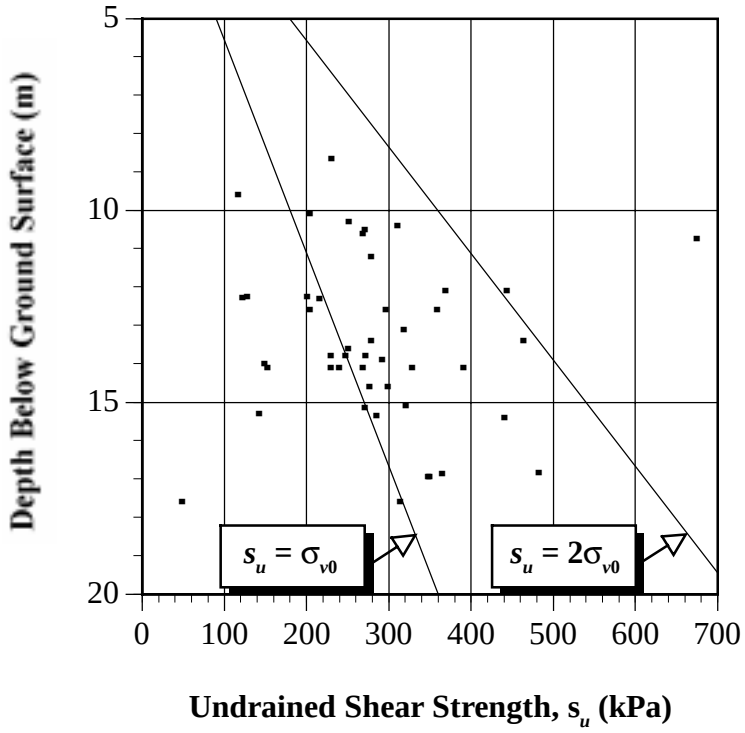

Figure 6.20 Undrained shear strength, s_u, of the Hindmarsh Clay Layer obtained from the first stage of UU tests.

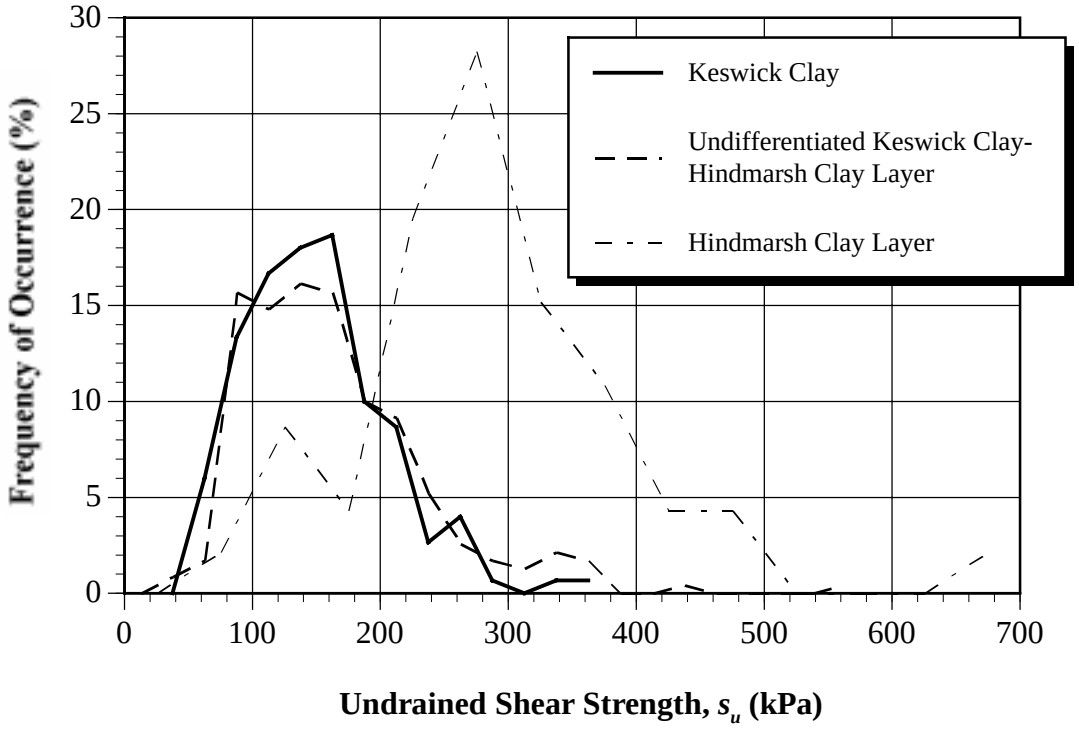

Figure 6.21 Histograms of the undrained shear strength, s_u, of the Keswick Clay, undifferentiated Keswick Clay-Hindmarsh Clay and the Hindmarsh Clay Layer obtained from the first stage of UU tests.

Clay. In addition, Table 6.3 and Figure 6.21 show that the mean value of s_u for the Hindmarsh Clay Layer, as well as the scatter of the data which is measured by the standard deviation, are somewhat larger than those for the other two soil types.

Figure 6.22 shows a plot of measurements of s_u against depth, obtained from a variety of in situ tests carried out in the Keswick Clay, undifferentiated Keswick Clay-Hindmarsh Clay and the Hindmarsh Clay Layer. As was evident with the plots obtained from the triaxial tests, the in situ measurements also indicate that s_u increases with depth, the majority of the values, again, lying between σ_{v0} and $2\sigma_{v0}$.

Figures 6.23 and 6.24 show measurements of the undrained shear strength of the Keswick Clay, undifferentiated Keswick Clay-Hindmarsh Clay and the Hindmarsh Clay Layer, plotted against moisture content and dry density, respectively. As one would expect, Figure 6.23 suggests that, as the moisture content of the soils increase, s_u decreases. Figure 6.24, on the other hand, indicates a positively increasing trend; that is, as the dry density increases, so too does s_u. However, there is considerable scatter about these trends and, as a result, it would be unreasonable to fit regression lines to these data.

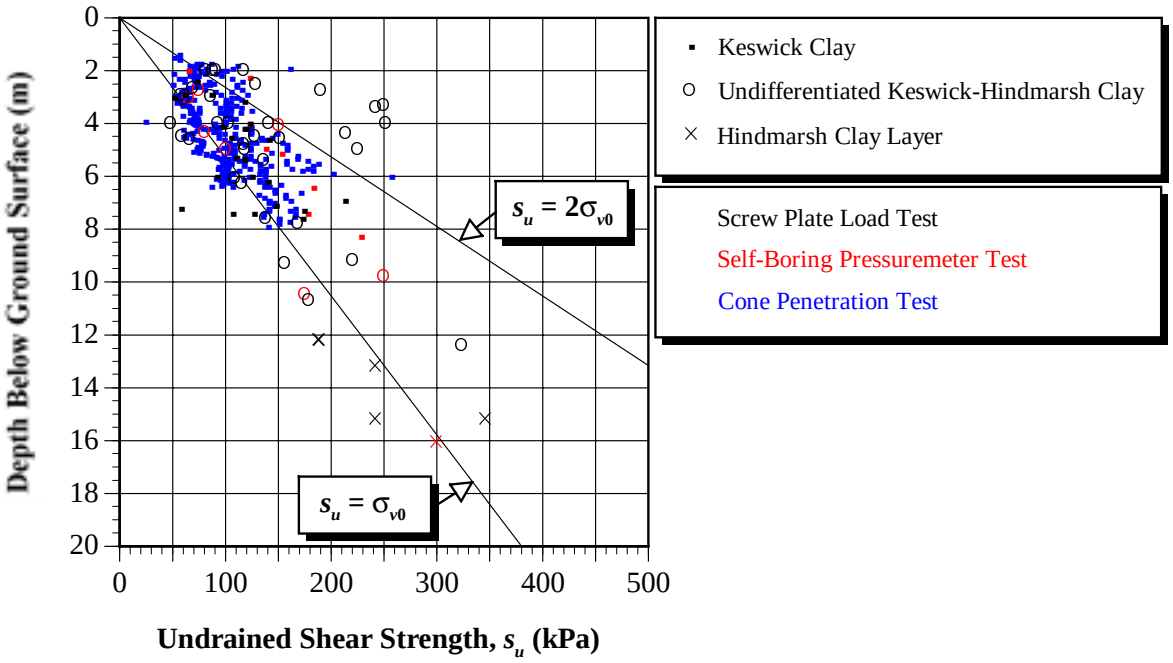

Figure 6.22 Relationship between s_u and depth below ground for the Keswick Clay, undifferentiated Keswick Clay-Hindmarsh Clay and the Hindmarsh Clay Layer obtained from several in situ tests.

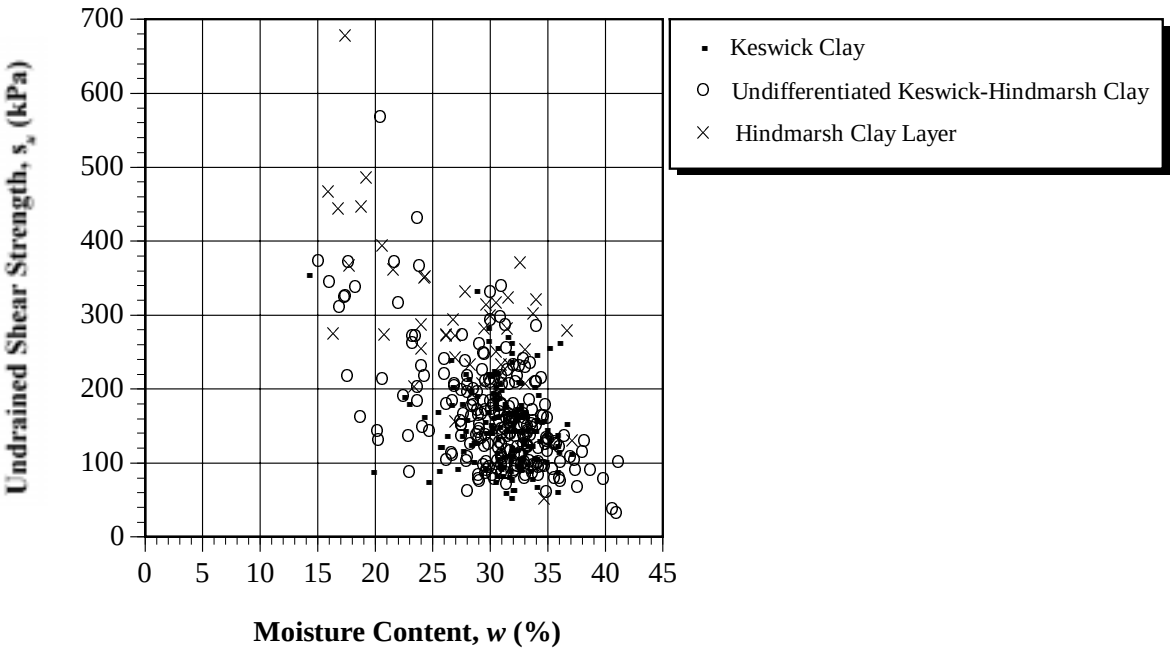

Figure 6.23 Relationship between s_u and w for the Keswick Clay, undifferentiated Keswick Clay-Hindmarsh Clay and the Hindmarsh Clay Layer obtained from the first stage of UU tests.

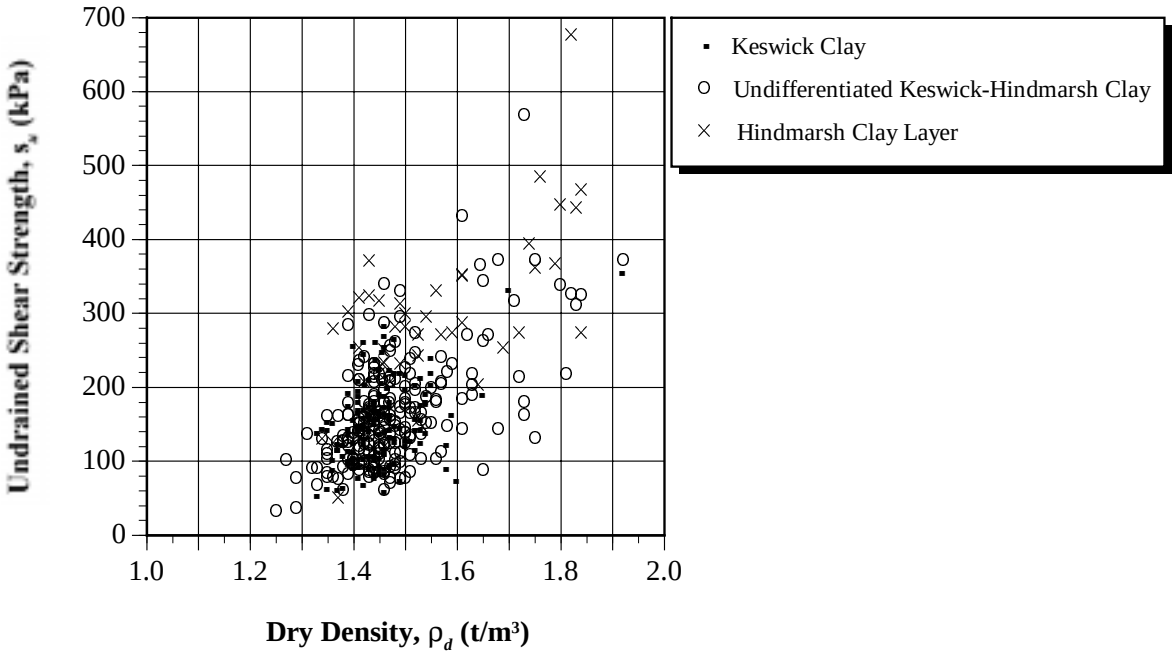

Figure 6.24 Relationship between s_u and ρ_d for the Keswick Clay, undifferentiated Keswick Clay-Hindmarsh Clay and the Hindmarsh Clay Layer obtained from the first stage of UU tests.

Figure 6.25 presents the results of the undrained shear strength of the Keswick Clay, undifferentiated Keswick Clay-Hindmarsh Clay and the Hindmarsh Clay Layer, plotted against the triaxial confining pressure, σ_3. The graph suggests, as one would expect, that, as σ_3 increases, so too does s_u. Again, however, considerable scatter is exhibited in the shear strength measurements for each of the soil layers, and it would be inappropriate to suggest any single regression line. Instead, Figure 6.25 indicates the ranges within which a UU measurement can be expected to lie.

It is often convenient to normalise s_u with respect to the overburden pressure, σ_{v0}. Figure 6.26 shows the relationship between values of s_u/σ_{v0} and depth below the ground surface. The plot confirms the observation that the Keswick Clay, as well as the undifferentiated clay soil, are overconsolidated as a result of desiccation. This is evidenced by values of s_u/σ_{v0} greater than unity close to the ground surface, and decreasing towards unity at depth. It can be seen from Figure 6.26 that, as expected, the Hindmarsh Clay Layer does not exhibit such behaviour.

Figure 6.27 shows the relationship between s_u and σ_3 for tests performed on samples from the Hindmarsh Clay Sand Member. It can be observed from this figure that a somewhat tenuous trend exists between these two parameters; that is, as σ_3 increases, so too does s_u. Particularly for a sand soil, one would expect to observe such a trend. However, the data

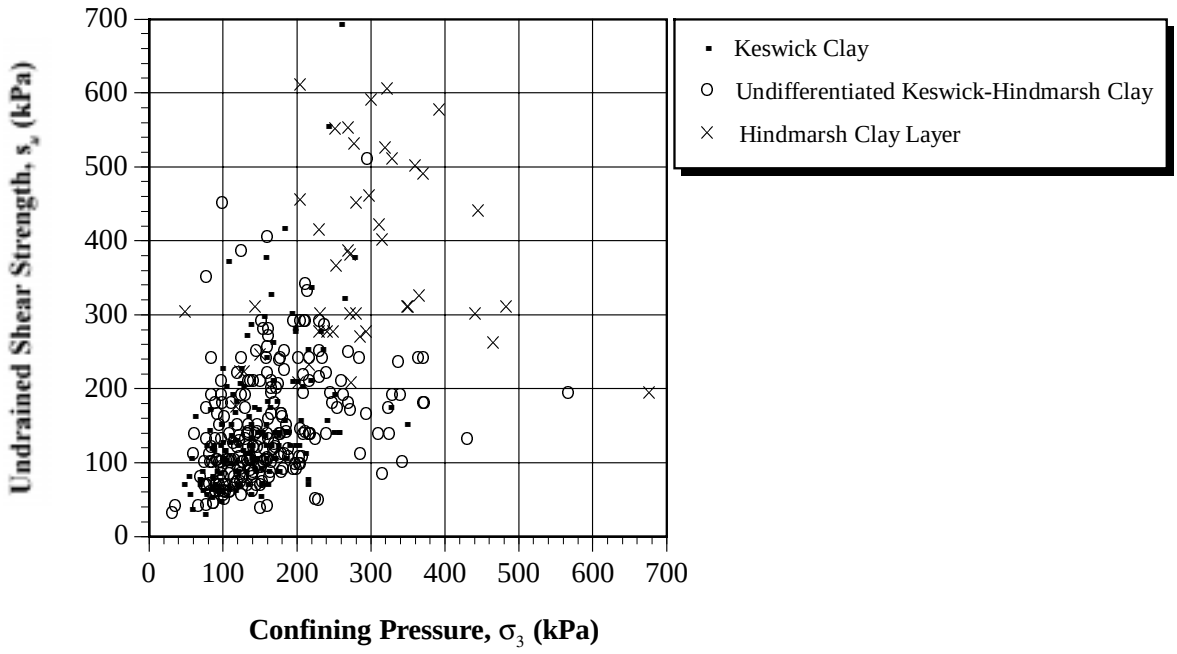

Figure 6.25 Relationship between s_u and σ_3 for the Keswick Clay, undifferentiated Keswick Clay-Hindmarsh Clay and the Hindmarsh Clay Layer obtained from the first stage of UU tests.

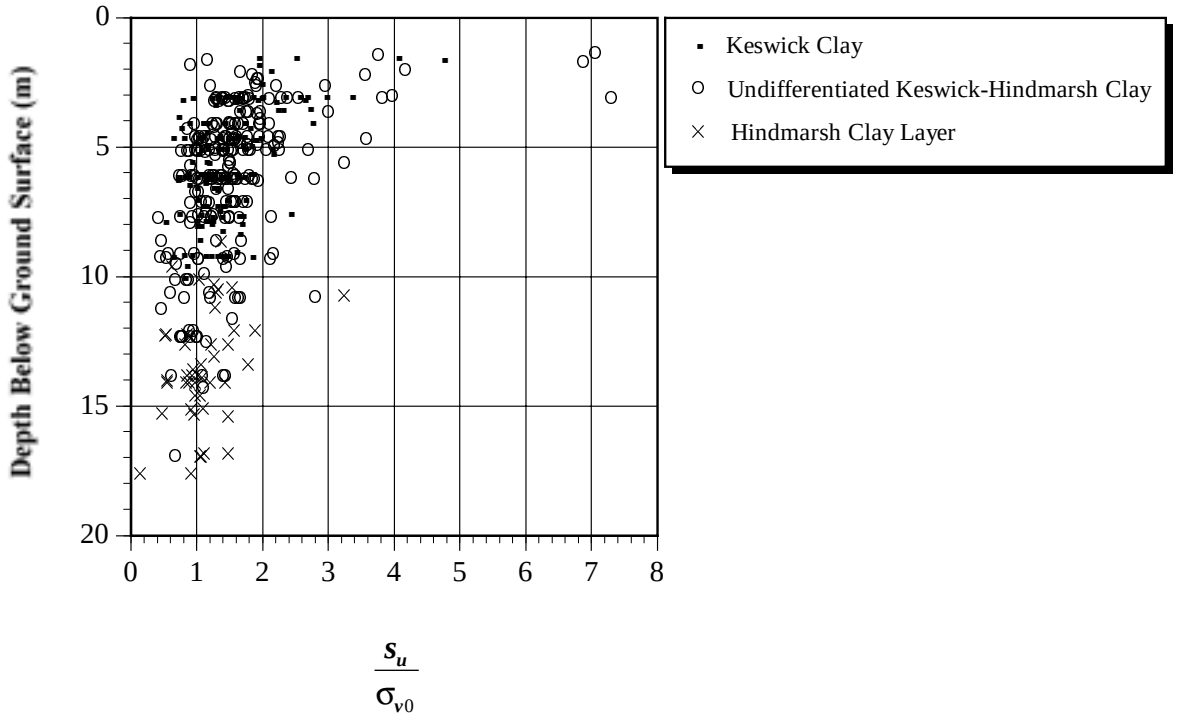

Figure 6.26 Relationship between s_u/σ_{v0} and depth below ground for the Keswick Clay, undifferentiated Keswick Clay-Hindmarsh Clay and the Hindmarsh Clay Layer obtained from the first stage of UU tests.

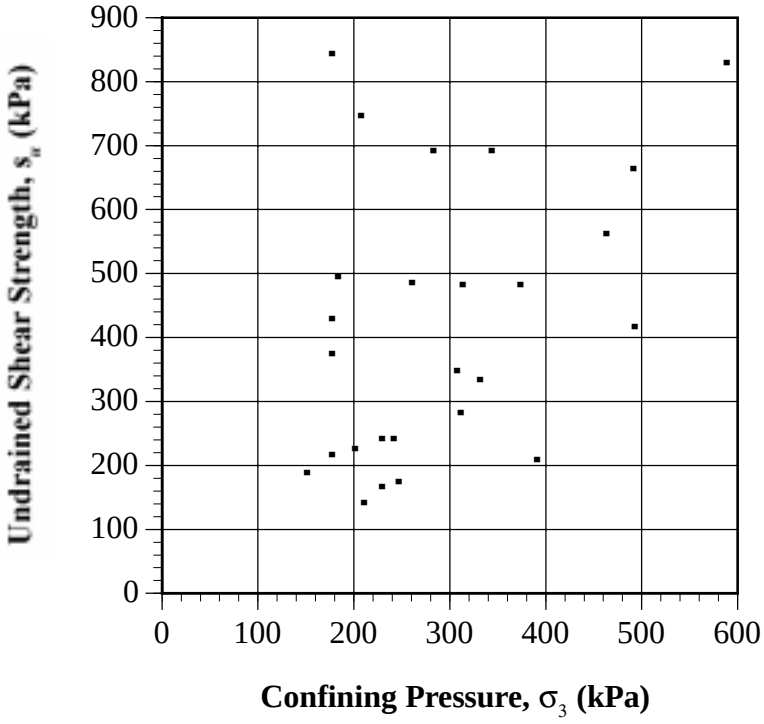

Figure 6.27 Relationship between s_u and σ_3 for the Hindmarsh Clay Sand Member obtained from up to three stages of UU tests.

set only consists of 28 tests and, as a result, it is inappropriate to draw general conclusions from this plot. The reason that so few triaxial tests have been included in the *KESWICK* data base is due to the fact that a limited number of tests have been performed on samples from the Hindmarsh Clay Sand Member. This is because the vast majority of geotechnical engineering consultants and government bodies use the standard penetration test (SPT) to measure the undrained shear strength of the sand. The results of these tests will be examined in §6.5.6.

6.5.5 Young's Modulus of Elasticity

Another very important parameter, also included in the *KESWICK* data base, is the undrained Young's modulus of elasticity, E_u. Figure 6.28 shows E_u plotted against the depth below the ground surface. Superimposed on Figure 6.28 are two lines representing $E_u = 500\gamma_w z$ and $E_u = 2000\gamma_w z$. It can be seen from this figure that E_u exhibits considerable scatter with respect to depth, and that a trend may exist, suggesting that E_u increases with depth below ground.

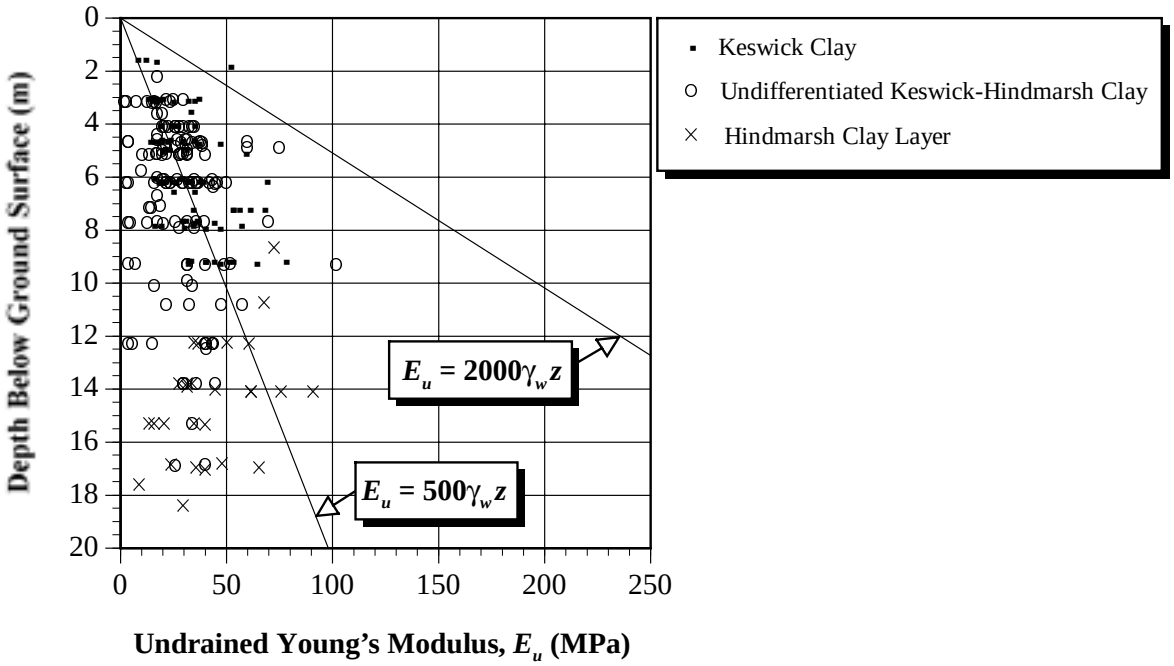

Figure 6.28 Relationship between E_u and depth below ground for the Keswick Clay, undifferentiated Keswick Clay-Hindmarsh Clay and the Hindmarsh Clay Layer obtained from the first stage of UU tests.

Table 6.4 summarises the statistics associated with the undrained Young's modulus of the various clay layers contained in the *KESWICK* data base, and Figure 6.29 shows the histograms of E_u for these clay soils. It can be seen from this table and figure that, once again, the Keswick Clay and the undifferentiated material exhibit similar properties. In addition, the Hindmarsh Clay Layer appears to be slightly stiffer than the other two soil types.

Table 6.4 Statistics associated with E_u (MPa) obtained from UU tests.

Soil Layer	No. of Data	Min.	Max.	Mean	Std. Dev.	*CV* (%)	Skew.	Kurt.
Keswick Clay	89	9	79	32.6	14.8	45.2	0.99	0.55
Undiff. Keswick Clay-Hindmarsh Clay	129	2	102	28.3	15.4	54.3	1.13	3.73
Hindmarsh Clay Layer	28	9	91	43.1	20.3	47.0	0.51	–0.25

A graph of E_u plotted against depth below the ground surface, for measurements obtained from the screw plate load test (SPLT) and the self-boring pressuremeter test (SBPT), is given in Figure 6.30. It should be noted that each of these two tests measure E_u in different directions: the SPLT measuring E_u in the vertical direction; and the SBPT measuring in the

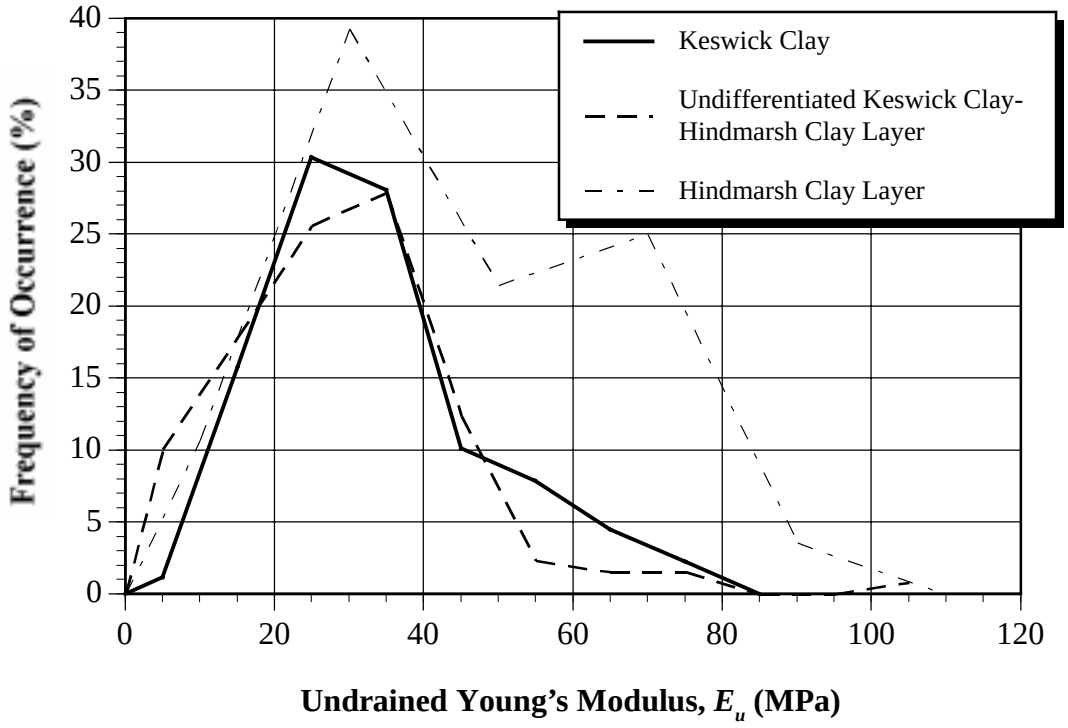

Figure 6.29 Histograms of E_u of Keswick Clay, undifferentiated Keswick-Hindmarsh Clay and the Hindmarsh Clay Layer obtained from the first stage of UU tests.

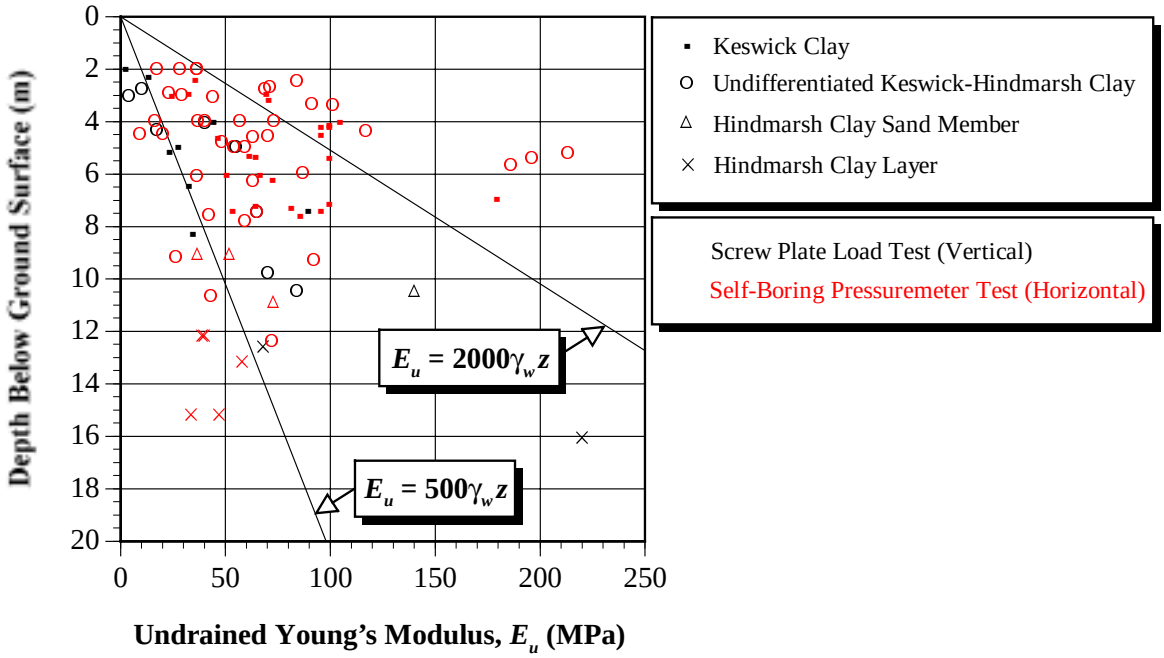

Figure 6.30 Relationship between E_u and depth below ground for the Keswick Clay, undifferentiated Keswick Clay-Hindmarsh Clay and the Hindmarsh Clay Layer obtained from a number of in situ tests.

Table 6.5 Statistics associated with E_u (MPa) obtained from SPLT and SBPTs.

Soil Layer	No. of Data	Min.	Max.	Mean	Std. Dev.	*CV* (%)	Skew.	Kurt.
Keswick Clay	32	3	180	66.6	35.9	54.9	0.74	1.70
Undiff. Keswick Clay-Hindmarsh Clay	46	4	213	61.2	45.1	73.6	1.81	3.96
Hindmarsh Clay Layer*	7	34	220	72.3	66.2	91.6	2.48	6.29

Note: * : Small number of data and, as a consequence, the statistics should be treated with caution.

horizontal direction. This is an important consideration as many clay soils exhibit anisotropic behaviour. Figure 6.30 again demonstrates that E_u displays considerable scatter with depth. However, from this figure, a more clearly defined trend of E_u increasing with depth can be observed. In addition, when compared with Figure 6.29, it can be seen from Figure 6.30 and Table 6.5 that the E_u measured using in situ tests, is somewhat larger than the E_u measured using laboratory based unconsolidated undrained triaxial tests. It is unlikely that these should differ so markedly (by as much as 115%). There are at least two possible causes for this. Either: (i) the UU tests are underestimating the 'true' E_u because of sample disturbance and initial consolidation influences (discussed previously in §4.5); or (ii) the insertion process, associated with in situ test devices, causes a consolidation of the soil resulting in an overestimate of the 'true' E_u. If either of these two errors are to be isolated, calibration studies are required, as it is impossible to distinguish between them using *KESWICK* alone.

Figure 6.31 shows the relationship between E_u, normalised with respect to σ_{v0} and depth below the ground surface. As was evident in Figure 6.26, Figure 6.31 also shows that the Keswick Clay and the undifferentiated clay are overconsolidated as a result of desiccation, since the soils near the surface are stiffer than the material at depth.

6.5.6 SPT Number

As mentioned previously, the vast majority of the strength measurements performed on the Hindmarsh Clay Sand Member have been obtained using the standard penetration test (SPT). The SPT number, *N*, is the number of blows required to drive a standard, 51 mm diameter, split-spoon sampler 300 mm into the soil, using a hammer of standard weight and drop height. If the values of *N* relating to the Hindmarsh Clay Sand Member are plotted as a function of depth below the ground surface, a relatively meaningless graph is obtained, with a considerable degree of scatter apparent. Figure 6.32, on the other hand, shows *N*

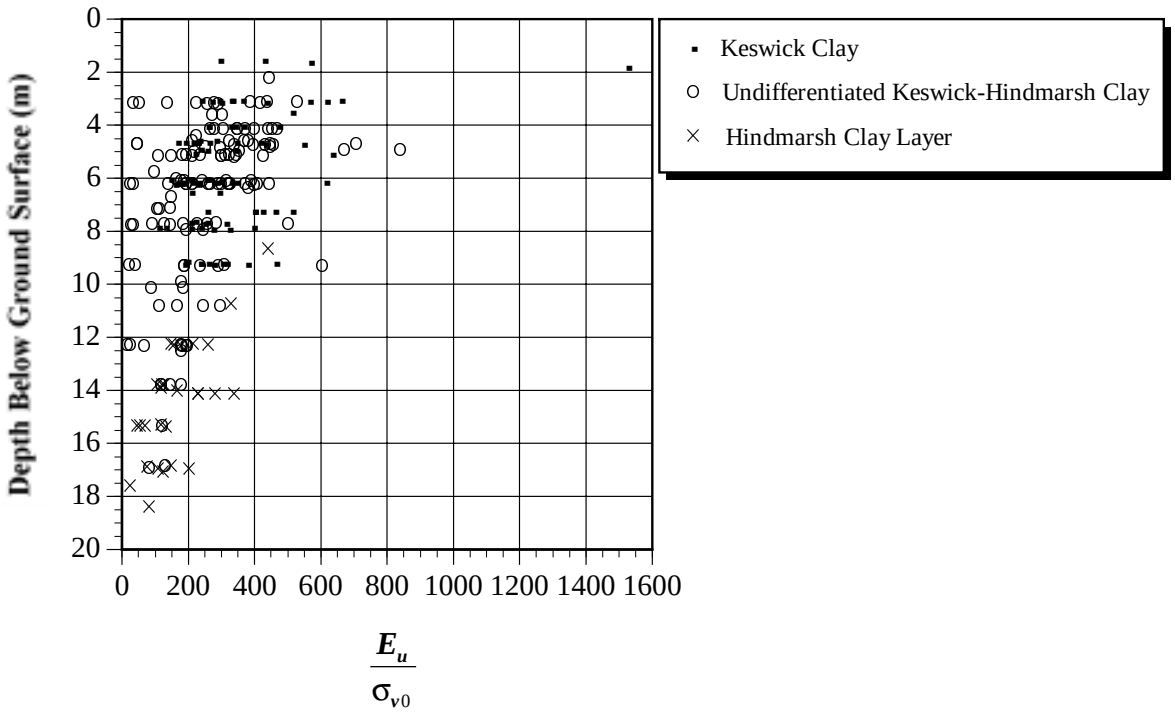

Figure 6.31 Relationship between E_u/σ_{v0} and depth below ground for the Keswick Clay, undifferentiated Keswick Clay-Hindmarsh Clay and the Hindmarsh Clay Layer obtained from up to three stages of UU tests.

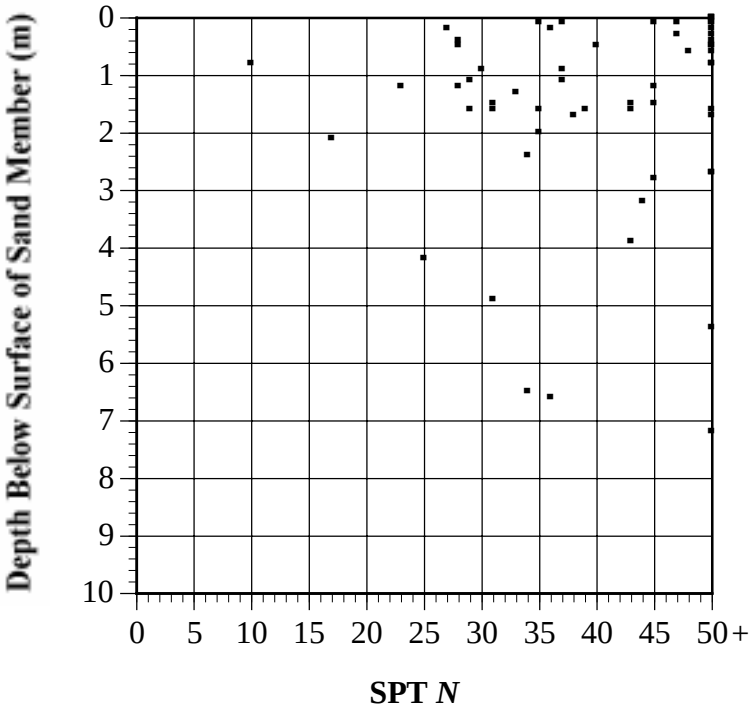

Figure 6.32 Relationship between SPT Number, *N*, measured in the Hindmarsh Clay Sand Member and the depth below the surface of this layer.

plotted as a function of depth below the surface of the Hindmarsh Clay Sand Member. While a significant degree of scatter is still evident, a trend, indicating increasing values of N with increasing depth below the surface of the Hindmarsh Clay Sand Member, can be seen. Again, it is inappropriate to suggest a line of best fit. Rather, Figure 6.32 is useful in that it provides ranges of expected values of N.

6.5.7 Soil Suction

One other geotechnical parameter that is worthy of investigation is the total soil suction, u. If one is able to establish a relationship between u and, either the moisture content, w, or the depth below ground, then it may be possible to normalise s_u with respect to this relationship. This is due to the fact that samples of soil, used to obtain measurements of s_u within *KESWICK*, were taken during different times of the year and, as a result, at different moisture contents. It was observed in Figure 6.23, and it is well established, that s_u depends greatly on w. Hence, if this effect can be removed from the s_u data, then the entire data set can be used to assess the spatial variability of the material itself. Thus, the entire s_u data set can be normalised with respect to w, implying that s_u depends on location alone and not w.

Figure 6.33 shows u, plotted with respect to w, for the clay soils contained in the *KESWICK* data base. Figure 6.34 shows u expressed as a function of depth below the ground surface for summer, autumn, winter and spring. Each of the 5 graphs exhibits considerable scatter and no appropriate relationship, or trend, can be established.

This result is not unexpected. Richards and Peter (1987) found considerable scatter between u and w and they subsequently concluded that w is not a unique variable of the soil, and that it is difficult to measure small changes in moisture content with time. In addition, the authors stated that correlations between w and s_u, and w and E_u, are generally poor unless other soil factors, such as density and clay content, are included. Similar correlations with u are often better, and are certainly never worse, than those made with w (Richards and Peter, 1987).

The next section will examine the variation of s_u with respect to location within the Adelaide city area. As a result of the preceding treatment, it is not possible to normalise the values of s_u with respect to moisture content.

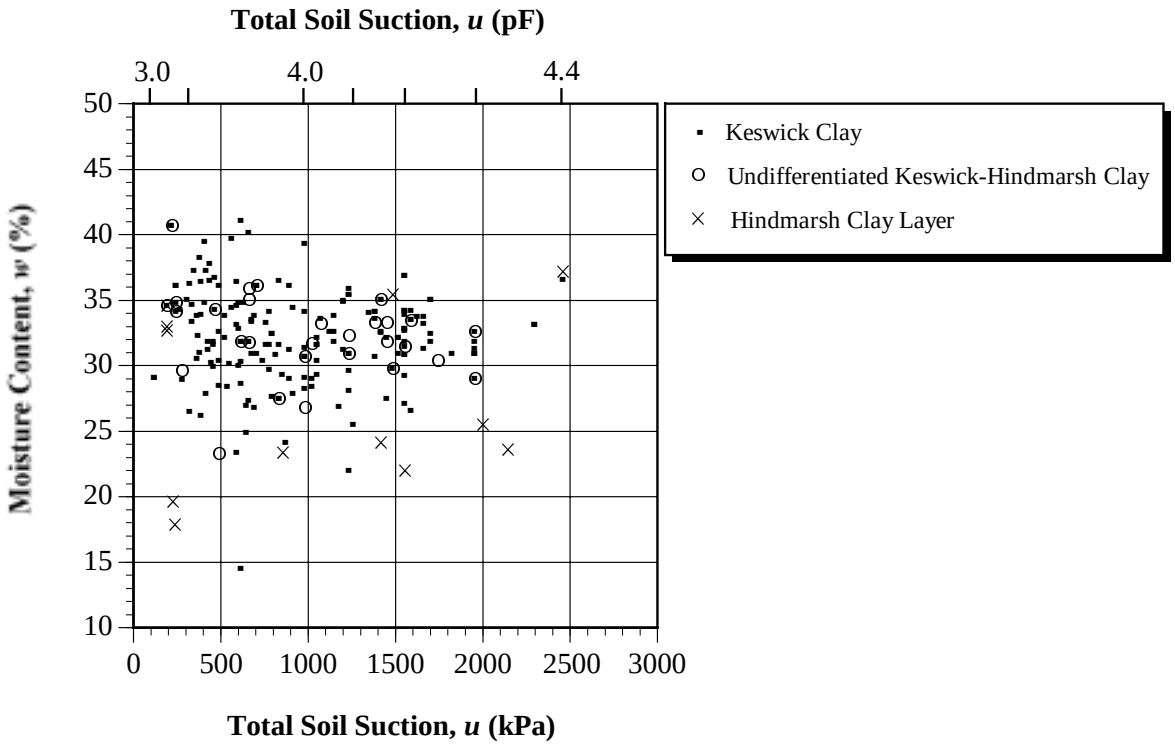

Figure 6.33 Relationship between total soil suction, *u*, and moisture content, *w*, for the Keswick Clay, undifferentiated Keswick Clay-Hindmarsh Clay and the Hindmarsh Clay Layer.

6.5.8 Contours of Undrained Shear Strength

With the large volume of s_u information contained within the *KESWICK* data base, it is possible to examine the variation of s_u across the Adelaide city area. However, as seen in the previous sections, the majority of these data relate to the Keswick Clay and the undifferentiated material. As a consequence, there are insufficient data to examine the variation of the undrained shear strength of the Hindmarsh Clay soils. In addition, the s_u data pertaining solely to Keswick Clay is relatively sparse throughout the Adelaide city area. As a result, in order to obtain sufficient data to enable a reasonably reliable spatial variability model to be generated, the s_u data pertaining to the undifferentiated Keswick Clay-Hindmarsh Clay has been combined with the Keswick Clay s_u data. This is not unreasonable, since it has been observed previously that the undifferentiated material exhibits very similar properties to those of the Keswick Clay.

As detailed in §6.4, each measurement of s_u has a three-dimensional coordinate associated with it. Hence, to fully describe the variability of s_u with regard to location, a 3D treatment of the data is required. Unfortunately, it is almost impossible to adequately display 3D information on a two-dimensional (2D) medium such as this. Perhaps the only sensible

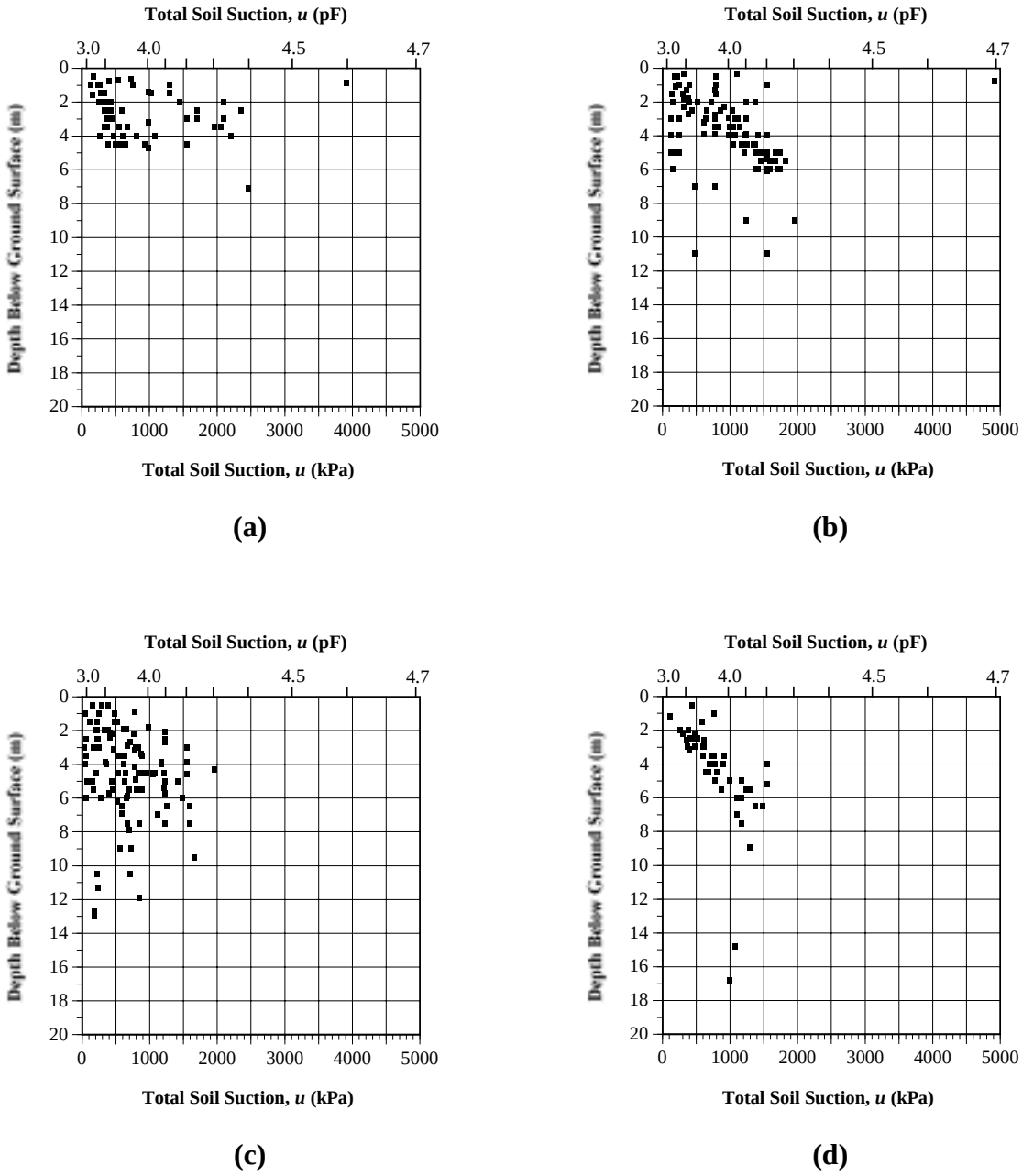

Figure 6.34 Relationship between total soil suction and depth below ground for: (a) summer; (b) autumn; (c) winter; and (d) spring.

method would be to present 2D horizontal slices at different depths throughout the soil mass. However, such a presentation is inappropriate in this case because: (i) there are insufficient data within *KESWICK*, at depth, across the Adelaide city area to provide reliable detail in 3D; and (ii) the layer depths vary dramatically from site-to-site as the result of gilgais and normal variations in stratigraphy.

As a result, and as a first attempt to visualise the variability of s_u within the Adelaide city area, the individual values of s_u will be *spatially averaged* in order to present a 2D picture of the undrained shear strength of the Keswick Clay. Consider, firstly, the general method of pile design. Initially, a geotechnical engineer would conduct a site investigation consisting of a series of vertical boreholes, including a programme of laboratory and/or in situ testing. From each borehole, a series of 'point' estimates of s_u would be obtained from the testing programme. The pile would then be designed using an average of the 'point' estimates of s_u for the borehole relevant to the pile under consideration. In this way, the depth dependent parameter s_u is 'averaged' with respect to depth, essentially along a vertical line, and a 2D point estimate for s_u is established. Figure 6.35 is a representation of such a 'vertical averaging' process.

An alternative, though similar approach, is to adopt the averaging process used in the design of raft or mat foundations. Since the raft is founded on a large volume of soil, bearing capacity failure, or settlement, requires much of the underlying soil to be mobilised. Hence, the geotechnical engineer will often spatially average the test data beneath the entire raft foundation. As a result, an average s_u is obtained for the 'block' of soil within the site, whose dimensions are the plan area of the raft (often the entire plan area of the site) by the depth of the soil affected by the imposed stresses. Figure 6.36 is a representation of such a 'site averaging' process and was generated by averaging the measured values s_u over the whole site.

Figures 6.35 and 6.36 are very similar, as one would expect; the latter being a slightly 'smoother' version of the former, as a consequence of the site averaging process. Again, values outside the Adelaide city area should be disregarded, or treated with caution, as no values of s_u have been measured outside of this region.

Contour maps, such as Figures 6.35 and 6.36, can provide useful tools for the preliminary estimation of values of s_u for a site within the Adelaide city area. However, Figures 6.35 and 6.36 are an over-simplification of the 'true' variation of s_u across this region. A number of factors combine to increase the uncertainty associated with the models represented in Figures 6.35 and 6.36. Some of these factors are listed below.

- The s_u data set is a combination of Keswick Clay and undifferentiated material and, while it has been seen that the properties and relationships of the undifferentiated clay are very similar to those of the Keswick Clay, some of the data undoubtedly include measurements of samples from the Hindmarsh Clay Formation.

- The variability associated with moisture content, as a function of time, has not been

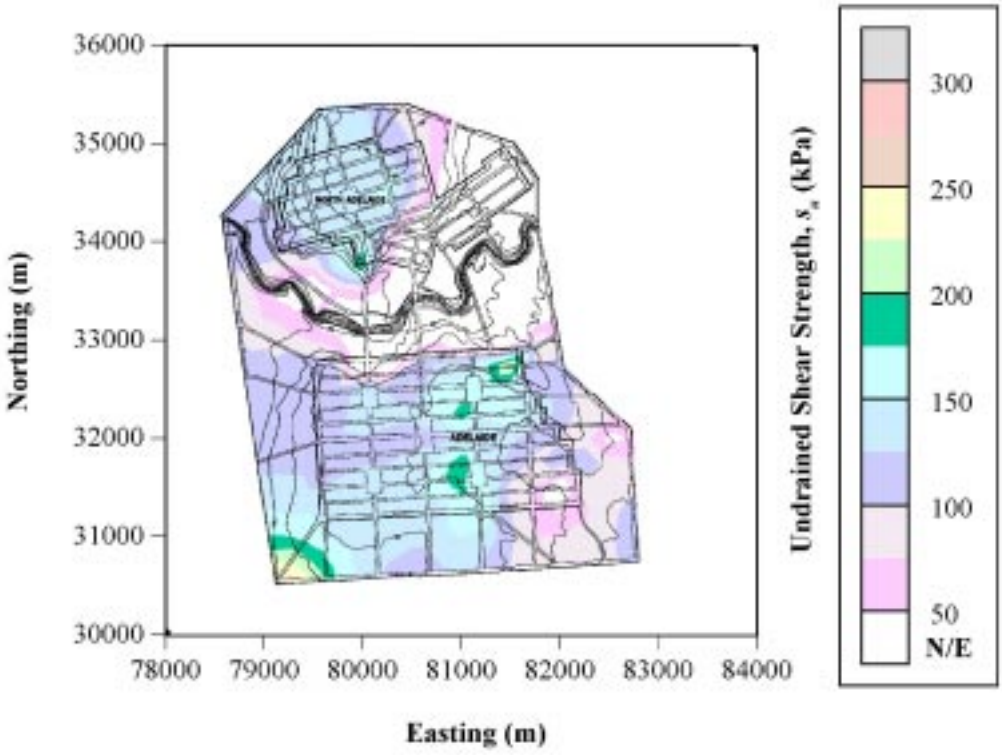

Figure 6.35 Contours of s_u for Keswick Clay based on the results of unconsolidated undrained triaxial tests using an averaging process based on pile design.

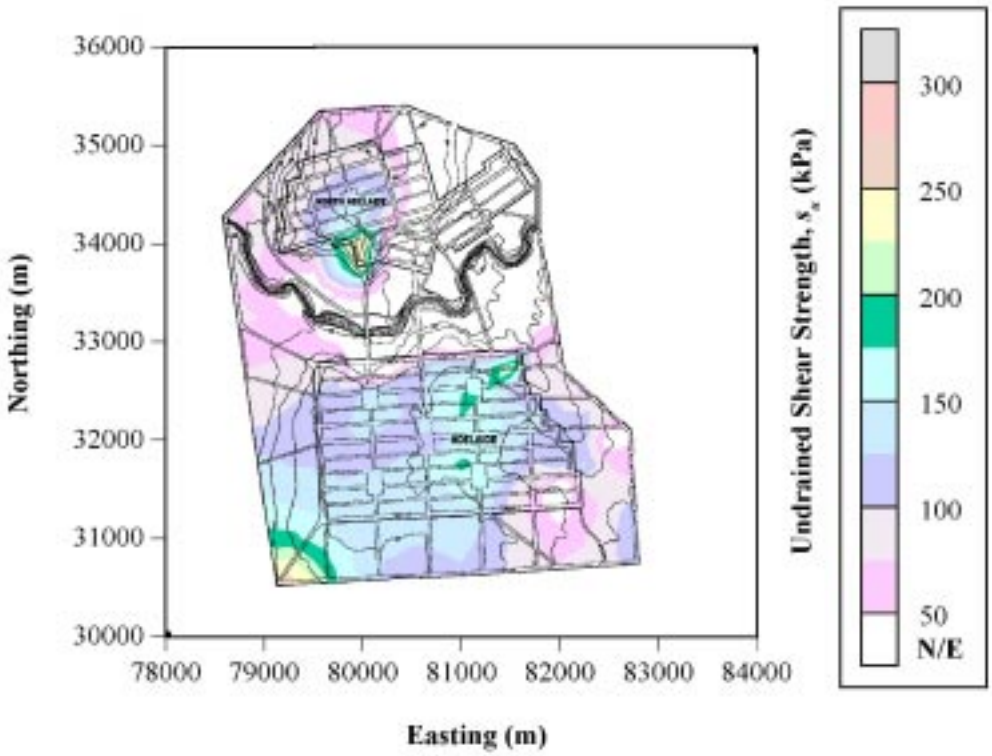

Figure 6.36 Contours of s_u for Keswick Clay based on the results of unconsolidated undrained triaxial tests using an averaging process based on raft design.

INTENTIONALLY BLANK

accounted for in the model. It has been seen previously in §6.6.5.7, that no relationship between *w* and *u*, or *u* and depth, has been able to be established and, therefore, it was not possible to remove the moisture variability from the recorded values of s_u. Consequently, any spatial description of these data will not only represent spatial variability, but will also include an uncertainty associated with moisture content and time.

- An uncertainty often overlooked by researchers who advocate the use of data bases, is the uncertainty associated with the data themselves. Since the data are obtained from several sources disassociated with the individual collating the data, there can be no guarantee that the data are accurate and that proper testing and sampling procedures were used in measuring the parameters. In addition, this measurement error varies between technicians and between testing authorities. So, not only is the uncertainty associated with the data unknown, it also varies from point to point. This is a significant and often understated limitation of using data collected from external sources.

- The contouring process, itself, increases the uncertainty. In order to obtain the contours expressed in Figures 6.35 and 6.36, the contouring algorithm first requires a regularly spaced grid of s_u values. As the data within *KESWICK* are irregularly spaced, the contouring package must interpolate between neighbouring points in order to generate this regularly spaced data set. This results in a further smoothing of an already spatially averaged data set. Figures 6.35 and 6.36 were generated using the *inverse distance squared technique*, a relatively low-level procedure which weights the neighbouring values according to the inverse of the squared distance to the point being estimated. The inverse distance squared estimation procedure, as well as other estimation regimes, are examined in the following chapter.

- In addition, as with any idealisation, the model is only as good as the data on which it is based. Where no values of s_u have been measured, the contouring process interpolates between neighbouring points which may be separated by large distances, thus introducing a further inaccuracy.

- Local perturbations, which include gilgais and structural defects, such as joints and fissures, can also further increase the uncertainty associated with the value of s_u obtained at any particular point.

6.6 SUMMARY

From the treatment given in the previous sections, it has been seen that data bases are useful tools for examining the relationships and trends that may exist between various geotechnical parameters. By obtaining data from third parties, one is able to acquire a large body of information that, if it were to be sampled and tested by a single research body, would involve a significant commitment of resources, labour and time. The relationships and trends can be used by the engineering community as a cost-efficient method for the estimation of parameters, necessary for preliminary geotechnical engineering design. In addition, individual test results can be checked against these correlations and trends, to assess whether the measurements lie within the expected ranges. If not, the data base can act as a catalyst for the geotechnical engineer to seek explanations for the reasons why the results fall outside these expected limits.

Furthermore, data bases provide an archive for the retrieval of information from nearby boreholes, which can assist in the design of site investigations in the event of a proposed development within the vicinity of these boreholes. In addition, such a data base need not be a closed source of information. Rather, as more data become available, the data base can incorporate this additional information. In this way, the archive is continually evolving and, hence, providing a better representation of the 'true' nature of the subsurface conditions, within the region specific to the data base.

It has been shown, however, that the *KESWICK* data base, on its own, is an inadequate facility for expressing the variation of the undrained shear strength of the Keswick and Hindmarsh Clays, across the Adelaide city area. For it to provide data sufficient to enable a reliable and accurate model of this spatial variability, a far greater volume of data is required.

While Figures 6.35 and 6.36 are a crude, first attempt at modelling the spatial variability of s_u of the Keswick and Hindmarsh Clays, they provide a mechanism for the estimation of depth averaged and site averaged, values of s_u, respectively. The following chapter combines the spatial variability models derived in Chapter 5, with the data described in this chapter, in order to generate a framework for estimating the undrained shear strength of the Keswick Clay at yet untested locations.

Chapter Seven

Examination of the Large-Scale Lateral Spatial Variability of the Keswick Clay

7.1 INTRODUCTION

In Chapter 5 it was shown that the small-scale lateral spatial variability of the undrained shear strength of the Keswick Clay was characterised by a nested structure, which could be conveniently modelled by the addition of two spherical semivariograms, whose ranges are equal to 0.2 and 6 metres, respectively. This nested structure was determined by examining CPT data obtained from the South Parklands and Keswick sites, which consisted of measurements obtained over a maximum lateral extent of 50 metres. This chapter examines the large-scale spatial variability of the Keswick Clay, using data contained within the *KESWICK* data base and which extends across the Adelaide city area, as detailed in the previous chapter.

7.2 INPUT DATA AND TRANSFORMATIONS

In order to assess the large-scale spatial variability of the undrained shear strength of the Keswick Clay, measurements of s_u contained within the *KESWICK* data base were used. As was described in the previous chapter, the *KESWICK* data base contains measurements of s_u from several different laboratory and in situ test methods. In order to assess spatial variability, it is essential to eliminate as many alternative sources of variability as possible. As a consequence, only measurements of s_u obtained from unconsolidated undrained triaxial (UU) tests were used to assess the spatial variability of the undrained shear strength of the Keswick Clay. It was shown in Chapter 4 that measurements of s_u obtained from UU tests are far from ideal and are dependent on a number of factors which include: sample disturbance; initial consolidation; strength anisotropy; and testing strain rate.

Unconsolidated undrained triaxial test results were used, rather than those obtained from other more reliable test procedures, because the majority of measurements of s_u, contained within the *KESWICK* data base, were derived from UU tests. In fact, the *KESWICK* data base contains too few s_u measurements obtained from any other test method to allow a reliable spatial variability model to be derived.

The measurements of s_u obtained from UU tests contain greater uncertainty than measurements obtained from other shear strength testing procedures. Furthermore, the s_u data, within the *KESWICK* data base, were obtained from several geotechnical engineering practices and laboratories using different sample preparation and testing procedures, equipment and operators. Hence, the s_u data used to derive the large-scale spatial variability model, the treatment of which is given below, contain uncertainties which are far from trivial. As a consequence, the derived large-scale spatial variability model will also contain significant and unquantifiable uncertainties. This needs to be borne in mind when comparing the results of the large-scale model with those of the small-scale model, detailed previously in Chapter 5. Nevertheless, the analyses presented in this chapter demonstrate the usefulness of geostatistics and its application to the spatial variability of soils and rock.

As indicated in Chapter 6, the total number of measurements of s_u, within the *KESWICK* data base and obtained from UU tests, is 150 for Keswick Clay and 229 for undifferentiated Keswick Clay-Hindmarsh Clay. It was also demonstrated that the undifferentiated Keswick Clay-Hindmarsh Clay exhibits similar properties to those of the Keswick Clay and, hence, may be regarded as being equivalent to Keswick Clay. It is evident from the number of s_u measurements that there is an insufficient quantity of data to allow reliable 3D modelling of the individual Keswick Clay, or undifferentiated data sets, or even a data set obtained from a combination of the two. However, in order to generate a series of 'pseudo-3D' data sets, which are similar in nature to the lateral data sets analysed in Chapter 5, the following procedure was followed:

- The measurements of s_u for Keswick Clay and undifferentiated Keswick Clay-Hindmarsh Clay were combined into a single data set.

- The data were then separated into 3 data sets, depending on the depth ranges below the surface of the Keswick Clay from which the samples used to measure s_u were obtained: from 0 to 3 metres; 3 to 6 metres; or greater than 6 metres. At this stage, each data set contained 4 columns of data, that is: Easting (m); Northing (m); depth below surface of Keswick Clay (m); and the measured undrained shear strength, s_u (kPa), from UU tests.

- Each of the 3 data sets contained the results of several boreholes distributed throughout the Adelaide city area, with each borehole containing one or more UU measurements at variable sample intervals. The s_u results for each borehole were then averaged in order to yield a single estimate of s_u for each borehole location. As a consequence, the resulting data sets contained 3 columns of information: Easting (m); Northing (m); and a 'spatially averaged' undrained shear strength, $\bar{s}_u$ (kPa).

The subsequent *0 to 3 metre* data set consisted of 143 estimates of $\bar{s}_u$; the *3 to 6 metre* data set consisted of 94 estimates of $\bar{s}_u$; and the *greater than 6 metre* data set consisted of 57 estimates of $\bar{s}_u$. Too few data were contained in the *greater than 6 metre* data set to allow reliable spatial variability modelling to be performed. Preliminary analyses performed on the *3 to 6 metre* data set indicated that it, also, contained too few measurements to allow reliable spatial variability modelling to be undertaken. As a consequence, only the *0 to 3 metre* data set provided a sufficient number of measurements of s_u to allow spatial variability modelling to proceed. Hence, the analyses which follow are based solely on observations of $\bar{s}_u$ obtained from within 0 to 3 metres below the surface of the Keswick Clay. The locations of these data are shown in Figure 7.1.

Prior to performing geostatistical analyses on these data, it is necessary to remove trends which result in non-stationarity, as mentioned previously. There appears to be no test to assess the stationarity of data in three dimensions, other than by eyeballing the scatterplot. Kulatilake (1989) fitted various 3D polynomial trends and estimated their degree of fit; that is the *multiple* r^2, in order to ascertain whether the trend was significant or not. Once having removed the trend, Kulatilake (1989) eyeballed the residuals and qualitatively assessed their stationarity.

In order to fit a 3D polynomial trend to the *0 to 3 metre* data set, the software package *S-PLUS for Windows*®[31] was used. *S-PLUS for Windows* is a PC-based, graphical and statistical data analysis system, and object-oriented programming language, that provides the user with a wide range of statistical functions. In Chapter 5, it was observed that, in general, removal of a second-order polynomial trend (quadratic) was sufficient to achieve stationarity. Therefore, in order to maintain some mathematical consistency between the small-scale spatial variability analyses and the large-scale analyses, a second-degree polynomial trend was fitted to the data; the resulting trend is expressed in Equation (7.1) and shown graphically in Figure 7.2.

[31] *S-PLUS* is a registered trademark of MathSoft Inc., Seattle, Washington.

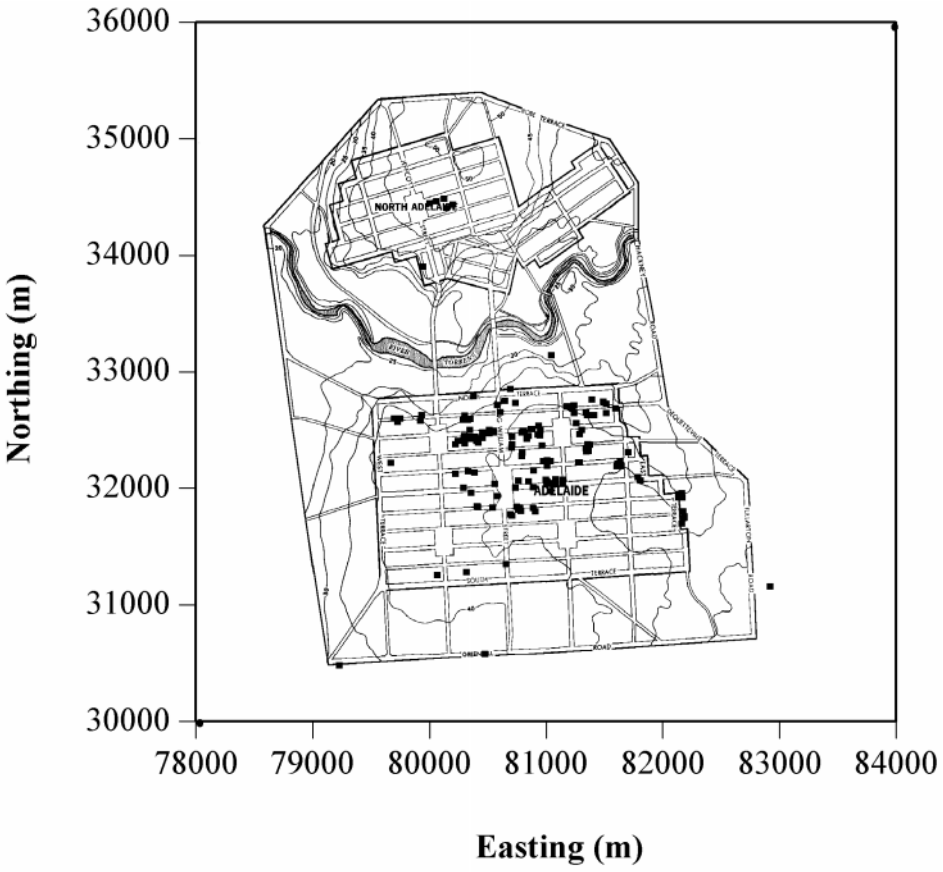

Figure 7.1 Locations of the spatially averaged s_u observations from the *0 to 3 metre* data set used in the large-scale spatial variability analyses.

$$\bar{s}_u = -12.264\times10^{-6}E^2 + 16.693\times10^{-6}N^2 + 2.149E - 0.708N - 4.509\times10^{-6}E.N - 76211.69 \quad (7.1)$$

where: E is the Easting (m);
N is the Northing (m).

Regression analyses, performed by *S-PLUS for Windows*, indicated that the second-degree polynomial trend possessed a multiple r^2, that is, a goodness of fit, equal to 0.151; by no means a significant trend. While it is possible to remove trends of higher order, such trend removal is not warranted due to the relatively limited number of available data. As a consequence, while the second-degree polynomial trend is not significant, and its presence is unlikely to result in significant non-stationarity of the data set, it will be removed in order to maintain some consistency with the lateral spatial variability models developed in Chapter 5. In fact, it will be seen later, that this second-order trend has little influence on the resulting estimates obtained from kriging. The following section describes the development of a geostatistical model, that is a semivariogram, which expresses the spatial variability of the undrained shear strength of the Keswick Clay.

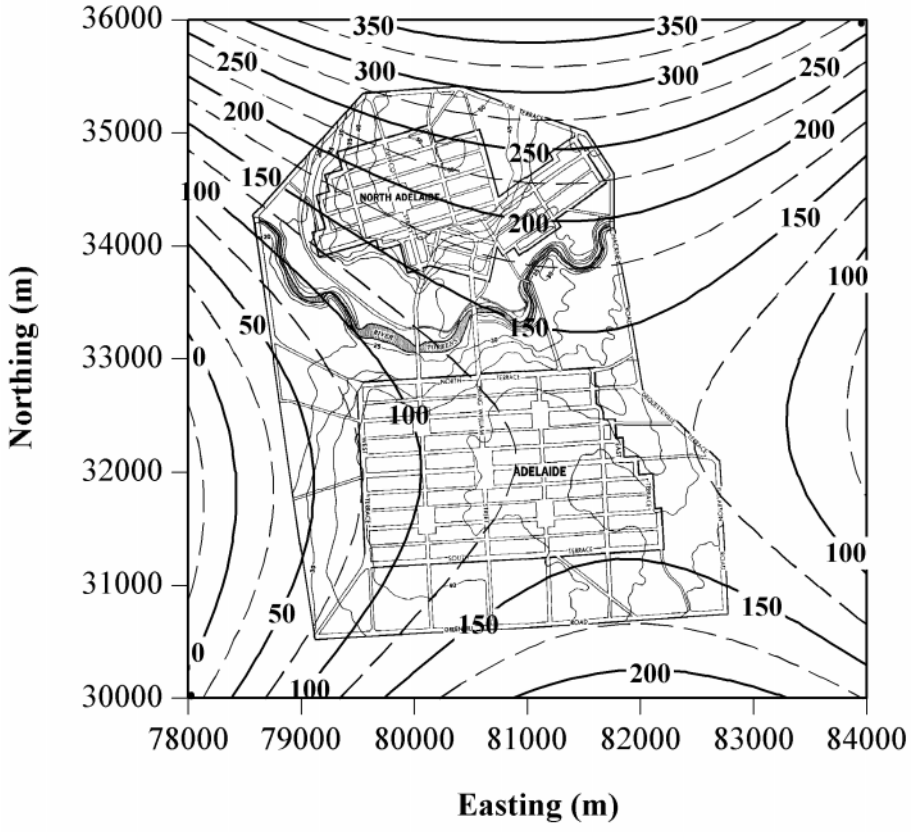

Figure 7.2 Second-degree polynomial trend surface of s_u (kPa) obtained by least squares regression of the *0 to 3 metre* data set using *S-PLUS for Windows*.

7.3 GEOSTATISTICAL MODEL

In order to determine the 2D semivariogram of the detrended data set, the *GEO-EAS* package (Englund and Sparks, 1988) was used, because of its excellent graphical interface and post-processing facilities. Firstly, as suggested by Englund and Sparks (1988), the data were entered into the pre-processing program, *PreVar*, which generates a *pair comparison file* which allows the semivariogram to be calculated more efficiently. The semivariogram was then obtained by entering the pair comparison file into the program, *Vario*, which uses the convention shown in Figure 7.3 to calculate the semivariogram.

Firstly, in order to ascertain whether the undrained shear strength of the Keswick Clay exhibits anisotropic behaviour, the North-South and East-West experimental semivariograms were calculated. These were obtained by means of *Vario* by: setting the direction angle to 0° and the tolerance angle to 22.5°, in order to generate a North-South experimental semivariogram; and the direction angle to 90° and the tolerance angle to 22.5°, to obtain an East-West semivariogram. These are each shown in Figure 7.4, and the

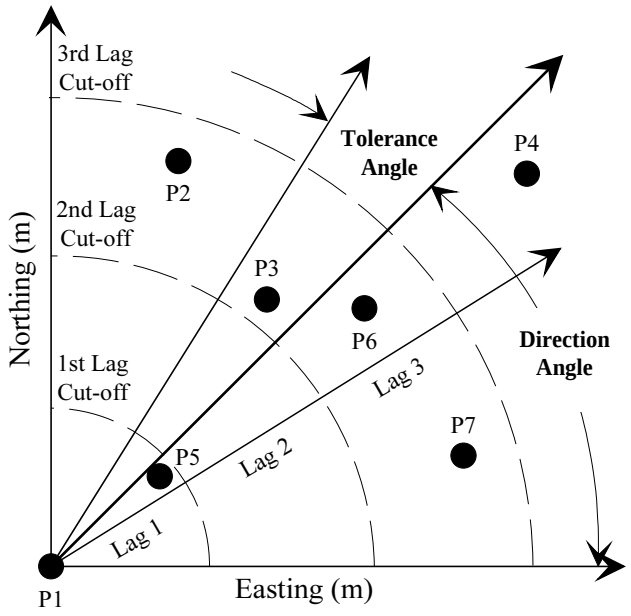

Figure 7.3 Convention used by *Vario* to calculate the semivariogram.
(Pairs P1 and P5 are included in the computation for Lag 1 whereas pairs P1 and P3, and P1 and P6 are included in the computation for Lag 3).
(After Englund and Sparks, 1988).

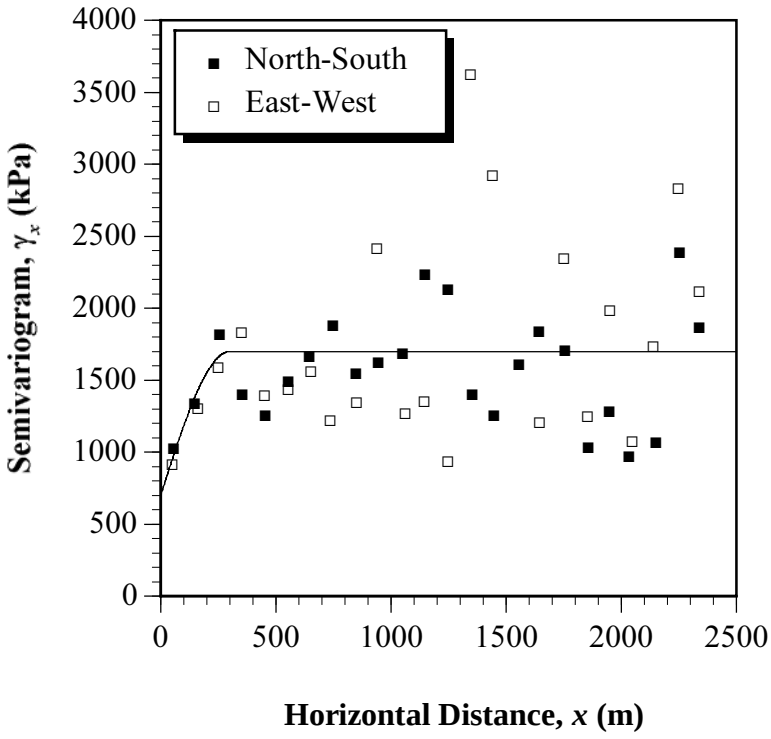

Figure 7.4 North-South and East-West experimental semivariograms, with associated spherical model, of the detrended *0 to 3 metre* data set.

number of pairs associated with the computation of these semivariograms are given in Figure 7.5. Superimposed on the experimental semivariograms in Figure 7.4 is an appropriate spherical model, which is expressed in the following equation:

$$\gamma_x = 1000\left(\frac{3x}{2a} - \frac{x^3}{2a^3}\right) + 700 \qquad \text{when } x \le a$$
$$\gamma_x = 1700 \qquad \text{when } x \ge a \tag{7.2}$$

where: a = 300 metres.

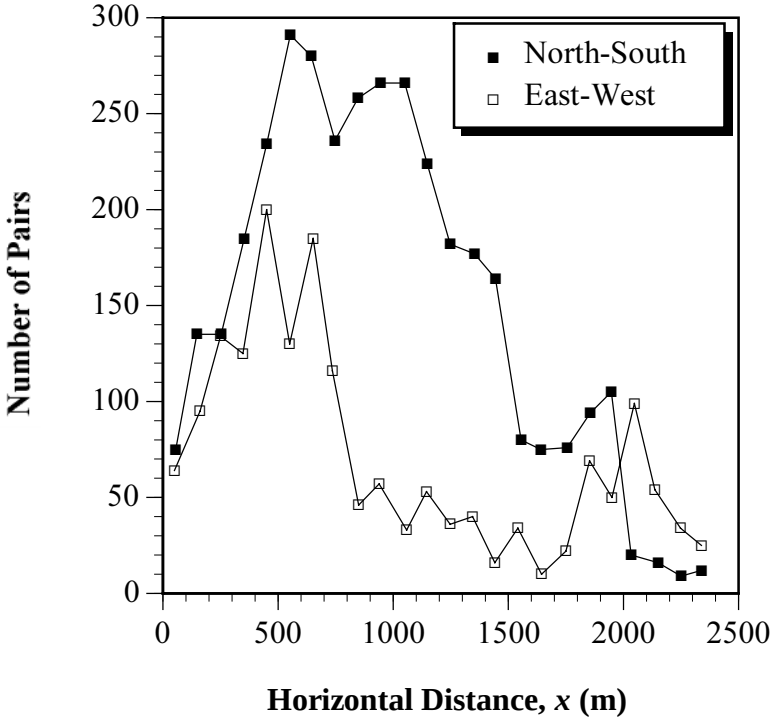

Figure 7.5 Number of pairs associated with the North-South and East-West experimental semivariograms of the detrended *0 to 3 metre* data set.

It can be clearly seen in Figure 7.4, that considerable scatter is associated with both the North-South and the East-West experimental semivariograms. In addition, the scatter associated with the East-West semivariogram is greater than that associated with the North-South semivariogram. It is likely that this scatter can be attributed, to some extent, to the number of pairs associated with the computation of each experimental semivariogram, as shown in Figure 7.5. For example, for the East-West semivariogram, the number of pairs used at separation distances beyond approximately 800 metres, is quite low; generally less than 50. In addition, as is evident from Figure 7.4, the semivariogram values associated with these separation distances vary considerably. Furthermore, the

North-South and East-West semivariograms indicate that there appears to be no evidence to suggest that the variability is different from one direction to the other. On the contrary, it appears reasonable to assume that the large-scale spatial variability of the undrained shear strength of the Keswick Clay is isotropic.

By setting the direction angle to 0° and the tolerance angle to 90°, *Vario* was used to generate an *omnidirectional* semivariogram. That is, an isotropic model which includes all data pairs regardless of their direction, and which Englund and Sparks (1988) suggested, provides the 'best' or 'smoothest' semivariogram. The resulting omnidirectional experimental semivariogram, generated from the detrended *0 to 3 metre* data set, is shown in Figure 7.6, in addition to the same spherical model used to describe the North-South and East-West semivariograms, as given previously in Equation (7.2). Figure 7.7 shows the number of pairs associated with the omnidirectional experimental semivariogram. It should be noted that the distances given by *Vario*, represented by x in this case, are the *average* distances separating the pairs in each lag interval.

It is evident from Figure 7.6, that the omnidirectional semivariogram exhibits less scatter than the North-South or East-West semivariograms, as expected. In addition, the spherical model adequately represents the experimental semivariogram. However, beyond a distance

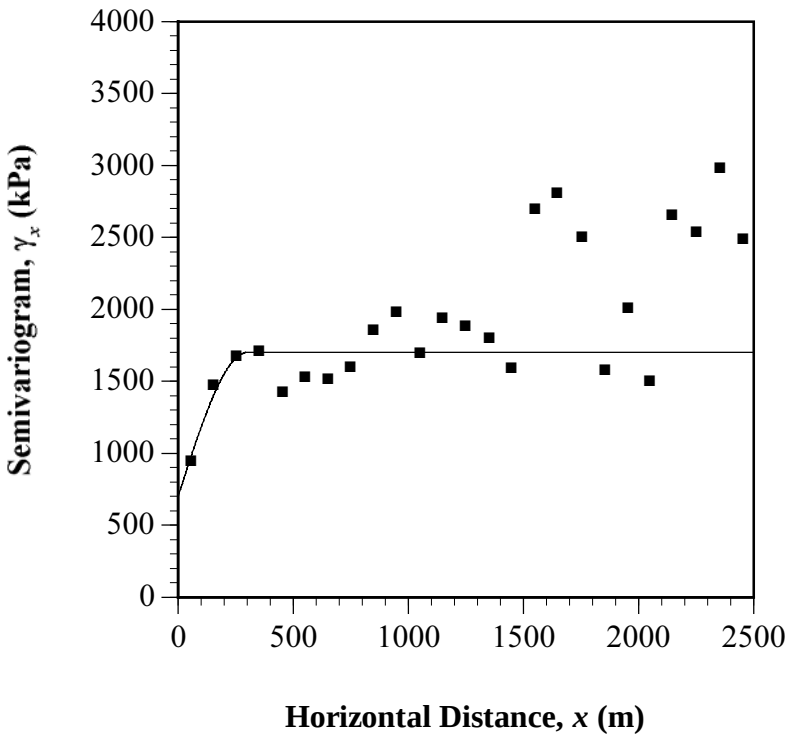

Figure 7.6 Omnidirectional experimental semivariogram, with associated spherical model, of the detrended *0 to 3 metre* data set.

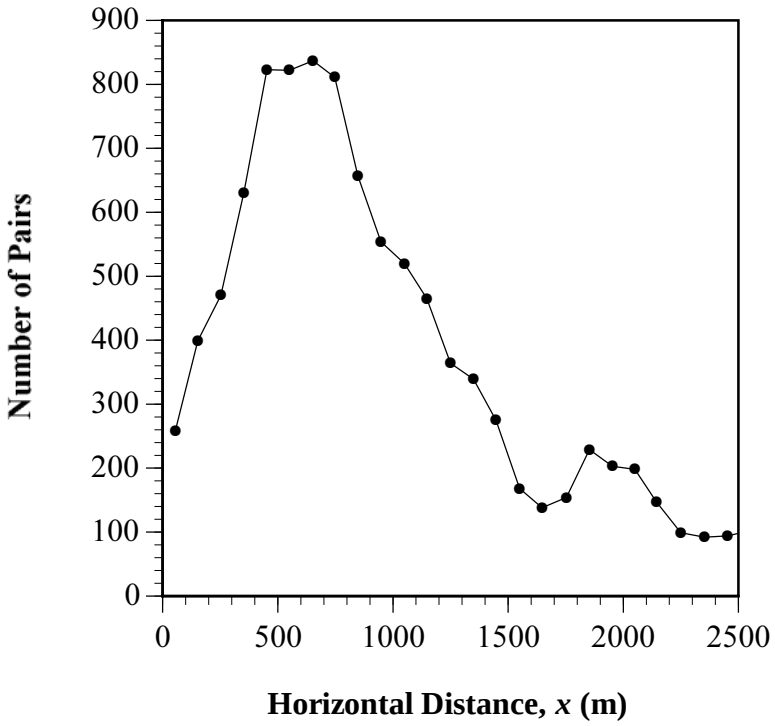

Figure 7.7 Number of pairs associated with the omnidirectional experimental semivariogram of the detrended *0 to 3 metre* data set.

of approximately 1,500 metres, there is greater divergence between the model and the experimental semivariogram. Examination of the number of pairs associated with the calculation of the omnidirectional experimental semivariogram, as shown in Figure 7.7, indicates that far fewer pairs are associated with distances greater than 1,500 metres. Hence, the uncertainty associated with the semivariogram values at these distances is somewhat greater than with the values at distances less than 1,500 metres. As a result, more importance should be given to these semivariogram values. While it can be argued that uncertainty exists with the level of the sill, it is apparent from Figure 7.6 that a greater level of confidence is associated with the nugget, C_0, of 700 kPa^2 and the range, a, of 300 metres.

At this stage, it is possible to amalgamate the small-scale nested model, given in Chapter 5, with the large-scale model, expressed in Equation (7.2), in order to generate a single function which describes the spatial variability of the undrained shear strength of the Keswick Clay. Figure 7.8 shows the large-scale model semivariogram relative to the two small-scale models, detailed previously in Chapter 5. Combining these three models yields the expression given in Equation (7.3), which is shown graphically in Figure 7.9.

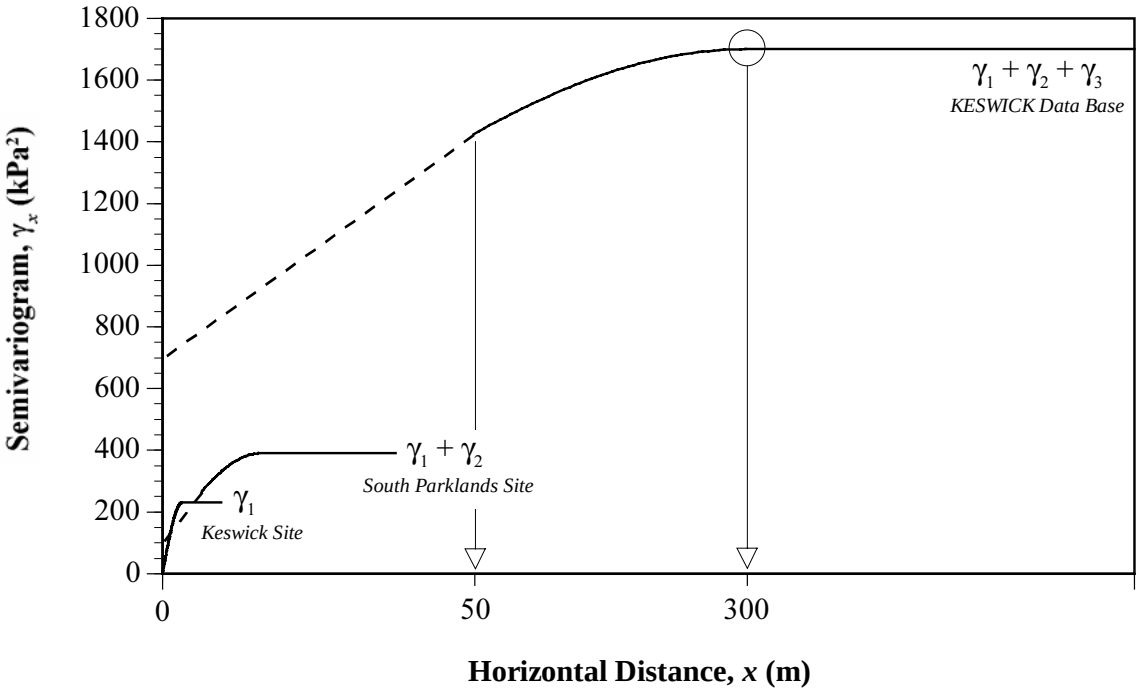

Figure 7.8 The three semivariogram models which describe the spatial variability of the undrained shear strength of the Keswick Clay.

(Note: x-axis is not drawn to scale).

$$\gamma_x = 0 + 230\left(\frac{3x}{2a_1} - \frac{x^3}{2a_1^3}\right) + 160\left(\frac{3x}{2a_2} - \frac{x^3}{2a_2^3}\right) + 1310\left(\frac{3x}{2a_3} - \frac{x^3}{2a_3^3}\right) \quad \text{when } x \le 0.2$$

$$\gamma_x = 230 + 160\left(\frac{3x}{2a_2} - \frac{x^3}{2a_2^3}\right) + 1310\left(\frac{3x}{2a_3} - \frac{x^3}{2a_3^3}\right) \quad \text{when } 0.2 \le x \le 6 \qquad (7.3)$$

$$\gamma_x = 390 + 1310\left(\frac{3x}{2a_3} - \frac{x^3}{2a_3^3}\right) \quad \text{when } 300 \le x \le 6$$

$$\gamma_x = 1700 \quad \text{when } x \ge 300$$

where: a_1 = 0.2 metres;
a_2 = 6 metres;
a_3 = 300 metres.

While the function shown in Equation (7.3) is an appropriate representation of the spatial variability of the undrained shear strength of the Keswick Clay, it must be emphasised that the accuracy associated with the small-scale model is quite different to that of the large-scale model. The small-scale study was conducted under very controlled conditions; that is, using consistent apparatus, procedures and operators, as well as under consistent climatic conditions. The large-scale model, on the other hand, was based on data obtained from several and diverse sources, which invariably employed different sampling, testing

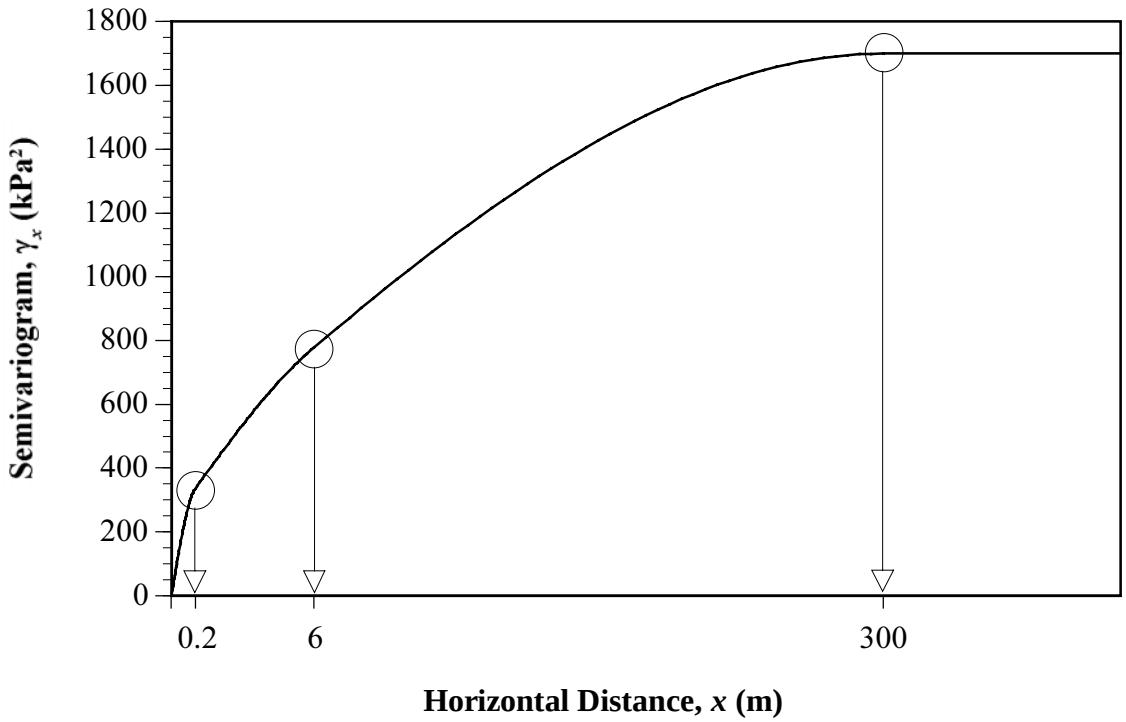

Figure 7.9 Nested model semivariogram of the spatial variability of the undrained shear strength of the Keswick Clay.
(Note: x-axis is not drawn to scale).

and reporting procedures; all of which contribute to the inaccuracy of the model. In addition, the large-scale variability was assessed using a great deal less data than those employed in the small-scale model. Hence, these effects combined, result in the uncertainty of the large-scale model being far greater than that associated with the small-scale model. This increased uncertainty is manifested by the difference between the sill of the $\gamma_1 + \gamma_2$ structure (i.e. $C + C_0 = 390$ kPa^2) and the nugget effect of the $\gamma_1 + \gamma_2 + \gamma_3$ structure (i.e. $C_0 = 700$ kPa^2). While this is not ideal, it is unfortunately an inevitable part of this study, which could only be altered if the large-scale model were based on consistent, more reliable, and more numerous data. As argued previously, such a notion would require a significant commitment of resources and labour well beyond the scope of this study, and it is questionable whether the outlay of such resources could ever be justified.

The following section makes use of the nested spatial variability model, expressed in Equation (7.3), to assess its suitability, and which forms the basis for estimation at unsampled locations.

7.4 ASSESSMENT OF THE GEOSTATISTICAL MODEL

The previous section presented a 2D geostatistical model which expresses, via the nested semivariogram, the spatial variation of the undrained shear strength of the upper 3 metres of the Keswick Clay. In order to evaluate the suitability of this geostatistical model, two assessment procedures will be employed. Firstly, several authors (Sandefur and Grant, 1980; Englund and Sparks, 1988; Isaaks and Srivastava, 1989; Deutsch and Journel, 1991; Olea, 1991) have suggested the use of *cross validation*, which enables the estimation method to be tested at the locations of existing samples, by using the neighbouring observations, but excluding the value of the point being estimated. Secondly, additional measurements of s_u, obtained *after* the *KESWICK* data base was compiled, are compared with the estimates obtained by kriging, using the geostatistical model presented in the previous section. Each of these assessments are treated separately below.

7.4.1 Cross Validation Analyses

Isaaks and Srivastava (1989) suggested that cross validation analyses provide useful quantitative and qualitative information regarding the suitability, or otherwise, of a spatial variability model, the estimation procedure and its associated parameters. *GEO-EAS* provides a facility for performing cross validation calculations, by means of the program, *XValid*. In order to assess the suitability of the nested semivariogram model, given previously in Equation (7.3), the original *0 to 3 metre* data set was input into *XValid*. Cross validation estimates were then provided by *XValid* at each sampled location by means of ordinary kriging, the results of which are summarised in Table 7.1, and Figures 7.10 and 7.11. In obtaining the cross validated estimates via *Xvalid*: (i) the search radius was set at 1,000 metres in order to be somewhat larger than the maximum range, a_3, of 300 metres; and the model semivariogram was represented by the nested model of Equation (7.3), and specified as isotropic.

It is evident from Table 7.1 that the cross validated estimates provide similar statistics to those of the original data. Though, as mentioned previously, the ordinary kriged estimates yield a more 'smoothed' representation of the sampled data, as is evident by σ, σ^2 and *CV*. Isaaks and Srivastava (1989) suggested that a *posting*, or plan, of the cross validated residuals, that is the difference between the observations and the estimates, can assist in identifying regions of local bias within the estimation procedure. Such local bias can be identified by clusters of overestimation or underestimation within the cross validated results. It is evident from Figure 7.10 that the cross validation analyses yield overestimates and underestimates which are somewhat randomly distributed throughout the Adelaide city

Table 7.1 Summary statistics of the results of cross validation analyses compared with the original data.

Statistic	Original Data	Cross Validation Estimates
Number, *N*	143	143
Mean, *m*	127.1	124.2
σ	46.2	29.4
σ^2	2129.8	866
CV	36.3%	23.7%
Skewness	0.994	0.775
Kurtosis	4.54	3.52
Minimum	31.0	66.0
25th percentile	93.8	101.7
Median	116.0	119.6
75th percentile	155.0	137.7
Maximum	316.0	219.7

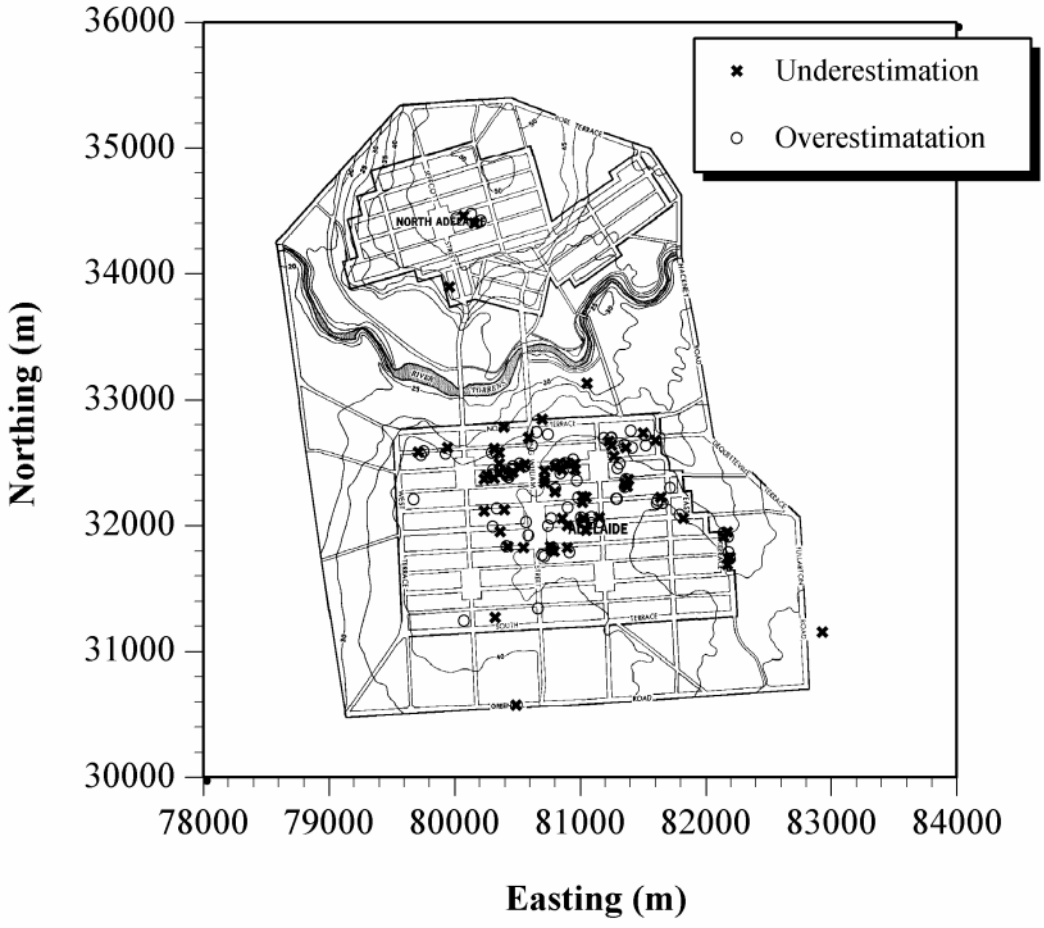

Figure 7.10 Map of the residuals obtained from the cross validation of the *0 to 3 metre* data set.

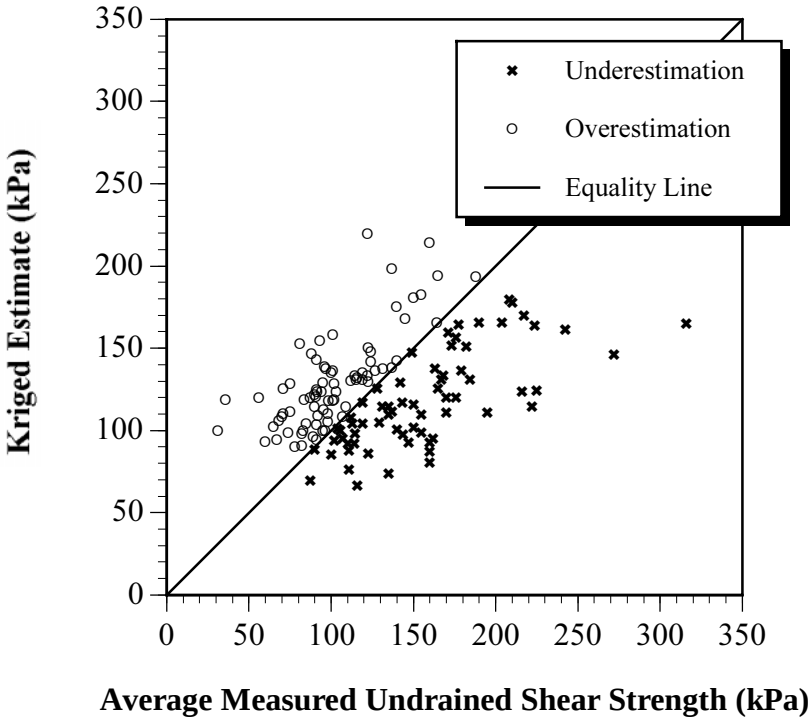

Figure 7.11 Scatterplot of the residuals obtained from the cross validation of the *0 to 3 metre* data set.

area. Hence, there is no evidence to suspect that the spatial variability model yields local bias. In addition, the scatterplot of original values versus cross validation estimates, shown in Figure 7.11, further indicates that the overestimates and underestimates are relatively evenly distributed.

The cross validation results, given in Table 7.1, and Figures 7.10 and 7.11, suggest that the nested semivariogram model appears appropriate. Isaaks and Srivastava (1989) suggested, however, that cross validation analyses have a number of limitations. Firstly, if the original data are spatially clustered, then, so too, are the cross validated estimates and, consequently, their usefulness is reduced. In other words, some conclusions drawn from the cross validated residuals may be applicable to the entire map region, whereas others may not. Secondly, since cross validation generates estimates at only the sampled locations, it is not possible to draw any conclusions regarding the suitability, or otherwise, of the estimation procedure at unsampled locations. Hence, while the cross validation results suggest that the nested spatial variability model is appropriate, further assessment is needed. The following section presents the results of ordinary kriging analyses, performed on new data obtained after the *KESWICK* data base was compiled.

7.4.2 Ordinary Kriging Analyses

A more robust assessment of the performance of the spatial variability model and the estimation procedure, is to estimate values and to compare these with their actual measurements. In order to achieve this, the consulting practices and government instrumentalities, listed in Chapter 6, were again approached in order to provide additional measurements of s_u, obtained from UU tests performed on samples of Keswick Clay, and obtained from the Adelaide city area, within 3 metres of the surface of the clay. These criteria were stipulated so that the newly acquired data could be compared with the estimates provided by the spatial variability model, presented previously in this chapter. However, since the *KESWICK* data base was last compiled, that is in October 1991, little major construction activity has taken place in the Adelaide city area. Unfortunately, only one geotechnical investigation performed since 1991, at the East End Market site, yielded s_u measurements which were consistent with the criteria listed above. Additional and suitable UU test data were published by Do and Potter (1992) and van Holst Pellekaan and Cathro (1993). In addition, the results of the UU tests from boreholes A10 and F5, presented previously in Chapter 4, were not included in the *KESWICK* data base, nor, consequently, the nested semivariogram model. These, together, yield 5 separate observations of $\bar{s}_u$ which may be used to assess the spatial variability model and estimation procedure. These data are summarised in Table 7.2 and their locations, relative to the *KESWICK* data, are shown in Figure 7.12. The values of $\bar{s}_u$, for each of the 5 boreholes, were obtained by averaging the measurements of s_u within the depth range of 0 to 3 metres below the surface of the Keswick Clay.

The geostatistical package *GEO-EAS* provides a facility for 2D ordinary kriging via the program, *Krige*. In order to obtain estimates of the data detailed in Table 7.2, the search radius was again set at 1,000 metres and the model semivariogram was represented by the

Table 7.2 Summary of additional $\bar{s}_u$ data from UU tests on Keswick Clay, used to assess the spatial variability model and estimation procedure.

Ref. No.	Easting (m)	Northing (m)	$\bar{s}_u$ (kPa)	*N*	Location	Source
1	81583	32664	250	1	East End Market	Coffey Partners International
2	80703	32006	92	30	Victoria Square	Do and Potter (1992) & van Holst Pellekaan and Cathro (1993)
3	80096	32407	105	8	Light Square	Do and Potter (1992)
4	80022	31172	139	6	A10	Chapter 4
5	80010	31139	111	6	F5	Chapter 4

Note: *N* is the number of individual measurements of s_u used to obtain $\bar{s}_u$.

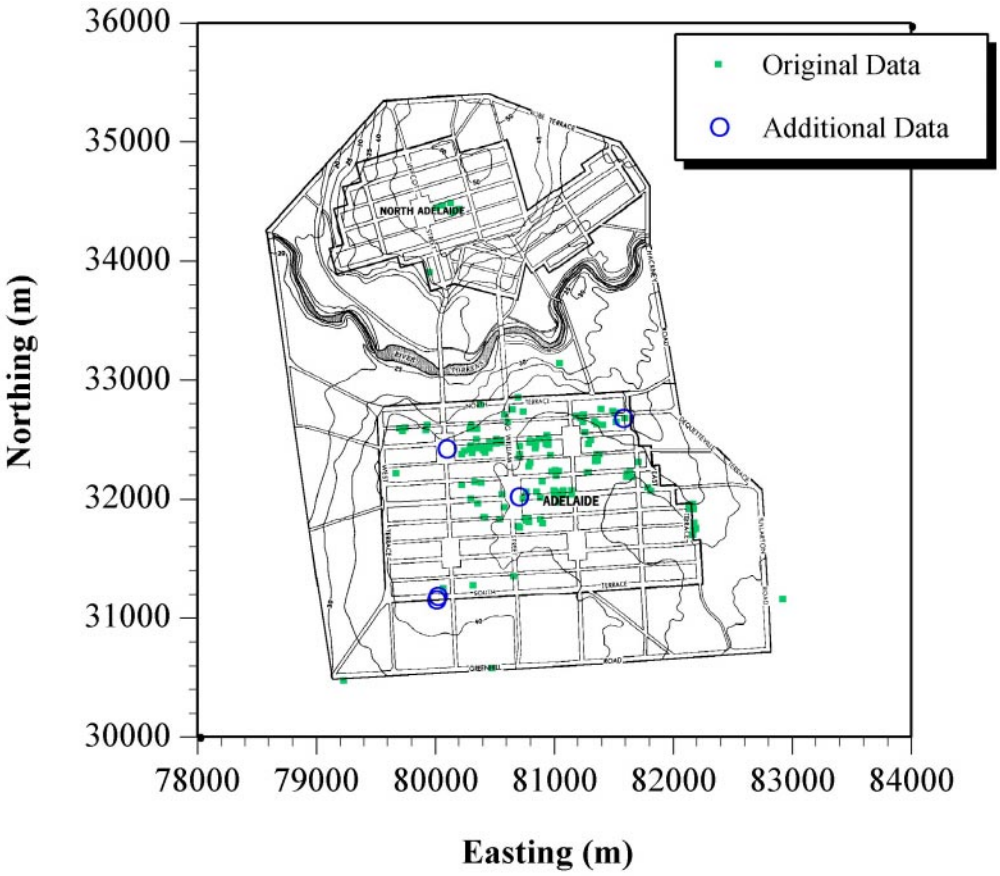

Figure 7.12 Locations of the additional data used to obtain kriged estimates.

nested semivariogram model, detailed in §7.7.3, and was again specified as isotropic. The results of the ordinary kriged estimation, given by *Krige*, as well as their associated kriging standard deviations, σ_k, using the original, non-detrended data, are summarised in Table 7.3. The results of the ordinary kriged estimation, using the detrended data, are summarised in Table 7.4. It should be noted that, as one would expect, the number of neighbours contributing to the ordinary kriged estimates and σ_k, using the detrended data in Table 7.4, are identical to those using the non-detrended data in Table 7.3. Brooker (1991) suggested that, while σ_k does not, of itself, allow calculation of confidence limits, it is common, under the assumption of normality for the error distribution, to use σ_k to calculate confidence limits. Hence, for the first data point (Ref. No. 1), the 95% confidence interval is 217 ± 54.7 kPa (i.e. $217 \pm 1.96 \times 27.9$), whose limits include the 250 kPa observation.

Tables 7.3 and 7.4 clearly demonstrate that the estimates provided by the nested semivariogram model, and the ordinary kriging process, provide very good preliminary representations of the actual s_u measurements. In addition, it is evident from the sum of the squared differences, *SSD*, that the original, non-detrended data yield superior estimates to those given by the detrended data. This is probably due to the fact that the OLS second-

Table 7.3 Summary of results of ordinary kriged estimates from *Krige* using original non-detrended data.

Ref. No.	Original $\bar{s}_u$, (kPa)	Estimate $\bar{s}_u^*$, (kPa)	σ_k (kPa)	Neighbours Used	% Error (kPa)	*SSD* (kPa^2)
1	250	**217**	27.9	16	13.2	1,089
2	92	**83.4**	31.2	16	9.6	74
3	105	**104.4**	42.1	16	0.6	0.4
4	139	**116**	37.9	16	16.5	529
5	111	**115**	40.2	13	–3.6	16
					Σ *SSD* =	**1,708**

Table 7.4 Summary of results of ordinary kriged estimates from *Krige* using detrended data.

Ref. No.	Original Value $\bar{s}_u$, (kPa)	Kriged Estimate (kPa)	OLS Surface (kPa)	Retrended Estimate $\bar{s}_u^*$,(kPa)	% Error (kPa)	*SSD* (kPa^2)
1	250	81.2	136.0	**217.2**	13.1	1,076
2	92	–37.5	121.0	**83.5**	9.5	72
3	105	–3.6	103.8	**100.2**	4.6	23
4	139	–1.2	110.1	**108.9**	21.7	906
5	111	–2.8	110.5	**97.7**	12	177
					Σ *SSD* =	**2,254**

degree surface is not significant, and its estimation is likely to add to the uncertainty of the overall estimate.

It is common practice in the mining industry to use other, more simplistic estimation regimes, such as *polygonal estimation*, *inverse distance weighting* and *inverse distance squared weighting* (Journel and Huijbregts, 1978; Clark, 1979; Isaaks and Srivastava, 1989; Brooker, 1991; Olea, 1991). With reference to the estimation of points, polygonal estimation assigns the value of the nearest neighbour to the point in question; whereas the inverse distance and inverse distance squared regimes, assign weights to the neighbours dependent on the distance from each neighbour to the estimation point. The inverse distance and inverse distance squared, weightings, w_i, are expressed by:

Inverse distance:

$$w_i = \frac{\frac{1}{d_i}}{\sum_{j=1}^{n} \frac{1}{d_j}} \tag{7.4}$$

where: d_i is the distance from the estimation point to the *i*th neighbour.

Inverse distance squared:

$$w_i = \frac{\frac{1}{d_i^2}}{\sum_{j=1}^{n} \frac{1}{d_j^2}} \tag{7.5}$$

The point estimate, s_u^*, is then, simply the summation of the individual weights multiplied by each associated observation, as shown in Equation (7.6). These estimation regimes will be used to assess the performance of the ordinary kriging estimation procedure.

$$s_u^* = \sum_{i=1}^{n} w_i s_{u_i} \tag{7.6}$$

where: s_{u_i} is the undrained shear strength of the *i*th observation.

Employing the *Excel* spreadsheet package, the same five data points, which were analysed above, were estimated using the polygonal, inverse distance and inverse distance squared, estimation regimes, and the results are summarised in Table 7.5. Examination of the total *SSD*s for each estimation procedure indicates that the inverse distance squared technique performs very well, whereas the polygonal and inverse distance methods perform relatively poorly. The results presented in Table 7.5, when compared with those given by ordinary kriging (ΣSSD = 1,708), as shown in Table 7.3, suggest that the inverse distance squared technique is superior to that of kriging. However, closer examination of these results indicates that, in all but the first data point (Ref. No. 1), ordinary kriging out-performed the inverse distance squared technique. Excluding the first data point from the evaluation of the total *SSD*, yields a value of 1,037 for the inverse distance squared procedure, as compared to 619 for ordinary kriging. It is reasonable to draw attention to the first data point, since, as shown in Table 7.2, its value is based on only one test result, taken from a depth of 2.6 metres below the surface of the Keswick Clay. Had this result been based on more test samples, one would expect the average value of s_u to be somewhat lower, due to the effect of increasing s_u with depth, as indicated in Chapter 6. Hence, it is justifiable to exclude it from any assessment of the performance of estimation regimes. With this in

Table 7.5 Summary of results of estimates of $\bar{s}_u^*$ (kPa) and sum of the squared differences, *SSD*, (kPa^2) from polygonal, inverse distance and inverse distance squared estimation regimes.

Ref. No.	Original Value	Polygonal		Inverse Distance		Inverse (Distance)^2	
		Estimate	*SSD*	Estimate	*SSD*	Estimate	*SSD*
1	250	272	484	155.2	8,989	233.1	284
2	92	89	9	121	843	106.7	215
3	105	119	196	116	121	107.3	6
4	139	103	1,296	121.9	292	110.5	810
5	111	103	64	122.5	132	113.4	6
		Σ *SSD* =	**2,049**		**10,377**		**1,321**
		Σ *SSD =**	**1,565**		**1,388**		**1,037**

Note: Σ *SSD** is the sum of the *SSD*s excluding the first data point (Ref. No. 1).

mind, the ordinary kriging procedure significantly out-performs the other estimation techniques, which is consistent with the geostatistical literature (e.g. Brooker, 1991). This is not surprising, since the polygonal, inverse distance and inverse distance squared estimation regimes do not correctly account for the variability of the material. That is, they treat highly homogeneous materials in the same way as highly heterogeneous ones.

While the preceding kriging analyses provided preliminary estimates of $\bar{s}_u$ at a given point, it is possible to obtain an overall picture of the spatial variability of the Keswick Clay by kriging a grid of points, and then using these estimates to generate a contour map of the Adelaide city area. In order to achieve this, the program, *Krige*, was used to generate a grid of 30 $\times$ 30 estimates of $\bar{s}_u$ across the Adelaide city area, using the nested semivariogram model, specified previously. The search radius was again specified as 1,000 metres and a minimum number of 4 points were used in the kriging process. The ordinary kriged point estimates for the undrained shear strength of the Keswick Clay, given by *Krige*, are summarised in Figure 7.13, and their associated kriging standard deviations are given in Figure 7.14. As one would expect, Figure 7.14 demonstrates that the uncertainty associated with the kriged estimates is greatest adjacent to the boundaries of the Adelaide city area, whereas lower levels of uncertainty are evident towards the centre of the estimation region.

Comparing Figures 7.13 and 6.35, it is apparent that the variability obtained by kriging is substantially different to the variability described by standard contouring procedures; in the case of Figure 6.35; inverse distance squared. However, it is not entirely correct to

INTENTIONALLY BLANK

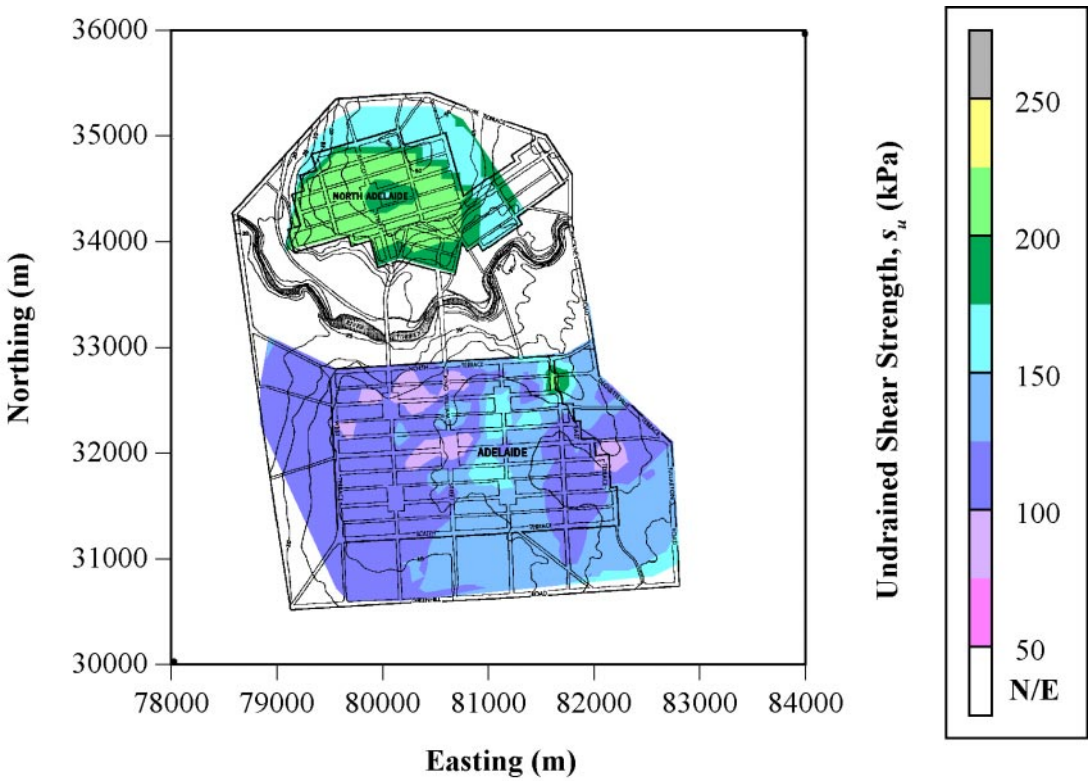

Figure 7.13 The spatial variation of $\bar{s}_u$ of Keswick Clay, within a depth of 3 metres below its surface, as given by ordinary kriging.

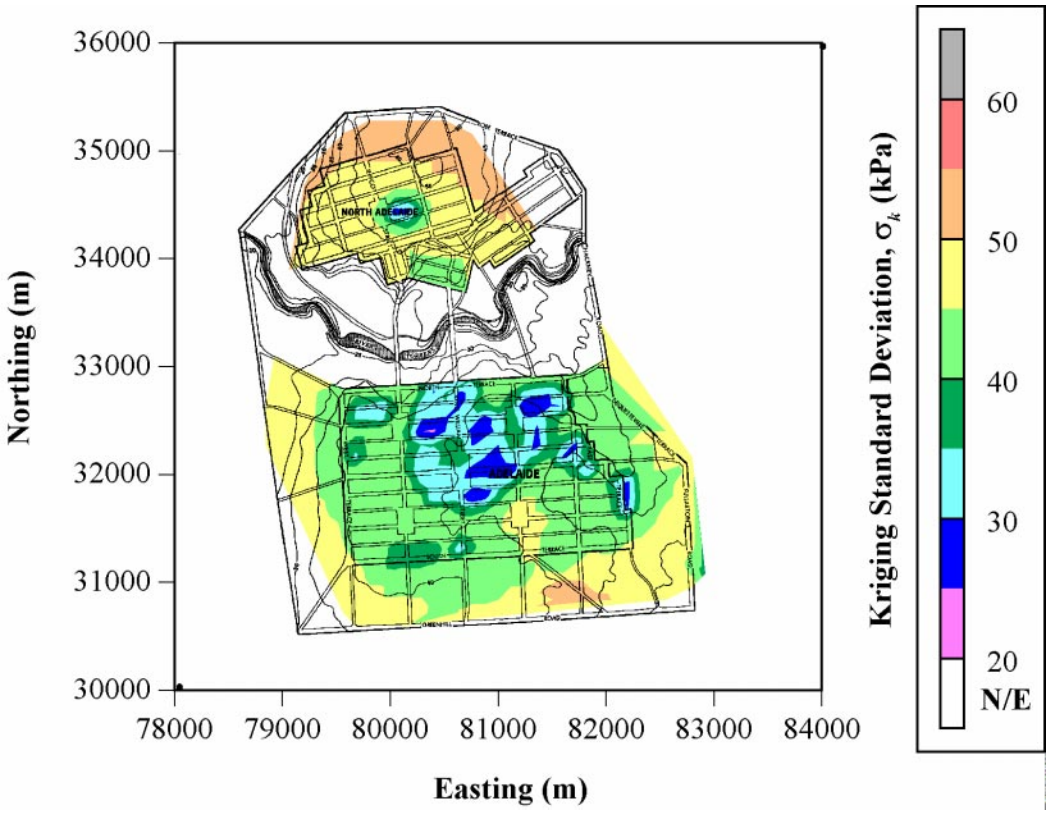

Figure 7.14 The variation of the kriging standard deviation, σ_k, associated with the estimates given in Figure 7.13.

INTENTIONALLY BLANK

compare these two diagrams, since Figure 6.35 was based on values of s_u averaged over the entire length of the boreholes, whereas Figure 7.13 was based on measurements of s_u averaged over a maximum interval of 3 metres. Figure 7.15 shows the variation of $\bar{s}_u$ across the Adelaide city area, as given by the *DeltaGraph* graphical package, using the non-detrended *0 to 3 metre* data set as input. Unlike *Surfer*, which was used to generate Figure 6.35 by means of the inverse distance squared estimation regime, *DeltaGraph* uses polygonal estimation. Furthermore, it should be noted that, in generating estimates, *DeltaGraph* allows only interpolation, a limitation of the polygonal approach. Thus, the contours are restricted to a triangular region of the city. It can be readily seen, from Figures 7.13 and 7.15, that they are substantially different. Whilst polygonal estimation has been used widely in the mining industry, it provides satisfactory results only for highly continuous variables, and it is essentially its poor estimation performance, which largely contributed to the development of geostatistics (Olea, 1991).

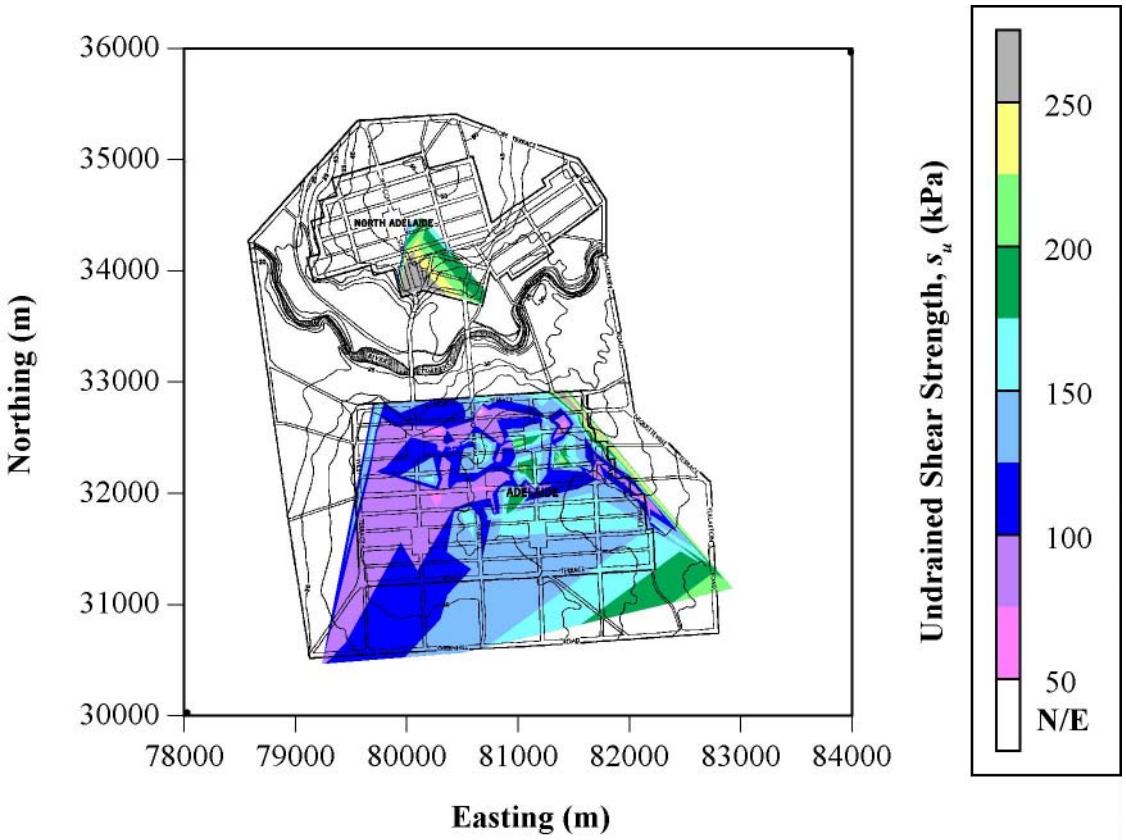

Figure 7.15 The spatial variation of $\bar{s}_u$ of Keswick Clay, within a depth of 3 metres below its surface, as given by polygonal estimation via *DeltaGraph*.

7.5 SUMMARY

In this chapter, a model has been developed which describes the small- and large-scale spatial variability of the undrained shear strength of the Keswick Clay. It has been observed that the model exhibits a nested structure which accounts for the spatial variability at 3 distinct scales; that is, at 0.2, 6 and 300 metres. In addition, it has been demonstrated that, when the spatial variability model is used in conjunction with the ordinary kriging procedure, very good preliminary estimates of $\bar{s}_u$ are obtained at unsampled locations. Furthermore, these kriged estimates have been shown to be superior to those obtained from other estimation regimes, such as polygonal, inverse distance and inverse distance squared. However, it must be emphasised that, while these kriged estimates are useful in providing an indication of the average undrained shear strength of the Keswick Clay, within a depth range of 3 metres below its surface, considerable uncertainty exists with these estimates. While the kriging standard deviation, σ_k, provides an estimate of this uncertainty, the total uncertainty is undoubtedly greater. This is due to the fact that the data on which the large-scale spatial variability model and the estimates are based, contain unquantified levels of variability due to inconsistencies in sampling, testing and reporting procedures. However, with these points in mind, it has been demonstrated that geostatistics provides a useful means by which preliminary estimates of undrained shear strength can be obtained.

As a preliminary design aid, Figure 7.13 provides an initial estimate of $\bar{s}_u$ for the Keswick Clay, within the upper 3 metres of the clay's surface. A more precise estimate, at a given location within the Adelaide city area, may be obtained by using the program, *Krige*, in conjunction with the nested semivariogram model. As a consequence, two levels of preliminary estimation of $\bar{s}_u$ are provided.

The following chapter examines the significance of the spatial variability of the undrained shear strength of soils, on geotechnical engineering design.

Chapter Eight

Significance of Spatial Variability with Respect to Geotechnical Engineering Design

8.1 INTRODUCTION

In Chapter 5 it was observed that the undrained shear strength of the Keswick Clay exhibited a vertical correlation distance equal to 0.2 metres, and a lateral variability model which was the combination of three separate structures with ranges: a_1 = 0.2 metres; a_2 = 6 metres; and a_3 = 300 metres. This chapter makes use of these results and investigates the influence of both the scale of fluctuation, δ_v, and the range, a, on geotechnical engineering design. Two areas of geotechnical engineering design are examined - slope stability analysis and pile design, and these are each treated, in turn, below.

8.2 SLOPE STABILITY ANALYSIS

Much of the research undertaken in the field of the spatial variability of geotechnical materials has focused on slope stability analyses. This is due mainly to the fact that, in general, the geotechnical engineering profession is presently unable to make reliable predictions of slope failure events (Vanmarcke, 1977b). This is because the vast majority of such predictions are based on a conventional design approach, where the computed factor of safety (*FoS*) is sought to be maintained above some minimum prescribed value. However, the *FoS* fails to make any allowance for the variability of the material and its properties, as well as uncertainties associated with the externally applied loads. Recently, the focus of slope stability analyses has been directed away from the *FoS* approach, and has concentrated on the evaluation of the probability of failure, P_f. It is in the calculation of P_f that spatial variability analyses have been primarily directed.

Li (Li and Lumb, 1987) developed a computer program, *PROBSN*, which includes the scale of fluctuation in the calculation of P_f. The program was originally written in Fortran 77 for a mainframe computer, but was subsequently converted to operate on a PC platform by Waddell (1988) and Mostyn and Soo (1992). *PROBSN* uses the first order second moment method to determine the failure probability of a slope using the generalised procedure of slices. The program accommodates circular and non-circular slip surfaces, and the method is rigorous in that both force and moment equilibrium are satisfied (Mostyn and Soo, 1992). *PROBSN* uses the *safety margin*, instead of the *FoS*, as the performance function, since the safety margin is more likely to be normally distributed. The analysis procedures used by *PROBSN* are treated in detail by Li and Lumb (1987).

In order to assess the influence of the scale of fluctuation on the probability of slope failure, an embankment was analysed using the program, *PROBSN*. The embankment shown in Figure 8.1, while fictitious, was given realistic geometrical and soil properties which are consistent with those of a typical slope, likely to be encountered in the Adelaide city area. The embankment was given an overall height of 10 metres, the slope angle, Θ, was varied from 20º to 85º, in increments of 5º or 10º, and the embankment material was assumed to be Keswick Clay with geotechnical properties, mean and standard deviation, of: undrained shear strength of 50 and 20 kPa; bulk unit weight of 18.8 and 1.9 kN/m^3; and internal angle of friction of 0º and 0º. These geotechnical and statistical properties are consistent with those given in Chapter 6 for Keswick Clay. The undrained shear strength, however, was chosen at the low end of the recorded values to ensure that the slope stability analyses yielded realistic factors of safety, *FoS*, typically less than 1.5. By setting $\delta_H = \delta_V$ (= δ_v), and allowing δ_v to vary between 0.001 metres (representing a completely random soil deposit), and 10,000 metres (a perfectly correlated soil profile), and by specifying a simple exponential ACF model, the probabilities of slope failure were evaluated using the program, *PROBSN*. The results of these analyses are summarised in Figure 8.2. It should be noted that, while this figure suggests that some of the calculated values of P_f were equal to zero, this was not the case. In fact, as δ_v decreased, the calculated values of P_f asymptoted towards zero, as expected.

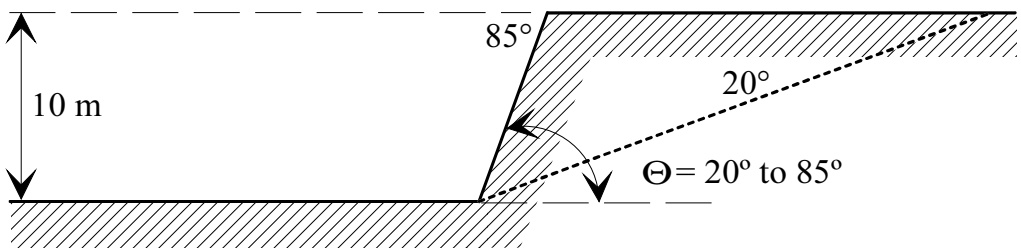

Figure 8.1 Keswick Clay embankment analysed using *PROBSN*.

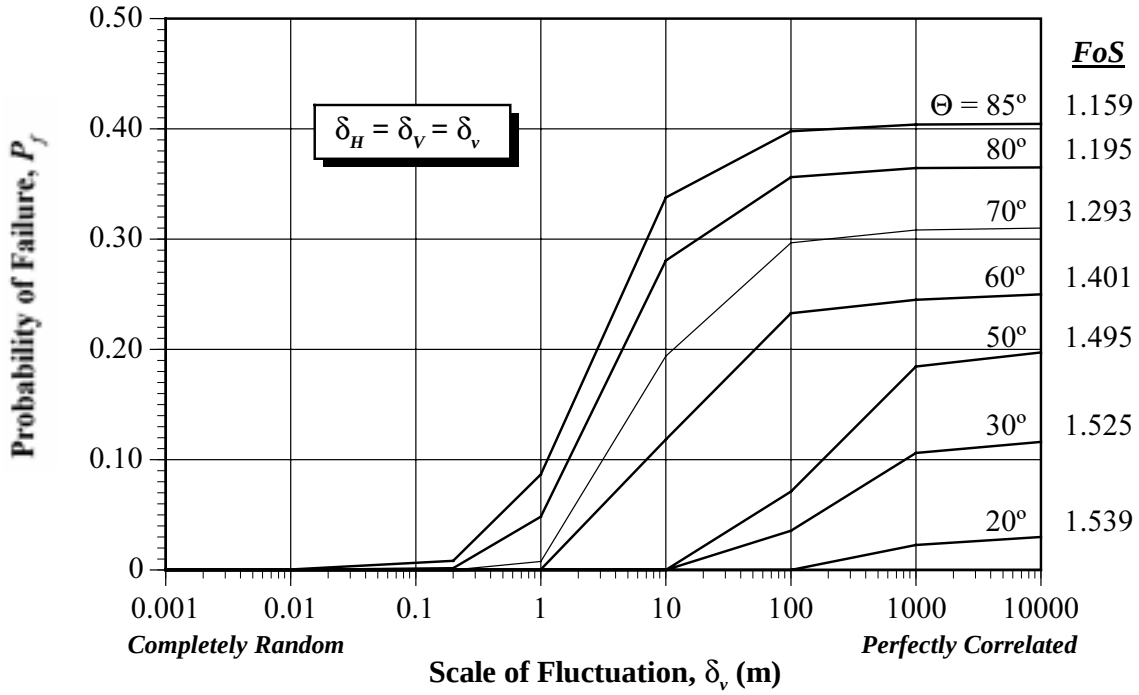

Figure 8.2 Influence of the scale of fluctuation, δ_v, on the probability of slope failure, P_f.

It can be concluded, from Figure 8.2, that:

- For all but the steepest slopes (Θ = 80º and 85º), P_f remains low when $\delta_v \leq 1$ metre;
- For $\Theta \leq 50º$, $P_f \approx 0$ when $\delta_v \leq 10$ metres;
- For all slopes examined (Θ = 20º to 85º), P_f is very small when $\delta_v \leq 0.2$ metres.

On the other hand, the factor of safety, *FoS*, is independent of δ_v, the model ACF and the standard deviation of the geotechnical properties. As a consequence, the traditional method of evaluating the *FoS* is not recommended, as this value gives no indication of the probability of failure of the embankment. For example, a slope whose soil properties are known with great accuracy, as the result of extensive testing, will possess the same *FoS* as a slope with identical geometrical and soil properties, which are known with a lesser degree of accuracy, as the result of a more limited testing programme.

It is evident from the foregoing discussion and analyses, that, for the embankment examined, the influence of the scale of fluctuation on P_f is negligible when δ_v is less than, or equal to, 0.2 metres. Conversely, the scale of fluctuation only influences P_f significantly when δ_v is greater than 1 metre, or in some cases 10, or 100 metres. It was shown in Chapters 2 and 5, that several researchers have observed scales of fluctuation for s_u between approximately 0.1 and 50 metres. Figure 8.2 indicates that, for soils with scales of fluctuation of the order of 1 metre or greater, the exclusion of δ_v in slope stability

analyses will significantly affect the results obtained. These conclusions are in general agreement with those given by Li and Lumb (1987), Li and White (1987b), and Mostyn and Soo (1992), who performed similar analyses. While the inter-relationship between δ_H and δ_V has not been examined in the present case study, Li and White (1987b) found that P_f is slightly more sensitive to δ_V than to δ_H.

In addition, Mostyn and Soo (1992) stated that the majority of current methods, used to determine the probability of slope failure, fail to account for the autocorrelation of the geotechnical properties of the slope material. By excluding autocorrelation from the analysis process, the majority of probabilistic slope techniques implicitly assume that a random variable, for example s_u, is perfectly correlated with itself over infinite distances. As shown in Figure 8.2, such an assumption often yields extremely conservative estimates of P_f, which are often several orders of magnitude in error.

In summary, soils with small scales of fluctuation, say less than one metre, will yield lower probabilities of slope failure than soils with large scales of fluctuation. The traditional, deterministic approach of evaluating the *FoS* of the slope is unaffected by, and takes no account of, the uncertainty and autocorrelation structure of the soil properties of the slope material. Such analyses are not recommended as the single parameter, *FoS*, gives no indication of the likelihood of failure of the slope. In addition, the majority of probabilistic slope stability techniques fail to account for the autocorrelation of the soil properties of the slope material. Such analyses assume perfect correlation, which yield unrealistically high estimates of P_f. While such estimates are conservative, Mostyn and Soo (1992) recommended that these analyses should not be used in economic assessments, but only to provide a ranking of preferred options.

8.3 PILE DESIGN

The main objective of pile foundations is to transfer any loads present at the surface, to the underlying strata; both safely and economically. Ideally, full-scale pile load tests should be performed at the locations of the proposed piles. However, such pile load tests are extremely expensive, and hence are impractical for most situations. An alternative approach is to use mathematical models to predict the behaviour of pile foundations under load. Many such techniques have been developed for this purpose, however, their accuracy is directly influenced by the quality and quantity of the data on which their predictions are based. As mentioned in Chapter 2, the CPT was originally developed to facilitate the design of pile foundations. Furthermore, in §2.4.4, it was demonstrated that, of all of the axial pile capacity techniques which are based on CPT data, the LCPC Method has been shown to provide the best estimates. The following section briefly details this technique.

8.3.1 LCPC Method

The LCPC (Laboratoire Central des Ponts et Chaussées, France) Method is used to predict the ultimate axial capacity of a statically loaded pile, Q_U, and is given by the following equation (Bustamante and Gianeselli, 1982):

$$Q_U = Q_B + Q_S \quad \text{(kN)} \tag{8.1}$$

where: Q_B is the resistance due to the base of the pile (kN);
Q_S is the resistance due to the shaft of the pile (kN).

For a multi-layered soil, Bustamante and Gianeselli (1982) suggested that Q_B and Q_S may be determined from the following relationships:

$$Q_B = q_{ca}\, k_c\, A_p \quad \text{(kN)} \tag{8.2}$$

where: q_{ca} is the *clipped average cone tip resistance* at the level of the pile base (kPa);
k_c is the *penetrometer bearing capacity factor*;
A_p is the area of the base of the pile (m^2).

and:

$$Q_S = \sum_{i=1}^{n} q_{si}\, C_p\, t_i \quad \text{(kN)} \tag{8.3}$$

where: q_{si} is the *limit unit skin friction* of the *i*th layer (kPa);
C_p is the circumference of the pile shaft (m);
t_i is the thickness of the *i*th layer (m).

Bustamante and Gianeselli (1982) suggested that the limit unit skin friction, q_{si}, may be determined from the following equation:

$$q_{si} = \frac{q_c}{\psi} \tag{8.4}$$

where: ψ is a constant which allows for the nature of the soil and the pile construction and placement techniques.

Bustamante and Gianeselli (1982) provided tabulated values for ψ dependent on the soil type and the pile construction method. In addition, the authors suggested maximum values for q_{si}, to account for: the presence of localised hard elements; non-compliance with

standard penetration rates; poor condition of cones; excess porewater pressures; and deviation of the CPT rods from the vertical.

The clipped average cone tip resistance, q_{ca}, is calculated using the following procedure (Bustamante and Gianeselli, 1982):

1. As shown in Figure 8.3, the intermediate parameter, q'_{ca}, is determined by averaging the measured values of q_c over the length, $L_p - a_p$ to $L_p + a_p$, where: L_p is the length of the pile; and a_p is equal to $1.5 \times D_p$ (where D_p is the width of a pile, or in the case of a circular cross-section pile, its diameter).

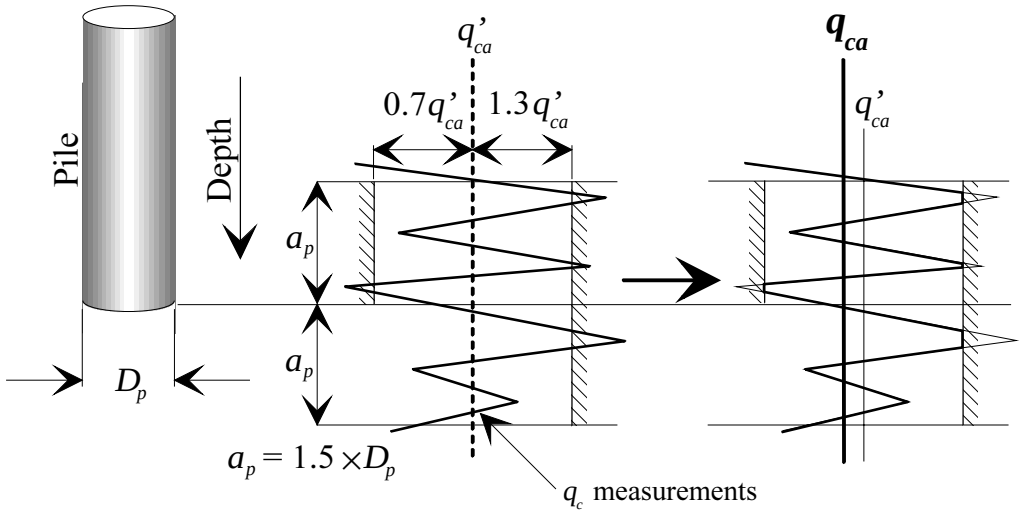

Figure 8.3 The procedure used to calculate q_{ca}.
(After Bustamante and Gianeselli, 1982).

2. The measured values of q_c are then *clipped* to remove local irregularities, such that q_{si} is in the range: $0.7q'_{ca} \le q_{si} \le 1.3q'_{ca}$.

3. The clipped average cone tip resistance, q_{ca}, is then determined by averaging the *clipped* values of q_c, over the length, $L_p - a_p$ to $L_p + a_p$.

Finally, Bustamante and Gianeselli (1982) recommended that the allowable *design* axial load, Q_A, that can safely be placed on the pile, is given by the following equation:

$$Q_A = \frac{Q_B}{3} + \frac{Q_S}{2} \quad \text{(kN)} \tag{8.5}$$

It can be seen from the preceding treatment that the LCPC Method makes use of only the q_c measurements; that is, sleeve friction measurements are not used in the prediction of the static axial load capacity of the pile. This is an advantage over other methods, since this reduces the computational effort required, as well as the uncertainty associated with the prediction itself. However, the use of clipped data may tend to result in underestimation of the pile capacity.

The following section details hypothetical field problems used to assess the influence of spatial variability on the design of pile foundations. The two field problems were based on piles *driven* into Keswick Clay. Bustamante and Gianeselli (1982) recommended that, for precast piles driven into a compact to stiff clay, k_c = 0.55, ψ = 40, and $q_{si(max)}$ = 80 kPa, where the piles are constructed with minimal disturbance to the soil in contact with the pile shaft, otherwise $q_{si(max)}$ = 35 kPa. These values will be used when applying the LCPC Method to the case studies presented below.

8.3.2 Hypothetical Field Problems

In assessing the influence of the spatial variation of the undrained shear strength of clay soils on the design of pile foundations, two case studies will be presented. Firstly, the CPT information obtained at the South Parklands site will be considered, and secondly, a series of simulated data will be examined. These are each presented separately below.

8.3.2.1 South Parklands Site

When designing a pile foundation it is necessary to obtain an estimate of the undrained shear strength, s_u, of each of the soil layers within the substrate. When based on laboratory testing, it is common practice to drill a borehole adjacent to the proposed pile, and to obtain sufficient undisturbed samples, from which, s_u is determined by means of a series of triaxial tests. It is becoming increasingly more popular to design piles on the basis of CPT data, as mentioned in §8.3. Again, it is common practice to perform a CPT adjacent to the proposed location of the pile. Often, however, limited budgets mean that at most only a few CPTs are performed at any one site, and piles are designed on the basis of CPT data obtained some distance away from the actual location of the pile. The CPTs obtained at the South Parklands site provide a useful data set for quantifying the effect of spatial variability on the design of pile foundations.

Suppose that a building is to be constructed at the South Parklands site. For a typical design situation, it is likely that a geotechnical investigation of the site would consist of a

CPT at each of the corners of the building, and perhaps one in the centre; being a total of 5 CPTs. Suppose that the structural layout of the proposed building requires a pile to be located at the centre of the site; that is, at location F5. Recall from Chapter 4, that 6 CPTs were performed in the vicinity of F5; that is, E54, F44, F5A, F5, F501 and F51, as shown in Figure 8.4. These 6 CPTs, when used together, provide a good description of the soils in the immediate vicinity of the proposed pile.

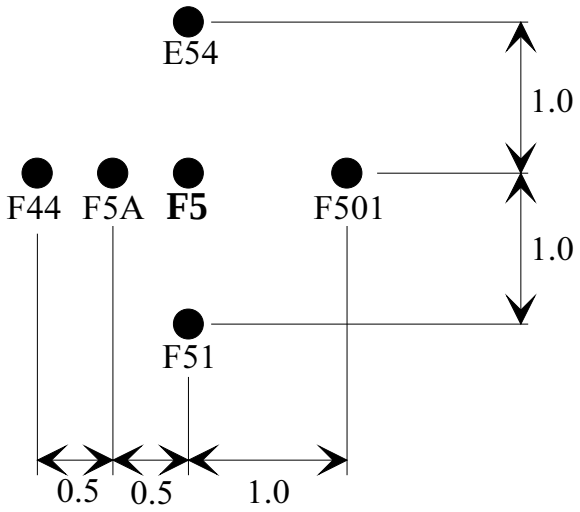

Figure 8.4 CPTs adjacent to F5.

Since each of the CPTs was driven to a maximum depth of 5 metres below the ground surface, it is only advisable to design piles up to 5 metres in length. As a consequence, let us assume that the proposed pile is to be a driven, precast concrete pile, 0.3 metres in diameter and 4.5 metres long. The LCPC Method recommends that to evaluate the base capacity of the pile (Q_B), CPT data over the depth range $1.5 \times D_p$, above and below the base of the pile, are to be used. However, little information is available regarding the lateral extent over which s_u of a clay soil contributes to the shaft capacity of a pile (Q_S).

Since a driven pile behaves in a similar fashion to the insertion of a cone penetrometer into the subsoil profile, it is possible to make some estimate of the radius of the cylinder of soil which contributes to the axial capacity of a pile. This can be achieved by means of the chart developed by Teh and Houlsby (1991) using a finite element analysis, and shown previously in Figure 2.10. Using $a_c = 0.15$ metres, $\beta = 60°$ and $I_r = 67.4$ (the average value of I_r determined in Chapter 4) as input, the radius of the elastic zone, $r_p = 1.0$ metre, and the depth of the base of the elastic zone, below the tip of the pile, $z_p = 0.54$ metres. The value of r_p compares well with the diameter of 2 metres suggested by Poulos (1995). In

addition, the value of 0.54 metres for z_p compares favourably with the $1.5 \times D_p = 0.45$ metres, suggested by the LCPC Method. As a consequence, the axial bearing capacity of a 0.3 metre diameter by 4.5 metre deep pile is assumed to be influenced by a cylinder of soil, 2 metres in diameter and 4.95 metres in height. Hence, since the 6 CPTs shown in Figure 8.4, are contained within this soil cylinder, it would be expected that the average of these 6 CPTs would provide a very good representation of the axial capacity of the proposed pile at F5, with a relatively low level of uncertainty. Figure 8.5 shows the measurements of q_c from each of these 6 CPTs, as well as their mean, which was obtained using the global statistics feature of *SemiAuto*.

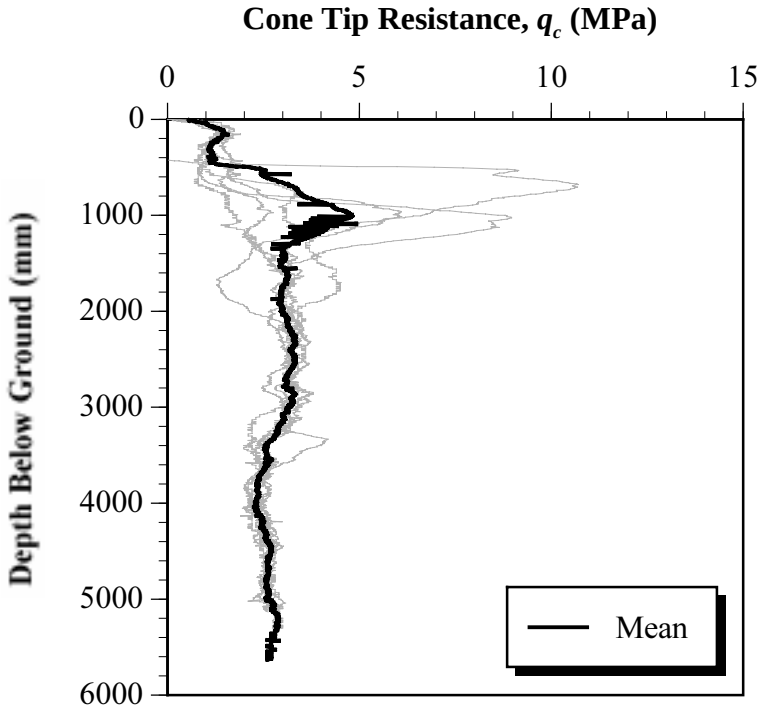

Figure 8.5 Data from the 6 CPTs adjacent to F5, including their mean.

In order to facilitate the calculation of the allowable axial capacity of a statically loaded pile, Q_A, by means of the LCPC Method, an *Excel* spreadsheet was developed. By entering the mean q_c profile of the 6 CPTs into the *Excel* spreadsheet, Q_A was found to equal 106.4 kN. However, as mentioned above, a typical geotechnical investigation would involve, at most, a single CPT adjacent to the proposed pile. Suppose that such a CPT was performed along the centreline of the pile, that is, at F5 itself. Substituting the measurements of q_c, from CPT F5, into the *Excel* spreadsheet yields an estimate of Q_A equal to 102.8 kN, a 3.4% underestimate; assuming 106.4 kN to be the 'true' value.

In order to assess, further, the influence of spatial variability on pile design, let us suppose that the budget for the geotechnical investigation did not allow a CPT to be performed at F5, but at some distance away from the pile location. How does the distance of the CPT, away from the location of the proposed pile, influence its design estimate? It is possible to assess this by examining the other CPTs performed at the South Parklands site. For example, for a radial distance of 1 metre, 4 CPTs; that is, E54, F501, F51 and F44, were drilled at the site, and by entering these into the *Excel* spreadsheet, it is possible to determine the error.

Figure 8.6 shows the envelope of the maximum percentage error between the value of Q_A obtained by using a single CPT, as a function of the radial distance from F5, compared with the 'true' value of Q_A, given by the mean of the 6 CPTs, as detailed above. A positive percentage error indicates an overestimation, whereas a negative percentage error indicates an underestimation. It can be seen from Figure 8.6, that a maximum overestimation of 3%, and a maximum underestimation of 8%, may be obtained when the location of the CPT, used to design a pile, is some 35 metres away from the location of the proposed pile itself. Such errors would be quite acceptable to a geotechnical design engineer. However, much of the spatial variability of the CPT data is 'masked' by the LCPC Method itself. For instance, Figure 8.6 was obtained using $q_{si(max)}$ = 35 kPa, which tends to limit the variability of Q_S, and as a result, Q_A. Figure 8.7 presents the same results as Figure 8.6, with $q_{si(max)}$ set to 80 kPa; and Figure 8.8 shows the same results, but with an unlimited $q_{si(max)}$.

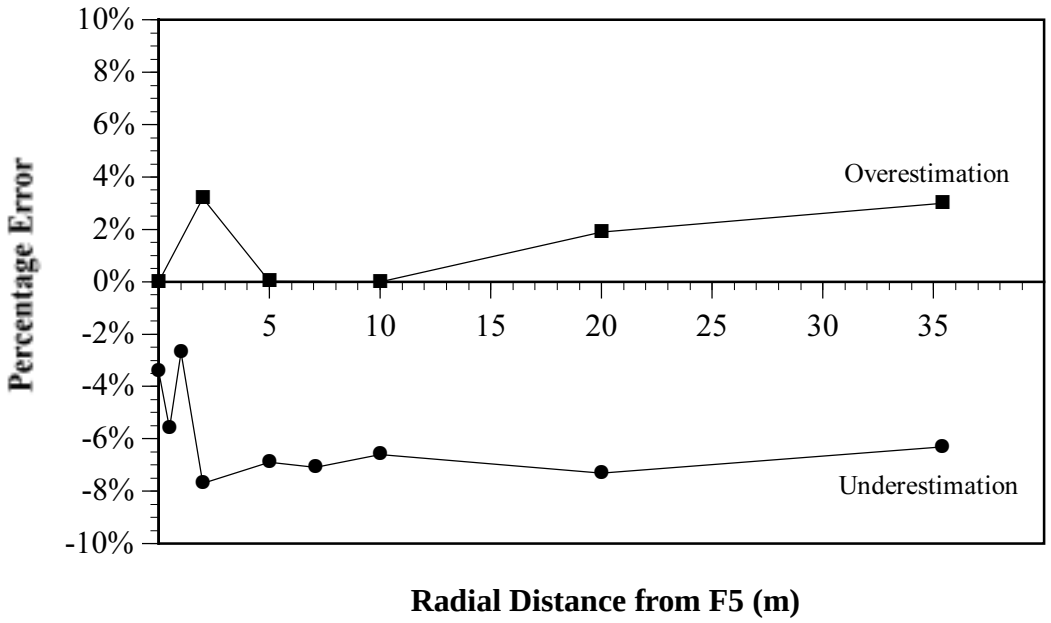

Figure 8.6 Relationship between the percentage error of Q_A and the radial distance of the CPT, used to determine the pile at F5, using $q_{si(max)}$ = 35 kPa.

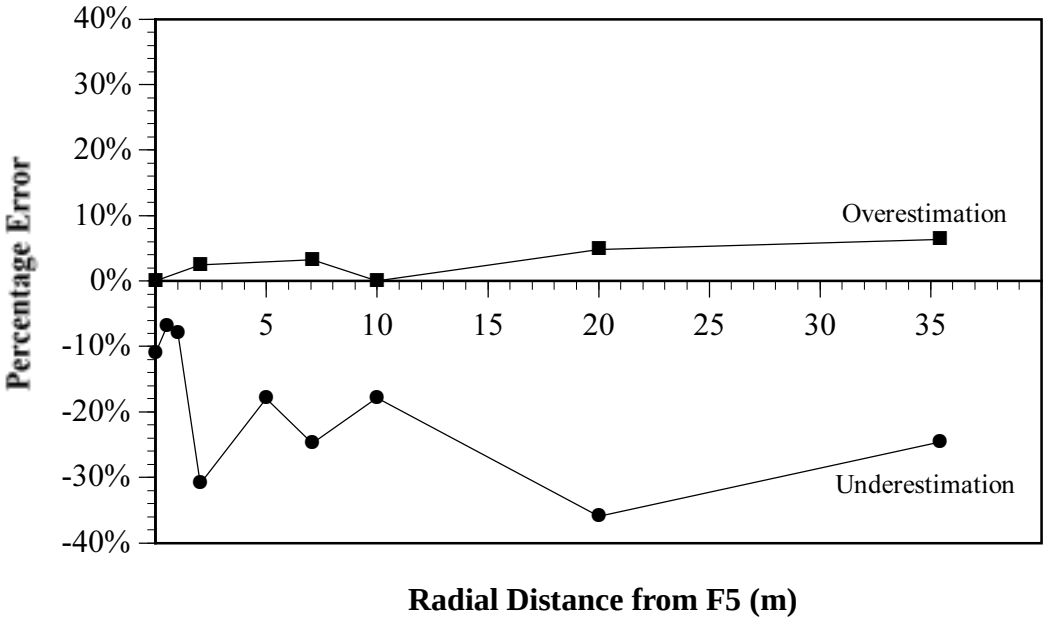

Figure 8.7 Relationship between the percentage error of Q_A and the radial distance of the CPT, used to determine the pile at F5, using $q_{si(max)}$ = 80 kPa.

It is evident from Figure 8.7 that, with $q_{si(max)}$ = 80 kPa, the maximum overestimation is 6%, and the maximum underestimation is 36%. The 6% overestimation, again, would be of little concern to a geotechnical design engineer, and, while the underestimation error is relatively large, the resulting estimates of Q_A are conservative, and hence, would result in overdesign, rather than compromising safety. Figure 8.8 demonstrates the spatial variability 'masking effect', or the inherent conservatism, of the LCPC Method. By not using a $q_{si(max)}$, the variability in the CPT data indicates a maximum overestimation error of 45%, and a 38% underestimation error. An overestimation of 45% could result in an unsafe design. However, by setting $q_{si(max)}$ = 35 kPa, or 80 kPa, the LCPC Method reduces the impact of spatial variability on the allowable axial capacity of the pile, particularly in regards to overestimation, and hence, unsafe design values. However, in soft soils, where q_c, and hence q_{si}, will invariably be low and generally less than $q_{si(max)}$, the influence of $q_{si(max)}$ will be minimal. In soft soils, therefore, the LCPC Method will result in less conservative designs than those given by stiffer soils.

In conclusion, this field problem has demonstrated that the spatial variability of the undrained shear strength of soils has a relatively minor influence on the design of pile foundations. However, the influence of spatial variability has been greatly reduced by the LCPC Method itself, which incorporates a maximum limit unit skin friction, $q_{si(max)}$, of either 35 or 80 kPa. The above study has been confined to the axial capacity of a single,

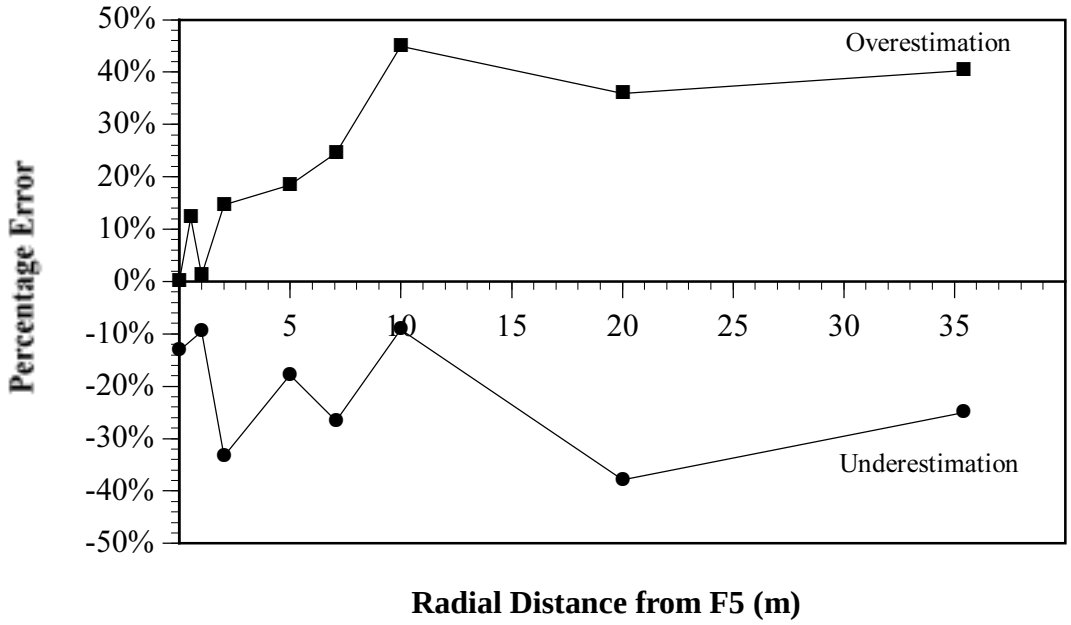

Figure 8.8 Relationship between the percentage error of Q_A and the radial distance of the CPT, used to determine the pile at F5, using an unlimited $q_{si(max)}$.

relatively shallow, pile located at the South Parklands site. It remains to be seen whether the same results would be observed at other sites, using different pile dimensions, and different pile design criteria, such as settlement.

8.3.2.2 Simulated Data

The previous field problem examined the influence of spatial variability on the design capacity of a statically-loaded shallow pile, using CPT data measured at the South Parklands site. However, these data were derived from a soil mass with fixed spatial variability parameters; that is, δ_v and the range, a. The situation presented in this section examines the influence of a on the design capacity of the same pile considered in §8.3.2.1.

In order to carry out such an assessment, it is necessary to generate a large number of realisations of three-dimensional data. At present, there are no readily available procedures for generating 3D simulated data based on random field theory, and hence the influence of δ_v cannot be examined. Geostatistics, on the other hand, provides several techniques for simulating data in three-dimensions. These techniques include: *the turning bands method*, *lower-upper (LU) decomposition*, *sequential Gaussian elimination*, *sequential indicator simulation*, and *simulated annealing* (Journel and Huijbregts, 1978; Olea, 1991; Deutsch and Journel, 1991). The geostatistical software library, *GSLIB*, provides generic Fortran code for each of these simulation techniques. However, the latter

three provide the facility for simulating *conditional* data, that is, where the measured values are honoured, as well as the histogram and model of spatial variability (Deutsch and Journel, 1991; Olea, 1991).

In order to assess the influence of the range, a, on the design axial capacity of the same pile examined in §8.3.2.1, q_c data were simulated using a grid layout as shown in Figures 8.9 and 8.10. The extent of the grid was determined by: the dimensions of the pile; the requirements of the LCPC Method; and the 2 metre lateral extent of the cylinder of soil, explained in the previous section. Hence, the overall grid dimensions were set at 2.0 by 2.0 metres in plan dimensions, by 5.0 metres in depth. The resolution of the grid, that is the spacing between adjacent data points, was chosen as a compromise between the following criteria: (i) to provide sufficient data to enable reliable modelling to be carried out; (ii) to ensure that the total number of simulated data did not exceed computer array and memory limitations; and (iii) to provide reasonable computer solution times. The resulting grid resolution was set at 0.1 metres in each of the three directions, which resulted in a $21 \times 21 \times 50$ grid, representing a total of 22,050 data points.

As mentioned previously, at best, a typical geotechnical investigation may include a single CPT performed along the centreline of each proposed pile. The uncertainty arises as to how well this single CPT represents the 'true' strength of the soil mass associated with the pile, and whether this CPT is influenced by the variability of the soil mass itself. In addressing these concerns, the case study presented in this section will be based on the following procedure:

1. The 'true' strength of the soil mass, which influences the behaviour of the pile, is assumed to be the *spatial average* of the simulated data within the $21 \times 21 \times 50$ grid. It has been argued previously, that the behaviour of many geotechnical engineering systems is governed, not by local parameters, but by spatially averaged characteristics. This is the case with the slope stability of embankments, as shown in §8.2, as well as with pile foundations. As a result, this spatially averaged strength is obtained by averaging the values associated with each depth level. That is, each horizontal plane, which consists of a 21×21 point grid, or 441 simulated values of q_c, is averaged to provide an estimate of the 'true' spatially averaged strength corresponding to that particular depth. The end result is 50 averaged values of q_c, with each one corresponding to a depth from 0.1 metres to 5.0 metres below the ground surface. That is: $(0.1, q_{c1})$, $(0.2, q_{c2})$, $(0.3, q_{c3})$, ... ,$(4.9, q_{c49})$, $(5.0, q_{c50})$.

2. The 'true' design axial capacity of the pile, Q_A, is then determined by substituting these data into the LCPC Method.

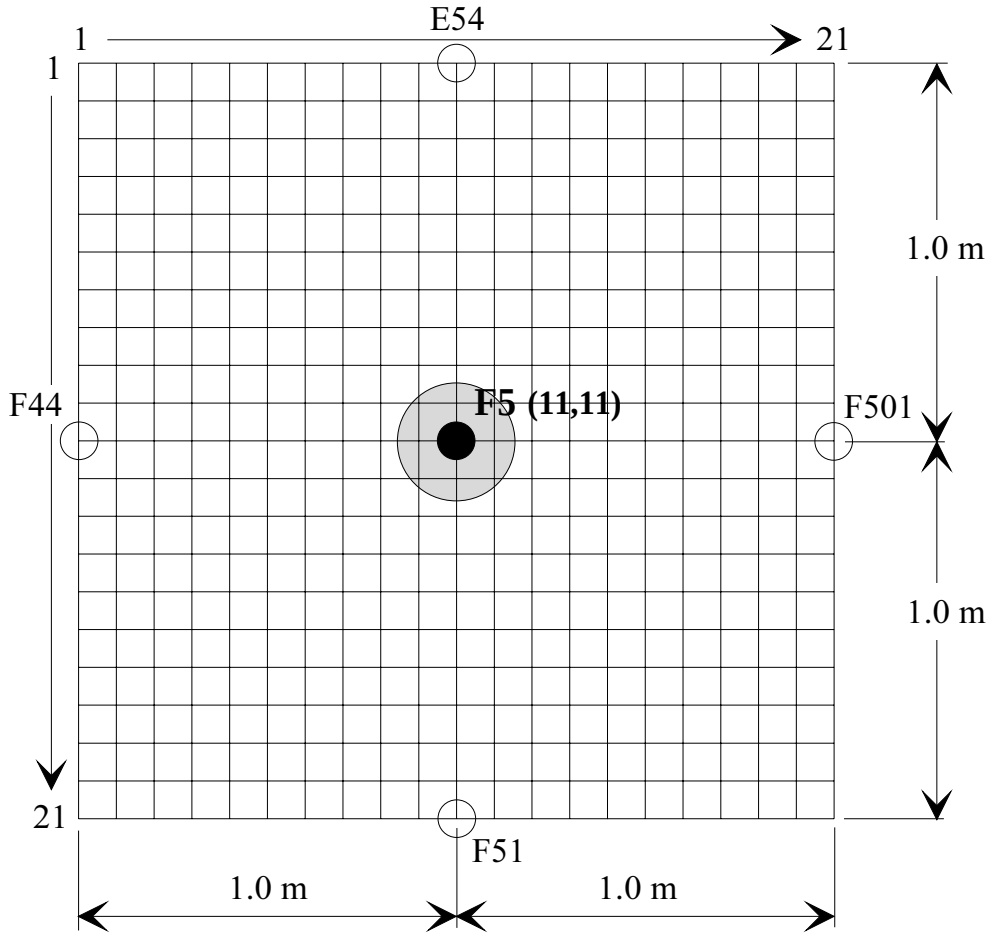

Figure 8.9 Plan view of the grid layout used for the simulated 3D data.

3. The centreline CPT, as shown in Figures 8.9 and 8.10, is obtained by identifying the simulated values associated with the central grid point corresponding to each depth level; that is, at grid coordinates (11,11), as shown in Figure 8.9. Again, the end result is 50 data values, each one associated with a depth from 0.1 metres to 5.0 metres below the ground surface.

4. An estimate of the design axial capacity of the pile, Q_A^*, based on the CPT measurements, is then made by substituting these centreline data into the LCPC Method.

5. The two values of Q_A and Q_A^* are then compared, and the percentage error, E_{Q_A}, is determined by:

$$E_{Q_A} = \frac{Q_A^* - Q_A}{Q_A} \times 100\% \tag{8.6}$$

6. This procedure is subsequently repeated for several different ranges, *a*.

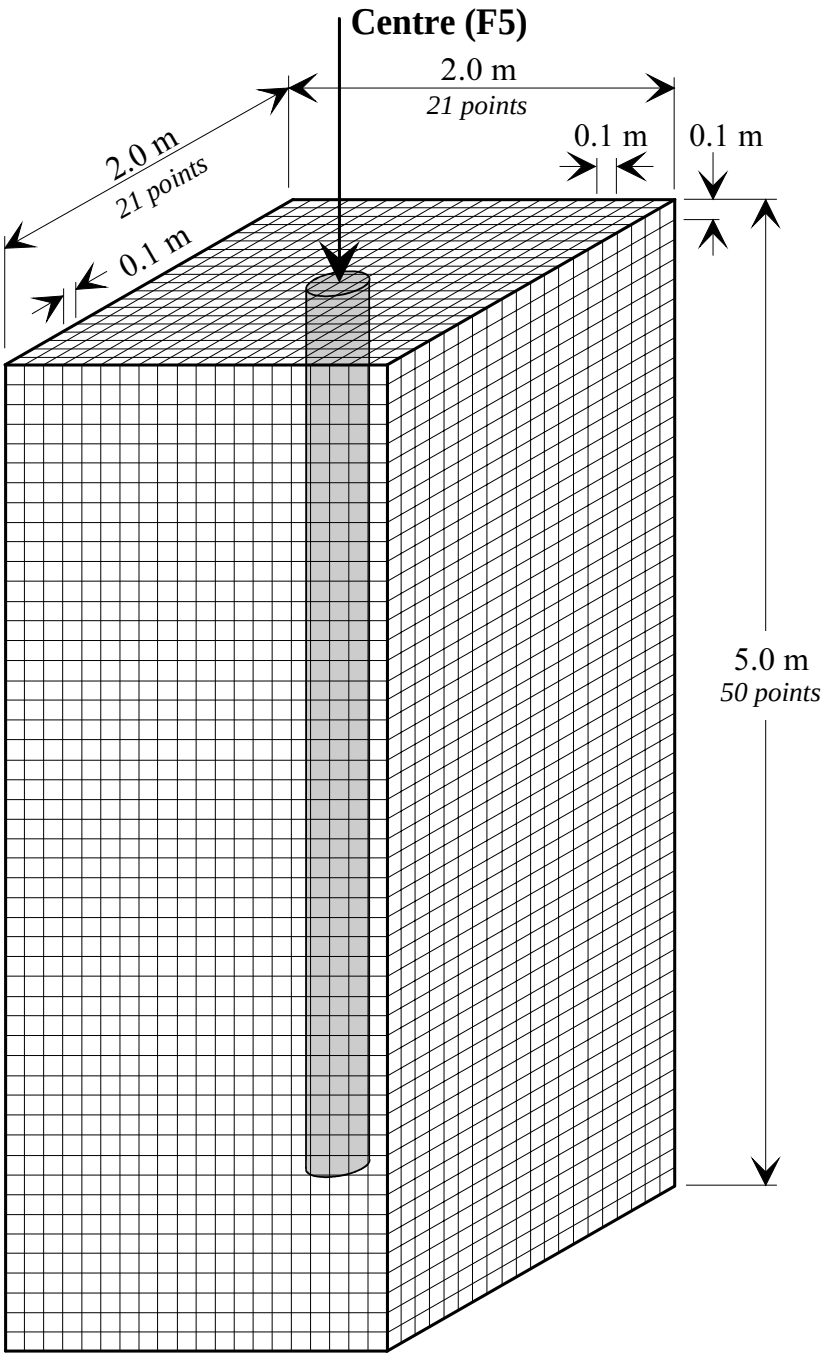

Figure 8.10 Isometric view of the grid layout used for the simulated 3D data.

In choosing a suitable simulation procedure, it is important that realistic and non-negative values of q_c are generated. This can be achieved by using conditional simulation. However, this is not desirable in this situation, since the measured values were derived from a soil deposit with a finite, and consistent, spatial variability structure. As mentioned previously, this field problem seeks to determine the influence of the range, a, on the design axial capacity of a single pile. Hence, if measured values of q_c were used to

condition the simulated data, the spatial variability model of the measurements, and their associated values of *a*, would unduly influence the simulated data.

As a consequence, it was decided to use the unconditional turning bands simulation technique (Journel and Huijbregts, 1978), which generates standardised data; that is, data which follow a Gaussian distribution, and which have a mean of zero, and a variance of unity. These standardised simulated values, $q_{cs}(i)$, can then be *de-standardised* to $q_c(i)$ by the following relationship:

$$q_c(i) = \sigma q_{cs}(i) + m \tag{8.7}$$

In this way, the simulated values honour a normal distribution with a mean of *m*, and a standard deviation of σ.

GSLIB provides a facility for simulating data via the turning bands method, by means of the *TB3D* program. In order to simulate data, *TB3D* requires: an input semivariogram model - either a spherical or exponential model; and a *seed* which is used to randomise the simulation process.

In order to generate realistic simulations, it was decided that the simulated data should honour the mean and variance of the CPT measurements, obtained at the South Parklands site. Two scenarios were assessed: (i) the pile is founded, exclusively, within the Keswick Clay; and (ii) the pile is founded within the soil horizons present at the South Parklands site.

With respect to the first case, 50 CPT data files, which had previously been edited, so that each file included only values of q_c measured within the Keswick Clay (as detailed in §5.3.1), were entered into *SemiAuto* in order to determine the global mean and variance of these data. The results are shown in Table 8.1.

The global statistics associated with the second scenario; that is, pertaining to all of the q_c measurements obtained at the South Parklands site, excluding CPTs CD1 to CD50; were

Table 8.1 Global statistics of measurements of q_c within the Keswick Clay, as well as all soils encountered at the South Parklands site.

Soil Type	Mean, *m* (MPa)	Variance, σ^2 (MPa^2)
Keswick Clay Only	2.495	0.4078
All Soil Horizons, including Keswick Clay	2.953	3.017

shown previously in Table 5.1, and are also included in Table 8.1.

In order to investigate the influence of the range, a, on the design axial capacity of a single, statically-loaded pile, it was decided to model the variability structure of the two soil types by means of an isotropic spherical semivariogram, and to allow a to vary between 0.001 (a completely random soil) and 2,000 metres (a perfectly correlated deposit)[32].

In order to simplify and expedite the simulation process, a pre-processing and post-processing program for *TB3D*, *LCPCSim*, was written using the Visual Basic programming environment. *LCPCSim* performs the following tasks for n simulations, for each of the ranges: 0.001; 0.01; 0.1; 1.0; 10; 100; 1,000; 1,500 and 2,000 metres:

1. Reads the *TB3D* parameter file.

2. Generates a random seed between 0 and 10,000.

3. Writes the random seed, and the range, a, to the appropriate location in the parameter file.

4. Executes *TB3D*, which reads the parameter file as input, and subsequently writes the results to the output file `tb3d.out`.

5. Reads `tb3d.out`.

6. Spatially averages the 50 sets of 21×21 simulated data.

7. Identifies the 50 centreline (F5) data values corresponding to the CPT.

8. The two data sets of q_c values are then substituted into the LCPC Method, and values of q'_{ca}, q_{ca}, Q_B, Q_S, Q_U, and Q_A are determined for each data set. It should be noted that the LCPC Method, as incorporated in *LCPCSim*, uses: $q_{si(max)} = 35$ kPa; $k_c = 0.55$; and $\psi = 40$, as specified in §8.3.1.

9. The percentage error, E_{Q_A}, is evaluated assuming that the spatially averaged strengths indicate the 'true' strength of the soil mass which influences the behaviour of the pile, and the centreline data correspond to measurements that would have been obtained had a CPT been performed at the location of the centreline of the proposed pile.

10. The results are written to an output file for subsequent examination.

---

[32] It was originally intended to examine data simulated using values of a between 0.001 metres (a completely random soil deposit), and 10,000 metres (a perfectly correlated soil profile). However, limitations associated with the *TB3D* program, meant that data could only be simulated with a maximum value of a equal to 2,000 metres.

A typical screen from *LCPCSim* is shown in Figure 8.11.

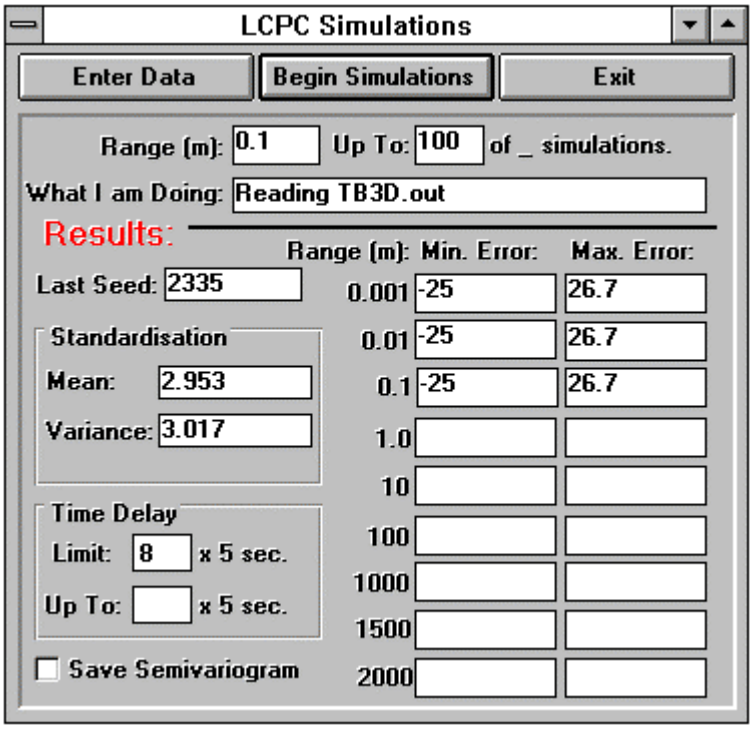

Figure 8.11 A typical screen from *LCPCSim*.

In addition, *LCPCSim* allows the user the option of saving the de-standardised data to a file, whose format is suitable to enable the *GSLIB* program, *GAM3*, to calculate the three-dimensional experimental semivariograms of the simulated data.

In order to assess the validity of these data, a limited number of simulations were entered into the *GAM3* program. The results of two such analyses are shown in Figures 8.12 and 8.13. It can be observed from these figures that the experimental semivariograms of the simulated data are adequate representations of the model semivariogram, which was specified as input to *LCPCSim* and *TB3D*.

In order to examine the influence of the range, a, of the material on the percentage error, E_{Q_A}, it is desirable to quantify the maximum and minimum errors after n simulations, rather than the error resulting from only one simulation. This is due to the fact that, since the simulations are random realisations of a stochastic process, it is not possible to draw any conclusions from a single simulation at each range level. In order to increase the reliability of the conclusions, many realisations at each range level are desirable. As a compromise between the reliability of the results and computer execution time, it was

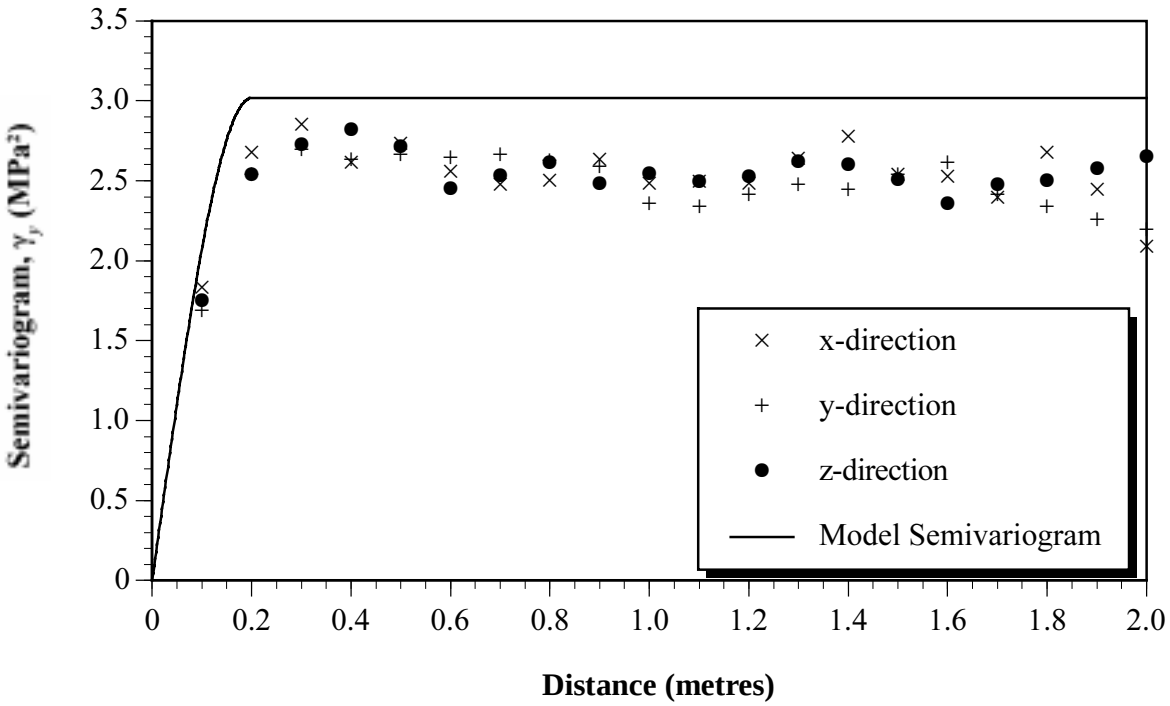

Figure 8.12 Experimental semivariograms for simulated data, compared with the model semivariogram for a = 0.2 metres.

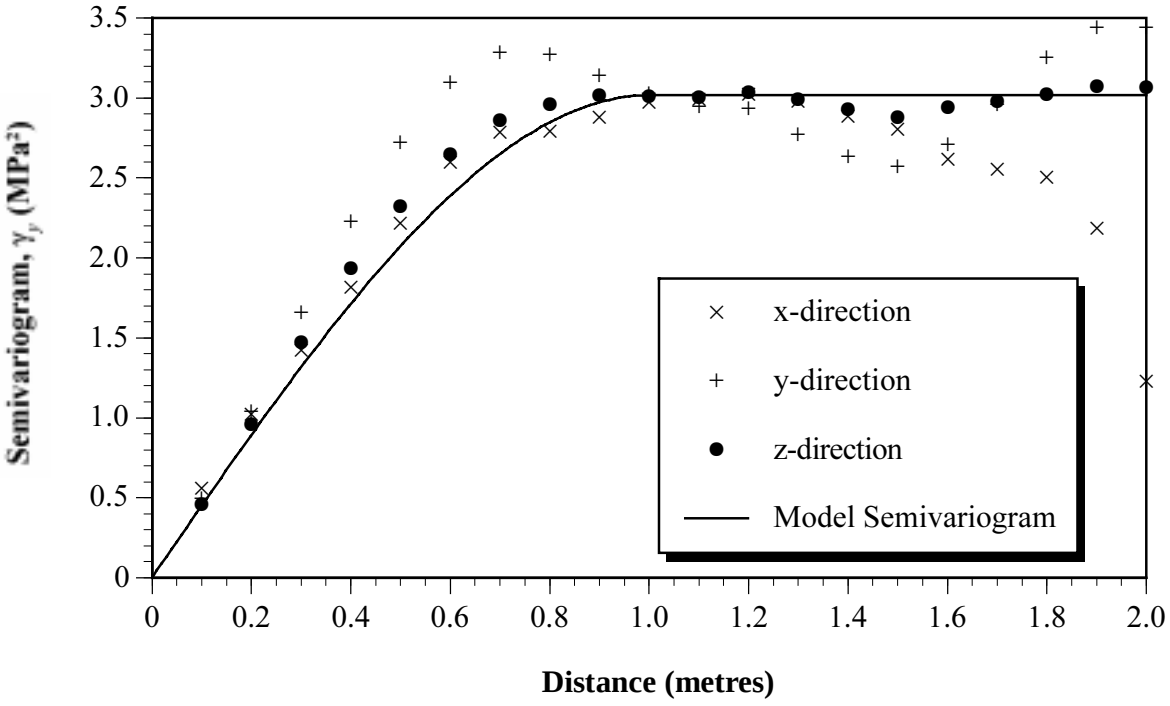

Figure 8.13 Experimental semivariograms for simulated data, compared with the model semivariogram for a = 1.0 metres.

decided to generate 100 simulations at each range level, for both scenarios. The results generated by *LCPCSim* and *TB3D* are summarised in Figures 8.14 and 8.15.

A number of conclusions can be inferred from these figures:

- Unlike the previous case study, considerable overestimates, that is, up to 27%, as well as significant underestimates, up to −25%, can be observed. This implies that the conservatism, which is part of the LCPC Method, has less of an effect when the range decreases; that is, when the randomness of the material increases.

- It should be emphasised that the maximum and minimum errors indicated in Figures 8.14 and 8.15, are exactly that, and in many individual simulations the observed error was significantly lower. As a consequence, one must be aware that there is a probability of occurrence associated with each of the maxima and minima shown in Figures 8.14 and 8.15. By performing many more simulations than have been carried out in this study; that is, many hundreds of simulations, it would be possible to quantify these probabilities, and associate a risk to each of them.

- Figures 8.14 and 8.15 clearly demonstrate that there is a strong relationship between the range, a, and the observed error, E_{Q_A}. As one would expect, for a very homogenous or highly correlated material, the error between the design axial capacity of the pile (as indicated by the central test) and the 'true' pile capacity is relatively low; both in overestimation and underestimation. That is, the test measurements provide a good representation of the 'true' strength. However, as one would expect, as the randomness of the material increases, represented by a decreasing range, the central test measurements fail to adequately represent the spatial average of the soil mass, and consequently, the observed error increases. What is surprising from Figures 8.14 and 8.15, however, is the magnitude of the errors and the degree of homogeneity associated with these errors. In Chapters 2 and 5, it was shown that several researchers have measured ranges, or scales of fluctuation, for s_u, between approximately 0.1 and 50 metres. The errors associated with these ranges can be as large as 20% or more, in both underestimation and overestimation, which is a significant error and compromise of safety, with respect to engineering structures.

- In addition, Figures 8.14 and 8.15 demonstrate that, as the variance of the simulated data increases (that is, the extent of the variability of the soil profile), the error, E_{Q_A}, also increases, as expected. As a result, if the variance associated with a particular site is greater than 3.017 MPa^2 (as given in Figure 8.15), one may expect somewhat larger errors than those indicated by Figures 8.14 and 8.15.

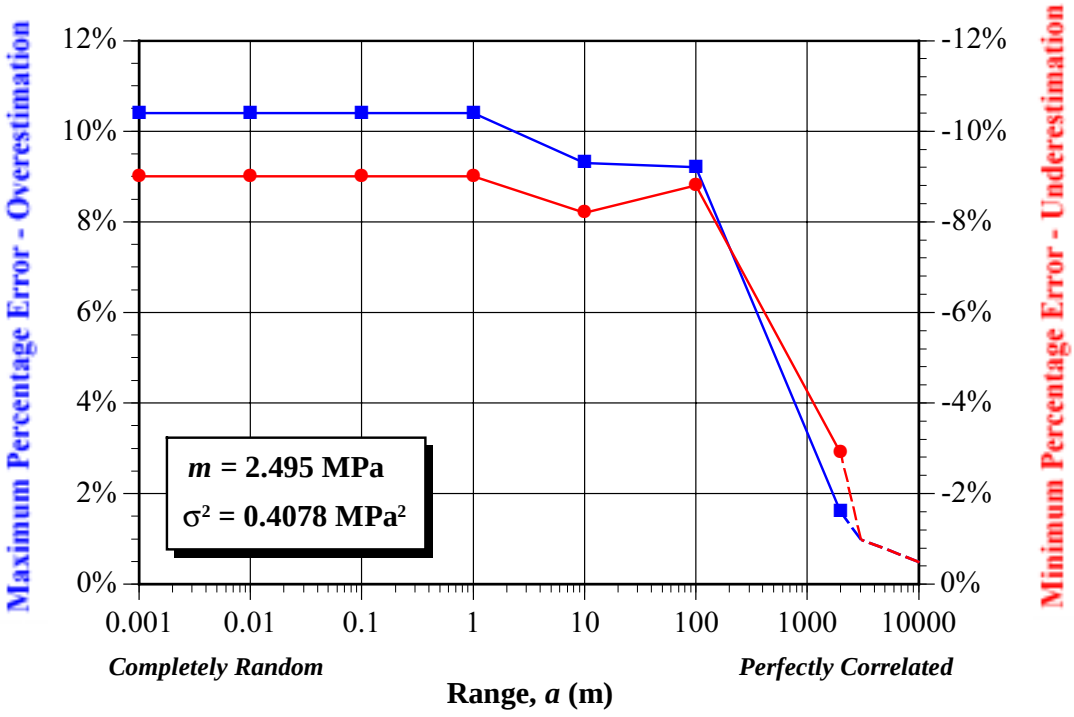

Figure 8.14 Relationship between the range, *a*, and the maximum and minimum percentage errors, E_{Q_A}, assuming the pile is exclusively founded within the Keswick Clay, and using 100 simulations at each range.

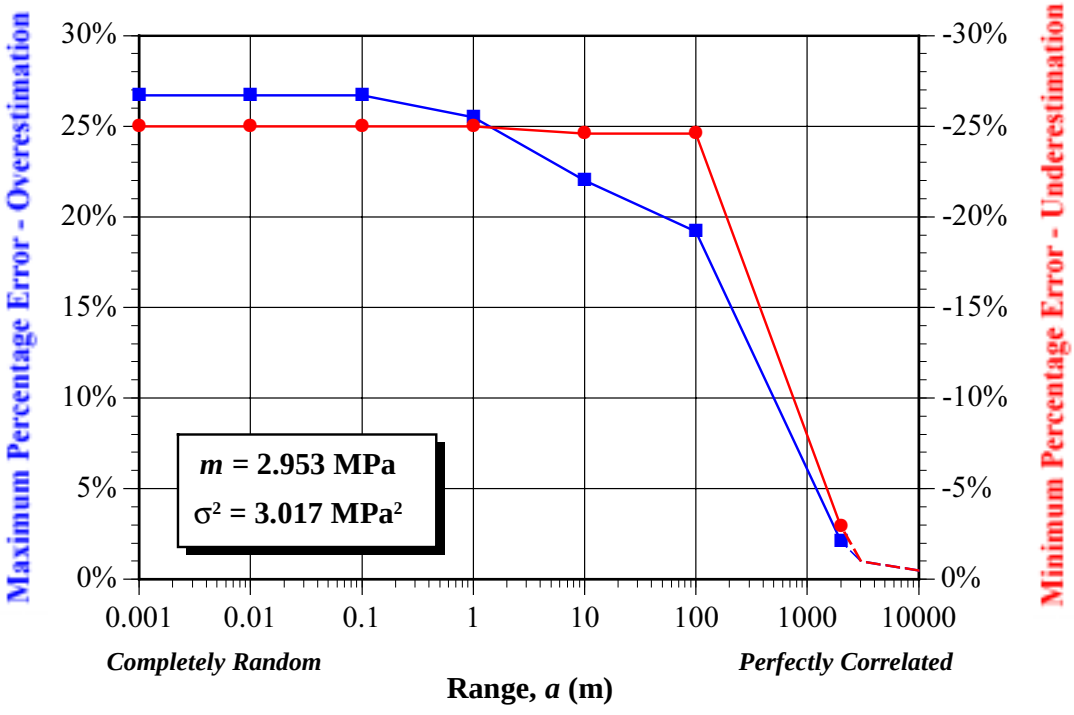

Figure 8.15 Relationship between the range, *a*, and the maximum and minimum percentage errors, E_{Q_A}, assuming the pile is founded within soils similar to those encountered at the South Parklands site, and using 100 simulations at each range.

- It is significant that relatively reliable and acceptable errors are associated with only highly correlated materials; that is, soils where $a \geq 500$ metres. Since the Keswick Clay was observed to exhibit a range, a_3, equal to 300 metres, one would expect the observed error to be relatively low. Figure 8.15 suggests an error of $\pm 10\%$, which compares well with the observed error of between 4% and 8%, shown in Figure 8.6.

- Figures 8.14 and 8.15 indicate that the observed error increases with increasing randomness of the soil mass. This suggests that, in order to reduce the error as the randomness of the material increases, more testing is needed to adequately quantify the soil mass, as one would expect. For example, more than one CPT may be required to satisfactorily estimate the spatial average of a relatively heterogeneous soil mass.

- Finally, it should be noted that the results presented in Figure 8.14, inherently assume that the measurements recorded along the centreline of the pile were obtained with zero measurement error. While the measurement error associated with the CPT was shown in Chapter 5 to be extremely small, other test procedures do possess non-trivial measurement errors, and had these been included in the simulation process, somewhat larger errors would have been observed.

8.4 SUMMARY

This chapter has examined the influence of spatial variability on the design of earth embankments, and the design of pile foundations. In the former case, it has been observed that soils with small scales of fluctuation, say less than one metre, yield lower probabilities of slope failure than soils with large scales of fluctuation. The traditional, deterministic approach of evaluating the *FoS* of the slope, makes no allowance for the uncertainty and autocorrelation structure of the soil properties of the slope material. Such analyses assume perfect correlation, which yield unrealistically high estimates of P_f. While these estimates are conservative, Mostyn and Soo (1992) recommended that they should not be used in economic assessments, but only to provide a ranking of preferred options.

In the case of pile foundations, it has been observed that spatial variability can have a considerable effect on the results obtained. This is particularly so for materials with ranges of influence less than approximately 100 metres. This is significant since no soils, other than the Keswick Clay which exhibits a nested structure, have been found to exhibit a range, or correlation distance, greater than about 50 metres. The observed error between the 'true' design capacity of the pile, and that indicated by measurements, can be as high as 25%, both in underestimation - resulting in a more costly design; or more significantly in

overestimation - resulting in underdesign, which compromises the safety of the overall structure.

In addition, it has been observed that the LCPC Method of pile design, regarded by many as being the most reliable CPT-based pile design technique, can substantially reduce the effect of spatial variability, and as a consequence, results in a more conservative design solution. However, significant errors, both in underestimation and overestimation, can occur when the LCPC Method is applied to soft soils, or to soils which are moderately to highly uncorrelated; that is, $a < 200$ metres.

Chapter Nine

Summary and Conclusions

9.1 SUMMARY

This study has quantified the spatial variability of the Keswick and Hindmarsh Clays, and has examined the significance of spatial variation on geotechnical engineering design. In addition, a methodology has been provided, which enables preliminary estimates of the undrained shear strength of the Keswick Clay to be obtained.

In Chapter 2 it was shown that the Keswick and Hindmarsh Clays are: relatively homogeneous, from an external appearance point of view; significantly fissured, both in the micro- and macro-scales; highly plastic; extremely expansive; overconsolidated, as a result of desiccation; and exhibit remarkably similar properties to those of the well-documented, and internationally significant, London Clay. It was also observed that several researchers have indicated that the cone penetration test (CPT) is an extremely useful measurement device, which exhibits the lowest measurement error of any in situ test procedure in common use, along with the Marchetti flat plate dilatometer. Furthermore, it was observed that, since the early 1970's, spatial variability research has focused on two stochastic techniques: (i) time series analysis, or random field theory when applied to geotechnical engineering; and (ii) geostatistics - the former being used to a far greater extent than the latter. In addition, the available literature demonstrated that these two techniques provide adequate frameworks for quantifying and estimating the spatial variability of geotechnical engineering properties. Finally, it was observed that the vast majority of spatial variability analyses, performed to date, have been based on limited data and on data obtained at relatively large sample spacings. This is particularly so in studies dealing with the lateral variability of geotechnical properties.

Chapter 3 described a micro-computer based data acquisition system for the CPT, developed in order to provide an efficient, reliable and accurate means of recording CPT

data, and in particular, to measure these data at relatively close spacings of 5 mm. Calibration tests performed on the data acquisition system indicated a low level of measurement error, which conformed to criteria specified by international and Australian codes of practice.

Chapter 4 described the experimental programme which consisted of: 222 vertical CPTs, performed to a typical depth of 5 metres, at the South Parklands site; and a single, 7.62 metre, horizontal CPT, performed at the Keswick site. Together, they provided the data for the small-scale examination of the spatial variability of the Keswick Clay. In order to reduce the total measurement error, these tests were carried out in relatively constant climatic conditions, using consistent procedures and equipment, and using a single operator. In addition, it was observed that unconsolidated undrained triaxial tests, performed on undisturbed samples of Keswick Clay, and obtained from the South Parklands site, were inconclusive. As a consequence, subsequent spatial variability analyses were based on measurements of cone tip resistance, q_c, rather than on estimates of undrained shear strength, s_u.

Chapter 5 detailed the spatial variability analyses performed on the CPT data, obtained from the South Parklands and Keswick sites. Due to limited measurements associated with the Hindmarsh Clay, these analyses focused on the undrained shear strength of the Keswick Clay. Both random field theory and geostatistics were employed to model these data, from which a number of conclusions were derived. These include:

- Using random field theory, and in particular the sample autocorrelation function (ACF), it was observed that the undrained shear strength of the Keswick Clay has a vertical scale of fluctuation, δ_v, of approximately 150 mm, with a coefficient of variation, *CV*, of 30%.

- By means of geostatistics, and specifically the semivariogram, it was found that the undrained shear strength of the Keswick Clay exhibits a lateral variability structure which comprises two separate scales of variability. It was shown that these structures could be satisfactorily represented by a nested spherical model, with ranges of influence, a_1 = 0.2 metres, and a_2 = 6 metres.

- By comparing the results given by random field theory and geostatistics, it was observed that, while δ_v and a essentially express the same quantity (that is, the distance over which the relevant parameter exhibits significant correlation), some differences existed between the results of the two parameters. By means of regression analysis, the following relationship between δ_v and a was obtained:

$$\delta_v = 2.559 a^{0.728} \quad \text{with} \quad r^2 = 0.829.$$

- In all of the analyses, it was found that the distance indicated by the sample autocorrelation function (ACF) and the $+2/\sqrt{N}$ line, referred to as *Bartlett's distance*, r_B, yielded almost identical values to those of δ_v. Since r_B is computationally, somewhat easier to evaluate, it was recommended that r_B be used to estimate δ_v.

- Cross-correlation analyses performed on measurements of q_c, and sleeve friction, f_s, indicated that, statistically, the most appropriate value for the shift distance associated with the Keswick Clay is approximately 120 mm, both horizontally and vertically. These analyses demonstrated the usefulness of the cross-correlation function.

- Random field theory model formulation, forecasting and data simulation, indicated that CPT data, detrended by means of an ordinary least squares (OLS) quadratic trend, were best modelled by an autoregressive process (AR) with up to 8 parameters. In contrast, first-differenced CPT data were most appropriately modelled by means of an integrated moving average (IMA) process with up to 5 parameters. When used to simulate CPT data, it was observed that the AR models, when recombined with the OLS quadratic trend, yielded more robust simulations than those given by the first-differenced IMA models.

- It was demonstrated that geostatistics provides a more flexible framework for the prediction of values at yet-to-be tested locations, than does the technique of random field theory. In a one-dimensional prediction sense, it was observed that kriging provided as good estimates as those given by random field theory, and in some cases, the predictions were significantly better.

- It was shown that the random measurement error associated with a particular test procedure, as well as the spatial variability parameters δ_v, a, the sill, C, and the nugget effect, C_0, are extremely sensitive to sample spacing and the degree of trend removed; particularly when the data are non-stationarity, as given by Kendall's τ test. Analyses which fail to include these aspects may yield misleading results. For example, it was demonstrated that by varying the sample spacing and the degree of trend removed from the data, Baecher's method for determining the random measurement error associated with a particular test method, yielded significantly different results.

- Finally, by means of Baecher's method, it was shown that the random measurement error associated with the CPT is extremely low; that is, of the order of 2%, or less.

In Chapter 6, the *KESWICK* data base, which was used to examine the large-scale spatial variability of the Keswick Clay, was described. It was observed that data bases are useful tools for examining the relationships and trends that may exist between various geotechnical parameters. In addition, it was found that, on its own, the *KESWICK* data base is an

inadequate facility for quantifying the spatial variability of the undrained shear strength of the Keswick Clay.

By combining the results obtained from Chapter 5, as well as the data from the *KESWICK* data base, Chapter 7 detailed the modelling of the large-scale lateral spatial variability of the undrained shear strength of the Keswick Clay, using geostatistics. It was found that the lateral variation of s_u of the Keswick Clay exhibits a nested structure at 3 distinct scales of variability. It was shown that the variability structure could be satisfactorily represented by a nested spherical model with three ranges of influence: a_1 = 0.2 metres; a_2 = 6 metres; and a_3 = 300 metres. Furthermore, it was demonstrated that the geostatistical process of kriging yielded very good preliminary estimates of the undrained shear strength of the Keswick Clay at untested locations. These were superior to the polygonal, inverse distance, and inverse distance squared weighting estimation regimes. Chapter 7 described two methods of predicting the undrained shear strength of the Keswick Clay, within the Adelaide city area, and the upper 3 metres of the surface of the clay. Firstly, a contour map (Figure 7.13) gave the gross variability of s_u across the study area, within a resolution of 25 kPa. The second method utilised the nested spherical model, and the kriging process, to describe a technique for estimating s_u at any given easting and northing within the Adelaide city area, with increased precision. It was noted that a significant advantage of geostatistics is, that it quantifies the error associated with any particular estimate, via the kriging variance, or the kriging standard deviation, σ_k.

Finally, Chapter 8 examined the influence of spatial variability on the design of earth embankments and pile foundations. It was pointed out that the traditional methods of slope stability analyses, which are based on a factor of safety approach, take no account of uncertainty and autocorrelation structure of the soil properties of the slope material, and hence assume that the soil is perfectly correlated. While this assumption results in conservative designs, such analyses may yield unrealistically high estimates of the failure probability, P_f; particularly when δ_v is relatively low. With regard to pile design, it was observed that spatial variability can have a considerable effect on the results obtained. To some extent, the LCPC Method of estimating the ultimate axial capacity of a single pile, provides conservative estimates. However, it was shown that as the randomness of the material increases; that is, as a and δ_v decrease; the error between the 'true' design axial pile capacity and that estimated from limited testing, can be unacceptably high. These errors can result in unacceptable over-conservatism, or an unacceptable compromise in the level of safety of the structure.

9.2 RECOMMENDATIONS FOR FUTURE RESEARCH

The spatial variability analyses presented in this thesis focused on two stochastic frameworks, namely, random field theory and geostatistics. While the results of these analyses were encouraging, the quality of their estimates was restricted by the relative simplicity of the linear models incorporated in each of the respective theories. One would anticipate that somewhat more accurate predictions would result by incorporating a more complex combination of the neighbouring observations in the relevant theories. Recently, more advanced time series analysis procedures have been developed which better model non-stationary or non-linear data, which may include sudden fluctuations, or discontinuities. These models, known as *time-variable parameter* (TVP) models, are based on random fields which incorporate five separate components, namely: trend; stochastic perturbation; signal; seasonal; and white noise (Ng and Young, 1990). Applications of these models have yielded encouraging results (Ng and Young, 1990; Young, 1994). In addition, other forms of kriging, notably universal kriging, have yet to be applied to the data presented in this thesis. Furthermore, *neural networks*, an estimation regime which has recently gained momentum and, which has only very recently been applied to geotechnical engineering problems (e.g. Goh, 1994; Hawtin and Lim, 1994), has the ability to model complex interactions between many parameters, and may be applicable to the estimation of undrained shear strength. All of these techniques need evaluation to ascertain whether any one, or more, of these methods can provide superior results to those presented in this study. In addition, tractable random field theory estimation procedures remain to be developed for two- and three-dimensions.

The application of random field theory and geostatistics presented in this thesis, has incorporated trend estimation based on ordinary least squares (OLS). As mentioned in Chapter 5, OLS is based on the assumption that the data are random and uncorrelated. This is inconsistent with spatial variability analyses which, having removed some trend determined by OLS, subsequently examine the correlation structure of the residuals. Li (1991) suggested that a technique based on generalised least squares (GLS) be used as an alternative to OLS, and that the trend may be modelled using a number of different mathematical functions; for example, cubic splines. It was demonstrated in Chapter 5 that data stationarity, or the type of trend removed from the data, can significantly influence the resulting spatial variability parameters. Research is needed to investigate the extent to which spatial variability parameters, and the subsequent estimates, are sensitive to the type of trend used in the modelling process.

The examination of spatial variability, presented in this study, has focused on the undrained shear strength of the Keswick Clay. Other geotechnical engineering design parameters,

such as: internal angle of friction, ϕ; Young's modulus of elasticity, E; coefficient of earth pressure at rest, K_0; and coefficient of consolidation, c_v, may, and are likely to, have different correlation distances to those of the undrained shear strength. In addition, only one soil type, a stiff, overconsolidated clay, has been examined. Several other soil types, including loose and dense sands, soft clays, silts, calcareous deposits, and organic soils, remain to be investigated in detail. As a consequence, a number of carefully controlled test programmes, with data measured at close-spacings, are needed to quantify the spatial variability of these geotechnical design parameters, in a variety of well-documented soil deposits.

In Chapters 5 and 7, spatial variability models were developed based on the parameters δ_H, δ_V and a, and data obtained from the CPT. The question arises as to whether these results are test dependent or not. In other words, would the same results have been obtained if the analyses were based on measurements of s_u from triaxial tests, vane shear tests, or self-boring pressuremeter tests? One would hope that the results are not test-dependent. However, while Chiasson et al. (1995) have shown that data, from vane shear tests and piezocone soundings, yielded the same spatial covariance and statistical distribution, more work is needed in this area.

By definition, the scale of fluctuation, δ_v, and the range of influence, a, are measures of the correlation distance; that is, the extent over which a parameter exhibits significant correlation. It was shown in Chapter 5, from an experimental view point, that random field theory and geostatistical analyses yielded comparable, though on the whole, different quantities for δ_v and a. Research is needed to identify the theoretical similarities and differences between these two parameters. In addition, the term *correlation distance*, appears to be somewhat loosely defined, and research is needed to theoretically determine the similarities and differences between it and the quantities δ_v and a.

It was evident from the treatment given to the design of pile foundations, in Chapter 8, that there is little information regarding the lateral extent over which the undrained shear strength of a soil deposit contributes to the load-carrying capacity of a pile. Research effort is needed in this regard. Furthermore, the assessment of the influence of spatial variability on the design of pile foundations, focused on the axial capacity of a single pile. It remains to be shown whether the same results would have been obtained using piles of different dimensions, or using different pile design criteria, such as pile settlement.

9.3 CONCLUSION

From the analyses presented in this thesis, it can be concluded that:

- the CPT has a very low random measurement error, of the order of 2%, or less;
- from closely-spaced data acquired from the CPT, nested structures have been observed within the Keswick Clay;
- the scale of fluctuation, δ_v, and the range of influence, a, essentially measure the distance over which properties exhibit strong correlation; that is, the correlation distance;
- the LCPC Method, for the estimation of the ultimate axial capacity of a statically-loaded pile, tends to under-predict the capacity, and hence, is conservative;
- the spatial variability of the undrained shear strength of a soil mass can greatly influence the axial capacity of a pile foundation. In particular, as the variability of the soil increases, so too does the error associated with the estimated capacity of the pile. In a very variable soil deposit, the estimated capacity of a pile foundation may result in an unsafe design.